Ultrafast electronic and coupled electronic-nuclear dynamics of solvated metal complexes

Diana Bregenholt Zederkof

15. December 2020

PhD thesis

DTU Physics
Department of Physics

Academic Advisors
Kristoffer Haldrup
Martin M. Nielsen
Kristian S. Thygesen

DTU Physics
Department of Physics

Preface

This thesis was submitted to the Department of Physics, Technical University of Denmark (DTU), as part of the requirements for obtaining the Ph.D. degree in Physics. The work described in the thesis was mainly carried out at the Department of Physics, DTU, under the academic advisors Sr. Scientist Kristoffer Haldrup, Professor Martin M. Nielsen and Professor Dr. Techn. Kristian S. Thygesen. Additionally, the work was carried out during several experiments (each 1-2 weeks) conducted at one of the large scale X-ray facilities, named the LCLS (USA), E-XFEL (Germany) or SACLA (Japan). Experimental work (over ∼3 weeks) was also carried out at the Department of Chemical Physics, Lund University in collaboration with Assc. Sr. Lecturer Jens Uhlig and (former) Post Doc Kasper S. Kjær. Furthermore, the work involved an external research stay of 7 months, and few short re-visits in Vienna, visiting the group of Univ.-Prof. Dr. Dr. h.c Leticia González, at the University of Vienna. The external research stay concerned excited state dynamics simulations carried out in close collaboration with Post Doc Sebastian Mai.

The prerequisites to read this thesis involve basic knowledge within the field of chemistry and physics taught at the university level. However, basic concepts of time-resolved studies, X-ray scattering and electronic structure calculations are also described.

Diana Bregenholt Zederkof

Acknowledgements

First of all, I thank my supervisors, Kristoffer, Martin and Kristian, for starting this Ph.D. project with me, and giving me the opportunity of starting a mixed theory and experimental Ph.D. project within a very exciting research field of ultrafast science. Thank you for giving me the opportunity to travel around the world for conferences, visits to collaborators and participation in numerous beamtimes. Additionally, thanks for being supportive during rough times at home. Also an enormous thanks to the head of the department, Jane for being so understanding of my situation and extending the deadline for this thesis. I would also like to thank all involved in the administrative work, Marianne, Hanne, Helle and Bettina. You were all very helpful.

Thinking back to when I started in the group, I would like to thank the people already in the ultrafast group, Elisa, Mads, Frederik and Tim, for letting me feel welcome in the office. Especially, I would like to thank Elisa Biasin for helping me with the $[Ru(bpy)_3]^{2+}$ data, and for being a mentor, when I was new to the field. Later, Mads G. Laursen taught me how to handle data reduction at beamtimes. I am very grateful of this, since during beamtimes most people are stressed, and are not in a position to help and explain. You are an amazing teacher who explains in a straightforward and understandeble manner, and test me with questions! Mads, you are such an awesome friend and I miss having you around as a colleague. I would also like to thank other people who were part of the ultrafast group for either shorter or longer times, Tobias, Kasper, Peter, Lise, Asbjørn, Anders and Asmund. Thanks to the bachelor students, I co-advised, for asking questions I could not answer immediately. It also helped me understand my own field even better, and especially the translation between the "language" of physics and chemistry. Also thanks to the

new people who joined the group Philipp, and Asmus (re-joined), after a time where I was very alone in the office. Especially thanks to Asmus O. Dohn for bringing new energy to the office, for listening to me complain sometimes (a lot!), and for understanding the importance of the choice of function for the dampening of calculated scattering. I hope you find someone else to steal chocolate from, once I leave the group.

I would like to thank everyone in the ultrafast group and collaborators for fun and frustration at beamtimes. Looking back, these times were some of the toughest times in terms of work/sleep/food balance, but also some of the times I enjoyed the most during my Ph.D. studies, with a lot of fun memories.

Thanks to other colleagues at DTU. I also enjoyed the company from many NEXMAP'ers and CAMD's, in particular for cookie-breaks. We could find a common understanding of the ups and downs of the Ph.D. life at DTU Physics. Thanks to Korina, Monish, Sten and Marianne from CAMD who gave me a warm welcome, when I began my Ph.D. studies. Thanks for your company and for helping me in the beginning. Later, also Estefania and Daniele joined CAMD, and thank you for your friendship and playing a lot of board games, also with Mads and Korina. I have really missed you all the past year, where I did not have any energy to socialize. I hope to see you again soon, when Corona is less in control of social events.

I have also collaborated with the Department of Chemistry, and I would especially like to thank Klaus, Matyas, Gianluca and Mostafa. Thanks for your insights into the theoretical side of structural dynamics, and for several fruitful discussions. You all helped me understand the theoretical simulations, and contributed with geometries, partial charges and QM/MM MD simulations that were crucial for the investigations on the $[Ru(bpy)_3]^{2+}$ system.

Additionally, I spent 7 months and a few re-visits in Vienna, and I would like to thank Leticia González for letting me visit her group. In particular, thanks to Sebastian Mai, for all the help with the simulations to someone who came from an experimental group. Thanks for answering all of my many questions, and for always being ready to assist and explain. Also, thanks to my supervisors to let me pursue my own wishes of going to Vienna for the external research stay. Thanks to all in the González group for letting me feel very welcome and for social events, Davide, Moritz,

Sandra, Clemens, Martina (+Lorenzo), Boris (+Veronika), Lea, Lin, Nadja, Julia, Isolde, Max, Pedro, Nico (+Alba), Gustavo, Leopold and Omar. I am especially grateful that so many of you came to my wedding in Denmark.

A great thanks also goes to all my other friends, especially Emma and Tine. Thank you for good times and for listening to me complain a lot during rough times. Thanks for reaching out when I was not good at keeping contact. I am deeply grateful. Emma, you mean a lot to me and always inspire me, and I would not have made it to the finish line without your advice and endless encouragement.

To my family: Tak til min familie. Kære far, mor og Vicktoria, tak for jeres kærlighed og for jeres anerkendelse af mit Ph.D. studie. I har alle rost mig for mit arbejde, og støttet mig i mange af mine rejser. Jeg husker tilbage på hyggelige stunder, og at I besøgte mig på flere af mine rejser. Også tak til Kirsten og Gustav for at få mig til at føle mig velkommen i svigerfamilien. Og tak til Edit, Kurt og Anette, for altid at lytte ivrigt, når jeg fortæller om mine eventyr.

Finally, my special thanks goes to my husband, Mads Bregenholt Jakobsen. There are not enough pages to express my gratitude to you, for all the support I received throughout these past years. My dearest Mads, you have been there all the way during this long journey giving me endless support, listening and even helping me with the mathematics or programming challenges I faced sometimes. I can never thank you enough for being there when I was most stressed and pushed to the limit. You even married me during a stressful time, and I am so grateful that we decided not to wait having our beautiful wedding. I look forward to a more relaxed future full of joy and happiness.

Contents

Abstract

The work presented in this thesis concerns the topic of ultrafast electronic and structural dynamics of solvated transition metal complexes induced by absorption of visible light. Methods of investigations include time-resolved X-ray scattering experiments conducted at an X-ray Free Electron Laser (XFEL), along with dynamics simulations of solvated metal complexes, at several levels of theory. In particular, the results of structural dynamics related to excited states of metal-to-ligand charge transfer (MLCT) character and the interaction of the metal complexes with solvent are presented.

The first part of the thesis describes the basics of the experimental work employing time-resolved wide angle X-ray scattering (TR-WAXS) measurements conducted at XFELs. The experimental part describes the background theory of X-ray scattering as a useful tool to determine changes in molecular structure, and how we apply the technique to study the structural dynamics of transition metal complexes in solution.

The second part covers the relevant aspects of the theoretical concepts of the computational methods for the studied transition metal complexes. It covers the different levels of theory involved in the study, including different ways to simulate the solvent, and how we employ simulations to study ultrafast structural dynamics.

The third part of the thesis is focused on the investigations of the structural dynamics of the two main systems under study, namely the $[Ru(bpy)_3]^{2+}$ and $[Fe(bpy)(CN)_4]^{2-}$ complexes (bpy = 2,2'-bipyridine) in aqueous solution.

The studies of $[Ru(bpy)_3]^{2+}$ concerns the analysis of the early (<3.5 ps) times after photoexcitation from ultrafast TR-WAXS measurements. The

analysis uses the methods described in part I, and several of the computational tools presented in part II, to create a model and compare to the experimental data. The results show only small structural changes (0-0.01 Å) of the bond lengths of the $[Ru(bpy)_3]^{2+}$ system in the MLCT excited states, following absorption of visible light. However, despite the small structural changes in the system, the structural dynamics give rise to a quite significant change in the measured scattering signals upon photoexcitation. The observed features in the signals are suggested to arise from structural changes in both the solute and solvent, with indications of the solvent response arising faster than the solute structural response.

The studies of $[Fe(bpy)(CN)_4]^{2-}$ in solution mainly employ ultrafast excited state dynamics simulations of the earliest 700 fs after excitation. Results include the simulated absorption spectrum, which shows good agreement with experiment, along with the time-dependant electronic populations, charge transfer character of the excited states, radial distribution functions (RDF), hydrogen bond analysis and calculated time-resolved difference scattering signals. Excitation into the lowest energy band of the absorption spectrum leads to populations of excited states of predominantly ^{1}MLCT character, which relaxes to triplet states of mainly ^{3}MLCT and ^{3}MC character in a branched decay mechanism. The study finds that ^{3}MC states are populated with a time constant of 0.53 ± 0.09 ps and the overall intersystem crossing time is 0.21 ± 0.01 ps. The RDFs shows a strong interaction between the solute and solvent through hydrogen bonding to the cyanides, which weakens following photoexcitation. The structural changes of the solute within the first 100 fs are small (~ 0.05 Å), in accordance with the observation of low structural changes associated with population of MLCT states.

For both systems, the nature of the solvent effects the photoinduced dynamics and thus the local environment plays a more important role than previously anticipated. For future investigations of structural dynamics related to MLCT excited states of transition metal complexes, the solvent effects should also be considered.

Dansk resumé

Arbejdet, der præsenteres i denne afhandling omhandler emnet ultra-hurtig elektron og strukturel dynamik for overgangsmetal-komplekser i opløsning, som er igangsat efter absorption af synligt lys. Metoderne for undersøgelserne involverer tidsopløst røntgenspredningseksperimenter, der udføres på en Fri-Elektron-Røntgen-Laser (XFEL), samt simuleringer af metal-kompleksers dynamik på forskellige teoretiske niveauer. Især præsenteres resultater for strukturel dynamik relateret til anslåede tilstande (excited states) karakteriseret som metal-til-ligand-ladnings-overførsels (MLCT) tilstande og vekselvirkningen af metal-komplekset og opløsningsmidlet.

Den første del af afhandlingen beskriver grundprincipperne for den eksperimentelle metode, der bruger tidsopløst bred-vinkel-røntgen-spredning (TR-WAXS), udført på XFELs. Den eksperimentelle del beskriver baggrunden for røntgenspredning som et nyttigt værktøj til at klarlægge ændringer i molekylær struktur, samt hvordan vi anvender denne teknik til at studere den strukturelle udvikling for metal-komplekser i opløsning.

Den anden del handler om de relevante teoretiske koncepter for de computerbaserede metoder til studiet af overgangsmetal-komplekserne. Delen omfatter de forskellige teoretiske niveauer, som er involveret i studiet, inklusiv forskellige måder at simulere opløsningsmidlet på, og hvordan vi bruger simuleringer til studier af ultrahurig strukturel dynamik.

Den tredje del af afhandlingen fokuserer på undersøgelserne af den strukturelle dynamik for de to systemer som primært er undersøgt, nemlig komplekserne $[Ru(bpy)_3]^{2+}$ og $[Fe(bpy)(CN)_4]^{2-}$ (bpy = 2,2'-bipyridin) i vandig opløsning.

Studierne af $[Ru(bpy)_3]^{2+}$ komplekset drejer sig om de tidlige (< 3.5 ps) tidsskridt efter den igangsatte anslåede tilstand, fra ultra-hurtige tidso-

pløste TR-WAXS målinger. Analysen anvender metoderne beskrevet i del I, og adskillige af de computerbaserede væktøjer beskrevet i del II, til at opbygge en model og sammenligne den med de eksperimentelle målinger. Resultaterne viser kun små strukturelle ændringer (0-0.01 Å) for bindingslængder i $[Ru(bpy)_3]^{2+}$ systemet i den MLCT anslåede tilstand opstået som konsekvens af absorption af synligt lys. Dog på trods af de meget små strukturelle ændringer i systemet, giver den strukturelle dynamik anledning til en ganske betydelig ændring i de målte spredningssignaler efter lysabsorption. Disse ændringer i signalerne tænkes at fremkomme som resultat af strukturelle ændringer i prøven fra både komplekset og opløsningsmidlet, endda med indikationer af, at opløsningsmidlet reagerer hurtigere end komplekset ændrer struktur.

Studierne af $[Fe(bpy)(CN)_4]^{2-}$ i vandig opløsning, handler primært om simuleringer af dynamikken bag de anslåede tilstande, især de første 700 fs efter lysabsorptionsprocessen er begyndt. Resultaterne indeholder det simulerede absorptionsspektrum, som viser god overensstemmelse med det eksperimentelle spektrum, og indenholder desuden information om den tidsafhængige elektroniske udvikling, samt typen af ladningsoverførsel i de forskellige tilstande, radiale distributions funktioner (RDF), analyse af hydrogenbindinger samt simulerede tidsopløste spredningssignaler. Lysabsorption for det laveste energi niveau bånd i absorptionsspektret medfører en aslået tilstand, der primært viser ^{1}MLCT karakter, som sidenhen udvikler sig til andre tilstande af både ^{3}MLCT og ^{3}MC karakter via en forgreningsprocess. Studiet kommer frem til at disse ^{3}MC tilstande opbygges indenfor 0.53 ± 0.09 ps, og den overordnede $1 \rightarrow 3$ (intersystem crossing) overgang foregår i løbet af 0.21 ± 0.01 ps. RDF'erne fra studiet viser en kraftig vekselvirkning mellem komplekset og opløsningsmidlet, via hydrogenbindinger til cyandiderne, hvilket svækkes efter lysabsorptionsprocessen starter. De strukturelle ændringer af komplekset er små (~ 0.05 Å), inden for de første 100 fs, i overenstemmelse med, at kun små strukturelle ændringer ses i forbindelse med anslåede tilstande, der viser MLCT karakter.

For begge systemer spiller typen af opløsningsmiddel en større rolle, for den igangsatte dynamik fra lys, end tidligere antaget. For fremtidige studier af den strukturelle dynamik relateret til MLCT anslåede tilstande for metal-komplekser bør opløsningsmidlet også tages med i betragtning.

List of Abbreviations

bpy 2,2'-bipyridine.

CN cyanide.

DFT Density Functional Theory.

DMA dimethylacetamide, $CH_3CON(CH_3)_2$.

DMF dimethyl formamide, $(CH_3)_2NC(O)H$.

DMSO dimethyl sulfoxide, $(CH_3)_2SO$.

ES excited state.

fs femtosecond, $1 \cdot 10^{-15}$ s.

FWHM Full-width at half maximum.

GS ground state.

IC internal conversion.

ISC intersystem crossing.

LC ligand-centered.

LMCT ligand-to-metal charge transfer.

MC metal-centered.

MCH Molecular Coulomb Hamiltonian.

MD Molecular Dynamics.

MLCT metal-to-ligand charge transfer.

MM Molecular Mechanics.

MO molecular orbital.

PAC Partial atomic charge.

ps picosecond, $1 \cdot 10^{-12}$ s.

QM Quantum Mechanics.

QM/MM Quantum Mechanics/Molecular Mechanics.

RDF radial distribution function.

SHARC Surface Hopping including Arbitrary Couplings.

TA Transient Absorption spectroscopy.

TD-DFT Time-dependent Density Functional Theory.

WAXS Wide Angle X-ray Scattering.

XAS X-ray Absorption Spectroscopy.

XES X-ray Emission Spectroscopy.

XFEL X-ray Free Electron Laser.

Å Ångstrøm, $1 \cdot 10^{-10}$ m.

Chapter 1

Introduction

Understanding the relationship between chemical structure and function of molecular systems in materials has been a long standing goal in chemistry, and remains of key scientific interest. Studying the fundamental behavior of small molecules and how they interact during a chemical reaction allows us to ultimately design materials with optimal desired properties from optimizations of the structure on the molecular level.

Additionally, understanding the flow of energy involved in excited state processes, allow us to ultimately steer the outcome of a given chemical reaction. In particular, materials of use within energy conversion from sunlight to electricity are of interest, due to the increasing need of sustainable energy sources. Hence, the interaction between light-absorbing materials and visible light are key principles to understand.

In particular, we wish to investigate the simultaneous evolution of the electronic and nuclear degrees of freedom in molecular systems after absorption of light, and how electronic and structural dynamics couple. For applications within solar-energy conversion, systems of interest include, so called transition metal complexes, due to their ability to interact with a wide range of visible light and the possibility to tune their photo-physical and -chemical properties by ”manipulation” of the molecular structure [1, 2].

In order to observe the dynamics of the molecular structure, in real-time, following absorption of light, we need to enter the so-called ultrafast regime. The following sections give a brief introduction to the field of ultrafast chemistry and how to observe ultrafast molecular dynamics experimentally. In addition, the following section gives a short overview

of the fundamental structure and relevant electronic transitions of transition metal complexes. Subsequently, the systems of interest for the work related to this thesis are presented. The final section gives an outline of this thesis.

1.1 Ultrafast dynamics in small molecular systems

Investigations of ultrafast processes concern the dynamics observed at very short time scales, namely down to the femtosecond (fs) time scale ($1\,\text{fs} = 10^{-15}\,\text{s}$). At such short time scales, we are able to observe molecular dynamics such as nuclear vibrational motion, and the movements of atoms during chemical reactions.

The field of femtochemistry [3] concerns the study of chemical reactions, and the reaction intermediates at the ultrafast time scales. The earliest ultrafast experiments were performed by the group of A. H. Zewail in the 1980's, which investigated the bond breaking mechanism in di-atomic [4] and tri-atomic molecules [5, 6], in real-time. Today, Zewail is considered the founder of femtochemistry, and hence of ultrafast science of fundamental chemical processes, and he was awarded the Nobel Prize in Chemistry in 1999.

Observation of ultrafast processes were made possible by the development of techniques using ultrashort (fs) pulses from optical lasers. The time dependence in such type of experiments is most often achieved using the pump-probe methodology, in which a first pulse (the pump) initiates a given chemical reaction, followed by a second pulse (the probe) that captures a snapshot of the atomic motion, at a time Δt later. The time dependence arise from the change in arrival time of the second pulse, at various delays, Δt after the first pulse, and a collection of the sequences of pump-probe events result in a "movie" of the chemical dynamics.

The earliest experiments with ultrafast time-resolution, employed optical lasers, which mainly controls and monitors the change in absorbed or emitted light. However, these optical measurements, do not necessarily correlate directly to the structural changes. Information on the structural changes in optical measurements arise indirectly from detailed knowledge of the electronic structure of the given system. In case of small sys-

tems such as diatomic or triatomic molecules, the information is easily obtained from electronic structure calculations [7]. As the system size grows, the electronic structure becomes increasingly complicated, which require more advanced and computationally expensive methods. In particular, systems involving solvent effects makes the problem even more complex.

A more direct probe of structural changes relies on the use of X-rays as the probe [8]. Obtaining intense ultrashort X-rays with fs pulses, have been a challenge, but is nowadays possible with the advent of the large scale facilities referred to as X-ray Free Electron Lasers (XFELs) [9, 10, 11]. The first XFEL with wavelengths on the order of atomic bond lengths ($1\text{Å} = 10^{-10}$ m) opened in 2010 [12], which makes use of XFELs a young field of research. These intense X-ray lasers are several hundred meters or even several kilometers long, and provide the necessary tools to perform pump-probe measurements with fs time-resolution and sufficient photon flux, using X-ray radiation.

In the work related to this thesis we employ ultrafast time-resolved X-ray scattering measurements, conducted at XFELs, to probe the ultrafast molecular dynamics upon absorption of visible light. The details of the optical pump, X-ray probe experiments will be presented in Part I, Chapter2 of this thesis. Additionally, we investigated the ultrafast coupled electronic and structural dynamics from a computational perspective. The basic theory and methodology behind the simulations will be presented in Part II, Chapter 3. The molecular systems, we studied are two transition metal complexes, and thus the following section give a brief introduction to the particularly interesting properties of these types of molecules.

1.2 Light absorption for transition metal complexes

Absorption of visible light for transition metal complexes and the associated excited state processes, often occur on ultrafast time scales, and thus they are popular candidates for the study of ultrafast processes and the fundamental understanding of photochemical processes, as they unfold. This section gives a brief introduction to chemical structure of transition metal complexes, and the electronic transitions associated with absorption of visible light.

Transition metals are found in the middle of the periodic table and are generally characterized by having unfilled d-orbitals either as atoms or ions, which give them a particularly rich chemistry. The International Union of Pure and Applied Chemistry (IUPAC) definition of a transition metal is: "*An element whose atom has an incomplete d sub-shell, or which can give rise to cations with an incomplete d sub-shell*" [13, 14]. The electronic configuration inside the d-orbitals allow transition metals a unique chemistry, for example, it allows them to form so-called coordination compounds, also referred to as metal complexes if the central atom is a transition metal.

Transition metal complexes consist of a central metal atom, M or ion, M^{n+}, that is bonded to one or more ligands, L. The ligands are ions or molecules, that contain electron pairs, which can be shared with the central metal. For a transition metal complex in the octahedral symmetry (O_h), there are six identical ligands, e.g. carbonyls (CO), cyanides (CN^-), hydroxyls (OH^-), that each bind to the central metal. Other larger ligands might have more than one point of attachment to the central metal, such as 2,2-Bipyridine (bpy) or 2,2';6',2"-terpyridine (terpy). These larger ligands formally reduces the octahedral symmetry to a lower symmetry, but from the point of view of the central metal, the bonding structure is very similar, and thus the energetics of the given metal complex are often considered in terms of the octahedral symmetry [15].

The interplay between the central metal and the ligands gives rise to a unique energetic landscape which is often the origin of very colorful solutions. The ability to absorb visible light gives rise to exceptional excited state properties for transition metal complexes, which makes them useful for photocatalytic processes e.g. within water splitting or CO_2 reduction. By varying the central metal or fine-tune the structure of the ligands, it is possible to optimize the energetic landscape, such that they will become useful for applicational purposes [1, 16, 17]. Thus, in order to develop and potentially design a photoactive compound for applications, it is essential to understand the fundamental excited state properties and underlying photo-physical and -chemical processes.

A molecular orbital (MO) diagram is a helpful tool, to identify the electronic excited states of metal complexes and relevant electronic transitions for the interaction with light [15]. Figure 1.1 illustrates the Molecular Or-

bital (MO) diagram, and relevant electronic transitions for a simplified metal complex in octahedral symmetry, along with an illustration of the crucial d-orbitals.

Part a) of the figure, shows the MO diagram and the shift of the energy levels when considering the metal orbitals and ligand orbitals independently, and when the metal and ligands form bonds between them. In the diagram, M, refers to the metal, L refers to the ligands, and ML_6 refers to the metal complex as a whole. The left column illustrates the valence atomic orbitals and the energy levels of the metal orbitals, which are the nd, (n+1)s and (n+1)p orbitals, where n is the row number of the periodic table (3, 4 or 5). The right column illustrates the energy levels of the valence orbitals on the ligands, which are mainly the π and π^* orbitals. The specific energy levels depends naturally on the nature of the ligands. The column in the middle of the diagram gives the shift in energy levels and the formed molecular orbitals of the metal complex, relative to the independent metal and ligands. The orange box highlights the most relevant molecular orbitals associated with absorption of visible light and fascinating excited state dynamics of metal complexes.

The most relevant atomic orbitals for the metal are the five d-orbitals that are illustrated below the diagram in part d). Considering the metal atom alone, these five d-orbitals are energetically degenerate, but the chemical environment in a metal complex leads to an energy splitting, referred to as the (octadedral) ligand field splitting, Δ_O, for the d-orbitals. A simplified model of an octahedral system, considers the energy splitting in terms of electrostatics, by placing the positively charged metal in the center, and the negatively charged ligands, at the verticies of an octahedron. Consequently, the orbitals that point directly at the six negatively charged ligands ($d_{x^2-y^2}$, d_{z^2}) are destabilized (energy levels increase), since population of an electron in one of these orbitals will be less energetically favorable due to electrostatic repulsion. In contrast, the remaining orbitals (d_{xy},d_{xz}, d_{yz}) are all oriented such that they point between the negatively charged ligands, and thus stabilizes energetically. The two destabilized orbitals are referred to as the e_g orbitals, and the three stabilized orbitals are referred to as the t_{2g} orbitals. Part b) of Figure 1.1, highlights the e_g and t_{2g} orbitals from the metal, and the π and π^* orbitals from the ligands, along with the ligand field splitting Δ_O. The specific energetic ordering of these orbitals depends on the nature of both the metal and the ligands.

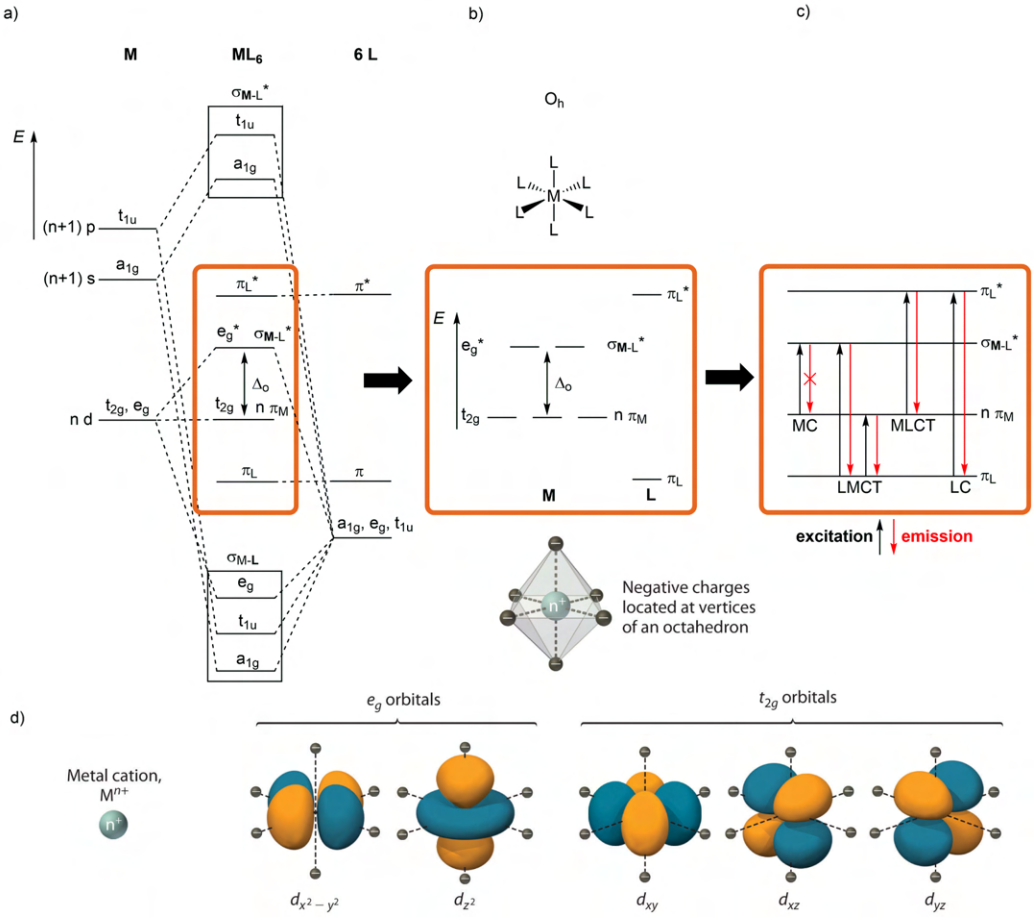

Figure 1.1: a) Molecular orbital diagram for a transition metal complex (ML_6) with Oh symmetry, with M showing the metal orbitals and, L the relevant ligand orbitals. b) extracted orbitals of interest for metal complexes with the field splitting, Δ_O shown. c) Transitions of interest for metal complexes and the assignment based on charge transfer character. d) Illustration of the metal d-orbitals and division into e_g and t_{2g} orbitals in an octahedral field. Adapted Figure from [1]

Finally, part c) shows the relevant electronic transitions for transition metal complexes, which are assigned according to the type of orbitals that are involved. Absorption of visible light, may promote an electron from/to orbitals that predominantly localized on the metal or the ligands. In the regime of visible light, the relevant electronic transitions for metal complexes are defined according to the following classes:

MC: Metal Centered. Electronic transitions from orbitals located mainly on the metal in both the ground and excited state (i.e. transitions between the e_g and t_{2g} orbitals).

LC: Ligand Centered. Electronic transitions between orbitals located mainly on the ligands (i.e. transitions between the π and π^* orbitals).

MLCT: Metal-to-Ligand-Charge-Transfer. Electronic transitions from orbitals located mainly on the metal to orbitals located mainly on the ligand (i.a transitions between the t_{2g} and π^* orbitals).

LMCT: Ligand-to-Metal-Charge-Transfer. Electronic transitions from orbitals located mainly on the ligand to orbitals located mainly on the metal (i.e. transitions between the π and t_{2g} or between the π and e_g orbitals).

The different classes are also illustrated in part c) of Figure 1.1. Several transition metal complexes also re-emit visible light as part of the relaxation pathway back to the electronic ground state, which we may observe as emission, as indicated in the figure by the red arrows. The relative order of the energy levels and the different transitions depend tremendously on the nature of the metal and the ligands. Structural refinement of especially the ligands allows us to ”push or pull” the energy levels in the desired manner, giving the optimum properties for the given application.

1.3 Applications of metal complexes and model systems

The interaction of metal complexes and visible light, and the associated exceptional excited state properties, make them attractive candidates for a wide range of applications [1, 16, 17]. This section briefly presents some

of the applications, and move on to describe key properties of interest and how to study these using model systems.

Transition metal complexes are often applied in devices that convert solar energy, into electricity in e.g. Dye-Sensitized-Solar-Cells (DSSCs) [18, 19, 20, 21, 22], or into chemical energy stored in solar fuels (e.g. H_2) based on artificial photosynthesis [23, 24]. Furthermore, metal complexes are used in photocatalysis, particularly within organic chemistry synthesis [25, 26, 27]. In addition, transition metal complexes show potential within biomedical applications, such as photo-therapeutic cancer treatment [28, 29, 30]. In modern photodynamic therapy (PDT), metal complexes act as photosensitizers that localizes to a target cell and/or tissue, absorbs light and transfers the energy from light to molecular oxygen, in order to generate reactive oxygen species that mediate cellular toxicity [29]. Other applications concern opto-electronic devices, in which transition metal complexes are used to produce light for display purposes in e.g. organic light-emitting diodes (OLEDs) [31, 32, 22, 33] or for illumination purposes e.g. in biological imaging [34] or biosensors [35].

Despite the wide range of applications, most often the transition metal complexes of use involve rare-earth elements (the lanthanides) or precious metals such as Ru, Ir, Pt or Au [1]. However, in order to use the metal complexes for applications, it is of key interest to understand the fundamentals behind the excited state dynamics of transition metal complexes. Key properties to investigate concerns the relationship between chemical structure and electronic configuration during excited state dynamics upon absorption of light.

One of the most studied compounds for investigations of photoabsorption processes is the $[Ru(bpy)_3]^{2+}$ complex (bpy = 2,2'-bipyridine), which, among other things, is well-known for its long MLCT lifetime (µs-ns range). The relatively long MLCT lifetime is a desired property for applications within DSSCs, since it allows for extraction of the energy delivered by the photoexcitation, and convert it to e.g. electricity or chemical energy storage. Promotion of an electron from the metal center of the complex, to the ligand, allows for extraction of the excited electron. However, the electron must stay "long enough" on the ligand before returning to the metal center, in order to be useful for DSSC purposes. Figure 1.2 illustrates the chemical structure of $[Ru(bpy)_3]^{2+}$ in part a).

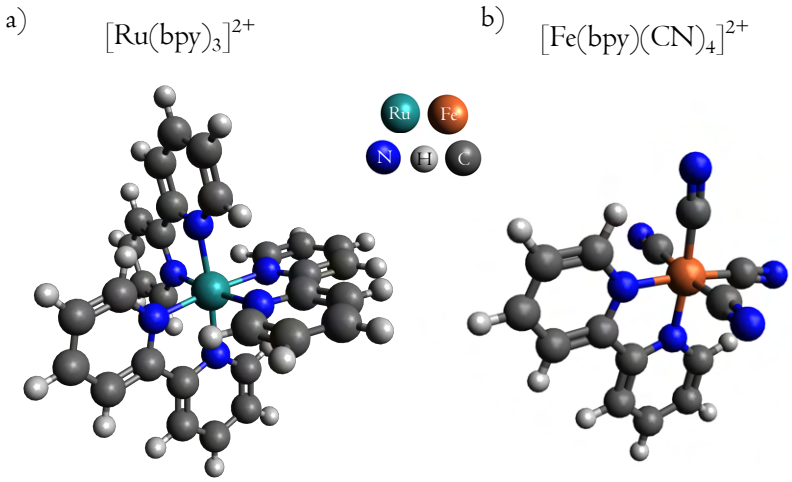

Figure 1.2: Illustration of the chemical structure of the metal complexes known as $[Ru(bpy)_3]^{2+}$ in part a), and $[Fe(bpy)(CN)_4]^{2-}$ in part b).

In recent years, scientists have gained an increased interest to develop photosensitizers or -catalysts using Fe based complexes [17, 36, 37]. The Fe-based complexes are of particular interest due to the large natural abundance of Fe, which ensures greater sustainability and would lower the production cost significantly. Hence, $[Fe(bpy)_3]^{2+}$ is the natural choice to consider as a replacement for the $[Ru(bpy)_3]^{2+}$ system, especially since Fe^{2+} and Ru^{2+} have very similar electronic properties since they belong to the same group in the periodic table. Both metals show the same ground state electronic configuration as d^6 compounds, and hence one might expect a similar structure, and excited state properties when bonded in a metal complex. However, extensive studies on $[Fe(bpy)_3]^{2+}$ show that this is not the case. For example, fs fluorescence up-conversion and transient absorption studies from 2007 [38] show very short lived MLCT excited state lifetimes and intersystem crossing (ISC) from ^{1}MLCT to ^{3}MLCT at a rate of 20±5 fs and a subsequent decay of the ^{3}MLCT on a time scales of < 150 fs. Work by Chergui et al.[39] employ transient absorption spectroscopy to conclude that after ISC the ^{3}MLCT depopulates directly into a quintet (HS) MC state in less than 50 fs, whereas work by Gaffney and coworkers [40, 41], employing ultrafast time-resolved X-ray studies conclude that the decay from the ^{3}MLCT excited state goes through a triplet ^{3}MC state before population of the quintet ^{5}MC state. Hence, the excited state energetic landscape is very different for $[Ru(bpy)_3]^{2+}$ and $[Fe(bpy)_3]^{2+}$.

Furthermore, other work on $[Fe(bpy)_3]^{2+}$ focusing on the structural changes of the solute and solvent report that the structural changes associated with the excited state dynamics reveals a strong coupling of the structural modes, in particular related to the Fe-N bonds, and the spin crossover dynamics into the ^{5}MC states [42, 41], along with the solvent impact and reorganization [43, 44, 45].

The main difference between $[Ru(bpy)_3]^{2+}$ and $[Fe(bpy)_3]^{2+}$ lies in the fact that Ru is a 4d metal, and Fe is 3d metal, and thus the valence electrons are closer to the metal core in case of Fe relative to the case of Ru [46]. As a result, the ligand field splitting in an octahedral symmetry becomes weaker in the case of Fe, making the MC excited states lower in energy than the MLCT states. Considering the energetic order from Figure 1.1, the e_g levels (from the metal) are lower in energy than the π^* level (from the ligands), in the case of a weak field splitting in Fe^{2+}, whereas for Ru^{2+}, the order is opposite due to the stronger field splitting of the t_{2g} and e_g levels, making the π^* level below the e_g levels. Consequently, the relaxation mechanism in the $[Fe(bpy)_3]^{2+}$ system undergoes a non-radiative, "barrier-less" deactivation mechanism to the MC states, following excitation into extremely short-lived (< 100 fs) MLCT states [38].

Figure 1.3 shows a comparison of the relevant potential energy surfaces between a 4d type metal complex, such as a Ru-based complex, and a 3d type metal complex, such as an Fe-based complex. In the case of ruthenium, the MC bands are "pushed" to higher energies, and thus excitation into the MLCT band shows a relatively long excited state lifetime, followed by either a radiative decay (emission), or a (slower) non-radiative decay through the 3MC band. On the other hand, for an iron, FeL_6 complex, the MC states are more energetically stable than the MLCT states, and thus excitation into the MLCT band often results in a very fast relaxation mechanism via the MC states, and a non-radiative decay to back to the ground state [47, 46].

Alternatively to exchanging the metal, it is possible to chemically modify the ligands, in order to change the excited energetic landscape. Different strategies exist for the design of Fe-based photosensitizers, as described in great detail in [46, 48, 47]. With an overall goal to prolong the lifetime of the excited MLCT state, the two main options are to either stabilize the MLCT states, or to destabilize the MC states.

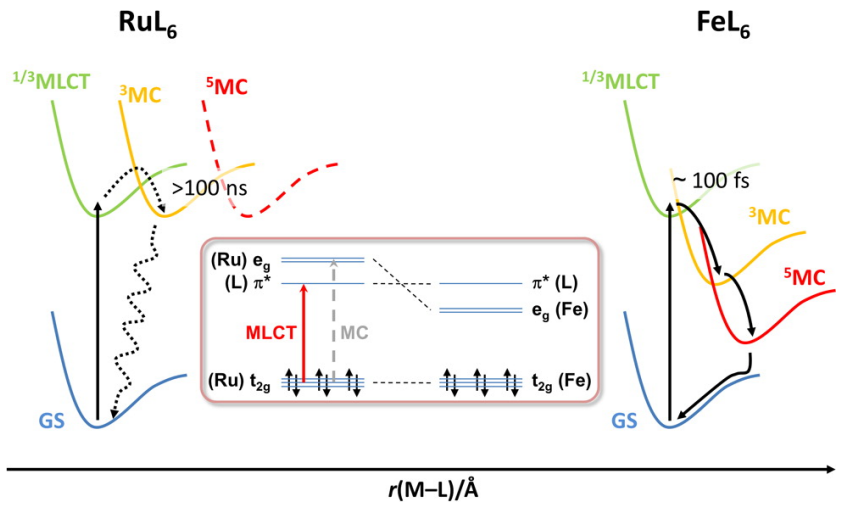

Figure 1.3: Schematic of the excited state energetic landscape in ruthenium (RuL_6) metal complexes and iron (FeL_6) metal complexes. The black arrows illustrate the different decay mechanisms with a long-lived (ns) MLCT lifetime in the case of RuL_6 and an ultrafast decay (fs) from the MLCT to MC states in the case of FeL_6. The inset shows the shift in the order of the t_{2g} and e_g levels from Ru to Fe. Figure from [47].

An example is the $[Fe(bpy)(CN)_4]^{2-}$ model system, (illustrated in Figure 1.2), in which the exchange of two bipyridines with four cyanides, influences the energetic landscape. Relative to bipyridine, cyanide is a strong field ligand (π-acceptor that increases the field strength), thus stabilizing the t_{2g} orbitals relative to the e_g, pushing the excited MC states to higher energies. Additionally, the absorption spectrum [49], and excited state dynamics depend on the nature of the solvent [50, 51]. The measured absorption maximum (of the MLCT transtion), shifts from ~500 nm in water to ~700 nm in dimethylsulfoxide (DMSO), and the lifetime of the MLCT excited state increases from the order of fs to ps. Hence, the interaction between $[Fe(bpy)(CN)_4]^{2-}$ and the solvent, besides the effect on the excited state dynamics of this compound is of interest, and is studied in greater detail, as described in Part III, chapter 6.

This thesis focuses on elucidating and understanding the excited state dynamics related to MLCT states, and the influence of the solvent. Hence,

$[Ru(bpy)_3]^{2+}$ is the natural choice of system to study, due to the property of a relatively long MLCT lifetime. The excited state dynamics of $[Ru(bpy)_3]^{2+}$ have already been studied extensively, but little information exists on the structural changes of the complex and the solvent response.

Furthermore, the thesis describes investigations of the excited state dynamics of the $[Fe(bpy)(CN)_4]^{2-}$ complex and compares the it to the more well known properties of the $[Ru(bpy)_3]^{2+}$ complex. Particularly the solvent effects on the MLCT lifetime of the excited states are of interest. In addition, the MLCT de-activation mechanism, and how it correlates with structural changes and solvent response.

The work of this thesis involves both experiments and simulations, and thus also investigates the connection between the two.

1.4 Outline of this thesis

This thesis involves studies of ultrafast dynamics using both theory and experiments, and the interplay between the two. The thesis is organized into three parts, one describing the experimental background, one describing the fundamental theory underlying computer simulations related to this work, and a third part describing the results.

Part I: The experimental part covers the basics of X-ray scattering in solution, the experimental setup for an ultrafast time-resolved X-ray scattering experiment performed at XFELs, along with a description of the treatment of the enormous amount of collected data, and how we model the reduced data.

Part II: The theoretical part covers the basic concepts of the computational methods of the systems under study. It covers the different levels of theory and the relevant approximations within the choice of method.

Part III: The third part concerns the results of the studies of $[Ru(bpy)_3]^{2+}$ and $[Fe(bpy)(CN)_4]^{2-}$ which presents both experimental and computational results on the ultrafast dynamics. The part also shortly presents other work carried out during the Ph.D. studies and give an overview of co-authored publications related to the work.

The final part of the thesis presents the main conclusions and outlook.

Part I

Experimental background

Chapter 2

Ultrafast dynamics studies using X-ray scattering

Contents

The ultrafast dynamics studies described in this thesis involve both experiments and simulations. This first part of the thesis describes the background elements which forms the foundation of experimental X-ray scattering studies of molecular ultrafast dynamics, namely: The fundamental X-ray scattering theory; the experimental setup of the typical time resolved X-ray scattering experiment; the treatment and reduction of experimental data and lastly how the experimental data is analyzed and modeled.

2.1 X-ray scattering theory

This section briefly summarizes the theory behind an elastic X-ray scattering process between X-rays and matter - A process which is at the basis of an experimental X-ray scattering experiment. The section focuses on the part of the theory which is relevant for molecular systems in solution. For an elaborate description of the theory the reader is referred to literature such as [52, 53, 54].

Shining X-ray light on a molecular system results in an interaction between the electric field of the light with the electrons in the sample, and as a result the light is scattered in different directions. Elastic X-ray scattering measures the intensity of the (elastically) scattered light as a function of the scattering vector $\vec{Q}$. The scattering vector is the vectorial difference between the incoming $\vec{k}_{\text{in}}$ and outgoing $\vec{k}_{\text{out}}$, wave vectors of the X-ray light with wavelength λ, and with magnitude $|k_{\text{in}}| = \frac{2\pi}{\lambda}$. The scattering vector $\vec{Q}$ is thus connected to the X-ray scattering angle θ through the expressions given in the illustration below:

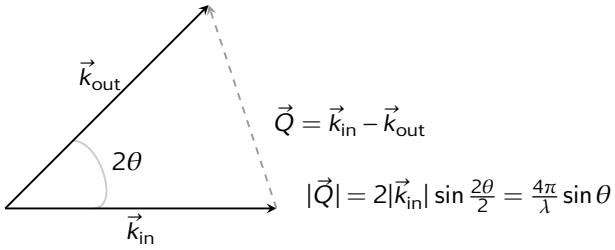

The scattering from a single electron is defined as the Thomson scattering length $r_0 = 2.28 \cdot 10^{-5}$ Å, describing the ability of an electron to scatter an X-ray photon. However, instead of considering the scattering from each of the electrons in a given molecular system, the electron density $\rho(\vec{r})$, for each of the atoms, is considered. The atomic electron density is estimated as a distribution of charge around each nucleus, and the ability of the atom, to scatter the light, is then given by the so called atomic form factor f, given by the Fourier transform of the electron density multiplied by r_0:

$$f(\vec{Q}) = -r_0 \int \rho(\vec{r})\, e^{i\vec{Q}\vec{r}}\, d\vec{r} \tag{2.1}$$

The measured intensity $S(\vec{Q})$ of the scattered X-rays is then modeled as a sum of the contributions from each of the atomic form factors multiplied with the phase factor, under the assumption of the Independent Atom Model (IAM):

$$S(\vec{Q}) = \sum_{i,j=1}^{N} f_i f_j^* \, e^{i\vec{Q}\vec{r}_{ij}} \tag{2.2}$$

where f_j^* is the complex conjugation of f_i, and N is the number of atoms, and r_{ij} is the distance between atom i and j. Allowing the molecules to orient in all directions, results in the orientationally averaged expression for the measured scattering:

$$S(Q) = \sum_{i,j=1}^{N} f_i f_j \frac{\sin Q r_{ij}}{Q r_{ij}} \tag{2.3}$$

where we also assumed that the atomic form factors are real valued, due to the electron density being radially symmetric around the atomic nuclei. The expression is also known as the Debye formula [55]. Despite the fact that the model ignores molecular bonding and electronic delocalization effects, it generally shows adequate results related to structure-determination [56].

As observed from the above equations, the measured X-ray scattering depends on the distances, r_{ij} between the atoms, which make the technique a useful tool to study molecular structure. Application of temporally short pulsed X-ray sources, such as X-ray Free Electron Lasers (XFELs), makes it possible to measure fs time-resolved X-ray scattering, in order to study molecular motion as it occurs in real time [10]. Time-resolved wide angle X-ray scattering (TR-WAXS) is one of many techniques that employs X-ray scattering to track the structural response of a given molecular system upon photoexcitation. Others also refer to the technique as X-ray Diffuse Scattering (XDS) [57], or X-ray Solution Scattering (XSS) [58], or X-ray liquidography (XL) [52]. In the work related to this thesis we will use either TR-WAXS, or simply WAXS or X-ray scattering to refer to this technique.

2.2 Principles of the experimental setup

Time-resolved X-ray scattering experiments with ps-fs time resolution requires large scale facilities such as synchrotrons, and XFELs to generate a sufficiently intense X-ray beam. Experiments performed at these large scale facilities, in particular at XFELs, require a lot of manpower, and often involve large collaborations.

A typical TR-WAXS experiment employs the setup of a pump-probe type experiment, with an optical laser pump, and an X-ray probe (the synchrotron or XFEL beam). In a pump-probe setup, the optical laser (the pump) excites the given system of interest, in this case transition metal complexes in solution, which initiates the photochemical process. Next, the X-ray probe reaches the sample, after a specified time-delay between pump and probe. The sample scatters the X-ray light in all directions and the forward scattering is collected by a detector. The X-ray scattering results in a unique pattern on the detector, depending on the structural changes in the sample, at the given time after excitation. The delay between optical pump and x-ray probe is then changed, and for each time delay a set of pulses is recorded for statistics and signal/noise purposes. For each pulse in the set of pulses the X-ray scattering is recorded and after outlier rejection these pulses form into a single scattering image, and in this way the images for different time delays combine into a small "movie" of the structural changes in the given system. Each pump-probe event may be regarded as an independent experiment, which is repeated thousands of times. Figure 2.1 illustrates the TR-WAXS experimental setup.

In a typical TR-WAXS setup, a free flowing liquid jet contains the sample, either as a round or flat jet with a diameter of typically 30-500 μm. The sample is set to flow through a capillary nozzle, and recycle with a high flow speed to ensure fresh sample between each pump-probe event.

The optical laser system typically produces laser pulses within the 260-800 nm range and with a pulse duration down to 10 fs [59], however, the specifics depend on the facility. Finally, beryllium lenses control the size (on the order of 100 μm) and position of the optical laser spot and focus it on the sample. The X-ray pulses have a pulse duration down to ~30 fs (at XFELs), along with a spot size on of ~50 μm, and the pulse must spatially and temporally overlap with the optical laser pulse, which is a

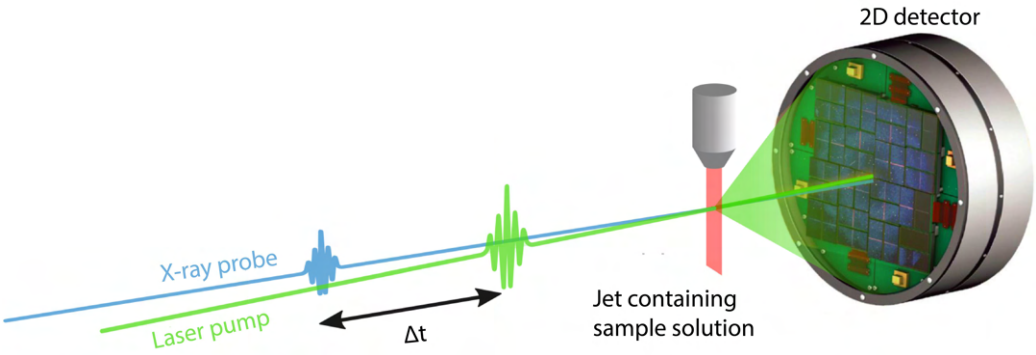

Figure 2.1: Illustration of the typical setup in a laser pump, X-ray probe experiment. A liquid jet contains the sample, which runs under high pressure to ensure sample renewal between each pump-probe event. First, an optical laser pulse (light blue) hits the jet and excites the system under study. Secondly, a specified time delay, Δt later, the X-ray probe (green) reaches the sample and scatters in a unique pattern, collected by a detector. Figure by Tobias C.B. Harlang from unpublished work.

non-trivial task. The ultra-short pulses are necessary to obtain the desired time-resolution, in order to study the structural dynamics that occur on the fs-ps time scales.

Collection of a 2D scattering image for each pump probe event at an XFEL requires a specialized detector and each collected image is on the order of MB. In a typical experiment, the delay stage that controls the time delay between the pump and probe, moves in steps of 10-100 time delays, and for each time step, thousands of images are recorded in a so-called time scan. Given a repetition rate of 120 Hz, such a scan takes a few minutes, and the size of the resulting data file is on the order of 200 GB. Thus, an experiment running for a couple of days results in a tens (or hundreds) of TB sized data set. From the collected 2D scattering images, we use the radial symmetry of the images to construct 1D scattering signals, which require a number of steps, before the data is analyzable. The steps involve a large data reduction, as described in the following, in section 2.3.

Furthermore, we collect scattering images, in which the sample was not pumped, i.e. without the optical laser pulse. This allows us to construct *difference* scattering signals from images with laser off (i.e. ground state) subtracted from images with the laser on (excited state). Section 2.4 elaborates on the construction and analysis of the difference signals.

2.3 Treatment of scattering data (Data reduction)

Once the scattering data is recorded it must undergo several data reduction and treatment processes before it is in a condition to be analyzed. This section briefly summarizes the process of going from the ”raw” data to analyzable data, which is a non-trivial process.

The data reduction and treatment steps have evolved over many different experiments and Ph.D. projects [60, 61, 62] and are also described in other publications [63, 57, 64]. The data treatment process is in constant development, as it depends on the XFEL facility and especially on the detector. The descriptions in the following are focused on the CSPAD [65, 66] detector at Linac Coherent Light Source (LCLS), and the data treatment procedure is now standard at the XCS endstation [67].

As part of the work during the Ph.D. studies, I participated in several TR-WAXS experiments at XFELs and assisted the reduction and quick analysis of the enormous amounts of incoming data. However, the thorough data treatment process for analyzable data was performed by other data specialists within the team. The final analyzable scattering data for the $[Ru(bpy)_3]^{2+}$ complex was reduced by Elisa Biasin, and Kathryn Ledbetter is currently treating and analyzing the data for the $[Fe(bpy)(CN)_4]^{2-}$ complex. At a given beamtime, we only perform the data treatment process in a simplistic matter, in order to obtain a fast visualization of data, which is key to make qualified decisions on how to run the experiment.

Figure 2.2 summarizes the data reduction and treatment procedure, and the following small paragraphs describe each of the steps.

Measure XDS: The first step is to measure and collect multiple scattering images. Each pump-probe event leads to a scattering image collected by the detector. For each image, the specific beam parameters and diagnostics information on each pump-probe event, are saved, which allows for filtering and corrections for each shot. Since, the LCLS and many XFELs employ the Self-Amplified Spontaneous Emission (SASE) process to produce the intense X-ray pulses, often large pulse-to pulse variations and time drift is observed. Hence, information on each collected image is useful for the the necessary filtering and corrections.

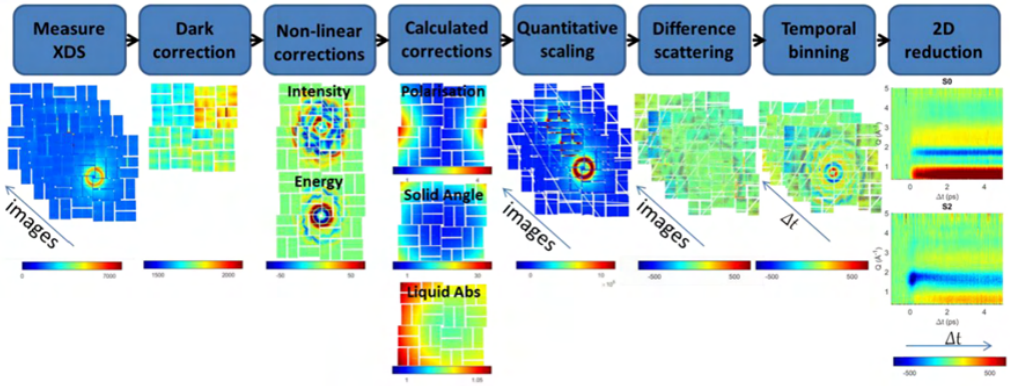

Figure 2.2: Workflow of the necessary data reduction and treatment before analysis of the scattering data begins. Figure from supplementary material of [63]

Dark Correction: The first data treatment step involves a dark correction, which subtracts the electronic background noise of the detector. Even if both the X-ray and optical laser is off, a small current will run through the detector, and this "dark" contribution to the image varies from pixel to pixel. Thus, a set of so-called dark images are collected throughout the experiment, and an average of many dark images are subtracted from each collected scattering image. Furthermore, a so-called mask might be applied, which removes unreliable pixels or areas of the detector e.g. from shadows arising from the given experimental setup.

Non-linear corrections: The stochastic nature of the SASE process leads to fluctuations in both intensity and energy. Fluctuations in energy (and thus λ) causes changes in the scattering vector, Q, due to their connection as section 2.1 described. Consequently, the collected scattering of a given angle, θ, for different X-ray energies are mapped differently on the detector. However, by knowing the pulse energy for each image, the effect can be reduced by correcting for the X-ray energy fluctuations. In addition, fluctuations in the intensity gives different responses of the detector. The CSPAD detector has a non-linear response to the X-ray intensity, which leads to artifacts. A procedure based on a Singular Value Decomposition (SVD) [68], makes it possible to correct for the detector response for non-linearities in X-ray energy and intensity, as discussed in greater detail by van Driel et al. [57].

The CSPAD detector has since been replaced by the ePix10k 2-megapixel

detector, in which the non-linear intensity dependence was determined to be ∼1.5 %, and found to be effectively corrected by the tools discussed in [69].

Calculated corrections: Upon subtraction of the SVD components that correlate with X-ray intensity and energy, every image undergoes additional corrections. The images are corrected for the geometric effect of the solid angle, since the scattered X-rays have a different projection area on the detector, such that the scattering is spread out on a higher number of pixels for large angles. In addition, the images are corrected for the X-ray polarization, which results in a different magnitude of the scattering depending on the scattering direction. Furthermore, the images are corrected for absorption effects in the detector as well as in the liquid jet. Each pixel on the detector contains an active silicon absorption layer 200 µm, in which the incoming X-ray photon may be absorbed and thus detected. However, for larger scattering angles the probability of absorption is larger, due to the longer path length of the X-ray photon through the layer. As a result, the measured signal shows an angle dependent increase, which must be corrected for. Likewise, for the liquid jet, a small fraction of the X-ray photons are absorbed by the jet, which is corrected for.

Quantitative scaling: Following the corrections, the data set is scaled according to the so-called liquid unit cell (LUC), as described in [70]. The LUC reflects the given concentration of the sample in terms of the ratio of solute to solvent molecules. The signal is then given in electron units per solute molecule. The scaling of the data allows for physical interpretations of scaler values of each model component in the later fitting procedure. The scaling factor is determined from a calculated signal of the total scattering from one LUC.

Difference scattering: Just before calculation of the difference signals, the data is examined for outliers. During an XFEL scattering measurement, the quality of the data differs substantially depending on several experimental conditions. For example, variations in X-ray intensity between shots, drift of the liquid jet, the degree of laminar or turbulent flow or clogging of the jet due to the formation of nanoparticles at the nozzle of the capillary tube, may all lead to severe changes in the measured signals.

The intensity from each image is compared to the mean of the rest, and rejected, if not within predefined limits of acceptance. Typically, about 5-10 % of the images are discarded.

From the filtered data, the difference scattering images are prepared. The difference signals are constructed from subtraction of the un-pumped images (laser off) from the pumped images (laser on). The un-pumped signals are commonly measured periodically throughout the beamtime. In order to reduce any effects from drifts in the experimental setup, the differences are calculated based on the 2 nearest laser off images for a given laser on image.

Temporal binning: Each difference image often shows a poor signal-to-noise ratio, and to improve the statistics, typically several thousands of images are binned according to the actual delay time (within ~10 fs accuracy) measured by the timing tool diagnostics [71], and images within the same bin are averaged. Hence, this step greatly reduces the amount of data, and at the same time improves the signal-to-noise ratio.

2D reduction: The final step in the data treatment, concerns the extraction of 1D scattering curves from the 2D images. In a typical scattering experiment performed on a synchrotron source, this step is often done by an azimuthal integration of the 2D images. However, as discussed later in section 5.2.2, due to the time resolution in the fs regime, the measured scattering intensity at the earliest delay times is asymmetric, i.e. depends on the azimuthal angle. Thus, the collected data is separated into an isotropic and anisotropic contribution, as described in greater detail in [72, 64].

In conclusion, several steps of corrections, scaling, filtering, binning and averaging are performed before the analysis of the science inside the data even begins. Furthermore, each facility and each detector is unique and the data handling is very different, and perpetually undergoes new development. The remaining sections of this chapter, focus on the information content of the collected difference scattering signals, and how such signals are analyzed in this work.

2.4 Difference scattering signals

The structural changes associated with the excited state dynamics processes are often very small, on the order of 0.1 Å or even less, and hence the changes in the collected scattering signals are very small. Furthermore, the concentration of the samples is typically around 10-100 mM, which means that each solute is surrounded by thousands of solvent molecules. Consequently, the images are dominated by scattering from the solvent.

In order to enhance the part of the signals of interest, namely the photoinduced changes in the sample, we analyze the *difference* scattering signals. As previously described, we construct the difference signals ΔS by subtraction of the collected signals without photoexcitation, S_{off} (optical laser off), from the signals with photoexcitation, S_{on} (laser on):

$$\Delta S = S_{\text{on}} - S_{\text{off}} \tag{2.4}$$

It is advantageous to carry out the analysis of the difference signals, since it effectively cancels out contributions to the total signal that did not change as a result of photoexcitation. Hence, only the part of the solvent that changed signal remains, which is typically on a similar order of magnitude as the signal arising from structural changes of the solute. Also, inelastic scattering effects are independent of structure and thus cancels out by analysis of the difference signals. An example of the simulated total and difference signal for the solute, is given below in Figure 2.3.

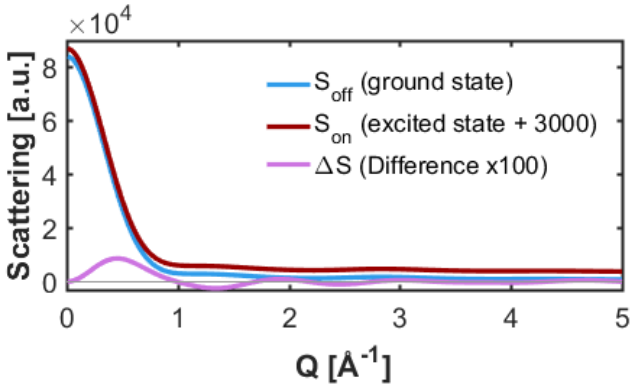

Figure 2.3: Example of the often very small difference between ground (laser-off) and excited state (laser on) solute scattering signals. The example is from classical MD simulations of the $[Ru(bpy)_3]^{2+}$ complex described in Chapter 5.

2.4.1 Laser-induced anisotropic X-ray scattering

In the analysis of scattering signals obtained from an XFEL experiment with time delays on the order of fs, it becomes relevant to consider effects arising from laser-induced alignment of the given system under study.

Since, the optical laser that initiates the photochemical process is linearly polarized, the probability that the photoactive system absorbs a photon, depends on the orientation of the system. As a result, the solute molecules oriented such that their transition dipole is parallel to the polarization axis of the laser, have a higher probability of absorbing a photon. Hence, the sample after the pump pulse consists of preferentially oriented excited state geometries. Figure 2.4 illustrates the concept of the photoselection process, which results in an asymmetric scattering pattern, at the earliest delay times.

The concept and analysis of laser-incduced anisotropy (azimutally dependant) signals in time-resolved scattering has been described both for electron diffraction [73, 74] and X-ray experiments [72, 64]. The literature describes the formalism necessary for the analysis of asymmetric scattering patterns and how it is possible to separate the scattering patterns into two main contributions.

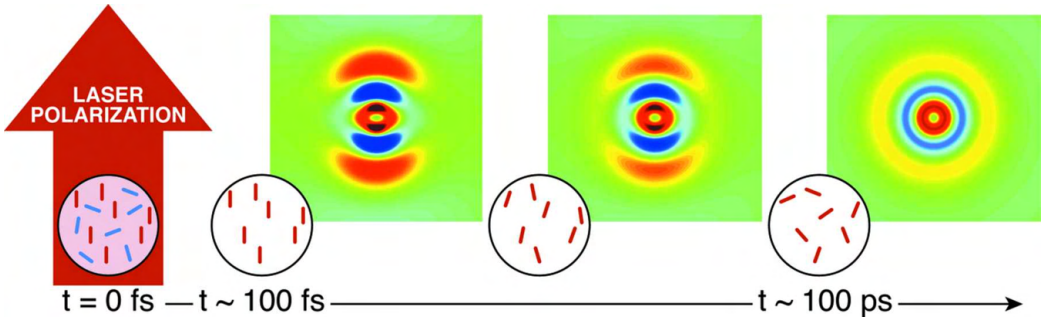

Figure 2.4: Illustration of the concept of photoselection and the resulting anisotropic scattering signal at early delay times. At time zero $t = 0$ fs the laser arrives to a solution of randomly oriented absorbing molecules. Then the laser preferentially excites the solute molecules, oriented such that their transition dipole associated with the given excited state, is parallel to the polarization of the pump laser (i.e. the red molecules). The effect results in an asymmetric scattering pattern at early times ($t \sim 100$ fs), and at later times the effect wears off due to the rotation of the excited state solute molecules making the solution isotropic again (t ~10-100 ps). Figure from [64]

Under the assumption that the absorbing molecule is a symmetric top with the transition dipole aligned with the main axis of symmetry, the n^{th} order scattering, S_n of an aligned ensemble may be expressed as:

$$S_n = c_n \sum_{i,j=1}^{N} f_i(Q) f_j(Q) P_n(\cos\theta_{ij}) J_n(Q r_{ij}) \tag{2.5}$$

which arises from the case where the angular distribution of transition dipole moments are expressed as an expansion of Legendre polynomials, P_n with expansion coefficients, c_n, and $n = \{0, 1, 2, ...\}$ is the order of the Legendre polynomial. The polynomial, P_n is a function of the angle θ_{ij} between the distance, r_{ij} of atom i and j, and the transition dipole vector of the absorbing molecule. J_n are spherical Bessel functions, of order n depending on the scattering vector Q and the interatomic distance r_{ij}. Finally, f_i,f_j are the atomic form factors of atom i, j summarized over the number of atoms in the given system, N.

In the case of single-photon absorption of the linearly polarized laser light by the isotropic ensemble, the distribution of transition dipole moments is proportional to a cosine-squared distribution about the laser polarization axis. As a result, the distribution of excited state geometries directly upon photoexcitation only has contributions from the $n = 0$ and $n = 2$ order of the Legendre polynomials. Hence, only the zeroth order, S_0 and second order, S_2 expressions of eq. 2.5 are relevant. First, the isotropic part, S_0 is written as:

$$S_0 = c_0 \sum_{i,j=1}^{N} f_i(Q) f_j(Q) \frac{\sin Q r_{ij}}{Q r_{ij}} \tag{2.6}$$

where the zeroth order polynomial is simply $P_0 = 1$, and the expression reduces to the expression recognized as the Debye formula (eq. 2.3), with the coefficient c_0 defining the magnitude of the isotropic contribution to the total scattering.

Next, the anisotropic part, S_2 is given as:

$$S_2 = c_2 \sum_{i,j=1}^{N} f_i(Q) f_j(Q) P_2(\cos\theta_{ij}) J_2(Qr_{ij}) \tag{2.7}$$

which holds information on the orientation of the interatomic distances r_{ij} with respect to the transition dipole associated with the given excited state. The second order polynomial is given as $P_2(x) = -\frac{1}{2}(1-3x^2)$ with c_2 as the coefficient defining the magnitude of the anisotropic contribution directly upon the excitation event.

Returning to the difference signals, the collected difference scattering patterns contain both an isotropic, ΔS_0 and an anisotropic, ΔS_2 part:

$$\Delta S_0 = S_0^{\mathrm{ES}} - S_0^{\mathrm{GS}}$$
$$\Delta S_2 = S_2^{\mathrm{ES}} - S_2^{\mathrm{GS}}$$

where the notation "GS", and "ES" refers to the ground state and excited state, respectively. The ground and excited state contributions are each calculated from the expressions given in eq. 2.6 and 2.7. In the work related to this thesis, the isotropic difference scattering, ΔS_0 dominates, since the anisotropic contribution is negligible. Hence, in the following chapters the difference scattering signals often refer to the isotropic contribution, $\Delta S = \Delta S_0$. The next section describes in greater detail, the different contributions to the difference scattering signal.

2.5 Components of the difference scattering signal

The change in the measured X-ray scattering signals arises from changes in the electron distribution, as a result of the photoexcitation process. X-ray scattering is a global probe, in the sense that all changes in the electronic distribution of the sample results in a change in the scattering signals. Hence, structural changes in both the solute and solvent contribute to the measured difference scattering signals. In the analysis of the of a system such as a solvated metal complex it is convenient to subdivide the difference scattering signal into different contributions, since they might show

structural changes on different time scales [52, 75]. Hence, we divide the difference scattering into contributions arising from changes in the solute, ΔS_{solute}, changes in the solvent, $\Delta S_{\text{solvent}}$, and in the solute-solvent cross-term, $\Delta S_{\text{cross-term}}$. The cross-term might also be referred to as the solvent-cage or simply the cage. The total expression of the difference scattering is then written as:

$$\Delta S = \Delta S_{\text{solute}} + \Delta S_{\text{solvent}} + \Delta S_{\text{cross-term}} \tag{2.8}$$

The following sections describe each of the contributions in greater detail, and how to model them.

2.5.1 Solute dynamics

The most obvious change in electron distribution arises from changes in the electronic density of the photo-absorbing component, i.e. the solute. However, the X-ray scattering probe is (currently) not able to observe a change in signal simply from the small change in electron density as a result of the excitation process. Rather the response of the excitation process that changes the overall geometry of the solute, e.g. bond elongation, bond breaking/formation or coherent oscillations, is observed.

The excitation process occurs on the attosecond (10^{-18} s) time scale [76, 77], which is out of our (current) time-resolution, and hence the excitation occurs instantaneously, from the perspective of the measured signals in these experiments. However, the structural response, meaning the change of the atomic positions (with many electrons), occurs on the femto- to picosecond (10^{-15}-10^{-12} s) time scales, which makes it observable in these type of experiments.

Once, in the excited state, several processes may occur [78], such as vibrational relaxation (often referred to as vibrational cooling, VC), internal conversion, (IC), intersystem crossing, (ISC) or luminescence processes. These processes may occur on different time scales ranging from fs to several seconds, depending on the system and process. We are particularly interested in the ultrafast processes that occur on the fs-ps time scales. These processes might lead to a slight change of the measured scattering patterns, if the structural response is large enough (estimated ~0.01 Å from the uncertainty of the fits from previous results [41, 79, 80], depending on the system, the available Q-range and choice of model).

The difference scattering signal arise from structural changes in the solute. The un-pumped scattering signal holds information on the ground state solute signal, S_u^{GS}. The excited state signal, S_u^{ES} is from an image where the pump laser was on. However, the pumped signal, S_{on} also contains signal from the remaining solute molecules, that was not excited. Hence the overall change in the solute signal is proportional to the fraction of excited molecules. Defining the excitation fraction as α, and $(1-\alpha)$ as the fraction of solute molecules still in the ground state, we express the difference solute scattering in the following way [81]:

$$\begin{aligned}\Delta S_{\mathrm{solute}} &= \left(\alpha S_u^{\mathrm{ES}} + (1-\alpha) S_u^{\mathrm{GS}}\right) - S_u^{\mathrm{GS}} \\ &= \alpha\left(S_u^{\mathrm{ES}} - S_u^{\mathrm{GS}}\right) \\ &= \alpha \Delta S_u\end{aligned} \tag{2.9}$$

where the full scattering signals of the solute in the ground, S_u^{GS} and excited, S_u^{ES} state typically are calculated from electronic structure methods and using eq. 2.6 or 2.7 for the computed geometries.

2.5.2 Solvent dynamics

The structural changes in the solvent occur on several time scales. Upon excitation of the solute, the change in electron charge distribution causes a response from the solvent, to stabilize the excited state configuration.

According to the Frank-Condon principle [78], the solute and solvent stays in the ground state equilibrium geometry configuration, during the photoexcitation process. However, as a response to the excitation, the solute and solvent reconfigure, due to the different energetic landscape in the excited state. From a classical description, the system is subjected to different forces in the excited state from those in the ground state, which direct the given molecule into a different configuration. Put in terms of energetic surfaces, the geometry changes, since the position of the ground and excited state minima are not necessarily located the same, which ”drives” the molecular system into a different geometry in the excited state. Consequently, the solvent will reorganize in order to stabilize the potential energy of the system for the new geometry. The reorganization of the solvent involves both electrostatic interactions, such as dielectric or polar effects, and structural interactions, such as steric or directional effects like H-bonding.

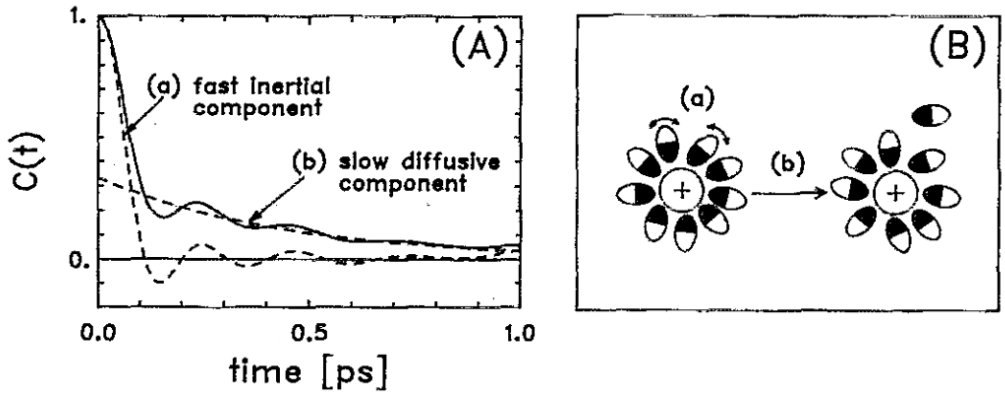

Figure 2.5: Decomposition of the solvent response, into an ultrafast inertial component and a slower diffusive component, based on simulations of non-equilibrium charge jumps ($S^0 \rightarrow S^+$) of monatomic solutes (S) dissolved in acetonitrile. The left plot illustrates the potential time correlation function of S^+, and the plot to the right depicts the physical interpretation of the fast (a) and slow (b) components. Based on work from [82]

The solvent response to the photoexcited solute occurs on multiple time scales [82, 83, 84, 85]. At the earliest times (within ~100 fs), mainly the nearest solvent molecules respond by independent inertial (mainly rotational) motions. Maroncelli et al. [83] discuss previous studies of the response of acetonitrile and water to a step function change in solute charge using both theory and experiments. They discuss results from a computational study where the solute change was described as neutral S^0 (ground state) and singly charged S^+ (excited state) Lennard-Jones spheres of diameter 3.1 Å. For both water and acetonitrile, a fast initial response accounts for at least 50 % of the solvent relaxation energy, and mainly involves the first solvation shell. The ultrafast solvent response does not depend on the intermolecular forces, and each solvent molecule may initially undergo free motions, of mainly rotational character, in small angles of 10-30°. At later times (within 0.5-2 ps), the solvent response shows diffusive motions and hence larger reorganizations of the solvation structure. The slower solvent response concerns correlated motions of several solvent molecules. Figure 2.5 shows a schematic decomposition of the fast and slow components of the potential time-correlation function of the S^+ in acetonitrile.

In terms of ultrafast TR-WAXS experiments, the fast solvent response of mainly rotational character would only give rise to a low structural difference signal, since the fast response was mainly a local phenomenon. However, the slower diffusional response might lead to a more significant difference signal.

From a modeling perspective, the solvent response is described within both the solute-solvent cross-term and the solvent term. The cross-term, $\Delta S_{\text{cross-term}}$ describes the changes in the solute-solvent distances, and the strongest signal is often observed for the structural changes within the nearest solvent shell. Similarly, to the case of the solute, we express the difference scattering signal from the solute-solvent cross-term, as the difference between the scattering signal related to the cross-term in the excited state, S_c^{ES} minus the ground state signal, S_c^{GS} with fraction, β [81]:

$$\begin{aligned} \Delta S_{\text{cross-term}} &= \beta\left(S_c^{\text{ES}} - S_c^{\text{GS}}\right) \\ &= \beta \Delta S_c \end{aligned} \tag{2.10}$$

Calculation of the cross-term requires information on the molecular level of the surrounding solvent shells, which is difficult to obtain experimentally, and therefore, it is most often based on simulations including explicit solvent. The following section, 2.6, describes how it is possible to calculate the cross-term from radial distribution functions (RDFs) associated with pairs of solute-solvent atoms.

The solvent response to the excited state configuration of the solute, also give rise to changes in the distances between the solvent-solvent atomic pairs, but since the main changes occur near the solute, the changes in structure of a few molecules of the solvent, does not contribute much to the overall change in the solvent structural signal. The contribution from the solvent structural response to the changes of the solute, are determined from simulations. Typically, we employ classical dynamics simulations of the solute in explicit solvent, allowing the solvent to equilibrate around the different solute geometries. From the trajectories, we collect RDFs of solvent-solvent atomic pairs, and calculate the scattering. We model the structural response of the solvent in a similar manner to the solute and cross-term with the difference scattering signal, ΔS_{v} with magnitude γ, however often the contribution is negligible.

Additional effects from the solvent contribution concerns the vibrational relaxation of the solute, thus an energy transfer from solute to the solvent. This energy transfer also gives rise to an observable difference scattering signal from the solvent, which occurs on two different time scales [86, 87, 81];

1. an initial increase in local temperature at constant volume and density which occurs on the 1-100 ps time scale.

2. an increase in solvent density which occurs much slower on a μs time scale.

The scattering signal arising from these changes in the bulk solvent are typically measured in separate experiments of the neat solvent and a dye, [87]. Since, the change in signal has shown to scale linearly with temperature (or density), the measured temperature differential, $\frac{\partial S}{\partial T}\big|_\rho$ and density differential, $\frac{\partial S}{\partial \rho}\big|_T$, may directly enter into a model for the solvent difference signal, $\Delta S_{\text{solvent}}$, with scaling factors, ΔT and $\Delta\rho$ describing the change in temperature and density, respectively. The total expression for the solvent difference signal is then:

$$\begin{aligned}\Delta S_{\text{solvent}} &= \gamma\left(S_v^{\text{ES}} - S_v^{\text{GS}}\right) + \Delta T \left.\frac{\partial S}{\partial T}\right|_\rho + \Delta\rho \left.\frac{\partial S}{\partial \rho}\right|_T \\ &= \gamma\Delta S_v + \Delta T \Delta S_{\text{temp}} + \rho\Delta S_{\text{dens}}\end{aligned} \tag{2.11}$$

However as discussed above, the contribution from a change in density, occurs on a very slow time scale (μs) from the perspective of ultrafast dynamics, and thus often the density contribution, ΔS_{dens} is not included in the model. Often, it is sufficient to include only the solvent heat component, ΔS_{temp}, if the structural response component, ΔS_v is negligible, and if the observed dynamics are faster than the thermal equilibration process leading to a change in bulk solvent density.

In conclusion, several processes in both the solute and solvent lead to a difference scattering signal, which we might observe using ultrafast TR-WAXS. Depending on the system each components of the model will show different contributions.

The following section describes how the different components, related to the solute S_u, the solvent, S_v and the crossterm, S_c signals, may be calculated from radial distribution functions.

2.6 Calculating scattering from RDFs

Employing the Debye formula (eq.(2.3)), is only practical for relatively small systems, and as soon as we wish to include the solvent and thus thousands of atoms, it becomes incomprehensible to use it for calculation of the total scattering. Hence, a method with lower computational cost is desirable, and Dohn and coworkers [88], presented a method on calculations of scattering signals from Radial Distribution Functions (RDFs). Furthermore, calculations of the scattering from a single geometry neglects any quantum or statistical ensemble effects since interatomic distances should be described as probability distributions. However, such ensemble effects are included in the RDFs.

For a given RDF, $g_{l,m}$ associated with atoms l, m, the calculation of the scattering signals in terms of the solute-solute S_u, solvent-solvent S_v and solute-solvent cross S_c interactions are expressed as:

$$
\begin{aligned}
S_u(Q) &= \sum_{l\in u} N_u(l) f_l(Q)^2 + \sum_{l,m\in u} f_l(Q) f_m(Q) \tfrac{N_u(l)(N_u(m)-\delta_{l,m})}{V} 4\pi \int_0^R r^2 \left[g_{l,m}(r)\right] \tfrac{\sin(Qr)}{Qr} dr \\
S_v(Q) &= \sum_{l\in v} N_v(l) f_l(Q)^2 + \sum_{l,m\in v} f_l(Q) f_m(Q) \tfrac{N_v(l)(N_v(m)-\delta_{l,m})}{V} 4\pi \int_0^R r^2 \left[g_{l,m}(r)-1\right] \tfrac{\sin(Qr)}{Qr} dr \\
S_c(Q) &= 2 \sum_{l\in u} \sum_{m\in v} f_l(Q) f_m(Q) \tfrac{N_u(l) N_v(m)}{V} 4\pi \int_0^R r^2 \left[g_{l,m}(r)-1\right] \tfrac{\sin(Qr)}{Qr} dr
\end{aligned}
\tag{2.12}
$$

where f_l is the atomic form factor of atom type l, and V is the simulated volume, and R is the max radial distance within the size of the simulated system, and u is the set of solute-type atoms, and v is the set of solvent-type atoms in the given system. In the case of $[Ru(bpy)_3]^{2+}$ or $[Fe(bpy)(CN)_4]^{2-}$ with water as solvent, then $u = \{Ru/Fe, N, C, H\}$ and $v = \{H, O\}$. Furthermore, for an atom of type l, then $N_u(l)$ and $N_v(l)$ give the number of atoms of that type l, in the solute and solvent, respectively.

For the surface hopping simulations involving the Fe-complex, the number of atoms, were the following:

$$\begin{aligned} N_u(\mathrm{Fe}) &= 1 & N_u(\mathrm{C}) &= 14 & N_v(\mathrm{O}) &= 5412 \\ N_u(\mathrm{N}) &= 6 & N_u(\mathrm{H}) &= 8 & N_v(\mathrm{H}) &= 10824 \end{aligned}$$

Hence, using the standard formulation of the Debye formula would involve thousands of atoms, and the calculation would be comprehensive. Furthermore, since, we apply the equation on a simulated system with finite size, the integrated volume is the size of the simulated volume.

The "trick" in employing above method, (eq. (2.12)) is to simply sum over the *types* of atoms (in u or v) and multiply with the number of that type, in contrast to summing over every single atom pair in the given system. For example, in the solvent contribution the sums only run over the two atom types (H, O), in contrast to summing over thousands of atoms.

Due to the finite size of the simulation box, integration might introduce unphysical truncation oscillations in the calculated scattering signal. To account for this problem, we employ a weight function, similar to other work [89, 90, 91], which ensures that the lowest distances of the RDF differences are given a higher weight, and long distances are set to zero. At long distances, the RDF differences should converge towards 0, however, they might not have fully converged or the numerical accuracy is too low (statistical noise), which may lead to spurious truncation ripples when taking the Fourier transform of the signals. Similarly, the structural changes of interest occurs at low distances from the solute. Therefore, the lowest distances are given a higher weight, w, defined as:

$$w(r) = \begin{cases} 1, & \text{if } r < r_{\mathrm{const}} \\ 1 - 3\left(\frac{r - r_{\mathrm{const}}}{r_{\mathrm{max}} - r_{\mathrm{const}}}\right)^2, & \text{if } r_{\mathrm{const}} \leq r \leq \frac{1}{3}(2\, r_{\mathrm{const}} + r_{\mathrm{max}}), \\ \frac{3}{2}\left(1 - (\frac{r - r_{\mathrm{const}}}{r_{\mathrm{max}} - r_{\mathrm{const}}})\right)^2, & \text{if } \frac{1}{3}(2 r_{\mathrm{const}} + r_{\mathrm{max}}) < r < r_{\mathrm{max}}, \\ 0, & \text{if } r > r_{\mathrm{max}}. \end{cases}$$

where r_{const} defines the distance without damping, r_{max} is the distance, where the weight is set to zero. Employing a mathematically well defined weight function, allows us to effectively remove the truncation oscillations, with a minimal distortion of the calculated scattering signal [90].

Furthermore, it is possible to calculate the total difference scattering signal directly from the difference RDFs, and including the weight, we express the formulation as:

$$\Delta S = \sum_{l,m\in t} f_l(Q) f_m(Q) \ \frac{N(l)(N(m)-\delta_{l,m})}{V} 4\pi \int_0^R r^2 w(r) \Big[g^{\mathrm{ES}}_{l,m}(r) - g^{\mathrm{GS}}_{l,m}(r) \Big] \frac{\sin(Qr)}{Qr} dr \tag{2.13}$$

where t is the total set of the type of atoms in the given system, $g^{\mathrm{ES}}_{l,m}(r)$ and $g^{\mathrm{GS}}_{l,m}(r)$ is the RDF for atom pair l, m for the geometry in either the excited state or ground state, respectively. Calculation of the scattering directly from the difference RDFs may be subdivded into the three contributions from the solute, ΔS_u, the solvent, ΔS_v and the solute-solvent cross-term, ΔS_c, similarly to the case of eq. (2.12).

The workflow of calculating the difference scattering signals is illustrated in Figure 2.6. The example, in the workflow procedure, is based on the simulations of the $[\mathrm{Ru(bpy)_3}]^{2+}$ system, as described in Chapter 5.

First, molecular dynamics simulations using explicit solvation is carried out for the system in the electronic ground and excited state(s). From the simulations, we calculate the pairwise RDFs from averaged trajectories. Secondly, the RDFs differences, between ground, $g^{\mathrm{GS}}(r)$, and excited state, $g^{\mathrm{ES}}(r)$, are calculated (yellow). The RDFs are divided into categories of atomic pairs of solute-solute (magenta arrow), solute-solvent (green arrow) and solvent-solvent (blue arrow) interactions. Finally, from the difference RDFs, we calculate the difference scattering components of the solute, ΔS_u (magenta), cross-term ΔS_c (green), and solvent ΔS_v (blue). The figure also shows an example of the calculated scattering signals without employing a weight function, w, which otherwise introduces unphysical ripples in the calculated scattering signals (black).

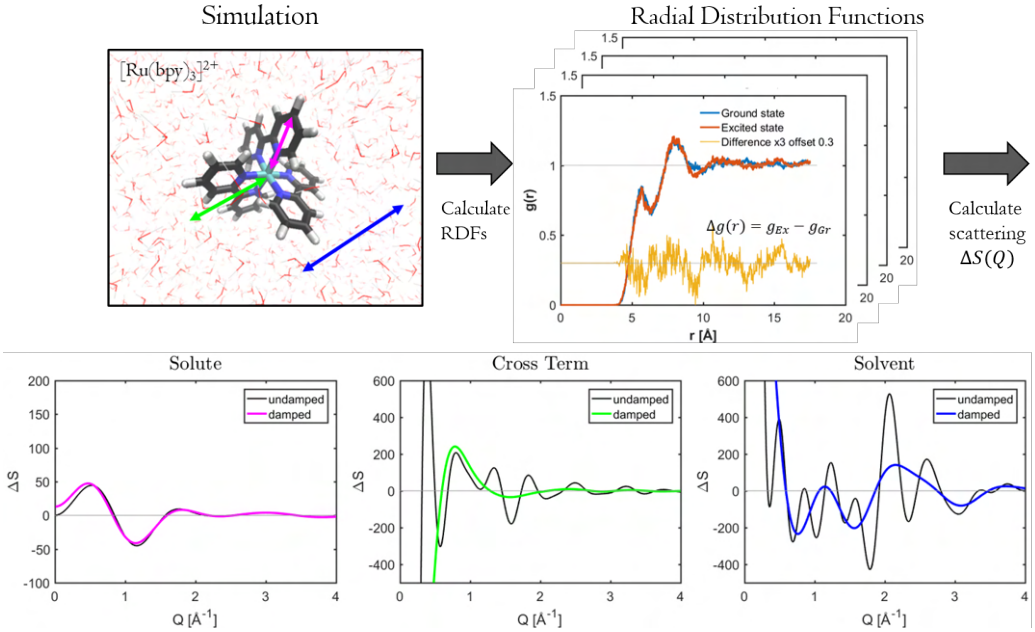

Figure 2.6: Workflow in the calculation of difference scattering signals from radial distribution functions (RDFs). From simulations including explicit solvent, we obtain radial distribution functions of the different types of atom pairs in the given system, solute-solute, solute-solvent and solvent-solvent. We carry out simulations for both the excited state and ground state of the solute, and calculate the difference RDFs (yellow), from which we calculate the difference scattering signals, ΔS of the solute (magenta), the solute-solvent cross-term (green) and the solvent (blue). The calculations employ a weight function, w, that ensures effective removal of artifacts, observed from the spurious oscillations in the undampened signals (black).

Part II

Theoretical background

Chapter 3

Ultrafast dynamics studies using simulations

Contents

The work included in this thesis involves the studies of ultrafast excited state dynamics using both experiments and simulations. The previous part of the thesis involved the experimental background theory, and

this part describes the fundamental theory behind the simulations. This chapter is dedicated to provide a short introduction of relevant theoretical concepts behind the applied methods used for the simulations.

Since, we are interested in electronic and nuclear dynamics in the excited state landscape, we are concerned with quantum effects, and hence we begin by introducing the Schrödinger equation in section 3.1. Subsequently, section 3.2 presents the basics of Density Functional Theory (DFT), which is one of the many practical implementations of electronic structure theory. Furthermore, the time-dependent (TD-DFT) variant is presented in section 3.3, which is a useful tool to study excited states. After that, section 3.4 introduces some classical treatments of molecular structure involving the study of large molecules or the implementation of solvent effects. Moving on to the motions and dynamics of molecular structure involves a time-dependent description of the atomic nuclei as well, which is presented in section 3.5. Finally, the last part of the chapter, section 3.5.3 describes the differences between the choice of representation of the electronic wave function, and this is important to remember when comparing simulations to experimental results.

3.1 The Schrödinger Equation

The Schrödinger equation is the foundation of most quantum chemistry theory. The original papers from 1926 introduces the theory behind what we today know as the Time-Dependent-Schrödinger-Equation (TDSE), which describes the time evolution of any quantum mechanical system [92, 93].

$$\hat{H}\,\Psi(\vec{R},\vec{r},t) = i\hbar\frac{\partial}{\partial t}\Psi(\vec{R},\vec{r},t) \tag{3.1}$$

where the Hamiltonian $\hat{H}$ is an operator acting on the wave function Ψ, which depends on all the n_N nuclear coordinates $\vec{R} = \{\vec{R}_1, \vec{R}_2, \ldots, \vec{R}_{n_N}\}$, all n_e electronic coordinates $\vec{r} = \{\vec{r}_1, \vec{r}_2, \ldots, \vec{r}_{n_e}\}$ and time t, of a given system. The Hamiltonian carries information about the total energy of the system, and describes the interactions between the given particles with each other, and with the surroundings. The wave function is the solution to the TDSE, and holds the complete information of a given system. For example, the absolute square of the wave function, $\Psi\Psi^* = |\Psi|^2$, gives the probability of finding a given particle at a given set of coordinates and time. [94]

In the case of the system being in a so-called stationary state, meaning an eigenstate of the time-independent Hamiltonian $\hat{H} \neq \hat{H}(t)$, one can separate the TDSE into a time-independent wave function and a time-dependent complex phase factor in the following way [95]:

$$\Psi(\vec{R},\vec{r},t) = \Psi(\vec{R},\vec{r})\, e^{-\frac{i}{\hbar}(E_{tot}\, t)}$$

where E_{tot} is the total energy of the system of the given stationary state, and $\hbar$ is the reduced Planck constant. With this separation, the absolute square of the wave function becomes independent of time. From the time-separated wave function, we obtain the Time-Independent-Schrödinger-Equation (TISE):

$$\hat{H}(\vec{R},\vec{r})\,\Psi(\vec{R},\vec{r}) = E_{tot}(\vec{R},\vec{r})\,\Psi(\vec{R},\vec{r}) \tag{3.2}$$

The TISE constitutes a central foundation for many applications in quantum chemistry. Considering a given system of interest, as a molecule with electrons e and nuclei N, the time-independent Hamiltonian consists of the terms:

$$\begin{aligned} \hat{H}(\vec{R},\vec{r}) &= E_{kin} + E_{pot} \\ &= \hat{T}_e + \hat{T}_N + \hat{V}_{ee} + \hat{V}_{NN} + \hat{V}_{Ne} \end{aligned} \tag{3.3}$$

where $\hat{T}$ denotes the kinetic energy of the electrons and nuclei, respectively, and $\hat{V}$ is the potential energy is split into by the Coulomb repulsion among the electrons $\hat{V}_{ee}$, and among the nuclei $\hat{V}_{NN}$, and the Coulomb attraction between the electrons and nuclei $\hat{V}_{Ne}$. For a molecular system consisting of n_e electrons, and n_N nuclei with mass M, the kinetic energy contribution is given, in atomic units as [96, p. 41]:

$$\hat{T}_e(\vec{r}) = -\sum_{i=1}^{n_e} \frac{1}{2}\nabla_i^2$$

$$\hat{T}_N(\vec{R}) = -\sum_{A=1}^{n_N} \frac{1}{2\,M_A}\nabla_A^2$$

where i runs over the n_e electrons, and A over the n_N nuclei. Similarly, the potential energy contributions runs all over electron pairs i, j and nuclei

pairs A, B, and are expressed as follows:

$$\hat{V}_{ee}(\vec{r}) = \sum_{i=1}^{n_e} \sum_{j>i}^{n_e} \frac{1}{\left|\vec{r}_i - \vec{r}_j\right|}$$

$$\hat{V}_{NN}(\vec{R}) = \sum_{A=1}^{n_N} \sum_{B>A}^{n_N} \frac{Z_A Z_B}{\left|\vec{R}_A - \vec{R}_B\right|}$$

$$\hat{V}_{Ne}(\vec{R}, \vec{r}) = -\sum_{A=1}^{n_N} \sum_{i=1}^{n_e} \frac{Z_A}{\left|\vec{R}_A - \vec{r}_i\right|}$$

where Z_A is the charge of nucleus A. It is important to note, that the above Hamiltonian eq. (3.3) does not include relativistic effects, nor effects from an external field [97], which we partly introduce later. Furthermore, since the TISE consists of an $(n_e + n_N)$-body problem, it is not possible to solve the TISE analytically for a system that contains more than 2 particles. This challenge leads us to the approximation introduced by Born and Oppenheimer in 1927 [98].

3.1.1 The Born-Oppenheimer Approximation

One way to simplify the obstacle of solving the TISE is to introduce the Born-Oppenheimer (BO) approximation [98]. The idea is based on the fact that an electron weighs approximately 1800 times less than the most simple atomic nucleus, the proton [97, p. 228],[99, p. 16]. Therefore, the velocity of the nucleus is slow from the perspective of the electrons, and the electrons around the nucleus instantaneously respond to the movements of the nuclei. Based on this, we can separate the electronic and nuclei movements, and split the wave function into an electronic Ψ_e and nuclear Ψ_N part:

$$\Psi(\vec{R}, \vec{r}) = \Psi_N(\vec{R})\, \Psi_e(\vec{r}; \bar{R}) \tag{3.4}$$

where the electronic wave function Ψ_e depends parametrically on a given set of (stationary) nuclear coordinates $\bar{R}$, and the electronic coordinates $\vec{r}$. The separation allows for the electronic structure part to be solved for each fixed nuclear geometry, which leads to the *electronic* TISE:

$$\hat{H}_e(\vec{r}; \bar{R})\, \Psi_e(\vec{r}; \bar{R}) = E^e_{tot}(\bar{R})\, \Psi_e(\vec{r}; \bar{R}) \tag{3.5}$$

where E^e_{tot} is the total electronic energy, which is a function of the fixed nuclei $\bar{R}$. The corresponding electronic Hamiltonian, $\hat{H}_e$ becomes:

$$\hat{H}_e(\vec{r};\bar{R}) = \hat{T}_e + \hat{V}_{ee} + \hat{V}_{NN} + \hat{V}_{Ne}$$

where the kinetic energy $\hat{T}_N$ is zero for stationary nuclei, and the potential energy $\hat{V}_{NN}$ is constant. The solution to the electronic TISE, eq. (3.5), gives the energy for a given nuclear configuration. The total energy, also called the potential energy surface (PES), forms from varying the nuclear geometries and calculating the specific electron energies. Solving the electronic Scrödinger, eq. (3.5) is often referred to as *electronic structure theory*, in contrast to solving the *nuclear* Schrödinger equation for Ψ_N, which is often termed quantum chemical dynamics.

By the introduction of the BO approximation, the many-body problem is significantly reduced, but even for small molecules it is still not possible to solve it analytically. Consequently, further approximations are necessary. A highly used method for electronic structure calculations is Density Functional Theory (DFT), which we will introduce in the following sections.

3.2 Basics of DFT

The main concept of Density Functional Theory (DFT) is to describe a given system in terms of its probability density, instead of the wave function. The idea is that the probability density carries all the necessary information, i.e. it is possible to calculate every necessary quantum mechanical observable from the ground state density. Hence, also the energy of a given system may be written as a functional of the density. [100, 101]

Using the probability density $\rho(\vec{r})$ in DFT, formally reduces the many-body problem in the Schrödinger eq., where the $3\,n_e$ electron coordinates ($4\,n_e$ with spin) are combined within the total electron density to only 3 (4) coordinates [99].

The electronic probability density $\rho(\vec{r})$, is given as the integral of the absolute square of the electronic wave function Ψ_e integrated over all but one of the electronic spatial coordinates $\vec{r}$ for the n_e number of electrons:

$$\rho(\vec{r}) = n_e \int \dots \int \left|\Psi_e(\vec{r},\vec{r}_2,...,\vec{r}_{n_e})\right|^2 d\vec{r}_2 ... d\vec{r}_{n_e}$$

The above expression for $\rho(\vec{r})$ describes the probability of finding any of the n_e electrons at position $\vec{r} = \{x, y, z\}$ within the volume $d\vec{r}_1$. Note, that the integration part of the equation gives us the probability of finding one electron within the volume element of $d\vec{r}_1$, but due the property of indistinguishability of all electrons, one might simply multiply the probability of finding one electron with the number of electrons n_e [101]. Note also that the spin coordinates should also be included, but they are excluded here for simplification.

We can write up the total electronic energy E^e_{tot} in the following way, as a functional of the electronic density $\rho(\vec{r})$:

$$\begin{aligned} E^e_{tot} &= E[\rho(\vec{r})] \\ &= T_e[\rho(\vec{r})] + V_{ee}[\rho(\vec{r})] + E_{ext}[\rho(\vec{r}; \bar{R})] \end{aligned} \tag{3.6}$$

where T_e is the kinetic energy of the electrons, V_{ee} is the potential energy among the electrons, and finally E_{ext} describes an external potential energy, which in the simplest case is calculated from the potential V_{ext} arising from the presence of the nuclei, from the perspective of the electrons (i.e. $V_{ext} = V_{Ne} + V_{NN}$). The external potential depends parametrically on the nuclear coordinates $\bar{R}$. The notation in square brackets shows that the energies are functionals of the electronic density.

The theoretical framework of DFT is based on the work by Hohenberg and Kohn [102] from 1964, and Kohn and Sham [103] from 1965, which in the following sections are described briefly.

3.2.1 Hohenberg-Kohn Theorem

The work by Hohenberg and Kohn describes two theorems [101, 102]

(I) There exists a one-to-one correspondence between the (ground state) external potential V_{ext} and the ground state electron density, ρ_0 of a given system.

(II) The total energy of a given system obeys the variational principle.

The first theorem determines that the external potential V_{ext} and thus the (ground state) electronic energy E are uniquely determined by the (ground state) electron density ρ_0, and vice versa. This also means that two different ground state electronic densities will not lead to the same external

potential. The designation *external* arises from the viewpoint of the electrons where they feel the Coulomb forces that the fixed nuclei exert on the electrons. A given nuclear configuration with n_N nuclei, each one with coordinates $\bar{R}_A$ and charge Z_A, leads to a unique external potential V_{ext}, given as:

$$V_{ext}(\vec{r};\bar{R}) = V_{Ne}(\vec{r};\bar{R}) + V_{NN}(\bar{R}) = -\sum_{A=1}^{n_N} \frac{Z_A}{\left|\vec{R}_A - \vec{r}\right|} + V_{NN}(\bar{R}) \tag{3.7}$$

where the nuclear repulsion term V_{nn} is reduced to a simple constant, when calculating the electronic energy within the BO approximation. With the correspondence between the electron density and the external potential defined, it is possible to write the total electronic energy, E^e_{tot} entirely as a functional of the (ground state) density ρ_0, as done in eq. (3.2).

Furthermore, Hohenberg and Kohn describes that the total electronic energy E^e_{tot} consists of contributions that are universal in the sense that they are independent on the nuclei, and contributions that depend on the given system. Combining the electronic kinetic energy T_e, and the electron-repulsion part V_{ee} leads to a new functional called the Hohenberg-Kohn functional, F_{HK}, which defines the universal part. The external energy, E_{ext} describes the part that depends on the given system, i.e. the external potential V_{ext} the electrons feel by the presence of the nuclei and potentially other external factors.

$$E^e_{tot}[\rho_0] = T_e[\rho_0(\vec{r})] + V_{ee}[\rho_0(\vec{r})] + E_{ext}[\rho_0(\bar{R};\vec{r})]$$

$$E^e_{tot}[\rho_0] = \underbrace{F_{HK}[\rho_0(\vec{r})]}_{\text{universally valid}} + \underbrace{\int \rho_0(\vec{r})\, V_{ext}\, d\vec{r}}_{\text{system dependent}}$$

The Hohenberg-Kohn functional, F_{HK}, represents the essence of DFT. If the correct functional is found, it is in principle possible to find the exact energy, however, the exact functional is not known.

The second theorem ensures that the true ground state density ρ_0 involves minimization of the energy E.

$$E[\rho] \geq E[\rho_0]$$

The two theorems are the foundation (cornerstones) of modern DFT calculations, and solves the many-body problem by use of the electron probability density.

Unfortunately, the Hohenberg-Kohn theorems only proof the existence of a functional that gives the exact ground state energy, but it comes with no guidance of how the functional is constructed. Furthermore, we have no information on how to derive the density without knowledge of the electronic wave function. This leads us to the introduction of the Kohn-Sham approach, which is the basic formulation of DFT mostly applied today.

3.2.2 Kohn-Sham Scheme

Kohn and Sham further developed the theory of DFT by suggesting a way to approach the F_{HK} functional [103, 101]. Their approach arises from the realization that a good description of the kinetic energy term is necessary, since it is the largest contributor to the total energy. The way to achieve this, is to extract as much as possible from the kinetic energy term that we know how to solve and describe the remaining part in an approximate way. They also realized that orbital-based methods performed better regarding the kinetic energy, and therefore, the Kohn-Sham approach also reintroduces the concept of orbitals. The main idea behind their approach is to introduce a fictitious reference system of independent non-interacting electrons, moving in an average potential field defined by the other electrons and nuclei, analogously to the mean-field approach from a wave-function based method such as Hartree Fock. We then know how to calculate the kinetic energy of the reference system, the non-interacting system, and the remaining part is described approximately. The assumption is that both systems have the same ground state electronic density.

The electronic density of the non-interacting system can be described as the sum of the individual electron Kohn-Sham orbitals ϕ_i^{KS}.

$$\rho(\vec{r}) = \sum_{i=1}^{n_e} \left|\phi_i^{KS}(\vec{r})\right|^2 \tag{3.8}$$

where n_e is the number of electrons with the corresponding kinetic energy of the independent electrons defined as T_s. The total kinetic energy of the non-interacting electronic system T_s cannot equal the kinetic energy of the true electron-interacting system T_e, however, Kohn and Sham accounted for this effect by splitting the term in two and introducing the so-called exchange-correlation functional E_{xc}. In this way, the kinetic energy part

which arises from contributions from the electronic correlation T_c, is included in the ex-change-correlation term. The functional also accounts for the part of the electronic correlation that is not already included in the Coulomb interactions V_J. This allows us to write the expression for the Kohn-Sham functional which involves the non-interacting kinetic energy T_s, the classical Coulomb interactions V_J and finally the exchange-correlation functional E_{xc}

$$F_{KS}[\rho] = T_s[\rho] + V_J[\rho] + E_{xc}[\rho] \tag{3.9}$$

with the non-interacting electronic kinetic energy T_s expressed using a set of n_{orb} Kohn-Sham orbitals ϕ with occupation number f_i, and the classical Coulomb repulsion energy V_J between electron densities of different coordinates $\vec{r}, \vec{r'}$ defined as:

$$T_s[\rho] = \int \phi^* \left(-\sum_{i=1}^{n_{orb}} \frac{1}{2} f_i \nabla_i^2 \right) \phi \, d\vec{r}$$

$$V_J[\rho] = \frac{1}{2} \iint \frac{\rho(\vec{r})\rho(\vec{r'})}{|\vec{r} - \vec{r'}|} d\vec{r} d\vec{r'}$$

The exchange-correlation term E_{xc} is the difference between the true, T_e, and non-interacting kinetic energy, T_s, and also the difference between the full electron correlation part E_{ee} minus the classical Coulombic interactions V_J:

$$E_{xc} = (T_e - T_s) + (E_{ee} - V_J) \tag{3.10}$$

The total electronic energy in Kohn-Sham DFT is then:

$$E^{KS}[\rho(\vec{r})] = T_s[\rho] + V_J[\rho] + E_{xc}[\rho] + E_{ext}[\rho] \tag{3.11}$$

The various methods of DFT concerns the functional describing the exchange-correlation functional, since the exact form remains unknown. The idea of splitting the unknown functional into separate terms is one key idea behind Kohn-Sham DFT, which greatly improved the quality of the results and thereby the usefulness. The kinetic energy is the main contributor to the total energy, so splitting it into a known and unknown part, greatly reduces the unknown part of the system. Hence, the exchange-correlation functional only has a small contribution to the total energy, which often makes DFT a useful tool even with the most simple functionals.

Many different functionals exist, since no functional is universally correct. Instead, one must perform a systematic study by comparison of the performance of different functionals, comparison to experimental observables, or to results on a similar system.

To calculate the total energy $E^{KS}[\rho]$ of a given system, one has to find the KS orbitals ϕ^{KS}, by solving the eigenvalue problem:

$$\hat{h}_i^{KS}\phi_i = \varepsilon_i\,\phi_i \tag{3.12}$$

where ε_i is the corresponding orbital energy and $\hat{h}_i^{KS}$ is the Kohn-Sham one-electron operator:

$$\hat{h}_i^{KS} = \hat{t}_i + \hat{v}_{ext} + \hat{v}_J + \hat{v}_{xc} \tag{3.13}$$

where the external potential $\hat{v}_{ext}$ most often is described by the potential that a given electron feels in presence of the n_N nuclei:

$$\hat{v}_{ext} = \hat{v}_{Ne} = -\sum_{k=1}^{n_N} \frac{Z_k}{\left|\vec{R}_k - \vec{r}_i\right|}$$

where Z_k is the nuclear charge of nucleus k, with coordinates $\vec{R}_k$ for the nucleus and $\vec{r}_i$ for the specific electron.

The term $\hat{t}_i = -\frac{1}{2}\nabla_i^2$ is the Kohn-Sham kinetic energy of the given electron, and the term $\hat{v}_J$ is the (Hartree) Coulomb repulsion energy between the given electron and the remaining electron density $\rho(\vec{r'})$.

$$\hat{v}_J = \int \frac{\rho(\vec{r'})}{\left|\vec{r}_i - \vec{r'}\right|} d\vec{r'}$$

Finally the term $\hat{v}_{xc}$ describes the gradient of the exchange-correlation energy E_{xc} dependent on the given functional chosen.

$$\hat{v}_{xc} = \frac{\delta E_{xc}[\rho]}{\delta\rho(\vec{r})}$$

Solving eq. 3.12 gives a set of orbitals, which allows one to compute the total energy given by eq. 3.11. However, since the electron density appears within the single-electron Hamiltonian $\hat{h}_i^{KS}$, the Kohn-Sham equations must be solved iteratively until the density has reached convergence.

To summarize, the method of DFT is a highly applied method, which uses the electronic probability density in contrast to the wave function based methods. The method is formally an exact method, meaning that the electronic correlation is not neglected and it is included in the exchange-correlation functional. As a result it is in principal possible to calculate the exact ground state energy, but it requires the correct energy functional, which is unknown. Instead of finding the true and only functional, one determines as much as possible with known formulation and approximates the unknown part within the exchange-correlation functional.

In the work related to this thesis, DFT was the main choice of method for the electronic structure calculations. In particular, calculations involved geometry optimizations for both the $[Ru(bpy)_3]^{2+}$ and $[Fe(bpy)(CN)_4]^{2-}$ complexes in both electronic ground state and excited state. However, as described, DFT is a method to study electronic ground states, and is not designed to study non-eq. phenomena. Hence, the excited state geometries are not direct excitations from the ground state, but the energy minimum of an excited state potential, and determined by adding a constraint that the spin multiplicity should be 3, to find the equilibrium geometry of the lowest (excited) triplet state.

3.3 Basics of TD-DFT

DFT is only designed to study electronic ground states, and time-independent problems. Even though it is possible to simulate some excited states by tweaking certain parameters or adding constraints, it is only an excited state energy minimum. Another way to compute electronic excited states, is using the time-dependent formulation of DFT [7, ch. 6.9],[100], [104] .

The formulation of time-dependent DFT (TD-DFT) relies on the Runge-Gross theorem, which was published in 1984 [105]. The theorem is a time-dependent analogue of the first Hohenberg-Kohn theorem, which describes the correspondence between the external potential and (time-dependent) density. Furthermore, a pendant to the variational principle was shown, which serves as a way to calculate the exact time-dependent electron density. Next, also time-dependent Kohn-Sham equations were developed as a method to compute the orbitals.

The time-dependent analogue of DFT, which we applied, is based on response theory, in which a small perturbation of the given system induces

a change (a response) in the electron density. This is done as an alternative to actually propagating the orbitals in time, in order to compute excitation energies. For the typical situation the perturbation is described as a time-dependent external electric potential $\hat{V}_{ext}(t)$, included in the total Hamiltonian:

$$\hat{H} = \hat{H}^{(0)} + \hat{V}_{ext}(t) \tag{3.14}$$

where $\hat{H}^{(0)}$ is the time-independent part, e.g. the ground state Kohn-sham Hamiltonian, and the zeroth order perturbation term. The most common application of TD-DFT involves a weak perturbation, where only the first order response $\hat{H}^{(1)}$ is included, which is referred to as Linear Response (LR) TD-DFT. Often the perturbation is described as an oscillatory electric field, which within the dipole approximation is given as:

$$\begin{aligned} \hat{V}_{ext}(t) = \hat{H}^{(1)} &= \mu F \cos(\omega t) \\ &= \mu \tfrac{1}{2} \left(F_{\omega} e^{-i\omega t} + F_{-\omega} e^{i\omega t} \right) \end{aligned} \tag{3.15}$$

where ω is the frequency, F is the field strength and μ is the dipole operator. The perturbed Hamiltonian involves both a positive and negative part, F_{ω} and $F_{-\omega}$, which leads to two parts in the wave function response of the perturbation. For a given frequency, the vector $(\vec{X}, \vec{Y})$ contains the coefficients from the two parts, also referred to as the excitation and de-excitation vectors. In order to compute the excitation energies, one determines the specific frequencies ω, of the oscillating field, for which the electronic density gives a resonant response. The problem can be expressed (within the adiabatic approximation) as a pseudo-eigenvalue problem, often referred to as the Casida equations [106, 107, 108]:

$$\begin{bmatrix} \mathbf{A} & \mathbf{B} \\ \mathbf{B}^* & \mathbf{A}^* \end{bmatrix} \begin{pmatrix} \vec{X}^n \\ \vec{Y}^n \end{pmatrix} = \omega_n \begin{bmatrix} 1 & 0 \\ 0 & -1 \end{bmatrix} \begin{pmatrix} \vec{X}^n \\ \vec{Y}^n \end{pmatrix} \tag{3.16}$$

where the excitation energy $\omega_n = E_n - E_0$ is the difference between the energy of state, n, relative to the ground state. The eigenvectors $(\vec{X}^n, \vec{Y}^n)$ for excited state, n, contain the resonant coefficients of the wave function, and they represent the particle-hole and hole-particle excitations, respectively. The matrix elements of $\mathbf{A}, \mathbf{B}$ involves orbital energy differences, from the resonant orbital energies involved in the transition, the coupling between the given states, and the exchange-correlation energy gradients. Both $\mathbf{A}$

and **B** have the dimension of the number of occupied, N_{occ} times the number of unoccupied, N_{uno} orbitals describing all single excitations between the orbitals. The matrices are real valued if the orbitals are real valued (hence, $\mathbf{A} = \mathbf{A}^*$, $\mathbf{B} = \mathbf{B}^*$). Using the molecular orbital index convention:

$$\underbrace{a,b,c,d,e,f,g,h}_{\text{unoccupied}} \quad \underbrace{i,j,k,l,m,n}_{\text{occupied}} \quad \underbrace{o,p,q,...,z}_{\text{free}}$$

allows us to write up the matrix elements of **A** and **B** in the following way:

$$\begin{aligned} A_{ij}^{ab} &= \delta_{ij}\delta_{ab}(E_a - E_i) + K_{ij}^{ab} + f_{ij,ab}^{xc} \\ B_{ij}^{ab} &= K_{ib}^{aj} + f_{ib,aj}^{xc} \end{aligned} \tag{3.17}$$

where K is the coupling matrix involving the exchange and Coulomb interactions, and f^{xc} involves the gradient of the exchange-correlation energy, both describing the change in electron-electron interaction upon a change in occupation from one orbital to another. The specific expressions depend on the choice of functional. An example of the expressions of K and f^{xc} for two electrons, with coordinates $\vec{r}_1$ and $\vec{r}_2$ is:

$$K_{ij}^{ab} = \langle ij|ab\rangle = \iint \phi_i^*(\vec{r}_1)\phi_j^*(\vec{r}_2)\frac{1}{r_{12}}\phi_a(\vec{r}_1)\phi_b(\vec{r}_2)\,d\vec{r}_1 d\vec{r}_2$$

$$f_{ij,ab}^{xc} = \langle ij|f_{xc}|ab\rangle = \iint \phi_i^*(\vec{r}_1)\phi_j^*(\vec{r}_2)\frac{\delta^2 E_{xc}}{\delta\rho(\vec{r}_1)\delta\rho(\vec{r}_2)}\phi_a(\vec{r}_1)\phi_b(\vec{r}_2)\,d\vec{r}_1 d\vec{r}_2$$

where $r_{12} = |\vec{r}_1 - \vec{r}_2|$ is the distance between the electronic coordinates, and E_{xc} is the exchange-correlation energy, and ϕ are the Kohn-Sham orbitals optimized in a proceeding ground state KS-DFT calculation, with $*$ denoting the complex conjugate.

The diagonal elements of matrix **A** give the orbital energy differences between the states, which are the main contributors to the excitation energy, ω_n. The contribution from matrix **B** is most often small relative to matrix **A**, and hence often negligible. The Tamm-Dancoff approximation (TDA) neglects the **B** matrix, giving in a simplified version of eq. 3.16:

$$\mathbf{A}\vec{X}^n = \omega_n \vec{X}^n \tag{3.18}$$

where $\vec{X}^n$ describes each orbital contribution to the given excitation n.

The use of TD-DFT involves excited state calculations and other time dependent external impacts on a given system. Work related to this thesis used TD-DFT within the TDA approximation in order to calculate excited states for absorption spectra, and in the excited state dynamics simulations using surface hopping as described in later sections.

3.4 Introduction to classical methods

If we wish to include the solvent in our simulations, the size of the system increases dramatically. One way to overcome this obstacle is to describe the solvent using classical molecular mechanics (MM) instead of quantum mechanics (QM) methods. The MM methods are also referred to as classical methods. Often this is sufficient, since we are not interested in breaking bonds of the solvent or transferring charge to the solvent. The interested reader is, referred to literature [7, 109, 110, 111] for an elaborate description of the theory. The following sections provide a short introduction to the methods used in the current work.

3.4.1 Molecular Mechanics (MM)

In molecular mechanics, the electrons are not considered as individual particles but rather as a charge distribution, which makes it is a purely classical approach to calculate the total energy of a system. The electronic energy is expressed in terms of a parametric function of the nuclear coordinates, and the parameters are determined from fitting procedures against experimental results or highly accurate QM calculations of small molecules. The set of functions combined with the fitted set of parameters forms the *force field* (FF). Many different types of FFs exist and are typically optimized for a certain property.

Generally, the total potential energy E_{pot} of a given system consists of contributions from bonded, and non-bonded interactions:

$$E_{pot} = V_{\text{bond}} + V_{\text{non-bond}} \tag{3.19}$$

The bonded interactions, V_{bond}, concern bond lengths, angles and dihedrals, and are typically described harmonically. The non-bonded interactions, $V_{\text{non-bond}}$, describe the electrostatic and Van der Waals interactions, often modeled by a Lennard-Jones potential.

A given molecule of interest has both bonded interactions between neighboring atoms, and non-bonded interactions between atoms with a larger separation, as illustrated in Figure 3.1. The non-bonded interactions also involve intermolecular interactions. A common approach to model the bonded interactions is the use of the following functions:

$$\begin{aligned} V_{\text{bond}} = & \sum_{b}^{\text{bonds}} k_b (R_{b_{ij}} - R_{b_{eq,ij}})^2 \\ & + \sum_{a}^{\text{angles}} k_a (\theta_{a_{ijk}} - \theta_{a_{eq,ijk}})^2 \\ & + \sum_{d}^{\text{dihedrals}} \sum_{p}^{\text{period}} \frac{1}{2} V_{dp} \left[1 + \cos\left(p\, \phi_{d_{ijkl}} - \gamma_p \right) \right] \end{aligned} \tag{3.20}$$

where the indices i, j, k, l refer to the different neighboring atoms, and the sums run over the number of bonds, angles, or dihedrals. There is no unique way to determine the number of bonds, angles, and dihedrals, and the input files for a given simulation must specify which atoms are involved. The bonded interactions account for the bond stretching, angle bending and torsions of the system. Typically, a harmonic potential describes the bond stretch R_b between two atoms (i, j) or angle θ_a of three atoms (i, j, k) relative to the equilibrium bond length $R_{b_{eq}}$ or angle $\theta_{a_{eq}}$ with force constant k_b or k_a, respectively. The dihedrals are often described by a Fourier series expansion of cosines. The parameters are the torsion dihedral ϕ_d of 4 atoms (i, j, k, l), and the torsion barrier V_{dp}, for each period p, and phase γ_p. The intramolecular interactions are illustrated in Figure 3.1. For the non-bonded interactions, the general approach is using the Coulomb and Lennard-Jones potentials (in atomic units):

$$\begin{aligned} V_{\text{non-bond}} = & \sum_{i,j,\ j>i}^{\text{atoms}} \frac{q_i\, q_j}{R_{ij}} \\ & + \sum_{i,j,\ j>i}^{\text{atoms}} 4\varepsilon_{ij} \left[\left(\frac{\sigma_{ij}}{R_{ij}} \right)^{12} - \left(\frac{\sigma_{ij}}{R_{ij}} \right)^{6} \right] \end{aligned} \tag{3.21}$$

Here, the non-bonded interactions are calculated for each atomic pair i, j with partial charge q and distance R between them.

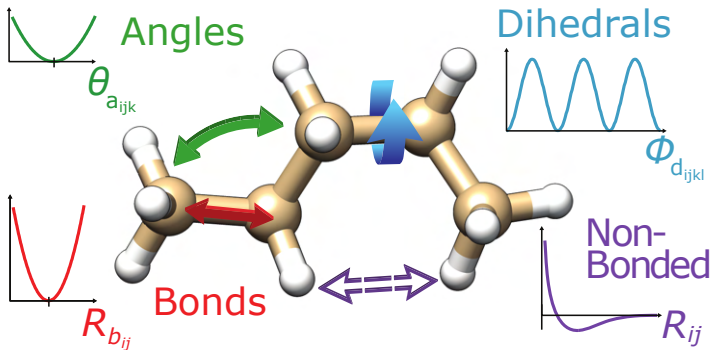

Figure 3.1: Illustration of the different types of interactions considered in a classical, molecular mechanics description of a given system. The bonded interactions include the bond lengths $R_{b_{ij}}$ between two atoms (i,j), the angles $\theta_{a_{ijk}}$ between three atoms (i,j,k), and the dehedrals $\phi_{d_{ijkl}}$ of four atoms (i,j,k,l). The non-bonded interactions involve the Coulomb forces and Lennard-Jones interactions between two atoms of distance R_{ij}. Adapted Figure from [112]

Additional parameters are the Lennard-Jones parameters σ_{ij} and ε_{ij}, which is sometimes expressed in terms of A, B or in terms of Van der Waals radii, R_{min} instead. In the above notation, σ_{ij} describes the distance where the potential is exactly zero, i.e., the shortest distance before the two atoms start to repel each other rather than attract. Similarly, ε_{ij} describes the depth of the potential well, in terms of energy.

For the excited state dynamics simulations carried out in this work, we used the SPC/Fw [113] type force field for the solvent water molecules. This MM water type is an extension to the widely used Simple-Point-Charge (SPC) [114] water model, which is a rigid body model with frozen intramolecular degrees of freedom. However, the extension is a flexible type water model, allowing for stretching and bending movements of the solvent bonds. The SPC/Fw model is a three-site model where the three interaction sites are centered at the positions of the atomic nuclei of the water molecule. The bonded interactions include two O-H bond lengths (R_{OH_1}, R_{OH_2}) and one H-O-H bond angle θ_{HOH}. There are no dihedrals, since there are only three interaction sites in the water model.

3.4.2 Quantum Mechanics/Molecular Mechanics (QM/MM)

Simulations of large systems such as large proteins or smaller molecules including solvation, very often necessitates the use of Molecular Mechanics (MM) methods. However, force fields are often not accurate enough, for the description of chemical phenomena such as electron transfer and excited state dynamics in general. Therefore, a combined QM/MM [115, 109, 116] approach might serve as a compromise between chemical accuracy and computational cost, for some systems. The main idea is to describe a small subset of the given system using QM, and the remaining part of the system using MM. The QM part involves the part of the system in which the chemical process takes place, which in our case is the transition metal complex. The remaining part involves the part of the system that is hardly affected by the chemical process, but might still have an influence, which in our case is the solvent water molecules. Figure 3.2 illustrates the aqueous $[Fe(bpy)(CN)_4]^{2-}$ system in the combined QM/MM approach with the different levels of theory for different regions of the system.

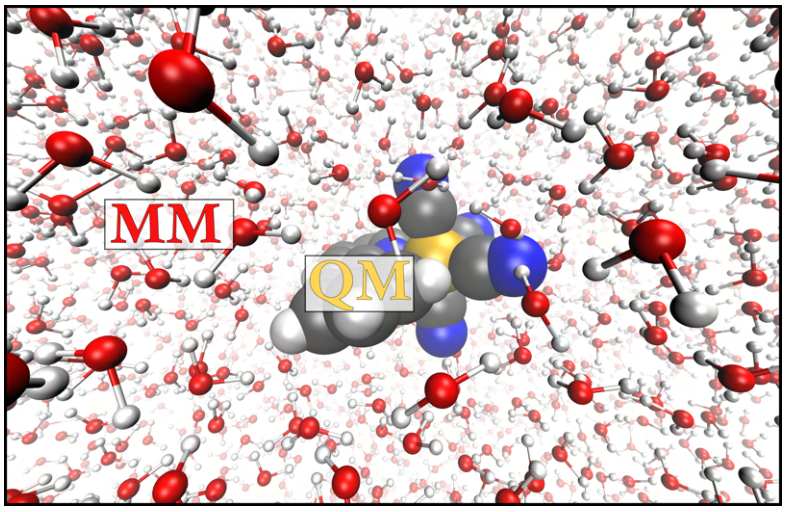

Figure 3.2: Illustration of the combined QM/MM approach for simulations of large systems or studies in solution. The idea is to divide the system into two parts, where one part applies QM theory and the other part MM theory. For the simulations described in this thesis the QM region was the metal complex and the MM part was the solvent.

The total potential energy, V_{tot}^{QMMM} of such a hydrid approach has contributions from three types of interactions; the QM region, the MM region, and the interaction between the two subsystems. The "pure" QM and MM regions can be described individually by the respective choice of method. However, the complexity lies in the description of the interaction between the two parts of the system. Generally, two main approaches exists; either based on subtractive or additive coupling schemes.

In the subtractive method, the total potential energy is computed, first at the MM level of theory for the total system, V^{MM}(MM+QM), then by a computation of the QM energy from only the QM sub region, V^{QM}(QM) and finally the MM energy of the QM sub region, V^{MM}(QM), is subtracted:

$$\begin{aligned} V_{tot}^{\mathrm{QMMM}} = {} & V^{\mathrm{MM}}(\mathrm{MM{+}QM}) + V^{\mathrm{QM}}(\mathrm{QM}) \\ & - V^{\mathrm{MM}}(\mathrm{QM}) \end{aligned} \tag{3.22}$$

In the additive methods, the QM sub part of the system is embedded within the MM part, and the total energy is computed as a sum of the MM energy for the MM sub region, V^{MM}(MM), the QM energy for the QM sub region, V^{QM}(QM), and the QM/MM coupling energy, V^{QMMM}(MM+QM), between the two sub systems:

$$\begin{aligned} V_{tot}^{\mathrm{QMMM}} = {} & V^{\mathrm{MM}}(\mathrm{MM}) + V^{\mathrm{QM}}(\mathrm{QM}) \\ & + V^{\mathrm{QMMM}}(\mathrm{MM{+}QM}) \end{aligned} \tag{3.23}$$

The superscripts describes the level of theory involved in the calculation of the energy, and the QM or MM text in parenthesis denotes which sub part of the given system is included.

The interaction energy in the additive scheme might be calculated in different ways. The most simple interaction includes only the *mechanical embedding*, in which the interactions between the sub regions are handled at the MM level of theory, by including QM atoms in the calculation of the MM potential energy. Hence, the electronic wave function is only evaluated for the isolated QM sub region, and the MM environment cannot induce polarization of the electron density in the QM part. In order to include polarization effects, the QM/MM interaction should include *electrostatic embedding* [117].

In the electrostatic embedding the MM partial charges are included in the QM Hamiltonian in the QM energy computation as a Coulombic interaction:

$$\hat{h}_i^{\mathrm{QMMM}} = \hat{h}_i^{\mathrm{QM}} - \sum_{J=1}^{n_{\mathrm{MM}}} \frac{Q_J}{|\vec{r}_i - \vec{R}_J|} \tag{3.24}$$

where $\hat{h}_i^{\mathrm{QM}}$ is the original one-electron Hamiltonian for electron i, as described in previous sections depending on the choice of QM method. In addition, $\vec{r}_i$ and $\vec{R}_J$ denote the positions of the specific electron i and MM partial charge J, respectively. The interactions are summed over the number of partial charges n_{MM} with charge Q_J, within the MM sub region.

The electrostatic embedding thus allows for polarization of the QM electron density by changes in distances of the MM partial charges and the QM sub system. However, the QM region does not allow for polarization of the MM charge density, which brings us to the next step of development in QM/MM interaction energies. The next level of QM/MM interactions is a polarizable MM part in which the MM part may induce polarization of the QM electron density, and the other way around, such that both sub systems continuously influence each other. However, for the polarization of the MM part, it is necessary to calculate the MM polarization for each iteration of the QM calculations which makes polarization embedding more expensive calculations. The polarizable embedding is a more complex approach and is still under development, some examples include [118, 119, 120].

For the simulations involving the $[\mathrm{Ru(bpy)_3}]^{2+}$ and $[\mathrm{Fe(bpy)(CN)_4}]^{2-}$ systems in aqueous solution, the QM/MM approach with electrostatic embedding was applied. The QM sub-part was the metal complex and the MM sub-part was the surrounding water molecules, which allowed for several thousand solvent molecules.

Section 3.4 introduced how to include the solvent in the simulations either by a computationally cheap MM method, or by a mixed QM/MM method. The next section introduces molecular movement of the given system.

3.5 Dynamics

Previous sections described how to model static molecular systems. However, to describe time dependent behavior, it is necessary to introduce nuclear motion in the equations. This is done either classically by solving Newton's equations, or quantum mechanically by solving the nuclear TDSE, or by a combination in a mixed-quantum-classical approach.

Pure quantum dynamics [121] involves expansion of the nuclear wave function as linear combinations of basis functions, and the time-dependent behavior of such a nuclear wave function is usually referred to as a wave packet. Unfortunately, pure wave packet dynamics simulations suffers from exponential scaling with the number of degrees of freedom, which fast makes these methods incomprehensible with an increasing size of system and is therefore limited to few-atom sized systems. Often it is a necessity to introduce several approximations or reduce the degrees of freedom, in order to study excited state dynamics. A popular method is Multi-Configurational Time-Dependent Hartree (MCTDH) [121], which employs a flexible wave function Ansatz, keeping the wave function representation as compact as possible. However, the MCTDH method still suffers from exponential scaling with degrees of freedom, and a much cheaper and faster approach is achieved by introducing classical or mixed-quantum-classical approaches. In the following, section 3.5.1 describe the pure classical approach and section 3.5.2 describes a mixed-quantum-classical approach referred to as surface hopping dynamics.

3.5.1 Pure classical dynamics

A very popular way of treating nuclear dynamics is Molecular Dynamics (MD) [111]. In such methods, the nuclei are described classically as point charges that move in the direction given by the forces $\vec{F}$ (energy gradients ∇E) acting on the nuclei. For a given nucleus A with mass m_A, acceleration $\vec{a}_A$, and coordinates $\vec{R}_A$, the dynamics is given via the force $\vec{F}_A$ acting on the nucleus as dictated by Newton's equation of motion:

$$\begin{aligned} m_A \vec{a}_A &= \vec{F}_A \\ m_A \frac{\mathrm{d}^2 \vec{R}_A}{\mathrm{d}t^2} &= -\nabla_A E(\vec{R}) \end{aligned} \tag{3.25}$$

The energy, E is computed from the total potential energy of the system depending on the choice of force field (FF) as described in section 3.4.1. The energy could also be from a QM/MM setup, as described in section 3.4.2, with the total system propagated classically. Integration of the above eq. (3.25), gives the complete set of time-dependent coordinates $\vec{R}_A(t) = \{\vec{R}_A(t_1), \vec{R}_A(t_2), ..., \vec{R}_A(t_{\max})\}$ for nucleus A, and the collection of all N nuclei in the given system is referred to as a trajectory, $\vec{R} = \{\vec{R}_A, \vec{R}_B, ..., \vec{R}_N\}$. However, it is not feasible to solve for the trajectory analytically because one deals with many-body equations. Instead, several numerical methods exists, and one method is called the Velocity-Verlet algorithm [122]. Here, the system is evaluated at a given time t and propagated to time step $t + \Delta t$. The atomic coordinates $\vec{R}$, velocities $\vec{v} = \{\vec{v}_A, \vec{v}_B, ..., \vec{v}_N\}$ and accelerations $\vec{a} = \{\vec{a}_A, \vec{a}_B, ..., \vec{a}_N\}$ are updated accordingly:

$$\begin{aligned} \vec{a}_A(t) &= -\tfrac{1}{m_A}\nabla_A E(\vec{R}) \\ \vec{a}_A(t+\Delta t) &= -\tfrac{1}{m_A}\nabla_A E\left(\vec{R}(t+\Delta t)\right) \\ \vec{v}(t+\Delta t) &= \vec{v}(t) + \tfrac{1}{2}\Big(\vec{a}(t) + \vec{a}(t+\Delta t)\Big)\Delta t \\ \vec{R}(t+\Delta t) &= \vec{R}(t) + \vec{v}(t)\Delta t + \tfrac{1}{2}\vec{a}(t)\Delta t^2 \end{aligned} \tag{3.26}$$

The main advantage of using pure classical approaches is the large reduction in required computational time. Classical molecular dynamics simulations treat the nuclei as individual point charges, placed locally in contrast to the delocalized wave packet formulation. Hence, the classical methods are free from exponential scaling with increasing size of the system as in pure quantum dynamics. MD simulations easily compute the motions of thousands of atoms in few hours. Therefore, pure MD simulations are highly applied for simulations of large systems such as proteins, or systems including solvation. However, classical methods fail to describe quantum effects like charge delocalization, tunneling and wave packet splitting.

A way to re-introduce some of the quantum effects is by use of a mixed-quantum-classical approach, often referred to as ab-initio Molecular Dynamics (AIMD). Since, the forces acting on the nuclei relies on energy gradients, one way to re-introduce some quantum effect is to calculate the electronic energy quantum mechanically. AIMD methods, use the electronic energy calculated by quantum electronic structure methods, to cal-

culate the forces acting on the classical nuclei. The AIMD methods such as Born-Oppenheimer MD (BOMD), have recently shown good results in comparison to X-ray scattering experiments [80]. However, BOMD methods still suffer from the dipute that classical nuclei only may follow one potential energy surface at a time, meaning that a nuclear wave packet is always localized and cannot split. A way to overcome this, is to allow switching between several potential energy surfaces, which leads us to Surface Hopping dynamics, and in particular, the SHARC (Surface Hopping including ARbitrary Couplings) program package.

3.5.2 Surface Hopping dynamics

Surface hopping dynamics is a method to describe a nuclear wave packet moving on several potential energy surfaces, in a mixed-quantum-classical sense [123, 124, 125, 126, 127, 128]. In a fully classical description, and BOMD simulations the nuclei only propagate along the same potential energy surface. However, in the QM picture there are several surfaces (electronic states), and a nuclear wave packet might split when approaching a region of high coupling between two states, such that part of the wave packet will propagate on the original surface and part of it will transfer to another surface, simultaneously. This splitting is not easy to simulate and surface hopping provide one way to approximate the situation. Figure 3.3 panel (a), illustrates the concept where an initial wave packet of a given system propagates along an excited state potential surface (red), and at a later time reaches a conical intersection (region of high coupling). After the intersection, the wave packet is split into 3 parts, one continuing on the same excited (red) surface and two on the another surface (blue), in separate directions.

Trajectory surface hopping describes the wave packet splitting by propagating several independent trajectories, that each only moves on one potential energy surface at a time, but are allowed to "hop" between the given surfaces. In this way, the trajectories move separately in different states, and with sufficient statistics (enough trajectories) one is able to describe the wave packet propagation by analysis of the ensemble of trajectories. Figure 3.3 panel (b) illustrates the surface hopping approach of starting several independent trajectories in the top left, and at later times, some of the trajectories stayed on the excited state surface and others "hopped" to another surface.

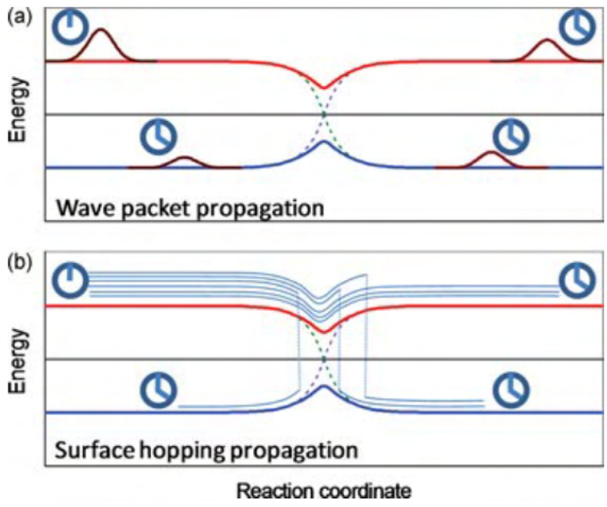

Figure 3.3: The concept of wave packet propagation and the surface hopping approach. The top, part (a), illustrates an initial wave packet moving along an excited state energy surface (red), which splits into several parts when reaching a region of coupling to a surface located at lower energy (blue). Part of the wave packet stays on the same surface and some transfers to the other surface in different directions. The bottom, part (b), illustrates the surface hopping approach, by initiation of many independent trajectories, which will propagate along different individual paths. Figure from [125].

In surface hopping, the electronic and nuclear motions are treated separately, but they are highly coupled. The motion of the electrons are described quantum mechanically and propagated using the time-dependent Schrödinger equation (TDSE), while Newton's classical equations describe the motion of the nuclei, as described in greater detail in the following. The connection between the two arises from the forces acting on the nuclei, which are calculated as the gradient of the potential energy surface, dictated by the so called *active* electronic state. The determination of the active state distinguishes the different variations of surface hopping methods, among other things as well. The SHARC (Surface Hopping including Arbitrary Constants) program, utilizes the so called *fewest switches* method to determine the active state, developed by Tully and coworkers in the 1990'ies [129, 123]. The method of fewest switches monitors the composition of the electronic wave function through the population in each state, $|c_\alpha(t)|^2$ in each time step of the dynamics. A decrease in the population of the current active state results in a calculation of the probability of switch-

ing the given active state to another state. According to the probability, a random number algorithm, determines if the active state stays the same or changes. A change in state corresponds to a "surface hop".

The motion of a given nucleus with mass m_A and position $\vec{R}_A$ follows Newton's second law (as eq. (3.25)) with the force acting on it given as the negative gradient of the electronic potential energy surface E^{el}_{act} of the active electronic state.

$$m_A \frac{\partial^2 \vec{R}_A(t)}{\partial t^2} = -\nabla_A E^{\text{el}}_{act} \vec{R}_A \tag{3.27}$$

The collective nuclear motion is given by $\vec{R}(t) = \{\vec{R}_A(t), \vec{R}_B(t), ..., \vec{R}_N(t)\}$, which holds the positions from each nucleus at each time step t, defining a classical trajectory. The electronic energy, depends on the given set of nuclear coordinates and this way, the electronic and nuclei dynamics are intimately coupled.

The dynamics of the electrons are described by a time-dependent electronic wave function Ψ_e expressed as a linear combination of electronic basis states, Φ_α :

$$\Psi_e(\vec{R}, \vec{r}, t) = \sum_{\alpha=1}^{N_s} c_\alpha(t) \Phi_\alpha(\vec{r}; \vec{R}(t)) \tag{3.28}$$

where c_α are the time-dependent coefficients summed over the number of basis states N_s, and $\vec{r}$ is the electronic coordinates for a given set of nuclear coordinates $\vec{R}$. The basis states are obtained from the solution to the electronic time-independent Schrödinger equation:

$$\hat{H}_e(\vec{r}; \vec{R}(t)) \Phi_\alpha = E^{\text{el}}_\alpha(\vec{R}(t)) \Phi_\alpha$$

where $\hat{H}_e$ is the electronic Hamiltonian, a function of the electron coordinates $\vec{r}$ depending on the given set of (stationary) nuclear coordinates $\vec{R}$ at the specific time t. The expression and properties of the Hamiltonian and the resulting basis states depend on the choice of *representation*, which is discussed in section 3.5.3.

In order to determine the time evolution of the electronic motion, we insert the expression for the total electronic wave function eq. (3.28) into

the total electronic TDSE, and begin by expansion of the derivative product:

$$\begin{aligned}
\hat{H}_e^{\text{tot}}\Psi_e &= \mathrm{i}\hbar\frac{\partial\Psi_e}{\partial t} \\
\hat{H}_e^{\text{tot}}\sum_\alpha c_\alpha(t)\,\Phi_\alpha &= \mathrm{i}\hbar\frac{\partial}{\partial t}\left(\sum_\alpha c_\alpha(t)\,\Phi_\alpha\right) \\
\sum_\alpha c_\alpha(t)\hat{H}_e^{\text{tot}}\Phi_\alpha &= \mathrm{i}\hbar\sum_\alpha\left[\left(\frac{\partial}{\partial t}c_\alpha(t)\right)\Phi_\alpha\right] + \mathrm{i}\hbar\sum_\alpha\left(c_\alpha(t)\right)\frac{\partial}{\partial t}\Phi_\alpha
\end{aligned}$$

Note that, for simplicity, the time dependence, t, as well as the dependence of the nuclear, $\vec{R}$, and electronic, $\vec{r}$, coordinates are suppressed from the total electronic Hamiltonian, $\hat{H}_e^{\text{tot}}(\vec{r};\vec{R}(t))$, and from the basis states $\Phi_\alpha(\vec{r};\vec{R}(t))$. By multiplication of the complex basis state Φ_β^*, integration over the electronic space $d\vec{r}$, and employing that Φ_α,Φ_β are orthonormal, we derive the equation of motion for the coefficients of the electronic wave function as:

$$\begin{aligned}
\sum_\alpha c_\alpha(t)\int\left(\hat{H}_e^{\text{tot}}\Phi_\alpha\right)\Phi_\beta^*\,d\vec{r} &= \mathrm{i}\hbar\sum_\alpha\left(\frac{\partial}{\partial t}c_\alpha(t)\int\Phi_\alpha\Phi_\beta^*d\vec{r}\right) \\
&\quad + \mathrm{i}\hbar\sum_\alpha\left(c_\alpha(t)\int\left(\frac{\partial}{\partial t}\Phi_\alpha\right)\Phi_\beta^*\,d\vec{r}\right) \\
&= \mathrm{i}\hbar\frac{\partial}{\partial t}c_\beta(t) + \mathrm{i}\hbar\sum_\alpha\left(c_\alpha(t)\int\left(\frac{\partial}{\partial t}\Phi_\alpha\right)\Phi_\beta^*\,d\vec{r}\right) \\
\frac{\partial}{\partial t}c_\beta(t) &= -\tfrac{\mathrm{i}}{\hbar}\sum_\alpha c_\alpha(t)\int\left(\hat{H}_e^{\text{tot}}\Phi_\alpha\right)\Phi_\beta^*\,d\vec{r} \\
&\quad - \sum_\alpha c_\alpha(t)\int\left(\frac{\partial}{\partial t}\Phi_\alpha\right)\Phi_\beta^*\,d\vec{r} \\
\frac{\partial c_\beta(t)}{\partial t} &= -\sum_\alpha\left[\tfrac{\mathrm{i}}{\hbar}\underbrace{\int\left(\hat{H}_e^{\text{tot}}\Phi_\alpha\right)\Phi_\beta^*\,d\vec{r}}_{H_{\beta\alpha}} + \underbrace{\int\left(\frac{\partial}{\partial t}\Phi_\alpha\right)\Phi_\beta^*\,d\vec{r}}_{T_{\beta\alpha}}\right]c_\alpha(t)
\end{aligned} \tag{3.29}$$

where the two integrals in the end, describe the coupling between the states, defined as $H_{\beta\alpha}$ and $T_{\beta\alpha}$, and their properties depend on the choice

of the set of electronic basis states Φ_α, referred to as different *representations*. Section 3.5.3 describes the different types of representations and the consequences for the couplings and appearance of the potential energetic landscape.

Integration of eq. (3.29) allows determination of the propagation of the set of coefficients, c_β from time step t to a later time step, $t + \Delta t$. In practice, in SHARC, this is done via the so-called *three-step propagator* method, which is described elsewhere [126, 127]. When the coefficients of both time steps $c_\beta(t)$, $c_\beta(t + \Delta t)$ are determined, we can compute the populations $|c_\beta(t)|^2$, $|c_\beta(t + \Delta t)|^2$ in order to determine if the population changed. As previously described, if the population of the current active state decreased, SHARC calculates the hopping probability, $h_{\beta\rightarrow}$ out of the current active state, β, via the expression:

$$h_{\beta\rightarrow} = \max\left(1 - \frac{\left|c_\beta(t+\Delta t)\right|^2}{\left|c_\beta(t)\right|^2}, 0\right) \tag{3.30}$$

which gives a probability of 0, if the populations are the same. The expression determines the probability of a hop out of active state β to any other state, and the specific state depends, among other things, on the coupling between the states, as described in [126, 127]. The first part in the parenthesis of eq. (3.30) becomes negative, if the population increased, and thus hopping probability becomes zero; hence only a decrease in population leads to a hopping probability greater than zero. Next, a random number r between 0 to 1, influences the choice of the next active state for time step $t + \Delta t$. A hop out of state β into state α, occurs if the random number is within an interval with a width proportional to the hopping probability, $h_{\beta\rightarrow\alpha}$.

$$\sum_{i=1}^{\alpha-1} h_{\beta\rightarrow i} < r \leq \sum_{i=1}^{\alpha-1} h_{\beta\rightarrow i} + h_{\beta\rightarrow\alpha}$$

Finally, a remark on the total electronic Hamiltonian used in the propagation of the electrons, eq. (3.29). If we want to describe excited state processes involving inter-system crossing (ISC), we need to include spin-orbit couplings in the total electronic Hamiltonian. The SHARC program involves surface hopping dynamics by extension of the total electronic

Hamiltonian to any arbitrary state-to-state couplings. The standard electronic Hamiltonian, applied in most standard quantum chemistry software, is here referred to as the Molecular Coulomb Hamiltonian (MCH) and involves the terms:

$$\hat{H}_e^{\mathrm{MCH}} = \hat{T}_e + \hat{V}_{ee} + \hat{V}_{NN} + \hat{V}_{Ne} \tag{3.31}$$

where $\hat{T}_e$ is the electronic kinetic energy, $\hat{V}$ is the Coulomb potential energy among and between the electrons e and the stationary nuclei N as described in the previous section 3.1. The MCH Hamiltonian does not include other interactions such as an external field, relativistic effects, or spin-orbit coupling but these are included by introducing an additional term, $\hat{H}_e^{\mathrm{additional}}$ in the total electronic Hamiltonian:

$$\hat{H}_e^{\mathrm{tot}} = \hat{H}_e^{\mathrm{MCH}} + \hat{H}_e^{\mathrm{additional}} \tag{3.32}$$

which allows the calculation of any type of additional coupling terms beyond the nonadiabatic couplings. As a result the SHARC program can describe excited state dynamics such as internal conversion, intersystem crossing and radiative processes. Unfortunately, determination of the eigenfunctions of $\hat{H}_e^{\mathrm{tot}}$ including any additional coupling terms is non-trivial, which brings us to the next section, which describes the appearance and properties of the basis states Φ_α according to the choice of representation.

3.5.3 Representations in SHARC

Because of the mixed-classical-quantum nature of surface hopping simulations, the SHARC results are not invariant to the choice of electronic basis [130], and this section explains the consequences of using one of the three different bases, in the following referred to as, diabatic, MCH or diagnonal [126, 127].

First of all, in SHARC everything works within the matrix representation, in contrast to operators. In the following, we omit the electronic part of the notation for the Hamiltonian $\hat{H}^{tot} = \hat{H}_e^{tot}$, for simplification, and also since the nuclei are described classically in surface hopping, no nuclear Hamiltonian exist. The matrix representation of the total Hamiltonian is $\mathbf{H}$, and a matrix element $H_{\beta\alpha}$ is defined as follows:

$$H_{\beta\alpha} = \left\langle \Phi_\beta \middle| \hat{H}^{tot} \middle| \Phi_\alpha \right\rangle = \int \Phi_\beta^* \hat{H}^{tot} \Phi_\alpha \, d\vec{r}$$

In a similar manner, we write the expression for the equation of motion of the electronic coefficients from eq. (3.29) in terms of the total Hamiltonian matrix **H**, and the coupling matrix **T** in the following manner:

$$\frac{\partial \vec{c}(t)}{\partial t} = -\left[\tfrac{i}{\hbar}\mathbf{H} + \mathbf{T}\right]\vec{c}(t) \tag{3.33}$$

where the time-derivative coupling matrix **T** describes how the states change in time into each other. Typically, **T** is computed from the nuclear velocities $\vec{v}$ and the non-adiabatic coupling matrix **K**, which describes the change of the states with geometry, such that $\mathbf{T} = \vec{v}\mathbf{K}$. The matrix elements are defined as:

$$T_{\beta\alpha} = \left\langle \Phi_\beta \middle| \frac{\partial}{\partial t} \middle| \Phi_\alpha \right\rangle = \int \Phi_\beta^* \frac{\partial}{\partial t} \Phi_\alpha \, d\vec{r}$$
$$K_{\beta\alpha} = \left\langle \Phi_\beta \middle| \frac{\partial}{\partial \vec{R}} \middle| \Phi_\alpha \right\rangle = \int \Phi_\beta^* \frac{\partial}{\partial \vec{R}} \Phi_\alpha \, d\vec{r}$$

All quantities in the equation of motion for the electronic propagation eq. (3.33) depend on the choice of basis states Φ_α, which in the following is referred to as different *representations*. The choice of representation has several consequences which are discussed in the following. In particular, the **H** and **T** matrices have different properties depending on the representation. The characteristics of the matrices are discussed with the notation $\mathbf{H}^{\text{rep}}$, $\mathbf{T}^{\text{rep}}$, where *rep* denotes the choice of representation. We discuss three different representations, referred to as the diabatic, MCH, and diagonal (adiabatic) representation [126, 127].

The **diabatic** or **spectroscopic** states is the representation that is typically used in experiments when discussing experimental observables. In the diabatic case, the electronic wave function of a given state is time- or geometry independent. As a result all states can freely cross each other. In the diabatic representation, the temporal coupling is zero $\mathbf{T}^{\text{diab}} = 0$ since the states do not change character with time. Instead, the couplings between the states are described in the Hamiltonian matrix, $\mathbf{H}^{\text{diab}}$, which contains both diagonal and off-diagonal elements. The off-diagonal coupling elements are often delocalized over the potential energy landscape, which is not ideal for surface hopping, since it might lead to non-zero probability transfers between states far away from crossing regions.

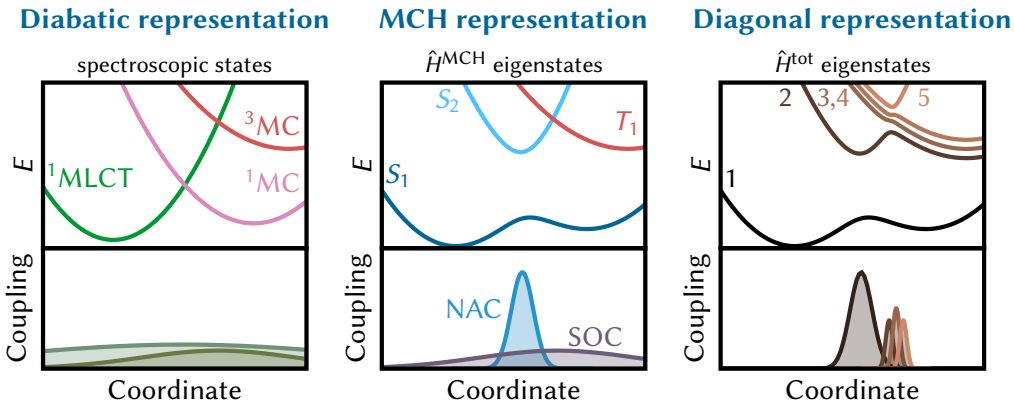

Figure 3.4: Schematic description of different wave function representations referred to as, the diabatic, molecular coulomb hamiltonian (MCH), and diagonal. The representation varies in the depiction of the potential energy surfaces (PES), and the coupling matrix elements, which are entirely delocalized in the diabatic case, localized in the diagonal case and in the MCH representation the non-adiabatic couplings (NAC) are localized whereas spin-orbit couplings (SOC) are delocalized. Adapted figure from [127]

Hence, simulations of more trajectories are necessary to sample the excited state dynamics correctly, because surface hops may occur in much larger regions of configuration spaces.

The diabatic states are often labeled according to symmetry or a given character of the state such as e.g. ^{1}MLCT or ^{1}MC. In contrast, for the MCH, or diagonal representation, the same state can show both ^{1}MLCT or ^{1}MC character depending on the nuclear geometry, whereas in the diabatic representation these are two different states.

The obvious advantage of the diabatic representation is the direct comparison to experiments, which most often uses the same description of the different states. The disadvantages include that most software for electronic structure calculations use a different representation, and hence a non-trivial diabatization procedure is necessary.

Next, the **MCH representation** is the one standard chemistry codes apply. In the MCH representation, the basis states, Φ are eigenstates of the MCH operator, $\hat{H}^{\text{MCH}}$, which contains only the electronic kinetic energy, and the classical Coulomb interactions within the molecule as shown in eq. (3.31). As a result, the Hamiltonian matrix, $\mathbf{H}^{\text{MCH}}$ in the MCH repre-

sentation is diagonal, with elements $H_{\beta\alpha} = \langle \Phi_\beta^{\mathrm{MCH}} | \hat{H}^{\mathrm{MCH}} | \Phi_\alpha^{\mathrm{MCH}} \rangle$. However, if additional terms ($\hat{H}^{\mathrm{additional}}$) in the total Hamiltonian operator ($\hat{H}^{\mathrm{tot}}$) are included, for example spin-orbit coupling, we can still represent the total Hamiltonian in the MCH basis with the matrix elements defined as $H_{\beta\alpha} = \langle \Phi_\beta^{\mathrm{MCH}} | \hat{H}^{\mathrm{tot}} | \Phi_\alpha^{\mathrm{MCH}} \rangle$. Then the total Hamiltonian matrix $\mathbf{H}^{\mathrm{MCH}}$ in the MCH representation is not diagonal anymore. The temporal coupling matrix $\mathbf{T}^{\mathrm{MCH}}$ is a block matrix, with blocks along the diagonal, since some basis functions can change into each other with time and nuclear geometry, and others cannot. As a result, the states are separated into different multiplicities i.e. S_1,S_2,S_3,...,T_1,T_2,T_3. Hence, states of the same multiplicity i.e. S_1, S_2 are strictly ordered according to energy, and cannot cross, whereas states of different multiplicity may cross, i.e. S_2, T_1 are free to cross each other. Multiplet components such as, $T_{1,-1}$, $T_{1,0}$, $T_{1,1}$ are completely degenerate.

The MCH states are often referred to as *adiabatic*, since a change in time or geometry allows the states to change, however, this is not true when additional terms, such as spin-orbit coupling, are introduced, hence other authors also refer to this representation as "adiabatic spin-diabatic" [131].

The main advantage of using the MCH representation is that it is the standard formulation in most quantum chemistry software, which makes it the natural choice of representation for the surface hopping dynamics simulations. However, as for the diabatic representation, the introduction of the off-diagonal elements in the Hamiltonian matrix lead to some couplings being delocalized, which is not ideal for surface hopping, as it affects the number of hops and population transfer. Furthermore, any multiplets are considered as degenerate, which is not truly accurate. For systems with high spin-orbit coupling, such as many transition metal complexes, the states are not always pure singlet or triplet states.

Finally, using a different basis, with a **diagonal** Hamiltonian matrix, $\mathbf{H}^{\mathrm{diag}}$, solves the challenge of delocalized couplings. It is possible to obtain such a diagonal matrix from a diagonalization of the MCH Hamiltonian matrix, which is how it is done in SHARC.

$$\mathbf{H}^{\mathrm{diag}} = \mathbf{U}^T \mathbf{H}^{\mathrm{MCH}} \mathbf{U} \tag{3.34}$$

where $\mathbf{U}$ is the unitary transformation matrix ($\mathbf{U}\mathbf{U}^{\mathbf{T}} = I$), and hence by definition the Hamiltonian matrix in the diagonal representation, $\mathbf{H}^{\mathrm{diag}}$ is di-

agonal, $H_{\beta\alpha} = \delta_{\beta\alpha} E^{\text{diag}}_{\beta\alpha}$. As a result, all states are fully adiabatic states, i.e. the states do not cross and are ordered according to energy, which is more correct in the description of multiplets. All couplings between the diagonal states are described in the temporal coupling matrix $\mathbf{T}^{\text{diag}}$, where high couplings occur when surfaces are close to each other. Hence, the requirement of local couplings is fulfilled, which is preferred for surface hopping, such that surface hops occur when states are close to each other and highly coupled. The basis states in the diagonal representation $\Phi^{\text{diag}}_{\beta}$ are eigenstates of the total Hamiltonian, $\hat{H}^{\text{tot}}$ and formed from a transformation of the MCH basis states:

$$\Phi^{\text{diag}}_{\beta} = \sum_{\alpha} \Phi^{\text{MCH}}_{\alpha} U_{\alpha\beta}$$

Consequently, the MCH and diagonal representation are only different if the total Hamiltonian operator, $\hat{H}^{\text{tot}}$ has any additional terms, $\hat{H}^{\text{additional}}$ besides the MCH Hamiltonian, $\hat{H}^{\text{MCH}}$. If the total Hamiltonian includes spin-orbit coupling, the states in the diagonal representation generally possess mixed spin. This gives a higher number of states because each of the multiplets will be separate states. Since, the states are not pure spin states, they are not assigned as in the MCH representation as a singlet or triplet state, but rather labeled as state 1,2,3,... etc. In the diagnonal representation, the electronic wave function changes according to the nuclear coordinates, such that e.g. the lowest excited state could show both MLCT and MC character depending on the time or nuclear coordinates.

The advantages of the diagnonal represenation of the states are the optimal conditions for surface hopping simulations with localized large couplings, and furthermore, it is a more accurate description of the energetics, since the states are ordered according to energy, and any multiplets are treated correctly. The main disadvantage of the representation is that it is not the usual representation in standard quantum chemistry software, and therefore, a diagonalization procedure is necessary. Furthermore, the consequence of treating multiplets correctly gives a larger number of states, which often makes simulations more expensive.

Figure 3.4 shows schematic examples of the appearance of the potential energy surfaces in the three different representations. The left panel shows an example of three diabatic states, with a ^{1}MLCT state, a ^{1}MC state and a ^{3}MC, which are all allowed to cross each other. The middle panel,

shows the same states in the MCH representation, in which the two singlet states are separated into S_1 and S_2 with energetic ordering. Now, the electronic wavefunction charge transfer character is not preserved and hence the character of the S_1 state can change with time or reaction coordinate. The singlet and triplet states are allowed to cross in the diabatic and MCH representation, but no states cross in the diagnonal representation. The right panel, shows an example of the same states in the diagonal representation, which split up the triplet into three separate states, giving a total of five independent states. The states might show mixed singlet-triplet character and therefore the labeling is simply according to the energy level.

Currently, most quantum chemistry software calculate the states in the MCH representation, and hence they are do not directly give the necessary properties needed for surface hopping simulations in the diagonal basis. Consequently, surface hopping simulations using the SHARC program involves both the MCH and the diagonal representation [126, 127].

- **MCH**. From a given input geometry, the electronic energies, gradients, and couplings, $\mathbf{H}^{\mathrm{MCH}}$,$\nabla E^{\mathrm{MCH}}$, $\mathbf{T}^{\mathrm{MCH}}$ are calculated using quantum chemistry software that typically uses the MCH representation.

- **diagonal**. Calculation of the hopping probabilities, h and the nuclear propagation $\vec{R}(t) \rightarrow \vec{R}(t + \Delta t)$, is carried out in the diagonal representation in SHARC, which involves a transformation from the MCH basis (eq. (3.34)).

The obvious advantage is that the SHARC program can work with many different quantum chemistry software programs because it transforms the necessary input. What actually happens within the SHARC part is described in the next section.

In summary, the choice of representation affects the form of the energetic landscape, such that in one representation, a given propagation leads to a change in electronic state, whereas in the other representation it does not change surface. The representations are quite different and hence, one should be careful when comparing simulations to experimental observables.

3.6 Workflow in SHARC

This section describes the workflow of the excited state dynamics simulations using SHARC, and this way also summarizes the theoretical chapter of the thesis. Section 3.1 and 3.2 described the basics of QM electronic structure methods, focused on DFT. To calculate excited state properties, section 3.3 presented the time-dependent variant of DFT. Section 3.4 introduced classical methods to include the solvent, where we employ the hybrid QM/MM methods. Section 3.5 focused on dynamics and presented the purely classical methods and the mixed-quantum-classical methods used in SHARC.

Figure 3.5 illustrates the typical workflow in surface hopping computations with SHARC. Before starting the dynamics simulations, the initial conditions must be prepared. This includes preparation of initial geometries, $\vec{R}$ and velocities $\vec{v}$, which in our case was prepared from purely classical molecular dynamics simulations (described in section 3.5.1). Additionally, the initial conditions contains information on the initially populated state(s), and thus the initial wave function coefficients c and initial active state β, in the current case determined from TD-DFT methods. Starting from the initial conditions, the algorithm for SHARC, involves the following steps:

1. **Velocity-Verlet $\vec{\mathbf{R}}$ step.** The cycle starts with a calculation of the new geometries $\vec{R}(t+\Delta t)$, from the initial conditions (or the previous time step). The atomic coordinates are calculated as described in sections 3.5.1 and 3.5.2 about classical and SHARC dynamics, using the last expression from eq. 3.26. In Figure 3.5, the process is marked as step 1, and the red boxes.

2. **Quantum Chemistry.** The second step involves calculation of the energy of the total system, as described in sections 3.2 on DFT, 3.3 on TD-DFT and 3.4 on classical methods. This includes calculation of the coupling matrices **H** and **T** discussed in section 3.5.3 and also the energy gradients $\nabla\mathbf{E}$. In our case, ORCA was used for the DFT, and TD-DFT calculations describing the QM, and QM/MM part of the system and TINKER was used to calculate the energy from the classical MM solvent. The diagram in Figure 3.5 shows that the new

nuclear geometries $\vec{R}(t+\Delta t)$ are given as the input to calculate new energies, couplings (**H**, **T**) and energy gradients (∇E), in step 2.

3. **Propagation of electrons.** The next step concerns calculations of the new coefficients $\vec{c}(t+\Delta t)$ using equation (3.29), and hence the propagation step of the electrons. As shown in the diagram the energy output giving the **H** and **T** matrices and the previous coefficients $\vec{c}(t)$, allows the calculation of the new coefficients $\vec{c}(t+\Delta t)$ in step 3, marked as the green boxes.

4. **Surface hopping decision.** The coefficients from step 3, determines if the population changed, and act as input for the determination of the hopping probability, from eq. (3.30). Based on the hopping probability h (and a random number generator), it is decided whether a surface hop is made or not, and which state is the new active state β. The process is illustrated in blue colors for step 4.

5. **Determination of gradients.** Depending on the choice of active state it is decided which energy gradient that acts on the nuclei. The gradients from all the different states were already calculated in the second step, and this step selects which gradient to use, based on the current active state. If a hop occurred, the gradient $\nabla E_{act}(t+\Delta t)$ from the new active state is applied, otherwise the gradient from the original time step $\nabla E_{act}(t)$ is used to propagate the nuclei.

6. **Velocity-Verlet $\vec{\mathbf{v}}$ step.** In the last step of the cycle, the velocities $\vec{v}(t+\Delta t)$ of the nuclei are adjusted to ensure total energy conservation, if a surface hop occurred. This step involves the first expressions from eq. (3.26) for the acceleration and velocities of the atomic nuclei, as described in section 3.5.1. Figure 3.5 shows step 6 with arrows from either the previous or the new energy gradient, and the previous velocities, as inputs to the new velocities.

With the new velocities, energy gradients, and active state determined, the cycle restarts with a calculation of the new geometries. The cycle continues until a maximum simulated time is reached. As discussed in section 3.5.3, the simulations involves both calculations in the MCH and diagonal representation, and therefore, the output of the simulations may be transformed to the preferred representation for analysis of the results.

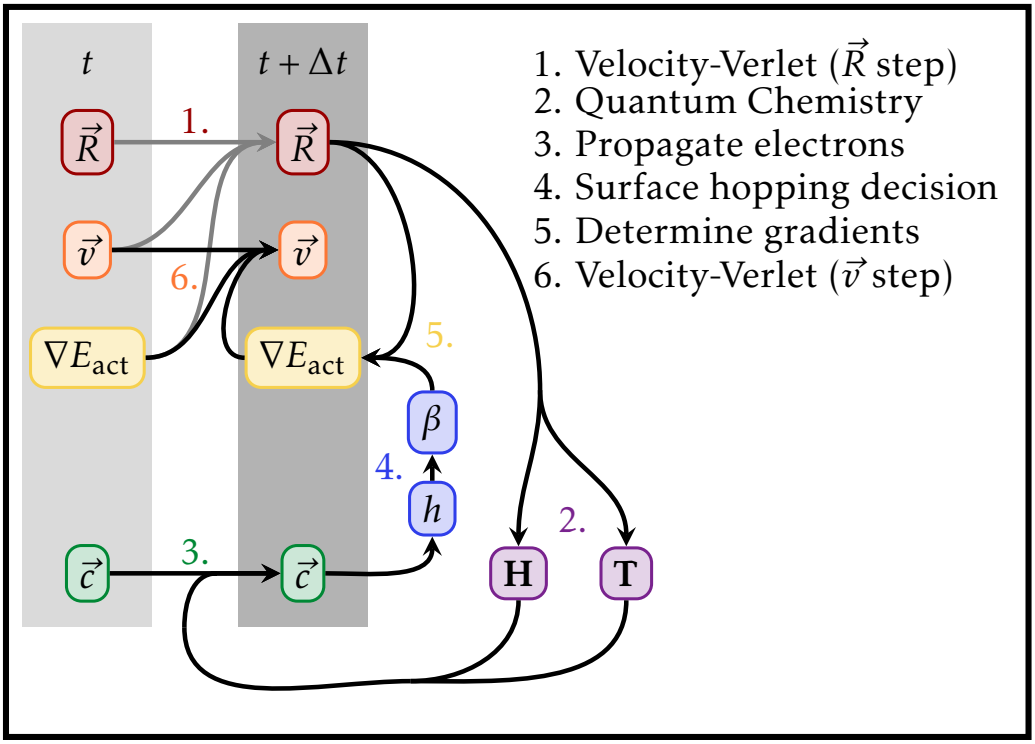

Figure 3.5: Workflow for the excited state dynamics simulations with SHARC. 1) The (nuclear) geometries, $\vec{R}$ are updated from the initial conditions or the previous step. 2) The quantum chemistry software (this case ORCA) updates the energy of the system in the new geometry by calculations of the coupling matrices **H**, **T**, and energy gradients ∇**E**. 3) The electrons are propagated by calculations of the new coefficients, $\vec{c}$. 4) From the new coefficients, the hopping probability h is determined, and thus which active state β is the next (or the active state is the same as the previous step). 5) The choice of which energy gradient ∇E_{act} is made, depending on the choice of active state. 6) The last step adjusts the velocities of the nuclei to ensure total energy conversion, if the active state changed. From the new velocities, active energy gradient and previous geometry, the cycle restarts and continues until the maximum time step is achieved.

Chapter 4

Useful tools for analysis of simulations

Contents

This chapter presents the basic theoretical principles of some of the tools used for the analysis of the excited state dynamics simulations. Section 4.1 describes two different ways to analyze the electronic populations from the simulations. Section 4.2 describes the basic concepts of the TheoDORE analysis tools, which are used to investigate the charge transfer character of the electronic wave function.

4.1 Population analysis

Determination of the electronic populations, depends on the choice of representation, as discussed in section 3.5.3. In the spin-free, MCH representation, the electronic populations can be computed in either a ”classical” or ”quantum” sense. In the ”classical” picture a given trajectory can only populate one surface at a time, and hence the system is in a given state at a given time. The ensemble populations is simply calculated by counting the number of trajectories that have the given state as the active state. However, if strong mixing is present, the counting becomes non-trivial.

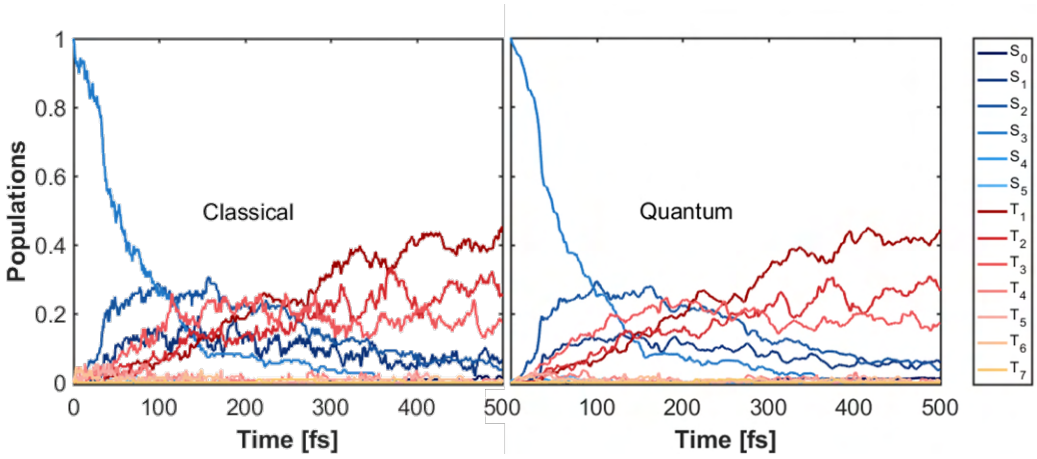

Figure 4.1: Comparison of the ensemble populations from the $[Fe(bpy)(CN)_4]^{2-}$ excited state dynamics simulations calculated either as "classical" by simple addition of the number of trajectories in the given state at each time, or as "quantum" populations by summation of the wavefunction coefficients squared.

In contrast, the "quantum" populations refer to a summation of the wave function coefficients squared for each state, which allows the system to be partly in different states simultaneously.

The populations in the MCH representation, P_i^{MCH}, is calculated according to the expression:

$$P_i^{\mathrm{MCH}}(t) = \frac{1}{N_{\mathrm{traj}}} \sum_{\mathrm{traj}} \left| \sum_{\alpha} U_{i\alpha} c_{\alpha}^{\mathrm{diag}} \right|^2 \tag{4.1}$$

where N_{traj} is the number of trajectories, i is an MCH state, α is a diagonal state, $U_{i\alpha}$ is the transformation matrix from diagonal to MCH representation, and $c_{\alpha}^{\mathrm{diag}}$ are the time dependent coefficients in the diagonal representation. Note that the "quantum" way of calculating the ensemble populations leads to a higher number of points being averaged, which generally improves the statistics. Figure 4.1 compares the ensemble populations calculated using either "classical" or "quantum" populations from the excited state dynamics simulations of $[Fe(bpy)(CN)_4]^{2-}$ in solution. The two cases are very alike, which indicates that the sampling (number of trajectories) was sufficient. In the analysis of the $[Fe(bpy)(CN)_4]^{2-}$ system, the MCH "quantum" populations were used.

4.2 Basics of TheoDORE analysis tools

The TheoDORE package is a useful tool for the analysis of excited state charge transfer character. It is a tool which gives a quantitative description of the charge transfer for a given excitation/excited state. The tools are developed by Plasser et al. and published in [132, 133, 134]. This section briefly describes the concepts of the tools.

Most often excited states such as MLCT, MC, LMCT or LC states in simulations, are identified by visual inspection of the relevant orbitals. However, the states are not always pure states and might show a mixed character, and the method of visual inspection is very subjective. Therefore, a quantitative measure of the excited state character is useful.

The concept of the TheoDORE analysis tool is to analyze the so-called charge-transfer numbers between different fragments of a given system. For a transition metal complex, the relevant fragments could be the metal center and each of the ligands, but it is possible to define the fragments as desired, e.g. each atom of the system. The fragments are usually defined by chemical intuition, such as the metal and each of the ligands.

Population of a given excited state usually involves charge transfer. We define the excitation *hole* as where the excitation originates from and where it goes as the excited *electron* location. A typical example is the excitation into an MLCT state, in which the excitation originates at an orbital localized at the metal, and it goes to a ligand localized oribtal. The TheoDORE analysis tools provide quantitative information about the charge transfer involved in the given excitation.

The central object is the one-electron-transition-density-matrix (1TDM), $\mathbf{T}$, which is involved in the description of the electronic transition between two states. The 1TDM is not a physical observable but it is related to observables like the transition dipole moment [133]. The first step of the TheoDORE mechanism involves a transformation of the 1TDM from the basis of Molecular Orbitals (MO) to an Atomic Orbital (AO) basis, for a given excited state n:

$$\widetilde{\mathbf{T}}^n = \mathbf{C}\mathbf{T}^n\mathbf{C}^T$$

where $\widetilde{\mathbf{T}}^n$ is the 1TDM in the AO basis, and $\mathbf{C}$ is the MO coefficient matrix.

The 1TDM is directly related to the response vector $\vec{X}^n$, within TDA based TD-DFT, which is described in section 3.3 and shown in eq. (3.18). A matrix element T^n_{ia} of the 1TDM is assigned as the same as an element of the excitation response vector X^n_{ia}, in the excitation process ($T^n_{ia} = X^n_{ia}$) from an occupied orbital with index i to a virtual orbital a, for a given excitation n. Therefore, we can write an element of the transformed 1TDM, $\widetilde{X}^n_{\mu\nu}$, in the following way, in the basis of two AOs with indices μ, ν:

$$\widetilde{X}^n_{\mu\nu} = \sum_{i,a} C_{\mu i} X^n_{ia} C_{\nu a} \tag{4.2}$$

where $C_{\mu i}$, $C_{\nu a}$ are elements of the MO coefficient matrix, $\mathbf{C}$. The square of an element from the transformed vector $(\widetilde{X}^n_{\mu\nu})^2$ is a measure of the contribution to an excitation originally located on an AO with index μ, transferred to another AO location with index ν.

Division of the electron density among the atoms of the given system requires a populations analysis scheme that takes the non-orthogonality of AOs into account. Several methods exists but the TheoDORE analysis tools use either Mulliken or Löwdin population analysis. This work used the Löwdin population analysis, since it is computationally more efficient, and often more numerically stable [134]. The Löwdin orthogonalization is applied to the transformed vector, $\widetilde{X}^n$, in the following way, where $\mathbf{S}$ is the AO overlap matrix:

$$\widetilde{\mathbf{D}} = \mathbf{S}^{1/2}\, \widetilde{X}^n\, \mathbf{S}^{1/2} \tag{4.3}$$

The next step concerns the definition of the charge-transfer matrix $\mathbf{\Omega}$, which involves division of the given system into appropriate fragments. When both of the involved orbitals (μ, ν), are located on the same fragment A, then a given excitation is considered a local transition. The charge transfer matrix element Ω_{AA} describes the weight of the local excitations on fragment A. In contrast, when the orbitals are located on different fragments A, B, the given excitation shows charge transfer character, and the associated matrix element Ω_{AB} is a weight of the charge transfer character. The elements of the charge transfer matrix consists of simple sums of the squared coefficients from the transition density matrix, $\widetilde{\mathbf{D}}$ obtained from the Löwdin orthogonalization:

$$\Omega_{AB} = \sum_{\mu \in A} \sum_{\nu \in B} (\widetilde{D}_{\mu\nu})^2 \tag{4.4}$$

The sum over all fragments equals 1, for a given excitation, which allows for a quantitative measure of each contribution to the total charge transfer. A system of n_f fragments results in a $n_f \times n_f$ sized charge transfer matrix Ω_{AB}. Examples of such a matrix are shown in Figure 4.2 for two singlet (S_1, S_7) and two triplet (T_1, T_4) excited states of a random geometry of the $[Fe(bpy)(CN)_4]^{2-}$ complex. The complex was divided into 3 fragments as the metal center, Fe, the four cyanides, CN, and the bipyridine ligand, bpy.

Starting in the top left corner, with the S_1 excited state, we observe that the strongest contribution (∼73 %, green), corresponds to an Fe→bpy excitation, but also with a contribution (∼15 %) from the CN→bpy charge transfer. The T_1 excited state, in the lower left corner, shows similar trends. However, the S_7 and T_4 excited states show very different charge transfer trends. The T_4 excited state in the lower right corner shows predominantly contributions corresponding to a local Fe→Fe (∼63 %) excitation.

For a metal complex it is often relevant to discuss the charge transfer in terms of metal centered (MC), metal-to-ligand charge transfer (MLCT), ligand-to-metal charge transfer (LMCT) or ligand centered (LC) excited states. For this example, if we define the Fe→Fe as the MC contribution, then we observe that the T_4 excited state shows ∼63 % MC character. The top right corner matrix shows the S_7 charge transfer matrix. In this state, we observe almost equal contributions from both the Fe→Fe (∼38 %) and Fe→bpy (∼39 %) transitions. For this situation it would be difficult to assign the excited state to a certain charge transfer type, from standard visual inspection of the orbital locations. The TheoDORE tools describe this excited state as a mixture of both MLCT and MC character.

For the work related to this thesis, the TheoDORE analysis tools were included for each time step for each trajectory in the SHARC excited state dynamics simulations of the $[Fe(bpy)(CN)_4]^{2-}$ complex. As evident from the above example, the tools provide a quantitative measure of the fragments involved in the charge transfer for a given electronic transition, and how ”pure” the character of the states are. This help us determine the wave function charge transfer character of the states involved and the development in time, which aids the comparison to experiments.

S1	Fe	CN	bpy	sum
Fe	5,2	1,4	72,8	79,4
CN	1,0	0,3	14,9	16,1
bpy	0,3	0,0	4,2	4,5
sum	6,5	1,7	91,8	100,0

S7	Fe	CN	bpy	sum
Fe	38,1	9,3	38,6	86,0
CN	4,2	1,0	5,7	10,9
bpy	0,9	0,1	1,9	3,0
sum	43,2	10,4	46,2	100,0

T1	Fe	CN	bpy	sum
Fe	6,2	1,2	67,9	75,2
CN	1,0	0,2	11,7	12,8
bpy	0,9	0,1	10,9	11,8
sum	8,0	1,5	90,4	100,0

T4	Fe	CN	bpy	sum
Fe	62,8	14,1	11,8	88,7
CN	6,3	1,5	1,3	9,1
bpy	1,5	0,3	0,2	2,0
sum	70,6	16,0	13,3	100,0

Figure 4.2: Example matrices of the charge transfer numbers for randomly selected excited states (S_1, S_7, T_1, T_4) of the $[Fe(bpy)(CN)_4]^{2-}$ complex. The colors show the magnitude (in %) of the matrix elements where green represents a high value, and red represents a low value, and yellow colors in between. The labels, Fe, CN and bpy give the fragments chosen for the complex, i.e. the metal center, the four cyanides and the bipyridine ligand, respectively. The vertically listed fragments are the electron "hole" location, and the horizontally listed fragments are the excited "electron" location. The matrices show how much each fragment contributes to the total charge transfer associated with the given electronic transition, such that e.g. the ground state to S_1 andT_1 transitions mainly show in Fe→bpy and CN→bpy charge transfers.

Part III

Results

Chapter 5

Analysis and results on the $[Ru(bpy)_3]^{2+}$ investigations

Contents

The previous Part I and II described the relevant background of the experiments and simulations found at the core of the ultrafast excited state dynamics studies. This third and final Part III, presents the analysis and the results on the two metal complexes studied in this thesis. The first metal complex is the $[Ru(bpy)_3]^{2+}$ (bpy = 2,2'-bipyridine) system, and the second metal complex is the $[Fe(bpy)(CN)_4]^{2-}$ system. Each study concerns both experimental and computational work, and the results on each system are discussed in separate chapters. This chapter presents the ultrafast structural dynamics studies on the $[Ru(bpy)_3]^{2+}$ system. I have been the main driving force behind the analysis of the $[Ru(bpy)_3]^{2+}$ XFEL data.

The $[Ru(bpy)_3]^{2+}$ system is one of the most studied metal complexes for investigations within photochemical reactions and excited state dynamics, and therefore, the chapter begins with an introduction of what is currently known from literature about the structure and ultrafast excited state dynamics, in section 5.1. Subsequently, we continue with the analysis and results from our ongoing studies. Section 5.2 briefly presents the XFEL scattering data used in our study - data which have undergone processing in terms of data reduction and filtering. The measured data is divided into an isotropic and anisotropic part, which provide different information on the solute and solvent dynamics, as discussed in the section. The remaining part of the chapter presents the analysis of the isotropic part of the scattering signals by use of both classical molecular dynamics (MD) simulations as presented in section 5.3, and by use of mixed quantum-mechanics/molecular-mechanics MD simulations as presented in section 5.4. Finally, the last sections of the chapter give a brief summary, the main conclusions, and an outlook.

5.1 Introduction to $[Ru(bpy)_3]^{2+}$

Due to the unique excited state properties, the $[Ru(bpy)_3]^{2+}$ system is a well studied metal complex as a model system to design new photoactive materials for applications. Therefore, a substantial amount of literature exist on the complex. The interested reader is referred to other reviews or book chapters [135, 136, 137, 138]. This section gives a brief introduction to the relevant background information related to the study of this thesis.

Molecular structure

The ground state molecular geometry of $[Ru(bpy)_3]^{2+}$ is illustrated in the inset of Figure 5.1. The central ruthenium atom coordinates three bipyridine ligands via six Ru-N bonds, in a pseudo-octahedral symmetry. X-ray diffraction studies [139, 140] of $[Ru(bpy)_3](PF_6)_2$ crystals report Ru-N bond lengths of 2.056±0.002 Å for all six bonds, and N-Ru-N angles of 78.8±0.1 ° within the same ligand. A true octahedral symmetry shows equal angles of 90 °, thus the symmetry is slightly distorted (to D_3) mainly due to the steric constraint from the bridging C-C bond between the pyridine rings in each bipyridine unit. Simulations of the ground state optimized structure with explicit solvation suggest slightly longer Ru-N bonds of either 2.077 ± 0.046 [141] or 2.069 ± 0.051 Å [142]. Hence, the ground state structure of $[Ru(bpy)_3]^{2+}$ is already studied by several methods, however, the excited state structural dynamics remain uncharted territory.

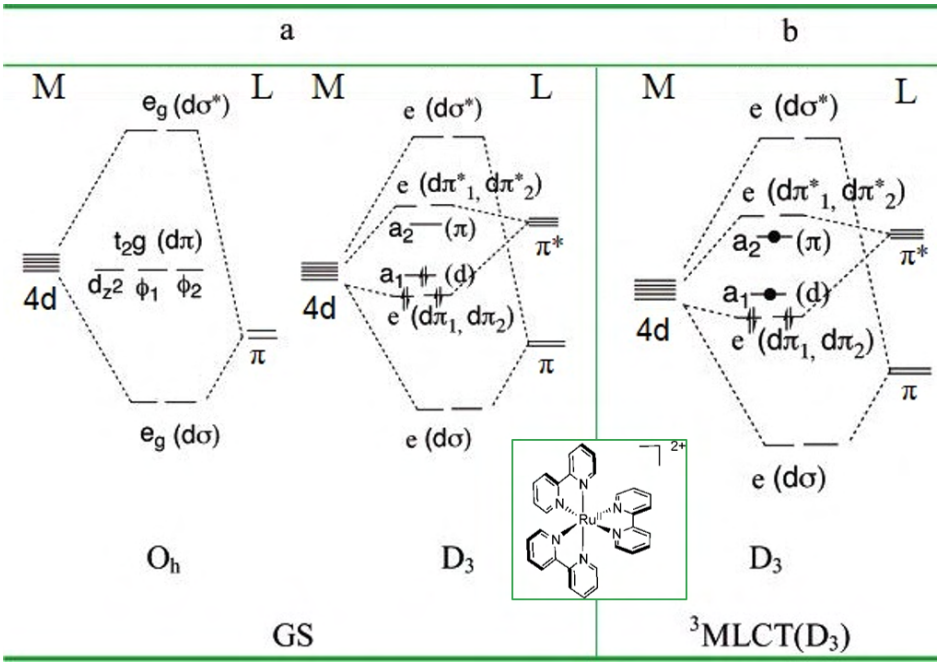

Figure 5.1: Electron configuration for the $[Ru(bpy)_3]^{2+}$ complex. a) left: the standard MO diagram for a 4d type metal complex in octahedral symmetry (O_h). a) right: distortion of the energy levels in a D_3 symmetry, with the ground state configuration. b): the excited ^{3}MLCT state configuration. Adapted from [143]

As discussed in the introduction (section 1.2), the metal-ligand bonds, of metal complexes in octahedral symmetry, form from the overlap between the ruthenium 4d orbitals and the π orbitals on the bipyridines. Figure 5.1 illustrates the molecular orbital (MO) diagram of a typical octahedral complex (part a, left) and for $[Ru(bpy)_3]^{2+}$ in the D_3 symmetry (part a, right). The D_3 symmetry distorts the t_{2g} orbitals into two energetic levels of e and a_1 symmetry. In the electronic ground state, these levels are occupied, as indicated by the spin arrows. Excitation of an electron from the metal d-orbital of a_1 symmetry to the lowest excited state leads to population of the ligand π orbital with a_2 symmetry, thus an MLCT transition - illustrated in part b) by the black dots. However, as discussed in the study by Alary et al. [143], the excited states are very close energetically, and promotion of an electron to one of the degenerate $d\pi^*$ orbitals also give rise to excited states of MLCT character, with a C_2 symmetry instead of D_3. Consequently, the excited state geometry of the complex shows analogous change in all the Ru-N bonds for the excited state of D_3 symmetry as opposed to the excited states of C_2 symmetry where Ru-N bond lengths vary. The excited state of D_3 symmetry corresponds to a delocalized excited state over all ligands, whereas the C_2 symmetry corresponds to an excited state localized on one of the bipyridine units.

Whether the excited ^{3}MLCT state is delocalized [144, 145, 146] or localized [147, 148, 149, 150] has been an ongoing debate, however, the ultrafast time-resolved X-ray scattering measurements presented in this thesis is (currently) not sensitive to the change in electron density from promotion of a single electron, but rather the structural response of the molecular complex and solvent. The goal is to study the overall change in geometry of both the solute complex and the response from the solvent.

Photoabsorption and excited state dynamics

Our eyes observe solutions of $[Ru(bpy)_3]^{2+}$ as having a bright red color. This is mainly due to the strong absorption band of the complex in the visible light range of 400-500 nm. Figure 5.2, to the left, shows the absorption spectrum (solid line) of the ruthenium complex in acetonitrile along with the emission spectrum (dashed line), and the molecular structure of the complex.

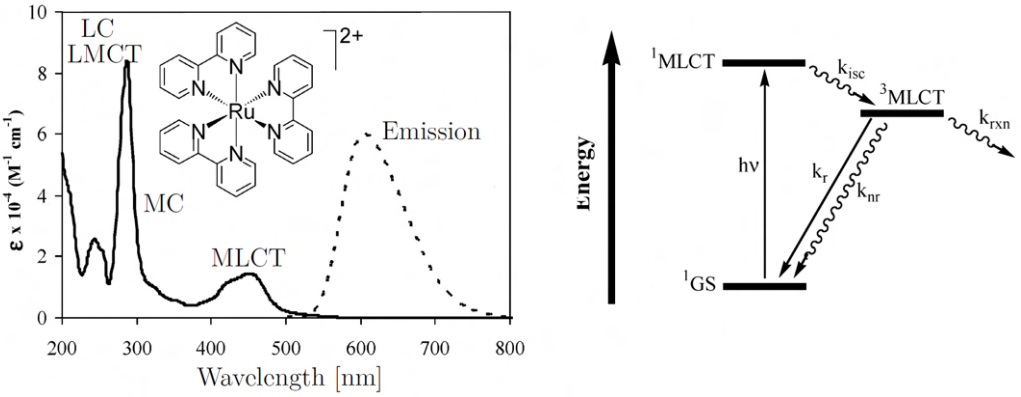

Figure 5.2: Left: UV-Vis absorption spectrum (solid line) and emission band (dashed line) of the $[Ru(bpy)_3]^{2+}$ system in acetonitrile, with the bands assigned to the type of charge transfer transition. The inset shows the chemical structure of the metal complex. Right: energy level diagram for the excited state dynamics of $[Ru(bpy)_3]^{2+}$ upon absorption from the ground state (GS) into the singlet metal-to-ligand-charge-transfer ^{1}MLCT band, along with the relaxation mechanism via intersystem crossing (ISC) to the triplet ^{3}MLCT band. Adapted figure from [138]

The band with a local maximum around 450 nm arise from the ^{1}MLCT transitions associated with the electronic transition from an orbital of predominantly metal d-character to the ligand π^* orbital. The X-ray scattering experiments described in this thesis employed an excitation wavelength of the optical laser of 530 nm, thus on the low energetic side of the MLCT band. The experimental conditions were optimized for a different study on a larger bimetallic complex containing the $[Ru(bpy)_3]^{2+}$ unit [151].

Photoexcitation in the range of the MLCT band leads to the interesting excited state dynamics, illustrated in 5.2, to the right. Following photoexcitation into the singlet ^{1}MLCT band, the system undergoes intersystem crossing (ISC) to the ^{3}MLCT band with a rate given by the ISC rate constant k_{ISC}. From the ^{3}MLCT manifold, several pathways of relaxation occurs. The system either decays by emission (k_r), or quenches into other states or participate in other electronic transfer reactions (k_{rxn}), or undergoes non-radiative relaxation into the ground state (k_{nr}).

The group of McCusker [147, 148] studied the complex in acetonitrile, using ultrafast transient absorption spectroscopy and reports that the population of the triplet state is complete within ~300 fs. Furthermore, work by Bhasikuttan et al. [152] measured the ultrafast time-resolved fluorescence spectrum and they propose that the ISC from higher excited ^{1}MLCT to vibrationally hot ^{3}MLCT states occurs with a time constant of 40±15 fs. Additionally, they propose a strong mixing of the higher levels of the triplet manifold with the singlet state due to the strong spin-orbit coupling of the system, which aids the ultrafast ISC. They also report, that vibrational cooling of the hot excited triplet state occurs on the time scale of 0.560±0.040 ps in propionitrile, (0.630±0.050 ps in acetonitrile), and is measured even slower (few ps) in alcoholic solutions.

However, broadband time-resolved fluorescence measurements of aqueous $[Ru(bpy)_3]^{2+}$ by the group of Chergui [153] contradict the findings of the vibrationally hot ^{3}MLCT states, as they find no detectable changes in the spectra at time delays longer than 300 fs, and find no hints of vibrationally hot emission from the ^{3}MLCT which would be observed from a broadening of the emission band. They also observe an ultrafast ISC from the ^{1}MLCT manifold to the ^{3}MLCT band on the order of 15±10 fs, which is significantly shorter than the previously reported measurements. The dissipation of excess energy is rather thought to occur via intramolecular vibrational energy redistribution (IVR) processes, which refers to the transfer of energy stored in high-frequency modes to low-frequency modes.

Recent work by Atkins and González [154], employs trajectory surface hopping simulations of $[Ru(bpy)_3]^{2+}$ in gas phase, and confirms the ultrafast ISC and report a time constant of 26±3 fs, and additionally states that population of 99 % of the triplet state manifold requires approximately 120 fs. However, they also note, that it is not a simple transition from a single state to another, but rather a thick manifold of near-degenerate states that is involved in the singlet to triplet population transfer. Furthermore, they report that ISC does not obey the "traditional" relaxation mechanism, explained from Kasha's rule [155] with a deactivation via IC from highly excited singlet states to the lowest excited singlet state (S_1), and subsequent ISC to the triplet states. Instead, they report ISC as a "horizontal" process between high-lying singlet and triplet states, as was also suggested by Cannizzo and the group of Chergui [153], previously discussed.

Other work, from the groups of Browne, McGarvey and Schepp [156, 157, 158] employing picosecond luminesence detection, supports the observations of a "slow" component in the 10-20 ps regime from non-thermalized excited states, which they assign to photophysical processes on the triplet surface either as a decay from a different MLCT state or a slow vibrational relaxation from a hot ^{3}MLCT state.

Regardless of the nature of the early excited state(s), and the lifetimes, we mainly observe the structural consequences using XFEL scattering techniques, and the structural changes between the different states of MLCT character most likely show very similar geometries of $[Ru(bpy)_3]^{2+}$. However, we do observe the structural response from the solvent in terms of the heat transferred from the solute to the solvent, which gives an indication of the time of vibrational cooling.

What the previous studies agree on is the long lifetime of the ^{3}MLCT excited state of the complex, which is exceptionally long for an MLCT state and for these types of systems. The lifetime shows a variation depending on solvent, with a lifetime of 860 ns in acetonitrile, and 580 ns in water [159]. In either case, the long MLCT lifetime, allows for its use for excited state energy and electron transfer reactions [138]. In fact, the excited state of $[Ru(bpy)_3]^{2+}$ is a more powerful reagent than the ground state both as an oxidizing and reducing agent [138]. Due to the long lifetime in the ns regime, the goal is not to study the decay mechanism from this state using fs time-resolution at XFELs. Rather, we are interested in the early dynamics and structural response of both the solute and solvent.

5.2 Presentation of XFEL scattering data

The experimental work described in this thesis, on the $[Ru(bpy)_3]^{2+}$ system was carried out at the X-ray Pump Probe (XPP) beamline, at the Linac Coherent Light Source (LCLS), located in California at SLAC National Accelerator Laboratory in the US. Unfortunately, I did not participate in the experimental work, including the necessary data reduction steps, which was prepared by Elisa Biasin. My work concerns the data analysis of the reduced X-ray scattering data on the $[Ru(bpy)_3]^{2+}$ system in aqueous solution. This section presents the results from the measured ultrafast time-resolved X-ray scattering signals.

The experiment was part of a collaborative work with members from both the departments of Physics and Chemistry at Technical University of Denmark (DTU), along with participants from Lund University, the PULSE Institute at Standford University and SLAC National Accelerator Laboratory, members from the FXE beamline at the European XFEL in Hamburg, and from the Wigner Research Centre for Physics as part of the Hungarian Academy of Sciences.

The measurements on the $[Ru(bpy)_3]^{2+}$ system was conducted as part of a study on the ultrafast excited state structural dynamics of the bimetallic RuCo-complex, $[(bpy)_2Ru(tpphz)Co(bpy)_2]^{5+}$ (with bpy=bipyridine, tpphz=tetrapyrido (3,2-a:2' 3'-c:3",2"-h::2"',3"'-j) phenazine) [151]. Additionally, sub-structures related to the bimetallic complex, were investigated independently, such as the metal complex, $[Co(terpy)_2]^{2+}$, (terpy= 2,2':6',2"terpyridine) [79], and the $[Ru(bpy)_3]^{2+}$ system, all studied in water.

The excited state dynamics measurements employed a combined wide angle X-ray scattering (WAXS) and X-ray emission spectroscopy (XES) setup. However, the XES setup was not optimized for the X-ray emission from the $[Ru(bpy)_3]^{2+}$ complex as the relevant ruthenium absorption edge requires higher energy. Instead, the time-resolved X-ray scattering patterns were collected for the $[Ru(bpy)_3]^{2+}$ system.

Relevant experimental parameters are reported in Table 5.1. The data was collected in an optical pump, X-ray probe setup with the X-ray scattering measured by the Cornell-SLAC Pixel Array Detector (CSPAD) [65]. The data described in this thesis is a combination of approximately 54000 images with time delays ranging from approximately -1 to 3.5 ps. Negative time delays simply refer to the arrival of the X-ray pulse before the optical pulse, thus creating an image without excitation of the sample.

Figure 5.3 presents the measured time-resolved X-ray difference scattering patterns in various ways, after the data reduction steps.

Table 5.1: Experimental parameters from the time-resolved X-ray scattering measurements on $[Ru(bpy)_3]^{2+}$, conducted at the LCLS.

Experimental conditions	
$[Ru(bpy)_3]Cl_2$ concentration	25 mM
Solvent	H_2O
X-ray energy	8.2 keV (1.3 fJ)
X-ray wavelength	1.5 Å
X-ray pulse temporal width (FWHM)	~30 fs
X-ray focal spot size (height x width)	50x50 μm^2
Repetition rate	120 Hz
Laser pulse energy	40 µJ
Laser wavelength	530 ±8 nm
Laser pulse temporal width (FWHM)	~70 fs
Laser focal spot size (diameter)	150 µm
Detector distance	~ 7 cm
Range of scattering angle (2θ)	3.3°-58.2°
Range of scattering vector (Q)	0.24-4.1 $Å^{-1}$
Range of time delays	-1.1-3.4 ps
Approximate time resolution	~150 fs
Liquid jet sheet thickness	100 µm
Jet angle (vertically rotated)	45°

The top panels of Figure 5.3 present the results following the decomposition of the measured difference scattering signals ΔS, into the ΔS_0 and ΔS_2 components, as described in Part I, section 2.4. The plots show the measured signals as a function of time delay between the pump and the probe, and the scattering vector Q, with the color scale according to intensity. Red colors refer to a positive feature whereas blue colors show negative features.

The lower panels show the difference scattering patterns of the ΔS_0 component as a function of Q for several time delays. The colors correspond to different time delays. The lower right plot shows the signals with an offset whereas the left plot is without an offset.

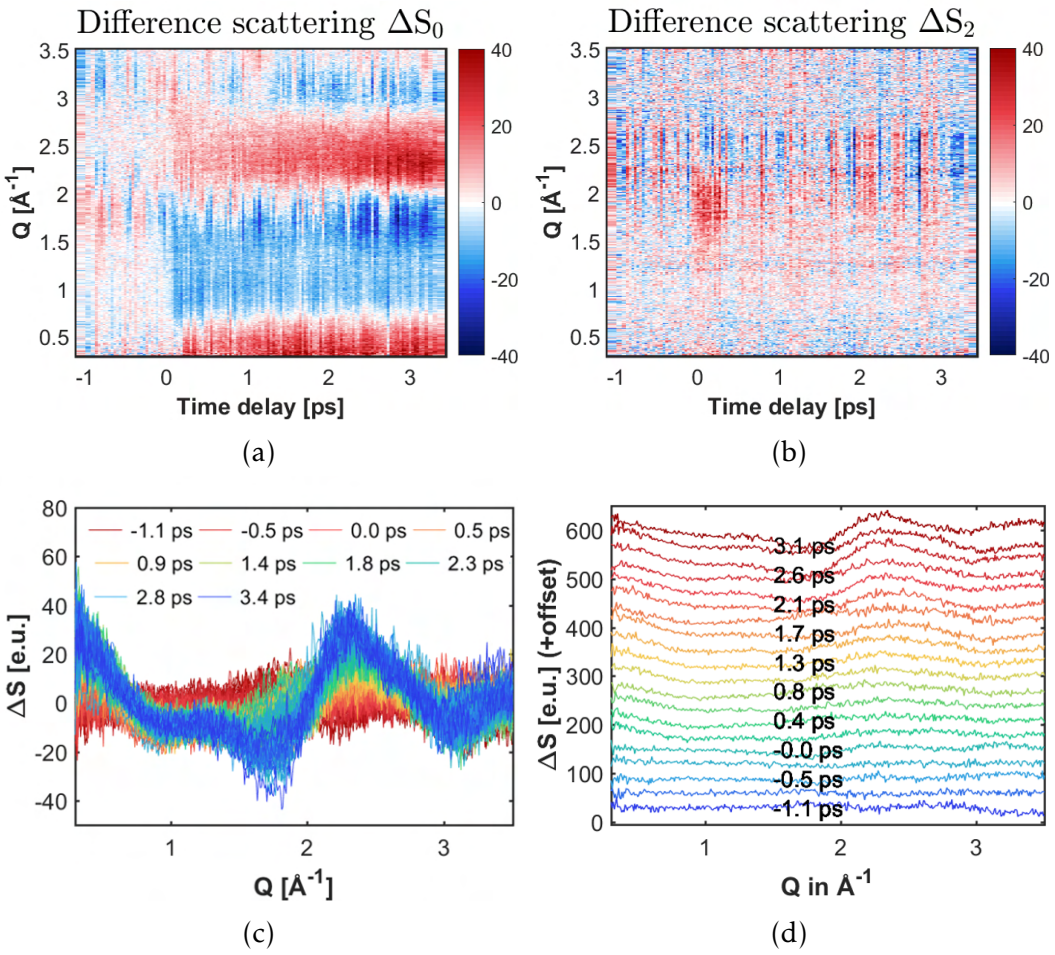

Figure 5.3: Measured time-resolved wide angle difference scattering signals as a function of scattering vector Q, at time delays from -1.1 to 3.4 ps. (a): the isotropic contribution ΔS_0. (b): the anisotropic contribution ΔS_2. (c) and (d) shows the isotropic part at selected times, with an offset for clarity in panel (d).

The dominant contribution to the collected difference scattering signals lies in the isotropic ΔS_0 component, where a large change are observed from the data before, and after time zero, $\Delta t = 0$. Thus, structural changes leading to a difference scattering signal is observed. However, the signals also show small features before time zero, which we assign to noise, since no difference signal should be observed without excitation from the optical pump. Therefore, the data was given a background subtraction using the Singular Value Decomposition (SVD) tools described in [160].

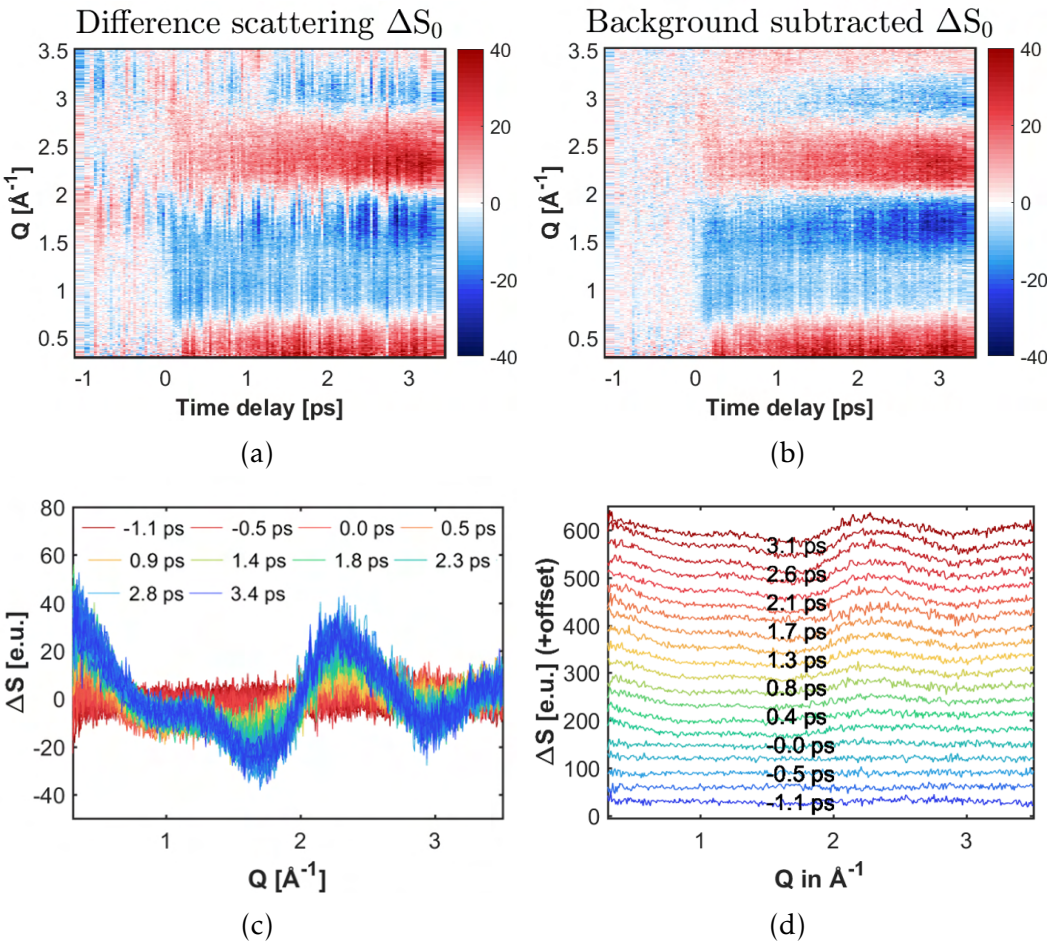

Figure 5.4: Background subtracted wide angle difference scattering signals ΔS_0 as a function of scattering vector Q, at time delays. (a): the data before, and (b): after background subtraction. (c) and (d) shows the background subtracted data at selected time delays with (d) or without (c) an offset.

The tools have shown to be a successful method for removal of spurious background contributions, in particular, when the noise is of a magnitude similar to the signal of interest.

Figure 5.4 shows the measured data upon background subtraction. Panel (a) shows the data before, and panel (b) after background subtraction, where the spurious features are effectively removed. Panels (c), (d) show that the qualitative features of the measured signals remain.

5.2.1 The isotropic difference scattering ΔS_0

The measured isotropic component of the difference scattering signal shows a sharp positive feature at $Q < 0.7\,\text{Å}^{-1}$, which grows in directly upon excitation. A positive feature indicates an increase in electron density, thus bond contractions or simply certain atoms moving closer to each other. We cannot assign any specific bonds to the range at this point, but from a comparison to the $[Fe(bpy)_3]^{2+}$ system [41, 45], the low-Q features are predominantly associated with changes in the Fe-N bond length, and the simulated cross-term signal for the solute-solvent interactions. Interestingly, the case of $[Fe(bpy)_3]^{2+}$ shows a negative feature at low Q, in contrast to the positive feature observed for the current data set of the $[Ru(bpy)_3]^{2+}$ system. However, we should note that the electronic excited state dynamics are quite different, since the initial excited state populations of MLCT states in $[Fe(bpy)_3]^{2+}$ quickly (fs) transfer to metal centered (MC) states, whereas the $[Ru(bpy)_3]^{2+}$ system remains in the ^{3}MLCT state throughout the measured time range.

Furthermore, the isotropic component of the measured difference scattering data shows a peak growing in more slowly, in the range of $2 < Q < 2.6\,\text{Å}^{-1}$, with negative features on both sides. The latter grow-in is also observed in $[Fe(bpy)_3]^{2+}$ and other similar metal-based systems [151, 79] and it is assigned to the ultrafast heating of the nearest solvent, in these types of experiments [86, 70, 87]. Later sections elaborate on that subject. Concrete assignment of the observed features requires further analysis and modeling.

Often computational methods assist in the interpretation and modeling of the measured scattering data. In particular, in terms of the solvent part and solute-solvent interactions that give rise to a change in the measured scattering signal. Thus, further analysis of the isotropic part of the measured scattering signals use the results from Molecular Dynamics (MD) simulations, as described later in section 5.3.

In the meantime, the next section presents the results from the analysis of the anisotropic part of the measured difference scattering signals.

5.2.2 The anisotropic difference scattering ΔS_2

The anisotropic component of the measured difference scattering signals, only shows a small feature at the earliest time delays, as shown in Figure 5.3 panel (b). Since, the $[Ru(bpy)_3]^{2+}$ system has three equivalent bipyridine ligands, in terms of symmetry, we do not expect an anisotropic component in the measured signals from excitation of the solute into the ^{1}MLCT states, since the transition dipole of either of the three ligands should be the same, and hence no preferential excitation with alignment of the optical laser polarization occurs. Instead, we observe an ultrafast component in the measured anisotropic signal arising from the transient response of the solvent water molecules to the electric field of the optical laser pulse [79, 64, 161]. This ultrafast component may be employed to estimate the Instrument Response Function (IRF) of the experiment as discussed in the Supplementary Material of [79].

Studies using both theory [162, 163, 84] and experiments [164, 165, 161] show that the structural response of solvent water molecules to an impulsive external electric field consists of two main contributions:

1. An ultrafast response arising from inertial motions of independent solvent molecules.

2. A slower response of diffusive character that occurs on time scales of hundreds of femtoseconds or few picoseconds.

Simulations by Jimenez et al. from 1994 [162] of liquid water, and other solvents, argue that the ultrafast motions are highly local mainly rotational motions. The ultrafast response contributes more than 50 % of the total measured or calculated signal, with a maximum at about 20 fs. As time proceeds, the interactions between the water molecules become more influential and lead to collective decaying oscillating features.

Castner and Chang [165], measured optical Kerr effect spectroscopy and present the intermolecular dyanmical spectrum of liquid water. An inverse Fourier transform of the (frequency) spectrum gives a representation in the time domain which they refer to as the 'nuclear-coordinate impulse-response function' describing the time-dependent nuclear intermolecular dynamics. The liquid water impulse response function shows a nearly instantaneous rise from time zero, along with three peaks at timescales of ∼20, ∼60 and ∼200 fs and a slower feature of several ps.

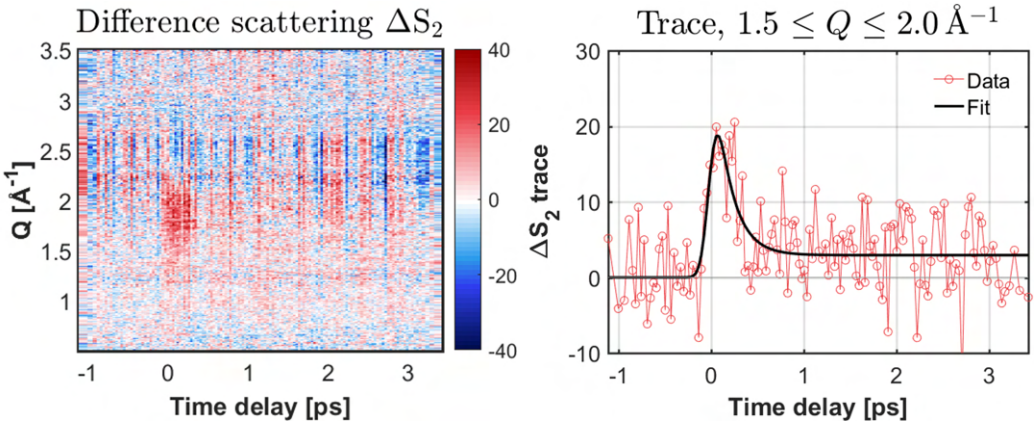

Figure 5.5: Left: measured anisotropic difference scattering signal $\Delta S_2(Q, \Delta t)$, of $[Ru(bpy)_3]^{2+}$ in water. Right: the average signal in the Q-range of 1.5 to 2.0 Å^{-1} (red) and the associated kinetic fit (black) as given in eq. (5.1) and (5.3).

The ultrafast components were assigned to the librational and translational modes of the water molecules, and the slower component was assigned to the diffusive motions.

In addition, a very recent anisotropic study by Kim et al. [161] on liquid water, using ultrafast time-resolved X-ray scattering show results indicating the existence of an ultrafast component of ~160 fs with an additional slower component on the order of ~1 ps. As for the $[Ru(bpy)_3]^{2+}$ data we also observe an ultrafast component in the ΔS_2 data and use this to determine the IRF, as detailed in the following.

Figure 5.5, to the left, shows the measured anisotropic difference scattering signal from the XFEL scattering experiments. At delay times directly after time zero, the signal shows a positive feature around Q =1.7 Å^{-1} and a negative feature around 2.5 Å^{-1}, although much less evident. The remaining features are assigned to noise, since they remain throughout the collected time delays, for both negative and positive delays. An average of the ΔS_2 data, in the most intensive region, in the Q-range of 1.5 to 2.0 Å^{-1} gives the trace shown in Figure 5.5, to the right (in red). This trace has been fit and modeled by a convolution of a broadened step function and a mono-exponential decay (in black), given in eq. (5.3). The resulting fit parameters are presented in Table 5.2. From the fit, we obtain a decay time of 0.178 ±0.14 ps, which is in qualitative agreement with the ultrafast com-

ponent observed from the previously discussed ultrafast components of the solvent response. Since, this data shows a relatively high noise level, we do not expect to observe the individual peaks observed in literature, but rather a combination of the decay times reported.

Determination of the instrument response function

Since, the electric field of the optical laser give rise to a nearly instantaneous (few fs) impulse-response [165] of the water molecules, the measured anisotropic signal may be employed in the determination of the instrument response function (IRF) of the scattering experiment. This section describes how to determine the IRF from the ultrafast solvent water response, observed in the anisotropic signals.

Assuming that the ultrafast water response shows an immediate grow-in (i.e. a step function) followed by an exponential decay, we model the response via $f(\Delta t)$:

$$f(\Delta t) = \begin{cases} 0, & \Delta t < 0, \\ (A - h_\infty)e^{-\Delta t/\tau} + h_\infty, & \Delta t \geq 0. \end{cases} \tag{5.1}$$

where A is the amplitude, i.e. the maximum height of the exponential converging to h_∞ as $\Delta t \to \infty$, and τ is the time decay constant, interpreted as the decay time of the ultrafast water response. However, due to the limited time-resolution of the experiment, we expect a broadening of the model, i.e. the IRF, which we model as a standard Gaussian function:

$$g(\Delta t) = \frac{1}{\sigma\sqrt{2\pi}} e^{(\Delta t - t_0)^2/(2\sigma^2)} \tag{5.2}$$

where σ and t_0 are the standard deviation and mean of the Gaussian, respectively, which we assign to the width of the probe (i.e. the time resolution), and to the true position of time zero. In the associated XFEL experiment, the position of time zero, is often set manually based on the position of the observed instantaneous difference signal. Thus, the current position of time zero is an estimate.

The observed measured signal is expected to follow the kinetics from $f(\Delta t)$ convolved with a Gaussian described by $g(\Delta t)$, thus the full expression becomes:

$$(g * f)(\Delta t) = \tfrac{1}{2}(A - h_\infty)\, e^{\frac{1}{2}(\frac{\sigma}{\tau})^2 - \frac{(\Delta t - t_0)}{\tau}} \cdot \left(1 - \operatorname{erf}\left(\frac{\sigma^2 - (\Delta t - t_0)\tau}{\sqrt{2}\,\sigma\,\tau}\right)\right) + \tfrac{1}{2}\, h_\infty \left(1 + \operatorname{erf}\left(\frac{\Delta t - t_0}{\sqrt{2}\,\sigma}\right)\right) \tag{5.3}$$

where $\operatorname{erf}(x) = \frac{2}{\sqrt{\pi}} \int_0^x e^{-t^2}$ is the error function, the anti-derivative of the Gaussian. Hence, we obtain five fit parameters $\tau, t_0, \sigma, A, h_\infty$, and the results from the fit are presented in Table 5.2.

Table 5.2: Resultant fit parameters having fitted the ΔS_2 trace using eq. (5.3).

Symbol	Value	unit
τ	177.9 ±138	fs
t_0	-15.9 ± 50	fs
σ	70.8 ± 51	fs
A	33.6 ± 20	e.u.
h_∞	2.9 ± 1	e.u.

The time resolution from these types of XFEL experiments comprise of three main contributions:

- The X-ray probe pulse width, which in the current experiment was ∼30 fs.
- The optical pump pulse width, which was approximately 70 fs in the given experiment.
- The travel path length through the liquid jet, which leads to a approximately 1 fs time mismatch per µm between the travel time of the X-ray and optical laser pulse through the jet, due to the wavelength dependant refractive index of water. The liquid jet in the current experiment was 100 µm in width, and angled at 45°, which gives a path length of approximately 141 µm through the jet.

Combining the three main contributions give an estimate of the expected time resolution of the experiment, in terms of the full width at half maximum (FWHM):

$$\text{FWHM} = \sqrt{\sim 70^2 + \sim 30^2 + \sim 141^2}\ \text{fs} = \sim 160\,\text{fs} \tag{5.4}$$

The best fit results from the anisotropic data give a probe width, σ of 70.8±51 fs, which corresponds to a FWHM of 167±120 fs (employing the relationship FWHM $\approx 2.355\,\sigma$). Thus, the fit results are in agreement with the estimated time resolution.

Brief summary and discussion

To summarize, section 5.2 presented the measured XFEL difference scattering data, as obtained after the data filtering and reduction. The isotropic component of the signals, ΔS_0 shows an instantaneous and remaining positive feature at $Q \leq 0.7\,\text{Å}^{-1}$, after time zero, and features in the range of $1.5 \leq Q \leq 3$ with a slower (ps) grow-in. As discussed in subsection 5.2.1, the latter feature is observed in similar systems and assigned to the response of the solvent to the excitation, in terms of heat [86, 70, 87].

The following subsection 5.2.2 presented the anisotropic component, ΔS_2 of the measured scattering signals. The anisotropic difference scattering signal is interpreted as a direct observation of the ultrafast solvent response of water to the linearly polarized electric field of the optical laser pump pulse. As discussed, previous theoretical [162, 163, 84] and experimental [164, 165, 161] studies assign the ultrafast component of the solvent response to motions of the independent solvent molecules of mostly rotational and translational character. Such type of motions show frequencies in the range of 60-600 cm^{-1}, corresponding to a period of 50-500 fs. The results from a kinetic fit of a region of the anisotropic signals, gives a time decay constant of $\tau = 0.178$±0.14 ps, which are thus in the appropriate time range. However, the data shows a poor signal-to-noise ratio, and thus a time resolution of $\sim$ 10-20 fs would be desirable for future studies, in order to gain a better insight of the ultrafast water response from the anisotropic component of the XFEL scattering signals.

Furthermore, section 5.2 discussed that previous measurements and computations found in literature, report a slower component of the water

response in the regime of ps, of mainly diffusional character. The reported time frame of such a feature matches the time frame as observed in our study of the solvent-related slow grow-in from the isotropic component of the signal. However, the isotropic component of the scattering signals requires additional analysis before such an assignment.

In addition, the anisotropic signal was used to estimate the instrument response function (IRF) and the position of time zero. The results show a slight shift in the position of time zero to approximately $t_0 = -15\,\text{fs}$ and a time resolution (σ), in terms of FWHM, of $\sim$160 fs. These parameters may be used in the analysis of the isotropic part of the signals, in order to reduce the degrees of freedom involved in the ultrafast dynamics.

Further analysis of the isotropic part of the signals requires additional tools. The next section presents the results from the computational study of the $[Ru(bpy)_3]^{2+}$ system in explicit solvent using Molecular Dynamics (MD) simulations, and how to employ the outcome for the analysis of the measured scattering data.

5.3 Molecular Dynamics simulations

The challenge of X-ray scattering in solution is that it is a global probe, meaning that we get contributions from structural changes in both the solute and solvent, which makes interpretation challenging. Information on the structural/electronic changes on the solute alone may be obtained from complementary methods, such as X-ray absorption (XAS), or X-ray emission spectroscopy (XES), which are both element specific tools probing the local environment. However, these methods do not provide information on the solvent structure. One way to disentangle the contributions is using simulations of the combined solute and solvent dynamics. The following sections present how to employ molecular dynamics (MD) simulations as a tool to understand the solvent behavior, by use of the associated radial distribution functions (RDFs) to calculate scattering signals.

The use of MD simulations to describe the solvent response for assistance of time-resolved X-ray scattering data has proven a successful method for structurally similar transition metal complexes such as $[Fe(bpy)_3]^{2+}$ [45], iron-carbene $[Fe(btbip)_2]^{2+}$ [166], and $[Co(terpy)_2]^{2+}$ [79].

5.3.1 Partial atomic charges

Computations of explicit solvent contributions using electronic structure methods quickly becomes computationally expensive, if several hundred solvent molecules are included in the simulations. Thus, classical MD approaches have been extensively applied, since they offer computationally cheap results using Molecular Mechanics (MM) force fields for the system under study. In particular, classical approaches have been employed for the calculations of RDFs and for the applications of the interpretation of solvent structure around transition metal complexes such as $[Ru(bpy)_3]^{2+}$ and $[Fe(bpy)_3]^{2+}$ [141, 167, 168, 169, 170]. However, the standard force fields available are typically developed for ground state calculations and are therefore often not well-suited for simulations of excited states involving charge transfer. Thus, the force fields essentially needs a re-parameterization, in which the partial atomic charges (PACs) come into play.

PAC methods partition the overall charge of the molecular system in question and distribute the charge across the individual atoms, in contrast to methods employing an electronic wave function for the description of the electronic charge distribution. The electrostatic interactions between solute and solvent atoms highly depend on the choice of the PACs, and hence in turn affects the solvent structural dynamics.

A part of the work on determination of the appropriate PACs for the solvated $[Ru(bpy)_3]^{2+}$ system, led to the publication, **Paper I**, presented in the Appendix. The PACs were calculated from DFT calculations of the solute, and used in the MD simulations while restraining the solute structure obtained from DFT, and allowing the classical solvent molecules to adjust their structural configuration. The study concluded that the best match between RDFs from classical MD and higher level theory QM/MM MD simulations, were the ChelpG[171]/RESP[172] or CM5[173] types of partial atomic charges.

Based on the results from the study of the different PACs, the ChelpG type was chosen for the study of the solvent response to the change in the solute structure from the electronic ground state to the ^{3}MLCT state of the solute. The following section presents the RDFs from the MD simulations.

5.3.2 Radial Distribution Functions

Figures 5.6 and 5.7 present the results of selected RDFs of atomic pairs with at least one atom associated with the solvent, from the classical MD simulations employing the ChelpG type partial charges.

DFT calculations optimized ground state and excited state (^{3}MLCT) geometries of the solute using the BP86[174, 175]/Def2TZVP[176] level of theory, and additionally derived the PACs through a fitting procedure in order to reproduce the molecular electrostatic potential (ESP) from the DFT calculation. The optimized geometries were solvated in water using the four-site TIP4P-Ew model [177], in a cubic box of 50 Å side length, under periodic boundary conditions. The MD simulations were carried out using the Desmond software package [178], in the constant temperature and volume, NVT ensemble, at 300 K, using the Langevin thermostat. In addition, two chloride ions, Cl^-, were included for neutralization of the total charge of the system. The production run was carried out for 2 ns with trajectories recorded every 50 fs. The RDFs of all the types of atomic pairs from the ground state and excited state were obtained using the VMD software [179] for a radial sampling of bin size of 0.01 Å.

Note that in the paper, we employed the B3LYP* [180, 181] functional (and the Nose-Hoover thermostat) for the MD simulations, and the BP86 functional for the QM/MM MD simulations of the $[Ru(bpy)_3]^{2+}$ complex, but the results presented here employs the BP86 functional (and Langevin thermostat), in order to minimize the differences between the classical MD and the combined QM/MM MD simulations discussed later in section 5.3.4. Furthermore, here I employed a larger cubic box (50 Å instead of 35 Å) due to the more favorable conditions of larger distances in the RDFs to calculate scattering signals, in order to minimize any truncation artifacts. However, the difference in the choice of functional results in only minor changes to the final RDFs, as discussed later. Additional computational details are presented in the published, **Paper I**.

The solute-solvent RDFs from the classical MD simulations employing the ChelpG type PACs is shown Figure 5.6. The RDFs show almost no structural changes from the ground state (GS, blue) to the excited state (ES, red). The differences are shown below (yellow), with an offset of 0.3. The left column shows RDFs of the solute type Ru, N and C atoms relative to the O-atom, and the right column relative to an H-atom of the solvent.

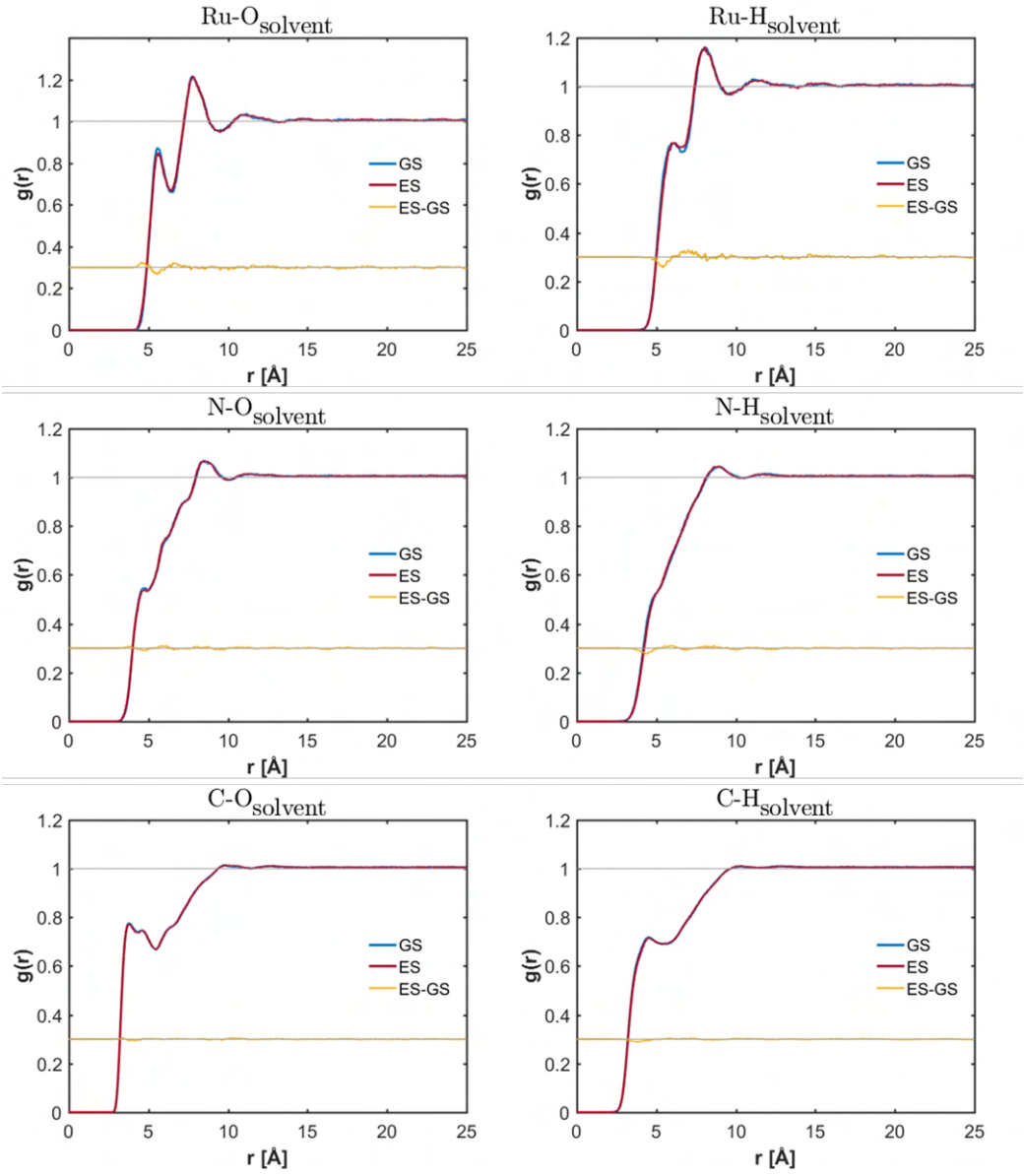

Figure 5.6: Radial Distribution Functions of selected solute-solvent atomic pairs obtained from classical MD simulations employing the ChelpG type partial charges obtained from DFT calculations of the solute using the BP86 functional. The solute structure was restrained to the DFT optimized geometries of the electronic ground state and ^{3}MLCT excited state, while allowing the water molecules to structurally adjust. Each plot shows the ground state RDF (GS, in blue), the excited state RDF (ES, in red), and the difference between them with an offset of 0.3 (in yellow).

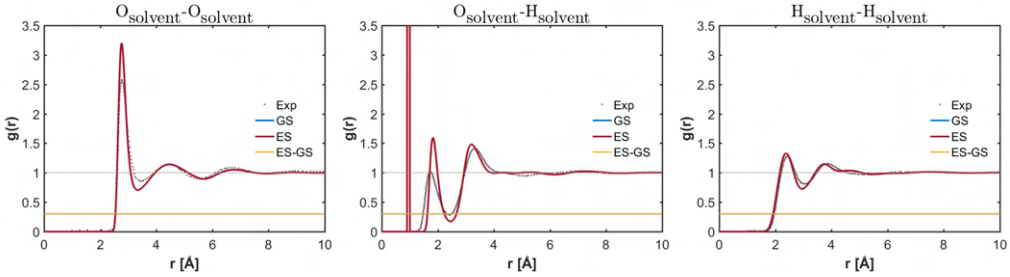

Figure 5.7: Radial Distribution Functions related to the solvent, obtained from the classical MD simulations, and RDFs (Exp) of pure water from literature [182]. Each plot shows the ground state RDF (GS, blue), the excited state RDF (ES, red), and the difference between them with an offset of 0.3 (yellow). The disagreement at low distances between the simulations and pure water are likely due to the often higher order of structure formed from packing around a solute.

Comparison of the RDFs of the Ru-$O_{solvent}$ atomic pairs with a similar MD study by Szymczak et al. [168], gives a qualitative agreement. However, the study reports RDFs that show a much higher structural order with peaks at 11 Å, 13 Å and 15 Å, which we do not observe to the same extend. Our results show only minor structural features at distances longer than 10 Å.

Figure 5.7 shows a comparison between the solvent-solvent atomic pair RDFs from the current study, and experimentally obtained RDFs of pure water from the study by Ceriotti et al. [182]. The results are based on combined X-ray scattering and neutron scattering measurements. The O-O RDFs show a good qualitative agreement with bulk water from experiments, with a slightly sharper peak, at ~3 Å, of the first solvent shell. This suggests a slightly higher order of structure in the simulations relative to the experiments on pure water. A similar trend is observed for the first solvent shell from the O-H atomic pair RDF, which shows a slightly sharper peak around 2 Å for the simulations. The higher order of structure in the simulations are not surprising since solvent packing around a solute leads to solvation shells, which are often more ordered than bulk water. At longer distances the simulations are in full agreement with the experiments on bulk water. The differences between ground and excited state are almost non-existing, as shown by the difference plots (in yellow).

The RDF differences were used to calculate the X-ray difference scattering signals as described in the following section.

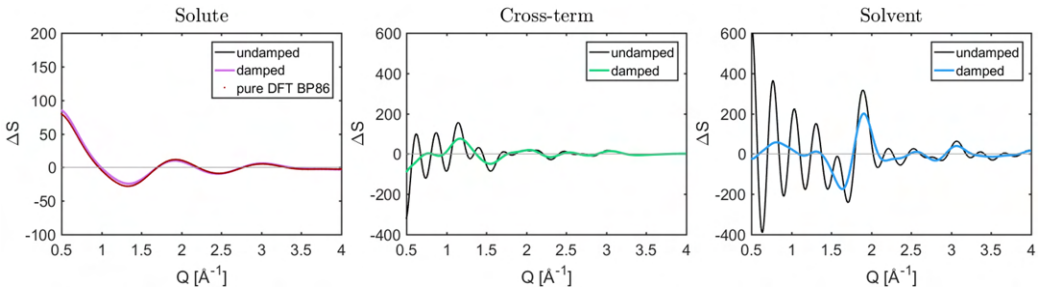

Figure 5.8: Calculated scattering from the radial distribution functions obtained from the classical MD simulations. Left: the solute difference signal, ΔS_u (in magenta) including a signal calculated from the DFT optimized geometry, with the standard Debye formula instead of RDFs. Middle: the cross-term difference signal, ΔS_c (in green). Right: the solvent difference signal, ΔS_v (in blue). The black lines show the spurious truncation artifacts as caused by an incorrect non-zero difference in RDF at large distances.

5.3.3 Calculated X-ray scattering signals

From the RDFs of the different types of atomic pairs, we calculate the X-ray difference scattering signals, using the method described in Part I, section 2.6. This section presents the results on the calculated scattering from the classical MD simulations.

Figure 5.8 shows the results on the calculated difference scattering signals from the RDFs, detailed in the previous section. The RDFs of the ground state simulations, are used to calculate total ground state scattering, in terms of the solute, solvent and solute-solvent cross-term, and likewise for the excited state. Subsequently, the *difference* scattering signal is constructed as the ground state subtracted from the excited state signals. Furthermore, due to the finite size of the box, the calculated scattering show spurious truncation artifacts without employing the dampening procedure discussed previously in Part I, section 2.6.

Figure 5.8 left panel, shows the calculated solute term from the RDFs (magenta line), along side the difference scattering (red dots) as calculated from the optimized DFT structure using the standard Debye formula (given in eq. (2.3)). The results show excellent agreement, confirming the reliability of the method employing RDFs.

The middle and right panels, show the calculated solute-solvent cross-term and the solvent term, respectively. Both of the calculated signals

show strong truncation artifacts (black line) with spurious oscillations, without employing a dampening weight function. Due to the very small structural changes from ground state to excited state, the RDF difference signals are very small, and thus artifacts become more dominant, especially for long distances in the RDFs, since the signal should converge towards 1, but small deviations from 1 will lead to non-zero differences between ground and excited state. Thus, we dampen the RDFs by including a weight function in the expression for the calculation of scattering, which ensures that the shorter distances (below 10 Å) are weighted higher than the longer distances, and that the difference signal is set to zero at the maximum distance (25 Å). The limit of 10 Å was chosen from inspection of the RDFs, by distinction between regions with evident structural features, which is given a full weight of 1 and the remaining "converging" region, which is weighted gradually less. The effect of applying the weight function is shown for the cross-term (in green), and for the solvent (in blue).

Once the solute, solvent and cross-term contributions to the difference scattering signals are calculated, we can directly employ the results in a fitting procedure against the measured isotropic difference scattering signals. The following sections present the results from the fitting procedure. First the results of a model using the classical MD simulations for the solvated $[Ru(bpy)_3]^{2+}$ system structure is presented. Following this, the results of a model using a QM/MM MD based description of the same system is presented.

5.3.4 Preliminary modeling of $[Ru(bpy)_3]^{2+}$ XFEL data

Analysis of the isotropic component of the difference scattering signal, ΔS_0 employs a modeling strategy of the different contributions that give rise to a change in the measured scattering signal, as described in Part I, section 2.5. The employed model, ΔS_{model} was given by the expression:

$$\begin{aligned} \Delta S_{\text{model}} &= \Delta S_{\text{solute}} + \Delta S_{\text{cross-term}} + \Delta S_{\text{solvent}} \\ &= \alpha \Delta S_u + \beta \Delta S_c + \gamma \Delta S_v + \Delta T \Delta S_{\text{temp}} \end{aligned} \tag{5.5}$$

where ΔS_u, ΔS_c and ΔS_v are the contributions to the calculated difference scattering signals from the RDFs, described in the previous section. The ΔS_{temp} term describes changes in the solvent as a result of the heat transfer from solute to solvent, and a local temperature increase of the solvent.

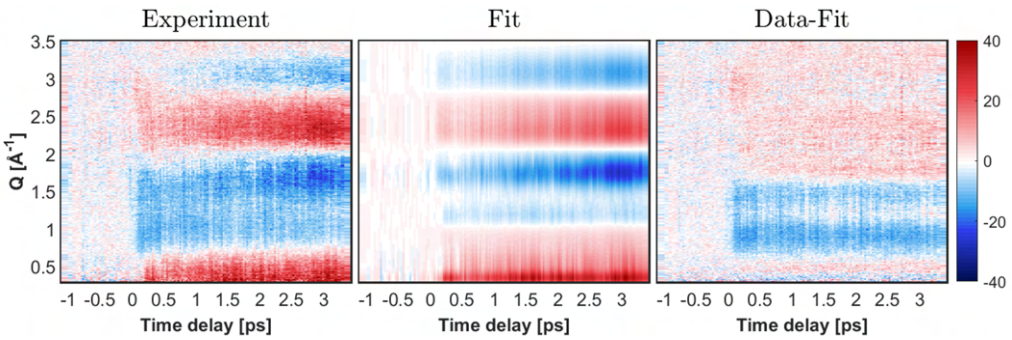

Figure 5.9: Comparison between isotropic experimental data ΔS_0 and and model, ΔS_{model}, based on the classical MD simulations. Left: the measured difference scattering. Middle: the total model from least squares fits of eq. (5.5) to the experimental data. Right: the residuals between data and fit.

The classical MD simulations do not include effects of vibrational cooling of the solute, and thus the local heating is not part of the calculated scattering. The local increase in temperature was modeled using the solvent temperature differential, $\frac{\partial S}{\partial T}\big|_\rho$, obtained from separate measurements on water [87]. Finally, $\alpha, \beta, \gamma, \Delta T$ are the factors scaling the contributions of the different components to the total model.

The model is evaluated against the experimental data via the calculation of a weighted least squares fit for each time delay separately. Figures 5.9 and 5.10 present the results from the fits.

Figure 5.9 shows the measured isotropic difference scattering signals, ΔS_0 to the left, and the total model after the fitting procedure in the middle, and finally, the residual between experimental data and fit, to the right. From inspection of the residuals, the model does not fit the experimental data well, especially for the Q-range, below 1.5 Å^{-1}.

Additional analysis considers the individual components to the total model, and the value of χ^2 for each time delay. Figure 5.10 shows the results from the individual components.

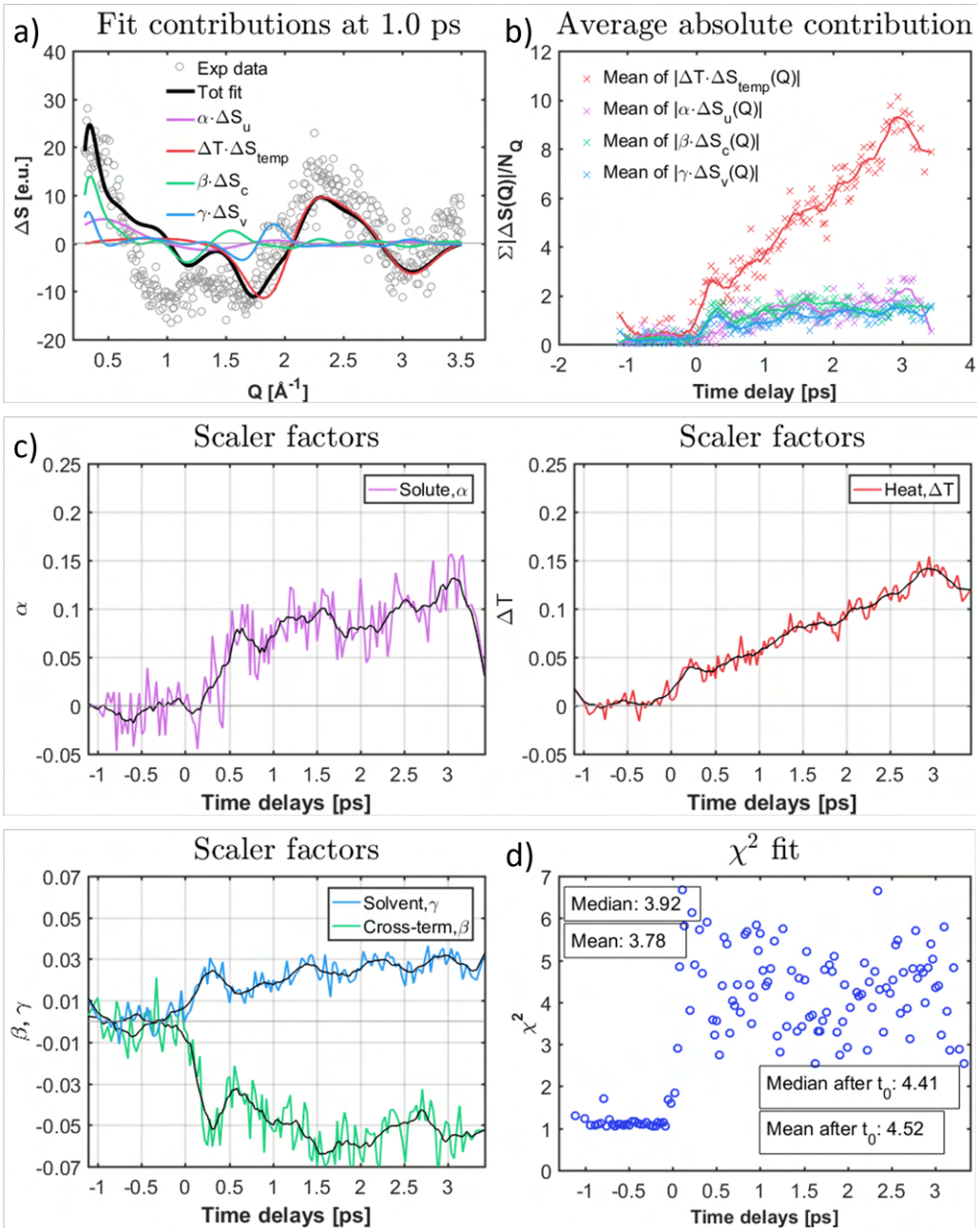

Figure 5.10: Overview of the fitting results using the model given in eq. (5.5), based on MD simulations. a) The isotropic scattering signal at 1 ps and the associated best fit components. b) The time evolution of the average absolute magnitude of the fit components. c) Time evolution of the individual scalar components, the solute (magenta), the temperature grow-in (red), the cross-term (green) and the solvent (blue). As a visual aid, full drawn black lines have been added in each of the temporal evolution plots. This was constructed as a 9-point smooth. d) The time evolution of the χ^2-value.

Panel a) shows an example of the isotropic scattering data and the fit, at a time delay of 1 ps. The total model (in black) mainly captures the features of the data (gray circles), in the Q-range above 1.5 $Å^{-1}$, in which the heat component (red) predominantly contributes to the model. The data is not well described by the model, by either of the simulated components (solute, solvent, cross-term). Panel b) shows the average (along Q) of the absolute magnitude of each fit contribution relative to each other. For each time delay, the average is shown as crosses for the heat (red), the solute (light purple), the cross-term (green), and the solvent (blue), along with full drawn lines showing smoothed data by a 9-span moving average filter. The plot shows that the components from the simulations contribute much less than the heat component to the total fit.

Panel c) in the middle and lower left corner, shows the time evolution of the scaler factors, $\alpha, \Delta T, \beta, \gamma$, in color and smoothed in black, for clarity of presentation. Three of the scaler factors $\alpha, \Delta T, \gamma$, associated with the solute, heat and solvent difference signals show an approximately zero contribution before time zero, followed by a remaining grow-in after time zero, as expected from the physics underlying the model. However, the scaler factors, β, associated with the cross-term difference signal (green), show negative values following excitation, which does not give any physical meaning to the model, and thus most likely the cross-term contribution compensates for another feature missing in the model.

Panel d) shows the χ^2-values for each time delay, which show high fluctuations, and a median value of 4.41 after time zero, which indicate high instability of the fits.

Based on the discrepancies between data and model, and the negative contribution of the cross-term, along with the highly fluctuating χ^2-values, we conclude that the model fails to describe the components, which were obtained from the MD simulations.

The result that the model from the classical dynamics simulations do not compare well with experimental data is not too surprising, since the simulations showed basically no structural changes, however, the measured scattering signals clearly show a changed signal after excitation. Thus, we conclude that the classical methods employing PACs from DFT optimizations are not accurate enough for the description of the excited state solvent changes, for this case.

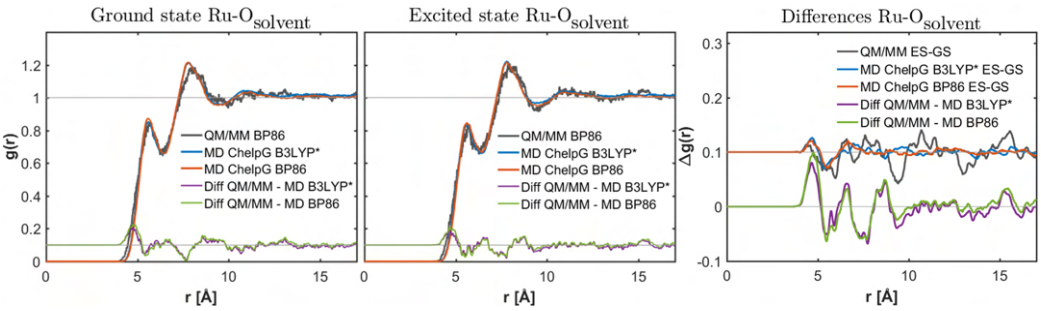

Figure 5.11: Comparison of the RDFs from the solute-solvent Ru-O atomic pair as found from mixed QM/MM MD (Black) and classical MD simulations using ChelpG type partial charges for the solute (Blue/Red). The partial charges for the classical MD simulations are obtained from DFT methods using either the B3LYP* or the BP86 functional. The difference between QM/MM and classical MD is shown in green and purple. Left) Ground state RDFs. Middle) Excited state RDFs. Right) The difference in RDF between QM/MM and classical MD compared with differences between ES and GS of the RDF of QM/MM and MD.

Comparison of the purely classical methods to mixed QM/MM methods

As outlined in **Paper I**, we carried out mixed QM/MM MD simulations to asses the performance of the PACs. We have calculated the RDFs for the higher level QM/MM MD and have used these to construct a new model for our experimental data, the results of which is described in the following section. This section compares the RDFs obtained from the MD and QM/MM MD methods.

Figure 5.11 compares the RDFs obtained using the classical ChelpG partial charges in the MD simulations with the RDFs obtained from the mixed QM/MM MD simulations. To rule out any effects from the computational differences employed in this work and the paper, the plots also show the results from the classical MD simulations using the B3LYP* functional for the calculation of the ChelpG partial charges as done in the paper, and results using the BP86 functional from this work. The figure shows RDFs for the Ru-O$_{solvent}$ atom pair in the ground state (left), in the ^{3}MLCT excited state (middle), and the differences (right).

In the plots showing the ground and excited state RDFs, the QM/MM MD results are shown in dark gray, the MD results with B3LYP* in blue, and the MD results with BP86 in red. A visual inspection shows a good qualitative agreement between QM/MM MD and the classical MD meth-

ods. Furthermore, the plots show the difference between the QM/MM MD methods and the classical methods (in green and purple). From the differences, we observe basically no difference between employing the B3LYP* or the BP86 functional, since they both show the same difference to the QM/MM MD methods.

The plot to the right shows both the difference between excited state and ground state for each method (black, red, blue), but also the compared to the difference between QM/MM MD and classical MD (green and purple). Thus, we observe that the differences between the level of theory (purple and green) are larger than the differences between ground state and excited state for each method (black, red, blue). From this perspective, the classical MD simulations do not predict the same structural changes for the excited state, as the QM/MM MD simulations do.

Hence, the analysis continues by use of the QM/MM MD results, as presented in the next sections.

5.4 QM/MM MD simulations

Since, the RDF differences from the classical MD simulations were markedly different compared to the QM/MM MD simulations, I continued the analysis by employing the QM/MM MD results. The QM/MM MD procedure is computationally a higher level of theory, and thus should be more accurate than classical MD methods. A detailed description of the applied QM/MM MD method implemented in the GPAW program package [183, 184], is provided by Dohn et al. [185].

The following sections present the main results from the QM/MM MD simulations of $[Ru(bpy)_3]^{2+}$ in solution, in terms of the RDFs, and the calculated X-ray scattering from these. Next, the section presents the results from using the calculated scattering in the analysis of the measured isotropic difference scattering signals.

Brief computational details

The computational details for the QM/MM MD methods are presented in the publication, **Paper I**, and here, for brevity, only the most important elements of the setup are outlined.

The QM part modeled the metal complex, and were carried out using the BP86/TZP(Ru)/DZP[175, 186, 187] level of theory. The MM part modeled the surrounding 1353 water molecules, using the TIP4P model, in a cubic box of 35 Å side length with periodic boundary conditions.

The simulations ran in the ground state, where after the system (45 random frames) was excited into the lowest ^{3}MLCT state using the ΔSCF method [188], recently implemented in GPAW. Following propagation on the excited state surface, RDFs were sampled over the equilibrated frames, and a total of approximately 110 ps of excited state trajectories were collected and averaged. The QM/MM MD simulations were carried out by Gianluca Levi, who kindly provided the RDFs.

5.4.1 Radial Distribution Functions

Figure 5.12 presents a comparison of results from our studies and computational studies from literature [141, 167], on the the averaged metal-solvent, Ru-O and Ru-H RDFs, obtained from the QM/MM MD simulations, of the ground state. Panel a) shows the RDFs from the QM/MM MD simulations described above, and panel b) shows the results from the study by Moret et al. [141] employing either QM/MM MD methods (top) or classical methods (bottom). They also show the running coordination number $N(r)$ as the dashed lines in the plot shown by the second y-axis. Panel c) shows the results from the study by Hoff et al. [167] by mixed QM/MM methods.

Panel d) shows a graphical depiction of the nearest solvation from the current study (left) and from Moret et al. (right), showing a chain-like structure from hydrogen-bonded water molecules around the $[Ru(bpy)_3]^{2+}$ complex. The general features of the RDFs of Ru-O and Ru-H atomic pairs, are in good agreement with literature.

The Ru-O distribution shows a relatively broad peak located at ~5.5 Å, followed by a dip at ~6.5 Å and a second peak located at ~8 Å, which are the same trends observed in literature. Similarly, the Ru-H distribution shows a first peak located around 6 Å and the second peak also around 8 Å. suggesting that there is a small preferential orientation of the O-atoms of the water molecules towards the metal center. Moret et al. also discuss the formation of a chain-like structure of the water molecules in the first solvation shell, which is linked together by hydrogen bonds.

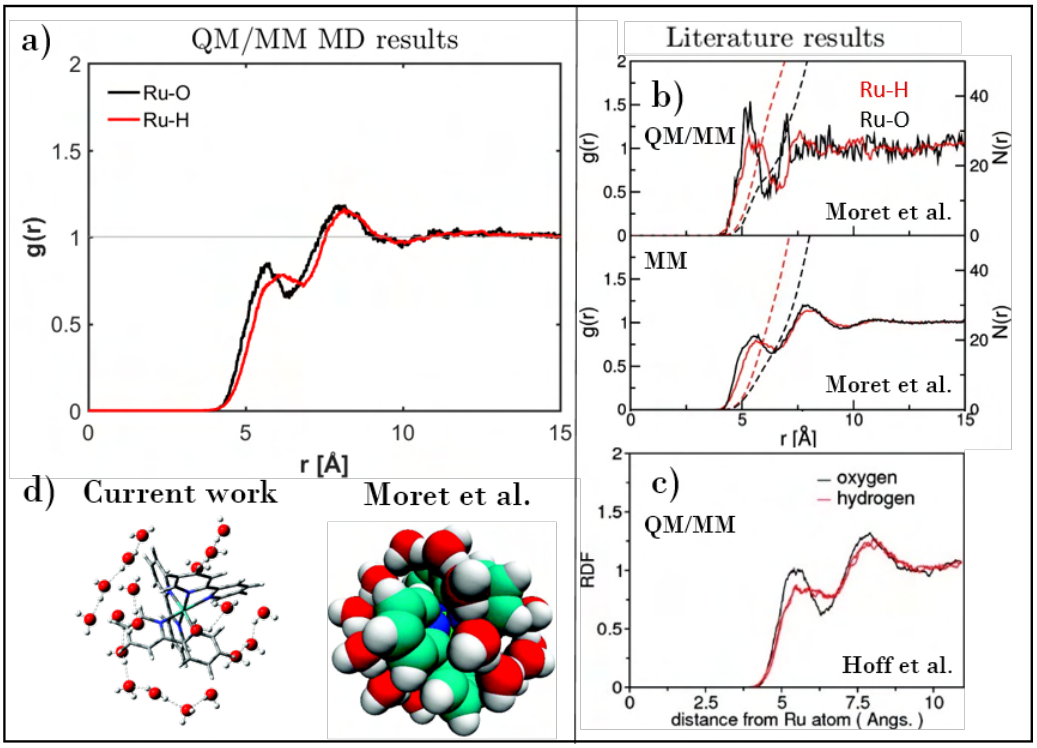

Figure 5.12: Comparison of ground state RDFs from the QM/MM MD simulations of this study (a) with results from Moret el al. [141] in part b), and Hoff et al. [167] in part c). Additionally, part d) illustrates the inner-most solvation shell that shows the chain of hydrogen-bonded water molecules from the current work and results from literature [141].

Additionally, we calculated RDFs from the excited state trajectories, and Figures 5.13, 5.14 and 5.15 present selected RDFs of both the ground state (GS), the excited state (ES) and the difference between them (in purple, with an offset). The type of atoms in the RDFs is shown for each plot in the title. For all atomic pairs of the distributions, the structural changes from the ground state to excited state are small. However, the small changes observed in the RDFs are larger than the differences observed from the classical MD methods. Thus, the structural changes are expected to show observable peaks in the calculated difference scattering signals.

Structural changes of the solute

Figure 5.13 presents RDFs from atomic pairs of the solute. Note that the differences (in purple) are offset by -20 for clarity.

The largest structural change observed in the solute arises from changes in the Ru-N bond length, which slightly elongates according to the QM/MM MD simulations from 2.080±0.018 Å in the ground state to 2.083±0.019 Å in the excited state (thus on the order of ∼0.003 Å). The observed metal-ligand structural changes are therefore, minimal.

The small structural changes are in agreement with other computational studies of the $[Ru(bpy)_3]^{2+}$ complex from the ground to an excited state of ^{3}MLCT character. For example, geometry optimizations of the metal complex in vacuum, report bond Ru-N bond contractions of 0.001-0.015 Å from the electronic ground state to an exctited state of ^{3}MLCT character, as reported from studies by Moret et al. [149], Alary et al. [143] and Diamantis et al. [142]. Additionally, the studies report a delocalized lowest excited state over all three bipyridines, and thus equivalent change of the six Ru-N bond lengths. Their results also show that the main structural changes are not the Ru-N bond lengths contractions but are associated with carbon bonds in the bipyridines which are on the order of 0.02 Å.

However, two of the three studies by Moret et al. [149] and Diamantis et al. [142] also studied the Ru complex in explicit solvation from mixed QM/MM methods, and report slightly different results. When including solvent molecules in the calculations, the Ru-N bonds show on average a slight elongation instead of contraction, on the order of 0.004-0.014 Å relative to the ground state. The bond contractions on the bipyridine ligands are still on the order of 0.02 Å from ground to excited state. Moret et al. also analyzed the three bipyridine ligands separately and they report asymmetric changes of Ru-N , and C-C bipyridine bond lengths from ground to excited state. They conclude that the explicit solvent induces a breaking of the symmetry (D_3 to C_2), resulting in a localized excited state on one (or two) of the bipyridines, and consequently the changes in the Ru-N bond length differs depending on which of the bipyridine ligands.

Experimental studies using X-ray Absorption Spectoscopy (XAS) on $[Ru(bpy)_3]^{2+}$ in aqueous solution, also report only minor structural changes of the complex. Gawelda et al. [189] reports an overall bond contraction of the Ru-N bond on the order of 0.03±0.02Å, based on the (Extended X-ray Absorption Fine Structure) EXAFS structural analysis.

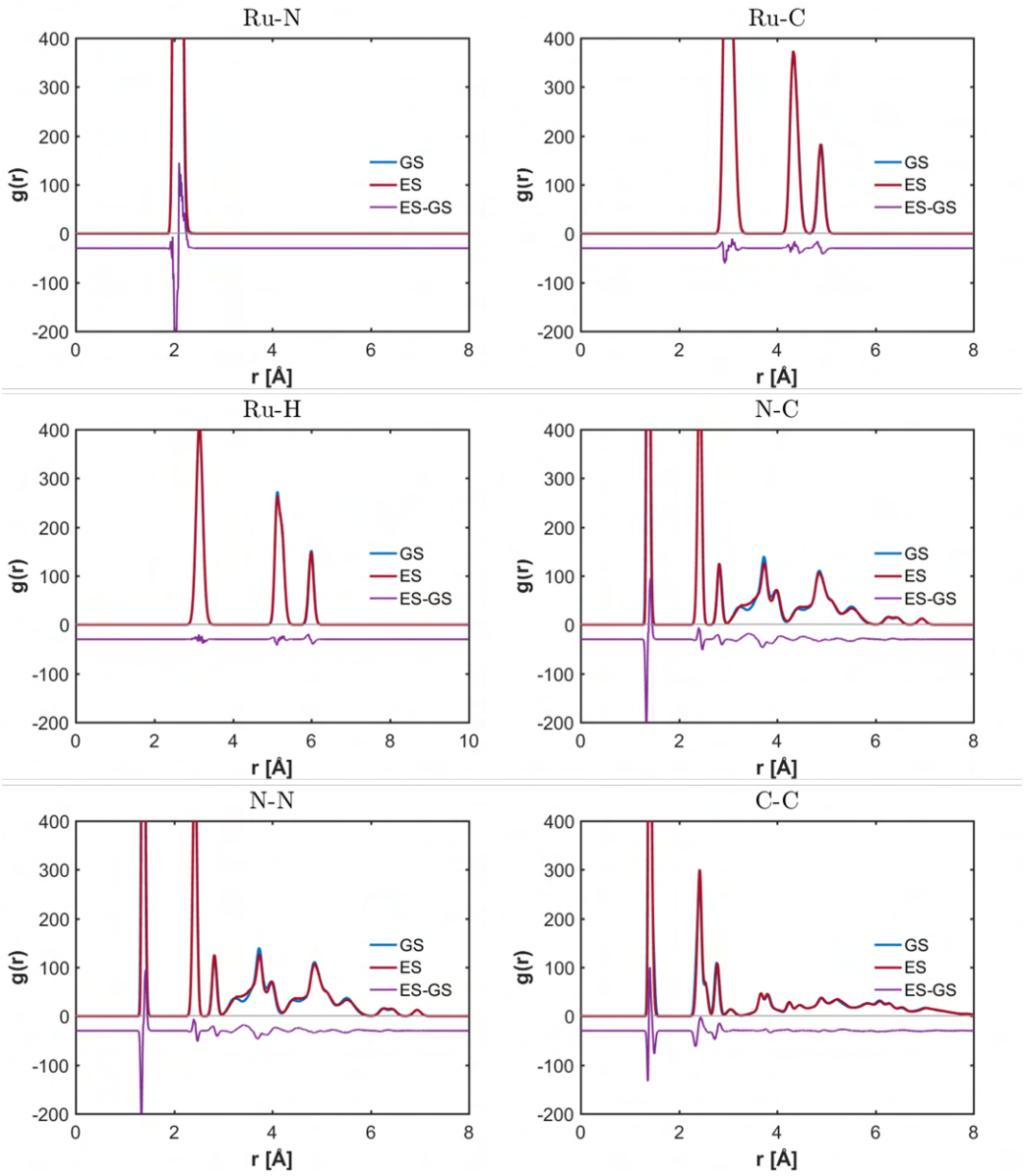

Figure 5.13: Radial distribution functions of solute-solute type atom pairs, obtained from the QM/MM MD simulations. The plots show a limited x-range and y-range for enhance the visibilty of the very small differences. Each plot shows the RDF from the ground state (GS, in blue), the excited state (ES, in red), and the difference between them with an offset of -20 for clarity (ES-GS, in purple).

Similar results were reported by Sato et al. [190] with an Ru-N bond contraction of 0.04±0.01Å, though with an increased Debye Waller factor hinting a distorted excited state geometry. The XAS data was analyzed using a fit procedure based on models of various Ru-N bond lengths. Sato et al. note that they only changed the Ru-N bond lengths in the models, disregarding structural changes of the bipyridine ligands, but justifies the method by the relatively small Ru-N bond length changes.

In conclusion, the observed structural changes of $[Ru(bpy)_3]^{2+}$ are minimal (≤0.015 Å), in the photoexcitation from ground state to an excited state of ^{3}MLCT character. Different results disagree whether the associated changes of the Ru-N bond lengths elongates or contracts, and are influenced by the solvent. Our QM/MM MD results show on average a slight elongation (∼0.003 Å) of the Ru-N bond lengths from the RDFs of the Ru-N atom pair.

Structural changes of the solvent

Figure 5.14 presents the RDFs from six of the solute-solvent atomic pairs. Similarly, to the RDFs from the solute pairs, the observed ground state and excited state RDFs are very similar, with only minor differences.

From the Ru-$O_{solvent}$ RDFs, we observe the first solvation shell within the first ∼4.0-6.4 Å and the second solvation shell up to ∼10 Å. Thus, the first solvation shell contains water molecules that show similar or even shorter distances to the ruthenium center than the most external hydrogens of the bipyridines. For larger distances, above 10 Å the statistical noise level is too high to assign peaks. Since, the differences between ground and excited state RDFs are so small, the noise become more influential. In particular, for the Ru-$O_{solvent}$ atomic pair, the observed differences show a similar magnitude for distances below or above 10 Å making assignment of true features challenging. If the differences observed for distances above 10 Å are the result of statistical noise, the calculated scattering will show artifacts. Therefore, in the calculation of the scattering signals, we employ a weight function that ensures that the first two solvent shells are given a full weight, whereas the remaining signal, at the larger distances, is dampened.

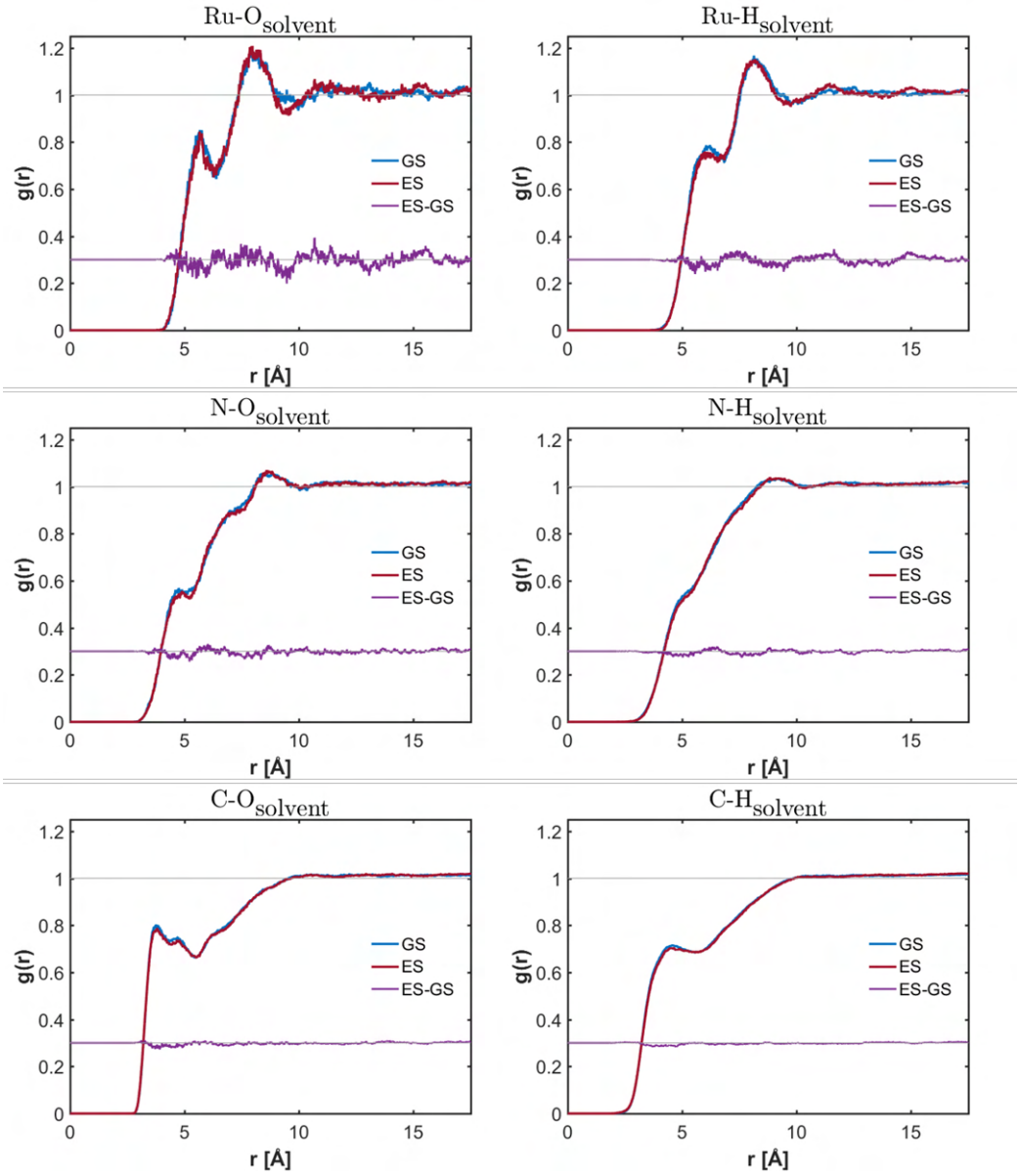

Figure 5.14: Radial distribution functions from selected solute-solvent atom pairs, obtained from the QM/MM MD simulations. Each plot shows the RDF from an average of the ground state (GS, in blue), the excited state trajectories (ES, in red), and the difference between them with an offset of 0.3 for clarity (ES-GS, in purple).

From the solute-solvent RDFs of the nitrogen and carbon atoms, and the solvent, we observe a much less ordered structure. For shorter distances than 8 Å the distributions are below 1, which suggests a hydrophobic behavior of the bipyridine ligands with the low interaction with the water molecules. We also observe this behavior for the $[Fe(bpy)(CN)_4]^{2-}$ system, Figure 6.21, described in a later chapter, section 6.3.6. The differences between ground and excited state predominantly show negative features at the shortest distances (below 6 Å), suggesting that the water molecules move slightly away from the complex.

In **Paper I**, we also calculated the running solvent coordination numbers from the integral of the curve. The coordination number for the Ru-$O_{solvent}$ RDF gives approximately 14 water molecules for the ground state which reduces to around 13.6 in the excited state. Additionally, the ratio between the coordination number for Ru-$H_{solvent}$ relative to Ru-$O_{solvent}$ is useful for the more detailed analysis of the solvent reorganization, since it is more sensitive to smaller re-orientations of the water. From the ratio, we observe a decrease of solvent hydrogen atoms relative to oxygen atoms at short distances below ∼5 Å from ground to excited state, which indicates that the water hydrogen atoms rotate slightly away from the metal in the excited state. Comparison of the location of the minima in the coordination number ratio (Fig. 4 in the manuscript) shows that the solvent re-organizes such that the solvent molecules move slightly closer to the metal (∼0.35 Å) and with the solvent oxygen atoms facing towards the ruthenium center to a higher extend in the excited state than in the ground state. However, the minimum of the ratio is above 1 for both the ground and excited state meaning that there are always at least as many hydrogen as oxygen solvent atoms within a given distance from the metal center.

The results from Moret et al. [141, 149] gives a number of 15 water molecules in the first solvation shell for the ground state, however, they do not report the RDFs and coordination numbers of the excited state. For the ground state they observe a chain-like hydrogen bonded solvation structure in the space between the ligands, as discussed above. The excited state studies show the same trend.

If the water molecules are placed in between the bipyridines with strong hydrogen bonds, I speculate that they form a rather rigid structure, which remains when the solute structural changes are minimal. Instead, the water molecules might respond to the change in charge distribution (more negative charge on the bipyridines) after population of an MLCT state.

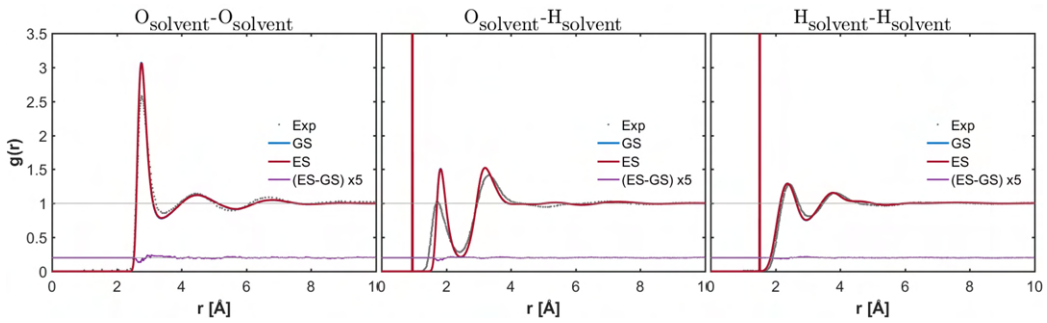

Figure 5.15: Radial distribution functions for the solvent obtained from the QM/MM MD simulations and RDFs from experiments (exp) on pure water [182, 191] (gray dots). Each plot shows the average RDFs of the ground state (GS, blue), the excited state (ES, red) and the difference (ES-GS, purple) with an offset of 0.3 Å. The differences are amplified by a factor of 5 for clarity.

Figure 5.15 presents the RDFs for the solvent-solvent pairs from our QM/MM MD simulations along with results from literature on pure water [182, 191]. The O-O distributions show a sharp peak located at ∼2.8 Å along with smaller and broader peaks at ∼4.5 Å and ∼6.7 Å distances. The results are in excellent agreement with the results from literature on pure water, however we observe a slightly sharper feature for the first solvent shell. A sharper peak indicates a slightly larger degree of structural order in the simulations for the first solvation shell, however this is expected since we simulate the solvation structure around a complex, in contrast to bulk solvent. The O-H distributions show similar trends for the innermost solvent shell, i.e. the peak at a distance of ∼1.9 Å.

The differences between ground and excited state are even smaller than for the solute-solute and solute-solvent atom pairs, and are multiplied with a factor of 5 for magnification of the signal. The small differences indicate a slight expansion of the solvent structure, based on the first peaks of the O-O and O-H distributions, which show a slight shift towards larger distances from ground state to excited state.

In conclusion, the RDFs from the QM/MM MD simulations show only minor structural changes from the ground to the excited state for the solute and the solvent. The structural changes of the Ru-N bond in the solute is ∼0.003 Å but with a large distribution of distances (±0.02 Å). Thus, only small bond elongations are observed. The nearest solvent shell shows a minor reorganization such that the O-atoms from the solvent are slightly closer (∼0.35 Å) to the ruthenium metal, with a slight rotation of the water molecules but maintaining a larger number of H-atoms in the closest proximity. The observed RDFs show deviations from the RDFs from the MD simulations, which we expect should give different results for the calculated scattering signals. The RDFs of the Ru-$O_{solvent}$ and Ru-$H_{solvent}$ are in good agreement with the results from Moret et al. [141, 149] on the same system. However, the small structural differences allow for a lower signal-to-noise ratio, which influences the reliability of the RDFs at long distances (above ∼10 Å).

In the next section, we present the calculated difference scattering signals from the RDFs of the QM/MM MD simulations.

5.4.2 Calculated X-ray scattering signals

With the new RDFs from the QM/MM MD simulations, discussed in the previous section, the expected X-ray difference scattering signals are computed. This section presents the results on the calculated scattering from the three different contributions defined as the solute-solute, solvent-solvent and the solute-solvent cross-term interactions.

Figure 5.16 presents the results on the calculated difference scattering signals, in terms of the solute ΔS_u (light purple), solute-solvent cross-term ΔS_c (green), and the solvent ΔS_v (blue). The difference scattering patterns are computed from the ES-GS difference RDFs. Furthermore, we employ a weight function, as discussed in Part I, section 2.6, since we observe spurious oscillations in the calculated signals without using the damping. The spurious oscillations arise due to the smaller box size (35 Å side length), poor signal-to-noise ratio, and lower statistics in comparison to the purely classical methods. The calculated signals without damping are shown in black, and particularly affects the cross-term and the solvent term.

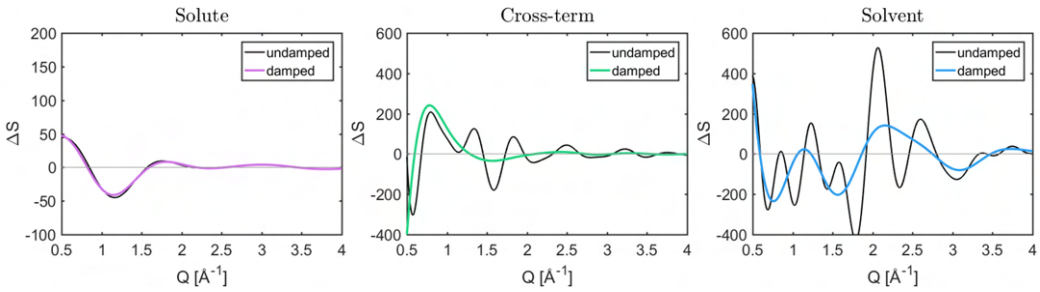

Figure 5.16: Results of the calculated difference scattering signals from the radial distribution functions obtained from the mixed QM/MM MD simulations. Left: the solute difference signal, ΔS_u. Middle: the cross-term difference signal, ΔS_c Right: the solvent difference signal, ΔS_v. The calculated signals show strong spurious features (black signals) without employing a weight function that gives RDF signals at lower distances a higher weight than for long distances and ensures that the difference RDF signals are zero at the maximum distance.

The calculated difference signal for the solute component is low in amplitude, (on the order of 50 e.u.), as expected from only the minor structural changes. Based on comparisons to other transition metal complexes, the anticipated difference scattering signal associated with photoexcitation into excited states of MLCT character, is a small signal. For example, the solute scattering contribution from results by Kunnus et al. [58] on an iron carbene system, the $[Fe(bmip)_2]^{2+}$ (bmip=2,6-bis(3-methyl-imidazole-1-ylidine)-pyridine) complex, shows a much weaker signal for the MLCT excited state than for the MC excited state. Based on their global analysis methodology, the extracted MC difference signal is about 6–8 times greater in magnitude than the ^{3}MLCT signal. The amplitude of the extracted MLCT signal is less than 100 e.u., which is on the same order of magnitude, that we observe for the calculated signal of the $[Ru(bpy)_3]^{2+}$ complex.

Comparison of the observed scattering signal of the more structurally similar $[Fe(bpy)_3]^{2+}$ complex, makes less sense due to the dissimilarity between the excited state relaxation pathway, since $[Fe(bpy)_3]^{2+}$ shows a fast population of MC states as opposed to the long lived MLCT states of the $[Ru(bpy)_3]^{2+}$ complex. Evidently, from comparisons to the results from Kjær et al. [41], the solute contribution is much stronger for the $[Fe(bpy)_3]^{2+}$ complex, with an amplitude down to approximately -1500 e.u. at the lowest Q-range. However, the observed signal at low Q, and at early

times, is below 200 e.u. which also indicates that the MLCT contribution to the difference signal is very small, and significantly less than the MC contribution. In addition, the solute difference signal shows the largest contribution to the total scattering for $Q < 1.5$ Å^{-1}, for both cases in literature, however in our case, the solute difference signal is on the same order of magnitude as the solvent and cross-term signals for the calculated signals.

The observation that the difference scattering signal observed for MC states is much larger than for MLCT states is in correspondence with the often larger structural changes for the metal-ligand bonds, associated with population of MC states rather than MLCT states. When the structural changes of the solute are small, and thus the difference signal becomes small, the contributions from the cross-term and solvent become more influential for the total signal. Since, the cross-term and the solvent term are the most difficult to model (often requires simulations using explicit solvent), the low solute contribution makes the analysis more challenging. However, the calculated scattering signals based on the QM/MM MD simulations differ from the calculated scattering based on the purely classical simulations, so we expect different results when comparing to experiment.

Following calculation of the of the scattering difference signals, we evaluate the signals by comparison to experimental data, via a fitting procedure.

5.4.3 Secondary modeling of $[Ru(bpy)_3]^{2+}$ XFEL data

With the newly calculated difference scattering signals based on the QM/MM MD results, we now employ these in the model described in eq. (5.5), and compare the model to the experimental data. This section presents the results from the fitting procedure of the model against the measured isotropic difference scattering signals.

Figure 5.17 presents the results from the evaluation of the model ΔS_{model} against the experimental data through calculations of a weighted least squares fit for each time delay, separately. The measured data is shown to the left, the middle shows the results from the fit, and the plot to the right shows the residuals between data and model.

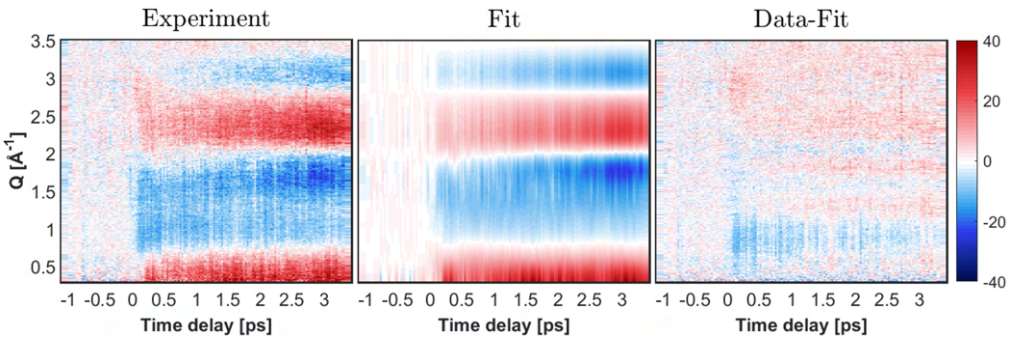

Figure 5.17: Comparison of the QM/MM MD based model and the experimental isotropic scattering data. Left: the measured difference scattering, ΔS_0. Middle: the total model, ΔS_{model} from least squares fits of eq. (5.5) to the experimental data. Right: the residuals between data and fit.

From inspection of the residuals, the model based on the QM/MM MD data shows a larger agreement with experimental data than the model based on the classical MD data. The main differences are observed around $Q = 1\,\text{Å}^{-1}$, where the experimental data shows a negative feature, which the model does not show to the same extend. Furthermore, small deviations at early times, below Δt=0.5 ps are observed.

Figure 5.18 presents the results from the analysis of the individual components to the total model, along with the calculated χ^2-values for each fit at each time delay.

Panel a) shows a snapshot at Δt=1.0 ps of the isotropic scattering data (gray circles) and the the model (black full line), and the contributions to the total model from the solute (light purple), the heat (red), the cross-term (green) and the solvent (blue). The data and model are in good agreement for most regions except around $Q = 1\,\text{Å}^{-1}$, where the data shows a larger "dip". Furthermore, the results show that only the solvent and temperature components of the model show features above $2\,\text{Å}^{-1}$, which are in good agreement with the data. The Q-range, below $1\,\text{Å}^{-1}$ shows contributions from both the solute, solvent and cross-term components, with a good agreement between the total model and the data.

Panel b) plots the average (along Q) of the absolute magnitude of each fit contribution, relative to each other. For each time delay, the average is shown as crosses. Full lines show smoothed data by a 9-span moving average filter. The plot shows that the solvent has the largest magnitude.

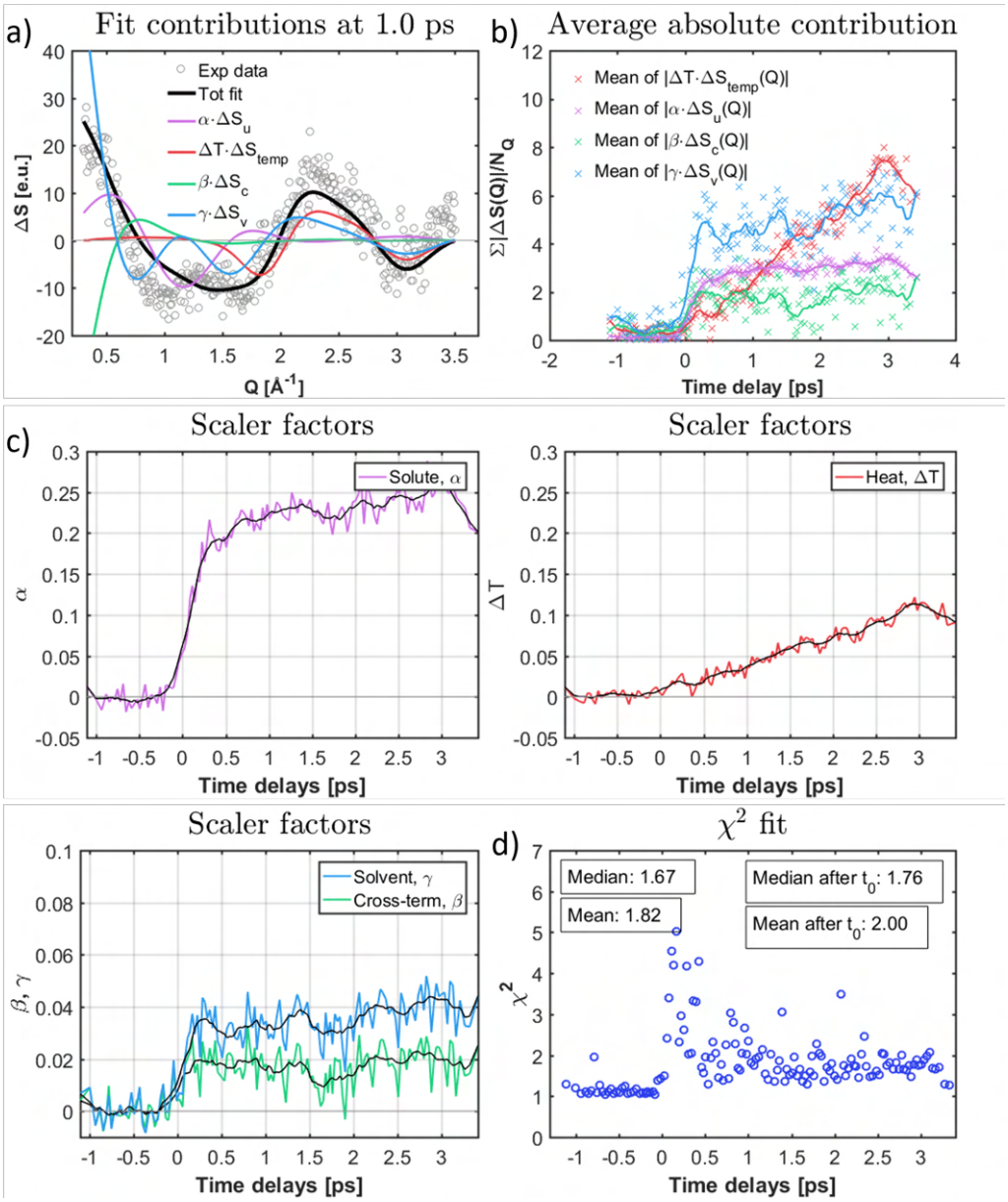

Figure 5.18: Overview of the fitting results using the model given in eq. (5.5), based on QM/MM MD simulations. a) The isotropic scattering signal at 1 ps and the associated best fit components. b) The time evolution of the average absolute magnitude of the fit components. c) Time evolution of the individual scalar components, the solute (magenta), the temperature grow-in (red), the cross-term (green) and the solvent (blue). As a visual aid, full drawn black lines have been added in each of the temporal evolution plots. This was constructed as a 9-point smooth. d) The time evolution of the χ^2-value.

Panel c) shows the time evolution of the magnitude of the scaler factors, in the middle and lower left corner. In contrast to the results based on the classical MD simulations, the results here show that none of the scaler factors are negative after time zero. Instead, the solute α, cross-term β and solvent γ factors all show an immediate grow in after time zero, whereas the heat ΔT grows in more slowly. Thus, based on this model, the solute and solvent structural rearrangements occur on similar time scales. In fact, as seen from panel b), the average of the solvent contribution, $\left|\gamma \cdot \Delta S_v\right|$ shows a slightly faster grow-in than the solute, which at a first glance would indicate that the solvent responds to the excitation, and change in charge density of the solute, rather than as a response to the structural changes of the solute. However, the solvent contribution might also compensate for something missing in the current model, at early times.

The scaler factors ΔT associated with the temperature differential, show a continuous grow-in throughout the measured time-frame of ~3.5 ps. The heat component in the model represents the local energy transfer from the solute to the solvent, which gives rise to a local increase in temperature of the solvent [86, 87]. The observed time development in the heat component matches the "slow" (ps) response of the solvent water molecules, discussed previously in section 5.2.2. Furthermore, studies from Henry et al. [157] discuss the time of the formation of a fully vibrationally relaxed ^{3}MLCT state (referred to as THEXI) in $[Ru(bpy)_3]^{2+}$ to be on the order of ~10-20 ps. The time scale matches our observation of the continuously increasing temperature component, but requires a data set with longer time delays for further analysis.

Panel d) lower right corner shows the calculated χ^2-values for each fit, which shows a reduction in the median value after time zero of 1.76 in contrast to the 4.41 observed from the fits based on the classical MD results. Thus, an effective reduction in χ^2 is observed. Furthermore, the χ^2 shows high values up to 5, at the very earliest times, which quickly drops to values below 2.5 after about 1 ps. Thus, our current model fits the data better for later time delays. The observation matches the fact that our RDFs are averages from the late time steps from the QM/MM MD simulations after solvent re-adjustments. However, the experiments at early times are very far from equilibrium, and thus model and data should not necessarily match at the earliest delay times.

In conclusion, the results based on the QM/MM MD RDFs is in better agreement with the experimental data, both from inspection of the residuals between data and model, the positive time evolution of the scaler factors, and from the significantly reduced χ^2-values. However, the model shows deviations from the data, especially at the earliest times. The observation is explained by the use of averaged RDFs from late time steps of the simulations, which allow the solvent to re-organize around the changed electronic and geometrical structure of the solute. Thus, the model does not include the direct response from photo-excitation, as the experimental data does.

5.5 Summary

This chapter presented the main results from the analysis of the excited state dynamics of the solvated $[Ru(bpy)_3]^{2+}$ system, observed from ultrafast X-ray difference scattering signals measured at an XFEL. Two models were analyzed; a model based on classical molecular dynamics (MD) simulations, and a model based on mixed quantum-mechanics/molecular-mechanics MD simulations.

The chapter presented the experimental data in terms of the isotropic and anisotropic contributions, as given after substantial data reduction and filtering steps. We observe a large change in the isotropic difference scattering signal before and after time zero, which means that the photoexcitation leads to structural changes in the sample. In addition, we observe a small feature in the anisotropic part of the scattering signals, and it was shown how to use the signal in the determination of the instrument response function. Based on the analysis of the anisotropic signals, a time resolution of ~160 fs (FWHM) was found for the given experiment.

Furthermore, the isotropic part of the difference scattering signals were analyzed by use of both classical MD simulations and mixed QM/MM MD simulations. From the simulations, we obtained radial distribution functions from an average of ground and excited state trajectories, and calculated the difference scattering signals. The calculated difference signals were evaluated against the measured isotropic scattering data through a fitting procedure, at each time step separately. The structural changes observed from the RDF differences related to both the solute and solvent

atomic pairs, were minimal for both the MD and QM/MM MD results. However, when calculating the difference signals, we find non-zero differences that should be observable in the measured scattering signals.

From evaluation of the two models based on either the classical MD or the QM/MM MD difference RDFs, a better agreement with experimental data from the QM/MM MD results was observed.

5.6 Main conclusions

The population of the ^{3}MLCT excited state of the $[Ru(bpy)_3]^{2+}$ system in water leads to only minor structural changes in both the solute and the nearest solvent, based on both our classical MD simulations, and mixed QM/MM MD simulations. Literature on other simulations and experiments agree that the structural changes of $[Ru(bpy)_3]^{2+}$ from the ground state to the ^{3}MLCT excited state are almost non-existing, on the order of $0.001 - 0.015$ Å. The very weak structural difference signal from the solute makes the analysis challenging. However, we do observe a measurable change in the isotropic part of the difference scattering signal, which means that structural changes in the sample does occur. The challenge is to decipher to what extend the origin of the signal arises from structural changes in the solute or the solvent. Especially, since the processes are highly coupled.

Furthermore, we conclude that the classical MD simulations are not accurate enough to describe the structural changes in the solvent associated with the excited ^{3}MLCT state optimized geometry relative to the ground state. The classical MD methods have produced good results in agreement with experimental scattering data in other metal complexes e.g. the $[Co(terpy)_2]^{2+}$ [79] and $[Fe(bpy)_3]^{2+}$ [45], however, these systems show much larger structural changes of the solute as a result of photoexcitation, and show fast (fs) populations of MC states, in contrast to states of MLCT character observed for the $[Ru(bpy)_3]^{2+}$ system. The populations of excited states of MC character often leads to much larger structural changes of the solute. Consequently, the solute difference signal, associated with populations of MC states, dominates the difference scattering signal. Hence, the cross-term, ΔS_c and solvent ΔS_v contributions might even become unnecessary to include in the model, which makes analy-

sis less challenging. In addition, the change in charge distribution on the solute complex associated with population of an MC state is very small from the perspective of the water molecules, and thus the solvent rather responds to the change in geometry and the overall expansion/contraction of the solute molecule. On the other hand, an excited state of MLCT character concerns charge transfer from the metal out on the ligand, which is closer to the solvent. Thus, the solvent must also show a response to the change in charge distribution, which makes more accurate methods of theory necessary, even though it might be a small effect.

In conclusion, we find two main reasons why the classical methods fail for the case of the $[Ru(bpy)_3]^{2+}$ complex:

1. The structural changes of $[Ru(bpy)_3]^{2+}$ from ground state to the lowest ^{3}MLCT state are minimal.

2. Population of excited states of MLCT character are fundamentally (much) different from states of MC character.

Additionally, results from the model based on the QM/MM MD methods show an instantaneous grow in of a component, which is faster than the grow in of the difference signal associated with the structural changes of the solute. This fast component suggests that the nearest water molecules reorient faster than the molecule changes structure as a direct response to the change in charge distribution, in support of the necessity of higher level theoretical methods.

The overall agreement is good between experimental data and the model based on the QM/MM MD results, but to a less extend at the earliest time delays below ~1 ps. We presume that the reason lies in the fact that the simulations are a result of an average over the structural rearrangement of the water after equilibration has occurred. From literature, the relaxation of the solvent response shows a component on the order of few ps, which matches the observed time for lower χ^2-values in our fits.

Hence, we conclude that theoretical calculations that considers the excited state dynamics away from equilibrium conditions, as it occurs, are necessary to capture the excited structure and solvent response of the photoexcitation. At least for this case and possibly for MLCT excited states, in general.

5.7 Outlook

The next steps in the investigations of the excited state dynamics of the $[Ru(bpy)_3]^{2+}$ system, would concern the structural dynamics at the earliest time delays as well as the solvent influence.

To investigate the earliest time delays in greater detail, in terms of experiments, requires a new data set with increased time resolution (30-50 fs), longer time delay scans than 3 ps to capture the differences between early and equilibrated solvent dynamics, and higher statistics in terms of more time delay scans. In terms of simulations, we need additional higher level theoretical calculations to capture the direct excited solute and solvent response. For example, using the excited state dynamics simulation tools discussed in Part II, section 3.5, which was applied for the $[Fe(bpy)(CN)_4]^{2-}$ system.

In terms of further investigations of the solvent influence, an idea was to collect time-resolved scattering data in different solvents. In addition, measuring the signals at a lower Q-range, which would allow us to better examine the solute and solvent (cross-term) contributions, since this region shows the strongest features from the solute and cross-term contributions. Such an experiment was already planned at the APS synchrotron facility in Chicago, however due to technical challenges at the beamline, and later due to the Corona pandemic, the planned experiment was canceled several times.

Otherwise, previous studies have benefitted from the use of complementary methods simultaneously, such as collection of the K_β X-ray emission spectra (XES) as well as X-ray scattering of the $[Fe(bpy)_3]^{2+}$ system [192, 41]. For example, the excitation fraction found from the XES data could be used as a set parameter to reduce the number of free parameters in the modeling procedure applied in the analysis of the scattering data. However, to capture the time-resolved K_β X-ray emission spectrum of the $[Ru(bpy)_3]^{2+}$ system, requires higher X-ray energy, ~ 22 keV [193]. Such experiments might become durable by the prospects of the European-XFEL going to 25 keV [194, 195] and high-energy upgrade at the LCLS [196, 197], in the near future.

Chapter 6

Analysis and results on the $[Fe(bpy)(CN)_4]^{2-}$ investigations

Contents

A central part of the work related to this thesis, is the studies of an Fe(II)-based metal complex, namely $[Fe(bpy)(CN)_4]^{2-}$ with the abbreviation bpy = 2,2'-bipyridine. The investigations are a collaborative work, but I have been the main driving force behind the investigations.

The studies mainly involve a computational study of the ultrafast excited state dynamics, including calculations of time-dependent X-ray scattering difference signals. The theoretical work was mainly carried out during a six months external research stay at the University of Vienna, visiting the group of Univ.-Prof. Dr. Dr. h.c Leticia González. I designed the scope of the project, and presented the ideas of the computational study, which was welcomed by Leticia González who initiated the collaboration with Post Doc Sebastian Mai, from the group. Sebastian Mai helped design the computational details of the study, and how to use the SHARC analysis tools, developed in the group. I continued the analysis of the data back in Denmark, in close collaboration with Sebastian Mai.

Furthermore, ultrafast time-resolved X-ray emission and X-ray scattering data, was measured at an X-ray Free Electron Laser (XFEL). The data was collected in collaboration with the group of Assc. Prof. Kelly Gaffney at the PULSE Institute at SLAC National Accelerator Laboratory in California. Treatment and analysis of the data is beyond the work of this thesis, and a future goal is to compare the simulations to the experimental results.

In addition, I studied the steady state absorption spectra of the metal complex in various solvent mixtures, and measured optical transient absorption spectra. The measurements were collected in collaboration with Assc. Sr. Lecturer Jens Uhlig and (former) Post Doc Kasper S. Kjær, both working at University of Lund, at the time of the experiments. This thesis presents the results from the steady state absorption measurements, and discusses the goal of the optical study.

This chapter focuses on the computational study of the ultrafast excited state dynamics of the $[Fe(bpy)(CN)_4]^{2-}$ complex. Section 6.1 gives an introduction to the complex and in particular the solvent influence on the photoabsorption properties and excited state dynamics from experiments. Section 6.2 presents the measured steady state absorption spectra in mixed solvents of water and dimethylacetamide (DMA). Section 6.3 describes the current analysis and results from the SHARC simulations. The final sections give a summary, conclusions, discussion and an outlook.

6.1 Introduction to $[Fe(bpy)(CN)_4]^{2-}$

The $[Fe(bpy)(CN)_4]^{2-}$ complex is of particular interest of solvent governed photodynamics of metal complexes, since the absorption of visible light depends on the type of solvent. A solution of the metal complex solvated in water is red, and especially absorbs green light ($\sim 500\,nm$) for the transitions associated with an MLCT transition. In contrast, when solvated in dimethyl sulfoxide (DMSO), the solution is green, and shows a strong absorption in the 600-800 nm range, in the regime of red light. Thus, the photo-chemical and -physical properties, such as the measured absorption spectrum [49] and the excited state dynamics [50, 51, 198] depends largely on the choice of solvent. Hence, the $[Fe(bpy)(CN)_4]^{2-}$ complex acts as a model system to investigate solvent effects on excited state dynamics, in particular related to MLCT and MC states. This section gives an introduction to the complex, in particular, the influence of the solvent on the changes in the absorption spectrum in section 6.1.1, and on the energetic landscape in section 6.1.2. Furthermore, section 6.1.3 describes the goal of our investigations on the ultrafast structural and electronic dynamics of the $[Fe(bpy)(CN)_4]^{2-}$ complex, and the solvent influence.

6.1.1 Photoabsorption and solvent acceptor number

Figure 6.1 presents the strong solvent effect on the measured absorption spectrum of $[Fe(bpy)(CN)_4]^{2-}$ in various solvents. The so called acceptor number is a measure of the ability of the solvent to act as an electron-pair acceptor, by a combination of the solvent polarity, polarizability and hydrogen bond donor ability as described by Taft and coworkers [199]. It has been proposed [198, 49] that the solvent acceptor number is an important factor in the observed solvent dependent trends. A Lewis acid is an ion or molecule, that can accept an electron pair [200, p. 142]. Thus, a solvent with a high acceptor number, is a strong Lewis acid, and a hydrogen bond donor, such as water, methanol (CH_3OH, called MeOH in the figure) or ethanol (CH_3CH_2OH, EtOH). On the other hand, solvents of low acceptor numbers are weak Lewis acids such as acetonitrile (CH_3CN, MeCN), dimethyl sulfoxide ($(CH_3)_2SO$, DMSO), or dimethyl formamide ($(CH_3)_2NC(O)H$, DMF) or dimethylacetamide ($CH_3CON(CH_3)_2$, DMA).

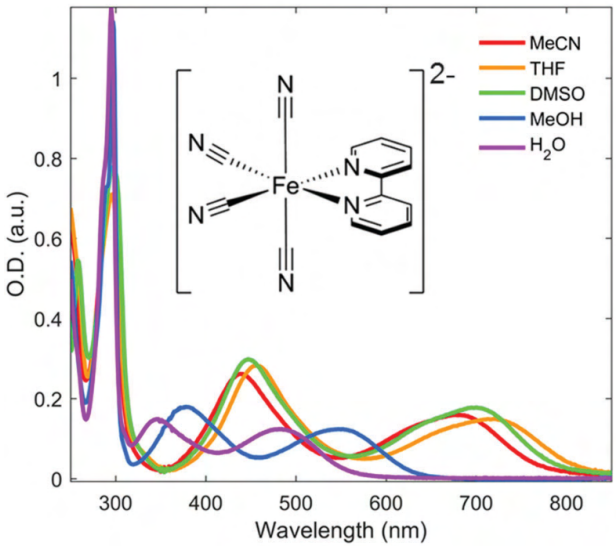

Figure 6.1: Solvent effect on the absorption bands of the $[Fe(bpy)(CN)_4]^{2-}$ complex. Optical absorption spectrum of the $[Fe(bpy)(CN)_4]^{2-}$ complex in a series of solvents of different Lewis acidity. Weak Lewis acid solvents are acetonitrile (MeCN), tetrahydrofuran (THF) and dimethyl sulfoxide (DMSO). Strong lewis acid, and hydrogen bonding solvents, such as water (H_2O) and methanol (MeOH), shift the absorption bands to lower wavelengths. Figure from [51]

For the $[Fe(bpy)(CN)_4]^{2-}$ complex this solvent dependence means that the first band in the absorption band, which is related to the MLCT transition, shifts from a maximum around 500 nm in water with a high acceptor number (54.8) to a maximum around 700 nm in solvents with low acceptor number, such as DMSO (19.3). Table 6.1 gives an overview of the acceptor numbers (AN), donor numbers (DN), and measured maximum absorbance of the lowest band in terms of energy (E_{max}) and wavelength (λ_{max}).

Additionally, from comparisons of Ru-based cyano-polypyridyl complexes, it was determined that the shift in the MLCT absorption band with solvent, also increases linearly with the number of cyano ligands [202]. Furthermore, a study by Toma and Takasugi [49] of several Fe-cyano-based complexes reports that the sensitivity of the complex to the acceptor properties of the solvent, increases with the number of cyanide ligands in the complex.

Table 6.1: Acceptor numbers (AN), donor numbers (DN) of common solvents, and the observed absorption maximum (in terms of energy,E_{max} and wavelength (λ_{max})) of the lowest energy band assigned to MLCT for the $[Fe(bpy)(CN)_4]^{2-}$ complex. Based on [49, 201]

Solvent	**AN**	**DN**	$\mathbf{E_{max}}$ (eV)	λ_{max} (nm)
H_2O	54.8	18.0	2.57	482
MeOH	41.3	19.0	2.26	548
EtOH	37.1	20.0	2.16	573
DMSO	19.3	29.8	1.80	690
MeCN	18.9	14.1	1.90	654
DMF	16.0	26.6	1.80	687
DMA	13.6	27.8	1.70	730
Acetone	12.5	17.0	1.71	724

The cyanide-dependent observations were rationalized as follows; Solvents of high acceptor number may interact with the the cyanide ligands through the available lone-pair, an interaction which "pulls" electron density from the cyanides, away from the metal center and towards the solvent surroundings. Shifting electron density from the cyanide ligands, allows for an increased π-back donation from the metal to the cyanides, strengthening the metal-ligand bond, which stabilizes the ground state of the complex. X-ray absorption measurements [203] on $[Fe(bpy)(CN)_4]^{2-}$ in different solvents and simulations on the $[Fe(CN)_6]^{4-}$ complex [204] support the rationalization. Consequently, the energy separation increases between the orbitals with a mixed character of Fe t_{2g} and CN π^* character, and the (un-occupied) orbitals with bipyridine ligand character, as illustrated in Figure 6.2.

Toma and Takasugi [49] also discuss an asymmetric solvation, and argue that the cyano ligands are more strongly solvated than the bipyridine ligand for the $[Fe(bpy)(CN)_4]^{2-}$ complex, in a solvent with high acceptor number. However, other types of ligands, such as pyrazine, are more strongly solvated than bipyridine, in solvents of large acceptor number. Hence, the nature of the ligands, and especially the cyano ligands play an important role in the solute-solvent interactions.

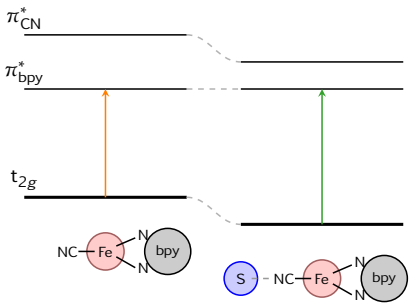

Figure 6.2: Energy level diagram illustrating the relative shift in transition energy arising from the interaction of the solvent (blue S) with the cyanide ligand (NC). Left part illustrates the situation without solvent interaction with a lower energy transition (orange arrow) from the metal centered (Fe) ground state (t_{2g}) to the orbitals of predominantly π^*_{bpy}, bipyridine ligand character. Right part illustrates the stabilization of the ground state and excited orbitals of predominantly π^*_{CN} cyanide character due to the solvent interaction (S). The drawing below illustrates the metal complex in a simplistic manner, ignoring the remaining bonds to other cyanides and within the bipyridine unit. The diagram does not include the excited MC e_g orbitals. Based on work from [49].

6.1.2 Energetic landscape

Figure 6.3 presents a qualitative overview of the suggested energetic landscape of the $[Fe(bpy)(CN)_4]^{2-}$ complex. In the following, each paragraph describes the different panels of the figure.

MO diagram

Panel (A) illustrates a qualitative MO-diagram, as presented by the work of Kjær and coworkers [51], of the complex in weak Lewis acid solvents, such as DMSO. The green arrows indicate how the energy levels shift when changing to a strong Lewis acid solvent, such as water, which especially affects the orbitals related to the cyanides. One should note that the energy splitting of the iron d orbitals into t_{2g} and e_g assumes octahedral (O_h) symmetry, and not the formally correct C_{2v} symmetry, and the correct energy splitting is more complex. The octahedral notation is chosen for simplification, and to facilitate comparison to other systems of near octahedral symmetry. An illustration of the molecular geometry is shown below the MO diagram.

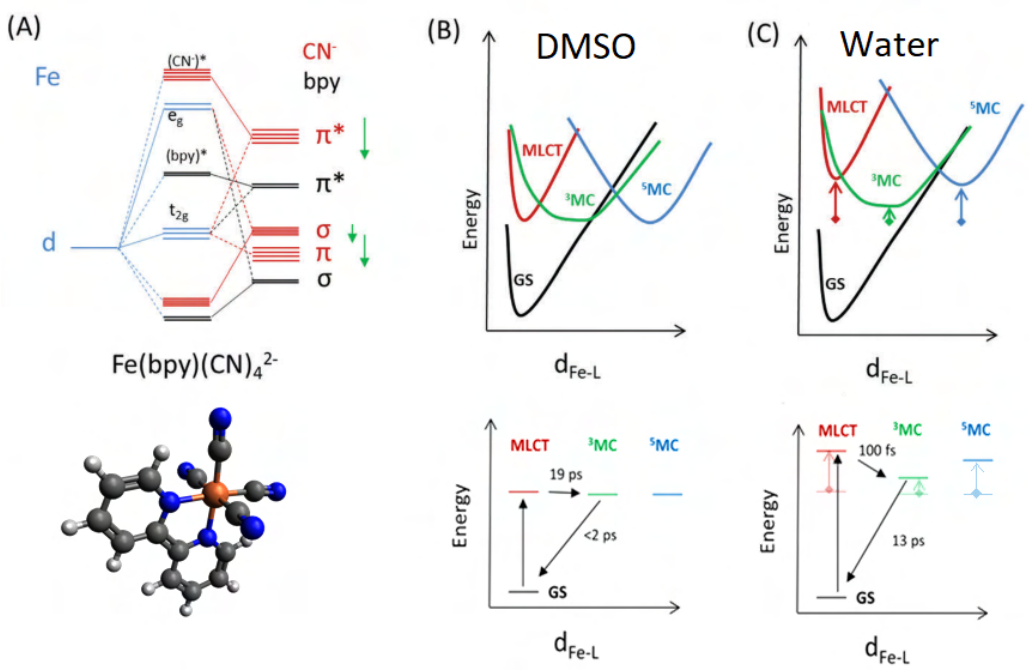

Figure 6.3: Overview of the energetic landscape of the $[Fe(bpy)(CN)_4]^{2-}$ complex presented in a qualitative manner. (A) Simplified MO diagram of the complex solvated in a weak Lewis acidity solvent (e.g. DMSO), with arrows indicating the shift in energy levels upon solvation in high Lewis acidity solvents (e.g. water). The geometry of the $[Fe(bpy)(CN)_4]^{2-}$ complex is shown below. (B) A schematic of the potential energy surfaces in a weak Lewis acidity solvent, such as DMSO, along with a diagram with the approximate excited state lifetimes shown below. (C) shows the same as (B) when the complex is solvated in a strong Lewis acid, such as water. Adapted figure from [51].

Potential energy surfaces in weak Lewis acids

Panel (B) illustrates the potential energy surfaces in a schematic form, under solvation in weak Lewis acids such as DMSO, as suggested from related work [50]. In addition, the assigned excited state lifetimes are shown below, based on transient UV-Vis absorption (TA) and ultrafast time-resolved X-ray emission spectroscopy (XES) measurements [50, 205]. The XES and TA results (excited at 650 nm) suggest an extended MLCT excited state lifetime, and find no evidence for excited state build up of ^{5}MC character, in contrast to the $[Fe(bpy)_3]^{2+}$ system [40]. Kinetic fits of the time-dependent absolute value of the difference XES spectra, find a decay time of 19±2 ps, and was assigned as an MLCT decay, based on fits of reference spectra. However, they argue that the ^{3}MC reference spectrum also provides a viable fit to the data, and discuss the possibility of an ultrafast ^{1,3}MLCT to ^{3}MC transition that may not be temporally resolved.

The TA data shows excited state absorption features at 370 nm and ground state bleach at 440 nm, which decay bi-exponentially with time constants of 2.5±0.5 ps and 18.5±0.9 ps. The fast component was assigned to intra- and inter-molecular vibrational re-distributions and solvation dynamics, whereas the slower component was assigned to populations of MLCT excited states. DFT calculations show states of ^{3}MC and ^{5}MC character at similar minimum energies as the ^{3}MLCT lowest excited state but with significantly different geometries. Furthermore, the calculations find very similar energies of a geometrically distorted ground state and the minimum of a ^{3}MC state. These results could explain the prolonged MLCT lifetime and lead to a fast deactivation through a ^{3}MC state to the ground state, while inhibiting build up of any ^{3}MC population.

Potential energy surfaces in strong Lewis acids

Panel (C) shows the suggested shift in the potential energy surfaces and excited state lifetimes, when solvated in strong Lewis acids, such as water [51]. The change of solvent leads to a shift in the lowest energy band in the steady state absorption spectrum from a maximum at ∼700 nm to ∼500 nm [51]. Hence, an increase in excitation energy, which was interpreted as a result of the nearest solvent molecules shifting electron density from the cyanides, decreasing the π(CN)→d(Fe) π-bonding and increasing the d(Fe)→ π^*(CN) π-backbonding. Consequently, the Fe t_{2g} levels are stabilized relative to the bipyridine-centered π^* levels, which destabilizes the MLCT states relative to the ground state.

Supporting this suggestion, a combination of TA and XES measurements [51] in water showed that the MLCT lifetime is on the order of 100-200 fs, which is an extensive reduction relative to the 19 ps observed in DMSO. The fitted time constants is faster for XES (87 ± 5 fs) than for the TA results (0.17 ± 0.03 ps), and the study discusses that the differences likely reflects the challenge of differentiating population decay from intramolecular vibrational relaxation in TA combined with possible cross-phase modulation artifacts. However the XES measurements used an excitation wavelength of 400 nm and the TA measurements were excited at 500 nm different wavelengths and with a lower pump fluence, which might influence the measured excited state dynamics. Furthermore, a second component of 12.7 ± 0.4 ps, with TA and 13.1 ± 0.4 ps with XES, was assigned to the lifetime of a ^{3}MC excited state, in aqueous solution of the complex. The study concludes that the ^{3}MC states must be stabilized relative to the MLCT states, indicating that the Fe e_g levels decrease in energy with increasing solvent Lewis acidity. The study argues that both the Fe t_{2g} and the e_g levels are shifted to lower energies, with t_{2g} shifting the most, resulting in a significant shortening of the MLCT lifetime, and longer MC lifetime, under solvation in water. However, the conclusions regarding the excited state energetic landscape and associated decay pathways are speculative, and one goal of our studies is to investigate this further.

Other solvents

Other recent studies by Kunnus et al., on $[Fe(bpy)(CN)_4]^{2-}$ and two related polypyridyl-compounds using TA measurements [205], assigned excited state MLCT lifetimes in a range of solvents. They observed ultrashort lifetimes of ~200 fs in H_2O and MeOH solvents, whereas the measurements in the solvents DMSO, MeCN, Dimethylformamid (DMF) showed longer MLCT lifetimes between ~16-30 ps. Table 6.2 summarizes the measured excited state lifetimes, τ_{MLCT} from the excited state absorption features positioned below 550 nm, assigned to intraligand transitions of the reduced bipyridine radical, and thus populations of MLCT states.

Additionally, the studies report observations of other absorption features decaying on a second time scale, τ_2. In solutions of H_2O and MeOH, the excited state absorption features below 550 nm decay without simultaneous ground state recovery, while other absorption features at higher wavelengths occur. Based on these observations and previous observations [51] from the XES measurements of $[Fe(bpy)(CN)_4]^{2-}$ in water, the second

component in solutions of H_2O and MeOH was assigned to the lifetime of a ^{3}MC state, and is on the order of ~ 10 ps. In solutions of DMSO, MeCN and DMF, they observed that the MLCT excited state absorption features decay concomitantly with the ground state bleach, and additionally a dynamic shift in MLCT excited state absorption features on the 1 ps time scale. This second component was assigned to solvation and vibrational energy redistribution. They also note that the simultaneous decay of absorption features below 550 nm and ground state bleach confirms that no population accumulates in excited MC states, although it does not necessarily mean that excited states of MC character do not participate in the MLCT relaxation mechanism. Rather it means that the lifetime of the excited states of MLCT character significantly exceeds the lifetime of the excited states of MC character in the solutions of DMSO, MeCN and DMF.

Additionally, the study reports estimated lowest vertical ^{1}MLCT energies (E_v) based on a vibronic band shape analysis of the lowest energy band in measured steady state absorption spectra, which are also shown in Table 6.2.

Table 6.2: Reported excited state lifetimes τ and lowest vertical energies, E_v. Based on work from Kunnus et al. [205]

Solvent	$\mathbf{E_v}$ (eV)	τ_{MLCT} (ps)	τ_2 (ps)
H_2O	2.64	0.18	12.4
MeOH	2.41	0.22	10.4
DMSO	1.95	16.5	1.3
MeCN	1.94	19.3	1.5
DMF	1.83	28.7	1.4

In conclusion, the measured MLCT lifetimes decrease by more than two orders of magnitude when dissolving in the hydrogen bonding solvents, H_2O and MeOH, in contrast to the DMSO, MeCN and DMF solvents. These observations comply with the theory that solvents of high acceptor number destabilizes the MLCT states (metal to bipyridine) relative to the ground state, as a result of strong interactions between the solute and solvent.

6.1.3 Goal of our investigations

Our studies are motivated by a wish to further investigate how the energetic landscape, and thus the excited state dynamics, are influenced by the solvent. Previous studies investigated the solvents that results in absorption of light either around ~ 700 nm or around ~ 500 nm, where the results differ quite significantly with e.g. MLCT lifetimes varying between 200 fs and 29 ps. However, the question remains, what happens in the range between, e.g. if the absorption peak is around 600 nm? The goal is to investigate whether a systematic shift of the absorption band is possible, and thus "manipulate" the energy levels and the excited state dynamics by using solvent mixtures. We carried out measurements of the steady state absorption spectra in solvent mixtures of water and dimethylacetamide (DMA), along with TA measurements. Water has a high acceptor number (54.8) and thus act as a strong Lewis acid and H-bonding solvent, and DMA is a weak Lewis acid with a low acceptor number (13.6) [199]. Furthermore, the goal is to study the interactions between solute and solvent during the excited state dynamics, and thus we carried out simulations of the Fe-complex in water. In particular, the interactions between the solute cyanides and the solvent is of interest. A computational study also allows us to study any coupled electron-nuclei dynamics, which has proven relevant for the electronic transitions in a study of $[Fe(bpy)_3]^{2+}$ [41].

6.2 Steady state absorption results

This section presents the results from the steady state absorption measurements of the $[Fe(bpy)(CN)_4]^{2-}$ complex in solvent mixtures of water and dimethylacetamide (DMA). The measurements were carried out as part of an Interreg project in collaboration with Assc. Sr. Lecturer Jens Uhlig and (former) Post Doc Kasper S. Kjær, who were both associated with Lund University, at the time of the measurements. The experiments were carried out at the department of Chemical Physics at Lund University.

The goal of the study was to investigate the ground state to MLCT energy gap, and the possibility of systematically shifting the MLCT absorption band of the steady state absorption spectrum along with its effect on the excited state dynamics based on optical transient absorption measurements.

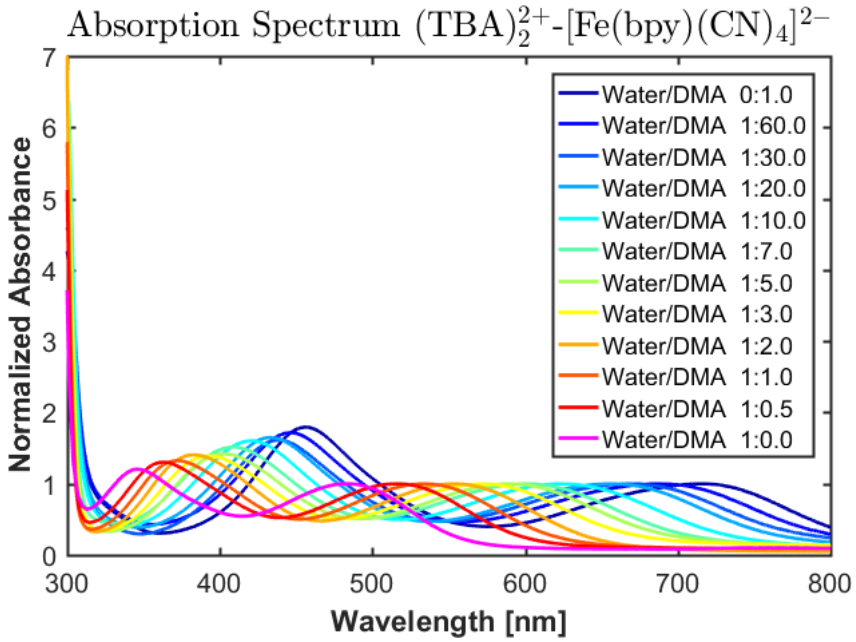

Figure 6.4: Normalized measured absorption spectra of $[Fe(bpy)(CN)_4]^{2-}$ in solvent mixtures of water and dimethylacetamide (DMA). The spectra are normalized to the maximum of the first absorption band located at the highest wavelengths. The band of interest shifts from an absorption max just below 500 nm in pure water to approximately 725 nm in pure DMA.

The earliest investigations concerned the solubility of the system, where we realized that the $K_2Fe(bpy)(CN)_4$ salt was not soluble in pure DMA (or acetonitrile). Thus, an ion exchange of the counter ion was necessary, into the larger and bulkier organic counter ion, tetrabutyl ammonium (TBA). Following the ion-exchange, the $(TBA)_2Fe(bpy)(CN)_4$ salt was soluble in both pure water, pure DMA and the solvent mixtures.

Figure 6.4 shows the results of the measured absorption spectra in the water-DMA solvent mixtures. The spectra are normalized to the maximum of the first absorption peak at the longest wavelengths. The results show a gradual shift in the lowest energy absorption band (assigned to the MLCT transition), with maxima ranging from ~485 nm (pink) in pure water to ~725 nm in pure DMA (blue).

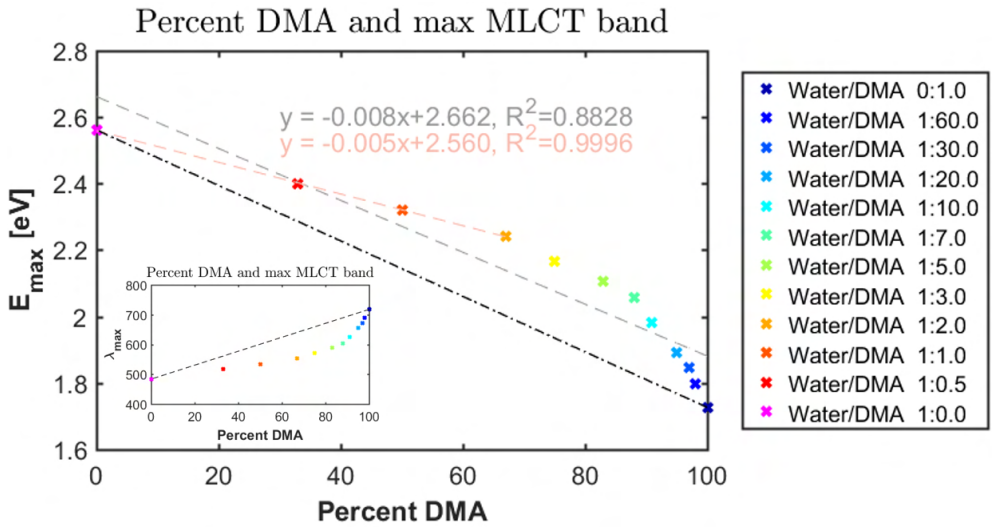

Figure 6.5: Shift in the MLCT absorption band of $[Fe(bpy)(CN)_4]^{2-}$ in solvent mixtures. Absorption maximum (in nm) converted to energy as a function of the amount of dimethylacetamide (DMA) in the water-DMA solvent mixtures. The inset shows the trend in nm. A linear regression of all points show clear deviance from a linear trend (gray). The first 4 data points show a linear trend (rosa). Black line plots a straight line from first to the last point indicating the behavior if the trend was linear.

Energy shifts in solvent mixtures

Since, the wavelength is not a linear scale energetically, the measured absorption maxima in terms of wavelengths were converted to electron volts. Figure 6.5 shows the absorption max (E_{max} in eV) as a function of the amount of DMA in the water-DMA solvent mixtures, in volume-percentages. The inset shows the same data in terms of the maximum wavelength, λ_{max}. The plot shows that the absorption maximum shifts with the solvent mixtures, but not in a linear manner. The black dashed line shows the anticipated behavior, if the trend was linear from the first to the last data point. A linear regression of the entire data range, also shows a clear deviation from a linear trend (gray, dashed line). However, the first four data points (with less than 75 % DMA) show a linear trend, as shown by the fit (rosa, dashed line). Although, more data should be collected for an accurate description of the trend.

Furthermore, the plot shows that relatively large amounts of DMA are required to shift the absorption max. Solutions containing 33 % DMA (1:0.5 mix) only shifted the absorption max from 2.56 eV to 2.40 eV, i.e. a shift of 0.16 eV, relative to pure water. On the other end of the scale, solutions containing predominantly DMA, leads to larger shifts the absorption maximum even with small amounts of water present. A solution containing only 1.6 % (1:60 mix) water, leads to a shift from 1.80 eV to 1.73 eV (shifts 0.07 eV) relative to pure DMA. Likewise, a solution containing about 3 % water (1:30 mix) leads to a shift from 1.89 eV to 1.73 eV, thus a shift of 0.16 eV. Hence, the presence of water affects the shift of the measured absorption maximum the most.

Assuming that the nearest solvation around the complex has the same composition as the bulk solvent, we would expect the system to show a linear behavior with respect to the amount of DMA in the mixture. However, here the plot showed the solvent composition in terms of volume and not the molar fraction, taking the weight and size of the solvent molecule into account. Thus, a 1:1 solvent mixture does not mean that there are equal numbers of DMA and water molecules in the solution, since the volume of 1 mole of DMA (C_4H_9NO) is larger than the volume of 1 mole of water molecules. Converting the volume percentages into the DMA molar fraction, gives the results in Figure 6.6.

Employing the molar fraction instead, shows a more linear trend of the shift with increasing amount of DMA present. The plot shows a linear fit (gray, dashed line) along with a simple straight line (black, dashed line) from the data point of pure water to pure DMA. The inset shows the trend in units of nm. Now, a linear behavior of the system with respect to the DMA molar fraction, would be expected if the nearest solvation shell of the metal complex has the same composition as the bulk solvent. Figure 6.6 shows that small amounts of DMA present, change the measured absorption maximum in a way that deviates most from a linear trend. The deviation, indicates that the water molecules remain preferentially in the bulk solvent for small amounts of DMA present, in contrast to the previous figure, based on volumen percentages. Concentrations of higher than ~50 % DMA lies closer to the anticipated linear trend, indicating that both water and DMA are equally present in the nearest solvation shell. The same trends were found in a similar study on several polypyridyl-Fe complexes, by Toma et al. [49] where the deviations from linear were most evident for water-acetonitrile and water-acetone solvent mixtures.

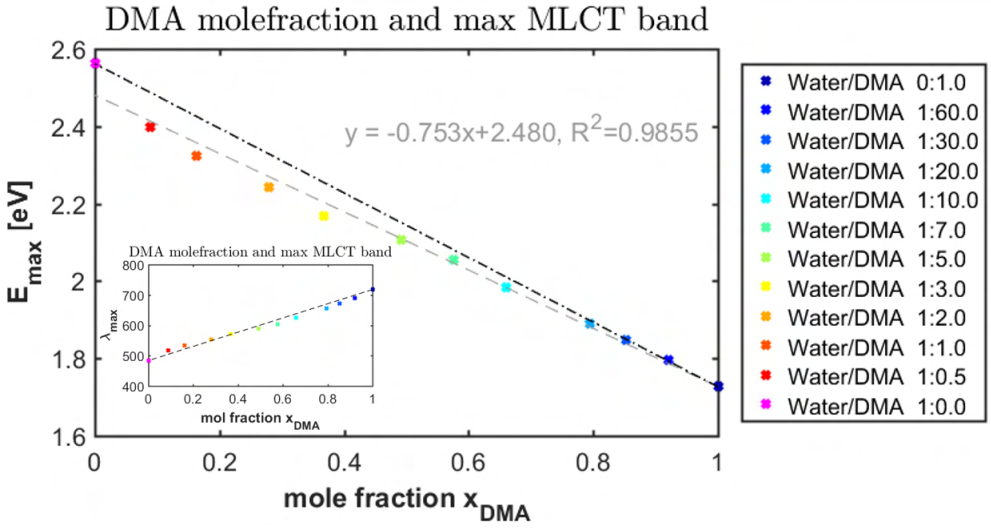

Figure 6.6: Shift in absorption maximum of $[Fe(bpy)(CN)_4]^{2-}$ in solvent mixtures. Absorption maximum in energy as a function of the DMA mole fraction in the solvent mixture. The inset shows the same in units of nm. A linear regression shows a small deviance from a linear trend (gray). A simple straight line (black) between the first data point (pure water) and the last (pure DMA), indicates the expected behavior of a linear trend without preferential solvation.

They conclude, somewhat speculatively, that high concentrations of water results in the formation of water clusters in the bulk solvent, allowing the acetone/acetonitrile molecules to enter the nearest solvent shell rather than the water molecules.

The shift in absorption maximum simply shows the shift in energy gap between the ground state and photo-active excited state, (most likely the MLCT state). Thus, in order to further investigate the excited energetic landscape, and relaxation pathways, we conducted optical transient absorption measurements for the complex in the various solvent mixtures. However, the analysis of these spectra is still ongoing.

Understanding the solute-solvent interaction in greater detail requires information on the solvent structure on the molecular level. Hence, the next step in the investigation of the solvent effects, involved excited state dynamics simulations of the $[Fe(bpy)(CN)_4]^{2-}$ system in water.

6.3 SHARC simulations

The main analysis and results related to the solvated $[Fe(bpy)(CN)_4]^{2-}$ system presented in this thesis concerns the computational study of the excited state dynamics. This chapter presents the main focus of the analysis and results. The goal of the computational study was to investigate the solute-solvent interactions during the excited state dynamics, and in particular the solvent response to the excitation and electronic transitions on ultrafast time scales. Furthermore, the goal was to investigate differences between solvation in water and a non-hydrogen bonding weak Lewis acid, such as acetonitrile, dimethylacetamide or dimethyl sulfoxide, that shows very different experimental results.

First, section 6.3.1 presents the crucial work of preparation of the initial conditions for the dynamics simulations. Next, the analysis and results of the calculated absorption spectrum are described in section 6.3.2. Furthermore, section 6.3.3 discuss the analysis of individual trajectories as opposed to analysis of the ensemble. Subsequently, section 6.3.4 and 6.3.5 present results on the electronic populations, charge transfer character, and associated kinetics. Section 6.3.6 presents the results on the solvent response in terms of radial distribution functions, which are used to calculate expected time-dependent X-ray scattering signals, as described in section 6.3.7.

6.3.1 Generation of initial conditions

Since, the idea behind surface hopping is based on a classical description where several independent trajectories together describe the wave packet dynamics, it is necessary to prepare several independent trajectories to use for the excited state simulations. The excited state dynamics depends on the initial geometry and velocity of both the solute and solvent, so we must have a good sampling procedure with many different and independent coordinates in order to obtain reliable results on the excited state dynamics.

The simulations should include the solvent, since the steady state absorption spectra from section 6.2, showed that the absorption highly depends on the solvent nature and composition. In addition, previous simulations of the complex [206, 51] in vacuum, implicit and few explicit solvent showed that the calculated absorption spectrum and optimized state energies changed significantly upon including few explicit water molecules.

Another goal of the study was also to compute the X-ray difference scattering signals, in terms of both the solute and solvent, from the radial distribution functions, as described in Chapter 2, section 2.6. Therefore, the excited state dynamics simulation were carried out with explicit solvation. This section presents the initial conditions generation employed for the simulations.

One way to include the solvent in the sampling procedure is to use Molecular Dynamics (MD) simulations. In 2018, Mai and coworkers [207] presented a new protocol for sampling of both the solute and solvent geometries using MD simulations in the generation of initial conditions for SHARC dynamics simulations. The quality assurance of the chosen computational details was mainly done by Sebastian Mai, since he co-developed the methods, and this field of method was very new to me at the time. The following paragraphs give a summary of the procedure. Figure 6.7 illustrates the steps of the procedure for the initial conditions generation leading up to the excited state dynamics simulations.

1. Force field - thermalization and equilibration: The first step was carried out using all classical MD simulations with AMBER17 [208]. The force field of the metal complex was calculated using the python-based Metal Center Parameter Builder, MCPB.py [209]. The method involves derivations of atomic partial charges for $[Fe(bpy)(CN)_4]^{2-}$ from RESP [172] fits to the electron density, obtained from QM computations, using the Gaussian G09 software [208]. The level of theory was the D3-B3LYP/LAN2DZ [210, 211, 212], but with the exact exchange adjusted to 15 % as for the B3LYP* [180, 181] functional. Additionally, the distributions of bond lengths and angles of the metal complex were compared to a few-ps QM/MM MD simulation, and the force field was updated until similar distributions were achieved. The iron-complex was solvated in a truncated octahedron box with an edge length of ~ 24 Å, and shortest diameter of ~ 60 Å containing 5412 flexible type SPC/Fw[113] water molecules, plus two sodium ions for neutralization. The initial simulations involved a minimization run, thermalization to 300 K for 20 ps, in the NVT ensemble followed by an equilibration run for 500 ps at 1 bar, in the NPT ensemble. The equilibration ran with periodic boundary conditions.

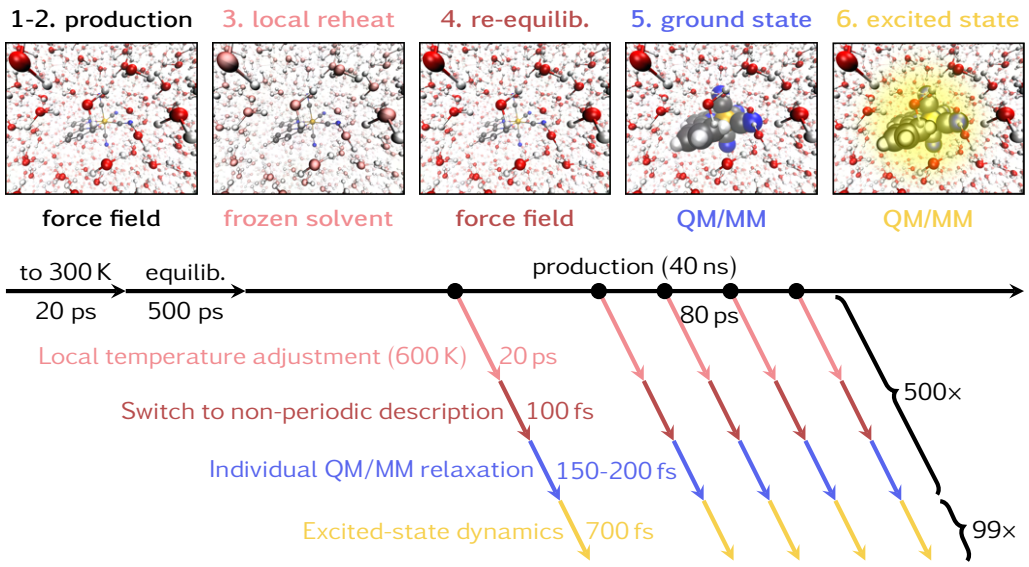

Figure 6.7: Overview of the MD sampling procedure and dynamics simulations. 1-2) classical force field MD simulations were carried out for a thermalization to 300 K, an equilibration run for 500 ps and a production run of 40 ns. 3) 500 individual snapshots were selected (black filled circles), and a local re-heating of the solute to 600 K (pink arrows), was applied. 4) short re-equilibration (dark red arrows) of each snapshot. 5) switch to a QM/MM description and short relaxation simulations for 150-200 fs (blue arrows) was run. 6) 99 of the 500 snapshots were selected for excitation, and ran 700 fs in the excited state (yellow arrows). Adapted figure from [213].

2. Force field - production: Following equilibration, a production run of 40 ns (NPT ensemble) was initiated, also with periodic boundary conditions. From the long production run, 500 independent snapshots were selected for every 80 ps, collecting the geometries and velocities. The 80 ps time span was chosen to ensure that the individual frames were uncorrelated. The following simulations continued as 500 individual simulations, using each snapshot as the initial frame.

3. Frozen solvent - local reheating: The next step included a local reheating of the solute Fe-complex in each of the 500 snapshots, as described in greater detail in [207]. The argument is that classical MD simulations at T =300 K leads to too low internal energy of a solute like $[Fe(bpy)(CN)_4]^{2-}$ compared to the QM zero-point energy, since classical

methods do not provide a good description of the partitioning of the internal energy among the degrees of freedom as discussed in [214, 215, 214, 216]. As a method to adjust for this low internal energy of the solute complex, a local reheating was carried out of the Fe-complex in frozen solvent. The solute was reheated by setting the thermostat to 600 K in an NVT ensemble and the re-thermalization ran for 20 ps with all water molecules constrained. The process is indicated in Figure 6.7 by the bright red/pink colors.

4. Force field - short re-equilibration: Before moving on to the SHARC simulations, we carried out a short (100 fs) re-equilibration run to allow the solvent molecules to reorganize around the heated solute. The short re-equilibration ran in the NVE ensemble with no periodic boundary conditions, since the SHARC simulations in the next step will run without periodic boundary conditions. The re-equilibration is illustrated by the dark red colors in Figure 6.7.

5. QM/MM - Ground state dynamics The end points from the short re-equilibration constituted the initial conditions for the SHARC ground state simulations. We ran short (150-200 fs) QM/MM SHARC trajetories in electronic the ground state (GS), in order to compensate for any effects arising from the change from the pure classical force field parameters to the QM/MM description. The length of the GS simulations were randomized between 150-200 fs for the 500 different trajectories in order to avoid any coherent motion arising from the switch from classical force fields to QM/MM methods. This step allows fast degrees of freedom like bond lengths and angles to relax towards the QM/MM equilibrium conditions. The GS dynamics simulations are indicated by the blue colors in Figure 6.7. The end points of these simulations were used as the initial conditions for the SHARC excited state simulations.

6. QM/MM - Excited state dynamics Before launching the excited state dynamics simulations, determination of the initial active state and electronic wave function coefficients are also required, in addition to the initial geometries and velocities. Therefore, the absorption spectrum was calculated from the end points of the GS trajectories, by calculation of vertical excitation energies from the individual geometries (using TD-DFT).

The spectrum was prepared by calculation of the lowest 20 singlet and 20 triplet excited states for each geometry. Excitation at ~525 nm resulted in ~100 geometries being excited into the S_3 state, as described in greater detail in section 6.3.2. The exact number of geometries depended on the width of the excitation window.

The resulting ~100 geometries that populated the S_3 excited state formed the initial conditions for the excited state SHARC simulations. The excited state simulations ran for 700 fs, with a nuclear time step of 0.5 fs, and this part of the process is indicated by the yellow colors in Figure 6.7.

In the excited state simulations we included 6 singlet states ($S_0 - S_5$) and 7 triplet states ($T_1 - T_7$), giving a total of 27 states ($6+3\cdot7$). The propagation of the electronic wave function was carried out in 0.02 fs time steps using the local diabatization algorithm [217]. The wave function overlaps were computed using the WFoverlap software [218]. Following a given surface hop, the velocities of the nuclei in the $[Fe(bpy)(CN)_4]^{2-}$ complex were re-scaled as part of the necessary kinetic energy adjustment after a hop. This re-scaling is necessary since a new active state likely will have a different potential energy than the former, and the total energy of the system should be conserved. In addition, an energy-based decoherence correction [219] adjusts for the dispute that the total electronic population of all states follow the gradient of the current active state, in contrast to the population of each state following the gradient of the given state.

Electronic structure calculations

The electronic structure calculations involved in the QM/MM dynamics, vertical excitation energies, and the excited state dynamics simulations employed the same electronic structure level of theory. The calculations were carried out using the ORCA 4.1.0 [220] software. The intention was to carry out the simulations using the B3LYP* [180, 181] functional, which previously has shown good results for the geometries and vertical excitation energies of other iron-based complexes [180, 221, 222]. The B3LYP* functional is a slightly modified version of the B3LYP [211, 223, 224] functional, with a reduction of the amount of exact exchange from 20 % in B3LYP to 15 % in B3LYP*. However, a "manual" adjustment of the functional in ORCA, led to an error, since the B3LYP* functional also carries LDA/GGA exchange, which was in error modified to 85 %, and should remain at 72 %, as for the B3LYP functional. The error was found after

the simulations finished, and the decision to continue the analysis was made, since the influence of the error likely is small. The good agreement between calculated and experimental absorption spectrum indicates that the results of the simulations are reliable. The calculations also included the DFT-D3 dispersion [210] and scaler relativistic effects via the ZORA [225, 226] formalism, as implemented in ORCA, and the excited states were computed within the Tamm-Dancoff approximation (TDA), as described in Part II, section 3.3. As a compromise between accuracy and efficiency, we employed a mixed- basis set combination with def2-TZVP [227] for the Fe atom, and def2-SVP for the remaining atoms of the metal complex. For the QM/MM simulations, the QM region described the $[Fe(bpy)(CN)_4]^{2-}$ complex and the MM region covered the water molecules and the sodium ions, and was carried out employing electrostatic embedding.

6.3.2 Absorption spectrum

Before launching the excited state dynamics simulations, the absorption spectrum was computed from the end points of the ground state SHARC dynamics simulations. This section describes how the spectrum was calculated, and used to determine the relevant number of excited states to include in the simulations. The section also presents an analysis of the charge transfer character of the bands in the spectrum, and describes the chosen excitation range for the dynamics simulations.

The spectrum is calculated from n_g =478 independent geometries, (since 22 trajectories did not finish). From each of these geometries g, we calculated vertical excitation energies E_{gi} and oscillator strengths f_{gi}, for the n_{state} =20 lowest singlet and triplet states, using TD-DFT. Each of the excitation peaks were convolved with Gaussians of full width at half maximum (FWHM) of 0.10 eV, as chosen for the complex, $[Re(CO)_3(im)(phen)]^+$ (im=imidazole, phen=1,10-phenanthroline) using a similar sampling procedure with explicit solvent [213]. The total absorption spectrum A was calculated as a sum of the Gaussians, according to the expression:

$$A(E) = \sum_{g=1}^{n_g} \sum_{i=S_0}^{n_{state}} f_{gi} \cdot e^{\left(-4\ln 2 \frac{\left(E-E_{gi}\right)^2}{\mathrm{FWHM}^2}\right)} \tag{6.1}$$

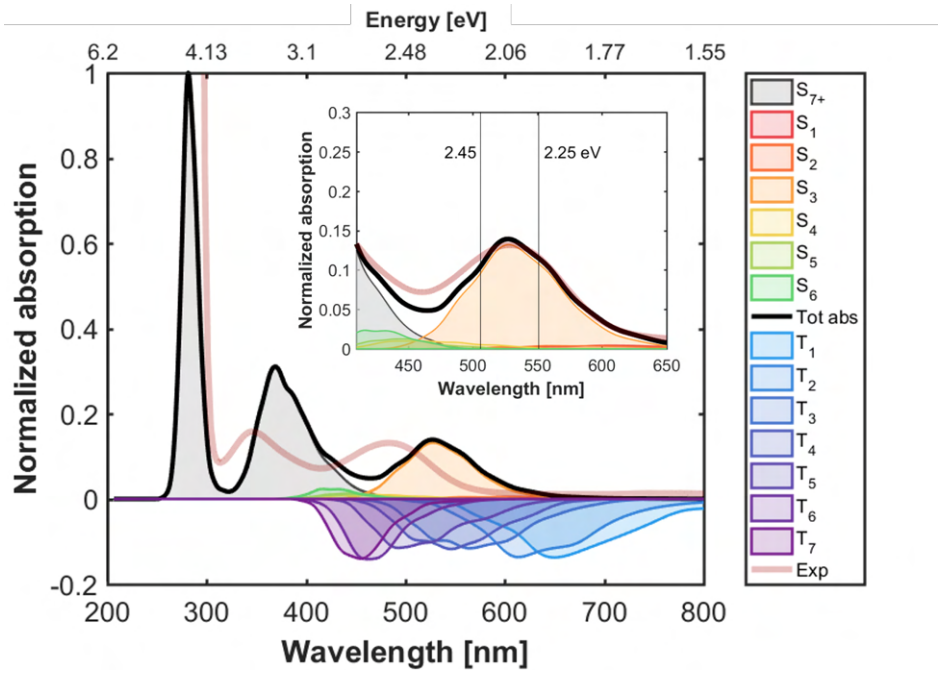

Figure 6.8: Absorption spectrum of $[Fe(bpy)(CN)_4]^{2-}$ in water, computed from 478 independent trajectories, generated from the sampling procedure. The total absorption spectrum (black) is the sum of the contributions from the singlet states (S_0-S_{19}, red, green, gray colors). An experimental spectrum is shown in pink. The inset shows that shifting the spectrum by 46 nm gives excellent agreement between experiment and theory. The negative region, below the absorption spectrum (shades of blue/purple), illustrates the density of the triplet states (T_1-T_7). The chosen excitation range is indicated in the inset by the vertical black lines.

Figure 6.8 shows the computed normalized absorption spectrum (black, thick line), along with an experimentally obtained spectrum (pink) of $[Fe(bpy)(CN)_4]^{2-}$ in water. The result shows a slight shift of ~ 45 nm (0.2 eV) towards lower energies for the computed spectrum relative to the experimental one (inset shows shift). The shape of the spectrum in three separated bands is in very good agreement with experiment. Each of the contributions from the states shows that primarily the S_3 state (orange) dominates the lowest energy absorption band, and states higher than S_5 contributes to the second or third band.

Based on the (limited) existing literature on other similar excited state dynamics simulations of transition metal complexes, it is rather unique that only a single excited state is the main contributor to the lowest energy absorption band. For example, surface hopping simulations [228] on the $[Fe(tpy)(pyz\text{-}NHC)]^{2+}$, (tpy=2,2':6',2"-terpyridine; (pyz-NHC=1,1-bis(2,6-diisopropylphenyl)pyrazinyldiimidazolium-2,2'-diylidene), iron carbene system present an absorption spectrum in which the lowest energy band shows contributions from five states, S_4–S_9. Likewise, for the complex $[Ru(bpy)_3]^{2+}$, a SHARC dynamics study [154] reports initial excitation into 9 different excited states (S_6–S_{14}), within the chosen energy range of the first band of the absorption spectrum. Another SHARC dynamics study of the $[Re(CO)_3(im)(phen)]^+$ complex in explicit solvent [213] reports similar contributions of states $S_1 - S_5$ of the lowest energy band of the spectrum, and thus initial excitation into all five excited states.

Despite the S_3 state being the most bright state in this band, the remaining states might still play an important role in the deactivation mechanism of the excited state dynamics. In our case, we are mainly interested in the energy region of the first band of the spectrum, since the experiments were excited at 500 nm. Therefore, we chose to only include the 6 lowest singlet states ($S_0 - S_5$) and 7 triplets ($T_1 - T_7$) out of the 20 calculated, for the excited state dynamics simulations.

Figure 6.8 also illustrates the density of states (DOS, ignoring oscillator strength), of the chosen triplets $T_1 - T_7$, in the negative region below the absorption spectrum.

Electronic character of the excited states

The absorption spectrum in Figure 6.8 shows that excitation within the lowest energy band mainly leads to population of the S_3 excited state. The TheoDORE analysis tools, described in Part II, section 4.2, gives information on the electronic character of the excited states. Figure 6.9 presents the absorption spectrum (positive spectrum) in terms of the amount of charge transfer character of the excited states.

The left plot decomposes the spectrum into contributions of MC character, and the right plot contributions of MLCT character. From this decomposition, we observe that the bright states of the first absorption band almost exclusively shows less than 10 % MC character (dark red), and predominantly 80-90 % MLCT character (bright blue).

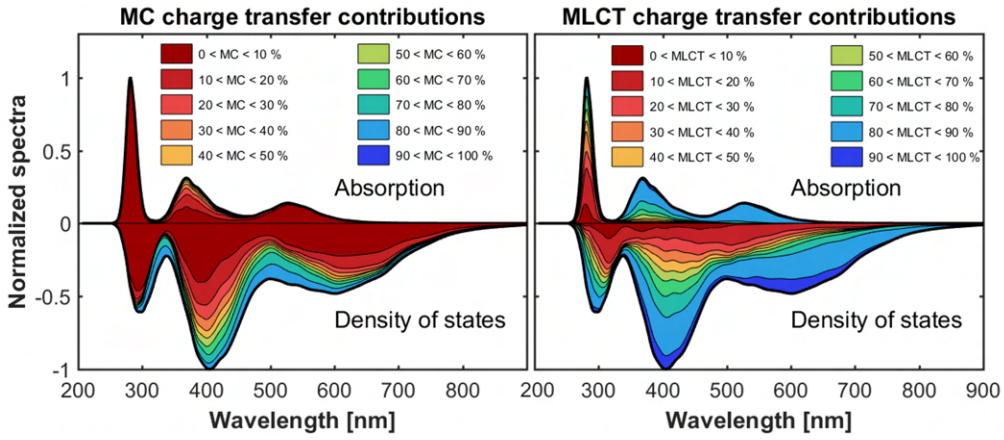

Figure 6.9: Simulated absorption spectrum and density of states (negative plots) decomposed into different charge transfer character and contribution. The left side, decomposes the spectra into different contributions of MC character, and the right side, decomposes into contributions of MLCT character.

In general, the MLCT states are much brighter than the MC states, especially at lower energies. The MC character predominantly contributes less than 20 or even less than 10 % throughout most of the bright states in the absorption spectrum. Thus, absorption at 2.35±0.10 eV (506-551 nm) leads to population of excited states with predominantly MLCT character. Excitation within the second band (around 3.4 eV / 365 nm) leads to population of excited states with less MLCT character, and more of a mixed character.

The excited states of transition metal complexes are often very close in energy, and thus there might be several dark excited states available with a different charge transfer character. Hence, analysis of the density of states (DOS) is useful, since the spectrum ignores oscillator strengths, and includes both the singlet and triplet states. Thus, the DOS spectrum gives information on whether any dark states of other charge transfer character exists. Figure 6.9 also presents the calculated DOS spectra in the negative regions decomposed into MC and MLCT character, respectively.

The DOS in the right plot of Figure 6.9, shows that the first band involves states with predominantly 80-100 % MLCT character, from the blue colors in the figure. However, also dark states of less than 20 % MLCT character exists (red colors). The second and third band also show contri-

butions with a lower MLCT character and thus consists of states of a more mixed type charge transfer character (both red and blue colors present). Similarly, from the DOS to the left, we observe that the lowest energy states show very low MC character, mainly states of less than 10 % MC character (dark red). However, also a small contribution of states with 70-90 % MC character is observable (light blue colors), hence at low energies, a few dark MC states exists. At higher energies, in the second band, the states show a larger degree of mixed MLCT/MC character. The third band shows predominantly neither MLCT or MC character (red colors) and thus involves other types of charge transfer character e.g. ligand centered (LC).

Our results showing that excited states within the lowest energy band predominantly show MLCT charge transfer character is in good agreement with TA experiments stating that the initially populated excited states are MLCT states [51].

In conclusion, the excited states within the first band (~525 nm) of the absorption spectrum shows predominantly MLCT character, and the MC states are not particularly photoactive. In general, the excited states of lower energies show predominantly MLCT character, whereas the excited states at higher energies show a more mixed MC/MLCT character, or other types of charge transfer character. Thus, the excited state dynamics might show very different results depending on the choice of excitation wavelength either within the first (~525 nm) or second band (~400 nm), as also discussed by Chábera et al. [36].

Excitation window

The excitation window was chosen from the maximum of the first band. In the TA and XFEL experiments we excited at 500 nm (2.48 eV) with a FWHM of about 50 fs. Since, the calculated spectrum shows very similar features as the experimental spectrum except for a slight shift, we expect a similar distribution of the excited states, and hopefully similar excited state dynamics, but with a slight shift in energy. We therefore, chose to excite at the calculated maximum of the first band, thus excitation at 2.35±0.10 eV corresponding to an excitation window of 506-551 nm. The chosen excitation window is indicated by the vertical black lines in the absorption spectrum, in the inset of Figure 6.8. Assuming a Gaussian shaped

pulse that is bandwidth limited, the excitation window of ±0.10 eV corresponds to a pulse width of about 18 fs. The energy broadening was necessary in order for a sufficient number of trajectories to be excited within the chosen range. On the other hand, an excitation pulse of about 50 fs, from the experiments, corresponds to an energy bandwidth of about ±0.04 eV, calculated using the time-bandwidth product of 1.82 fs·eV. Hence, the energy range used for excitation in the simulations are slightly broader than in the experiments. The composition of the excited states within the broader range show similar contributions, thus we expect the slightly broader range to be insignificant.

Excitation at 2.35±0.10 eV resulted in 116 out of 478 geometries were excited into the S_3 excited state. These 116 trajectories formed the initial conditions for the excited state simulations. Unfortunately, due to technical problems, 17 of these trajectories crashed and did not make it to the end of the 700 fs simulation time. In the end, 99 of 116 trajectories finished the excited state dynamics simulations.

Whether a given geometry, g is selected for excitation within the given range or not, is based on the excitation energies E_{gi}, and oscillator strengths f_{gi} for each excited state i. For all excited states of all geometries, the maximum value $p_{\max}$ is found of the expression:

$$p_{g,i} = \frac{f_{gi}}{E_{gi}^2} \tag{6.2}$$

Next, for each excited state, a random number $0 < r_{gi} < 1$ is determined. An excited state is selected as a valid initial condition, if the random number is less than:

$$r_{g,i} < \frac{p_{g,i}}{p_{\max}}$$

It is also possible to restrict the selection by imposing a constraint on the transition energy, such that one chooses an excitation energy E_{exc}, and a tolerance ΔE and then only states and geometries with excitation energies within the interval $E_{\text{exc}} \pm \Delta E$ are considered. The excited state selection procedure is based on the algorithm employed in the Newton-X trajectory surface hopping software [229, 230].

A quick summary of the number of trajectories in each step:

- Initial MD sampling → results in 500 individual trajectories.
- QM/MM SHARC ground state individual relaxation → results in 478 finished trajectories (22 crashed). Simulation length random between 150-200 fs.
- Excitation at 2.35±0.10 eV (~527 nm) → results in 116 geometries (out of 478) being excited into the S_3 state.
- QM/MM SHARC excited state dynamics → results in 99 (of 116) trajectories which completed the 700 fs simulation time.

Thus, by the end of the simulations, we obtained 99 independent excited state dynamics simulations, where each starting geometry might have taken different relaxation pathways. Therefore, we have a choice to analyze each simulation independently or analyze the ensemble of trajectories. The next section presents an example of a single trajectory, and later sections use the ensemble.

6.3.3 Single trajectories

From the successful excited state dynamics simulations, we have 99 independent trajectories, which each followed their own pathway throughout the simulations. This provides us the opportunity to study each of the pathways individually, or together as an ensemble. This section describes an example trajectory.

A single trajectory, holds information on one example of the excited state dynamics and the energetic landscape, changes in the specific geometry, the specific populated states, and hopping probabilities. An example of the energetic landscape of a single trajectory, from `TRAJ_00029`, is shown in Figure 6.10. The figure shows the potential energy surfaces, with colors according to spin (top part) or to MC charge transfer character (bottom part), against the simulated time. As discussed in part II, section 3.5.3, the MCH representation separates the states into singlets and triplets, and thus the states do not change spin throughout the simulated time in the plot. The energy surfaces are shown relative to the ground

state S_0, for clarity of presentation, since the states lie very close in energy. The red curves are the triplet states $T_1 - T_7$, and the blue curves are the singlet states $S_0 - S_5$. The black dots show the current active state.

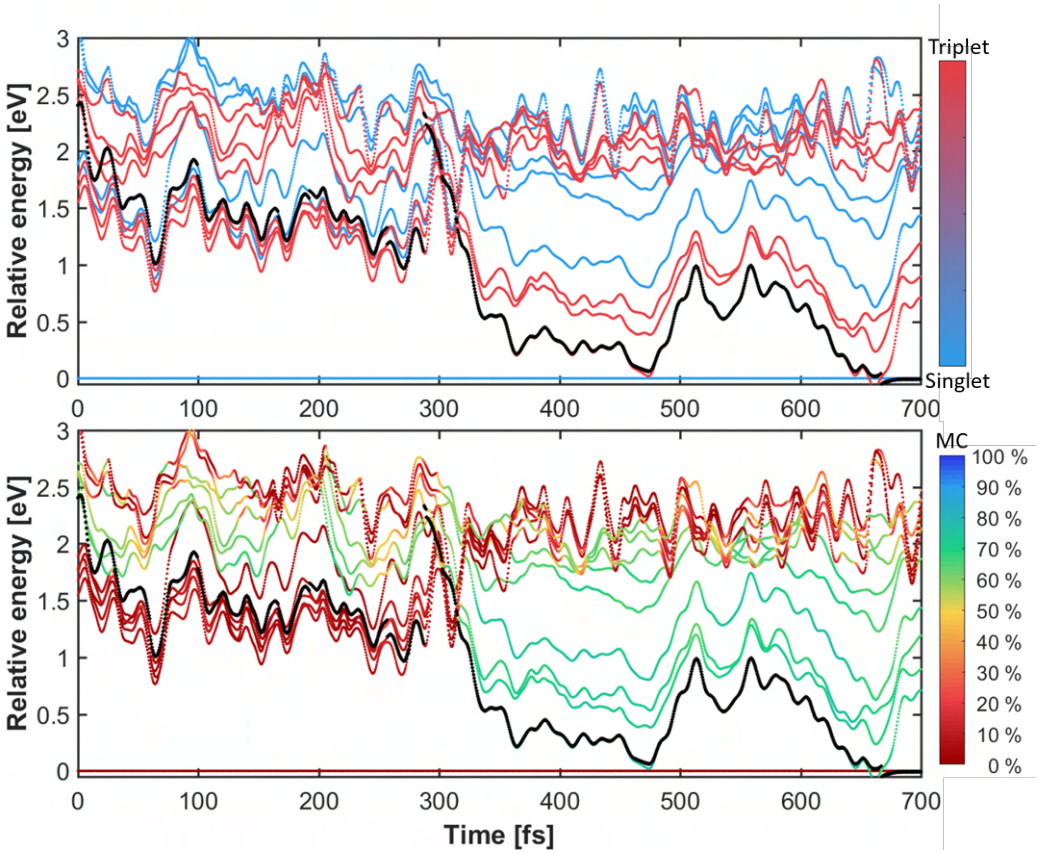

Figure 6.10: Example trajectory from the excited state dynamics simulations (traj 00029). The energy levels are shown relative to the ground state. The color coding shows the singlet/triplet character of each state, in the top plot, and the percentage MC character for each state and time, in the lower plot. The black dots shows the current active state.

The plots show a clear separation, at early times, between the ground state and the band of excited states in the range of 1.5-3.0 eV, relative to the ground state. Later, at ∼300 fs, the excited state band separates, where the energy separation of especially the lower triplet states $T_1 - T_3$ decrease to below 1 eV, relative to the ground state. The stabilization of the energy indicates that the electronic charge transfer character changes, e.g. from predominantly MLCT to MC character. Evidently, from the lower plot, just after the band separation, the lowest excited states change from below ∼10 % MC (dark red) to above ∼60 % MC (green) charge transfer character. Other states remain in the same energy region or even increase relative to the ground state.

Additionally, the plots show the current active state as black circles. The intersystem crossing (ISC) occurs at ∼250 fs from the S_1 to the T_2 state, and transfer to a state of more than 60% MC charge transfer character occurs around ∼300 fs. Around ∼470 fs there was a high possibility to cross to the ground state since the surfaces briefly overlap, but the system remained on the excited state surface.

The oscillating behavior of some states is an interesting feature, that we did not examine the origin of. It could be related to solvent effects that particularly impact e.g. MLCT states. The oscillations are not as evident for the lowest excited states after the band separation, but remains for some of the destabilized states. To examine this, we could analyze the charge transfer character in greater detail, and investigate any correlations.

Each individual trajectory might show very different results, and therefore, it is difficult to assign general trends based on the results of a few individual trajectories. Besides, experimentally we do not (yet) observe the dynamics of a single molecule. Hence, an analysis of the ensemble of trajectories is advantageous and more reliable for the understanding of the overall trends. The following sections involves ensemble analysis.

6.3.4 Electronic population analysis and results

A key interest in the study of excited state dynamics is the location of the excited electron, and thus the electronic populations in each state. One of the great advantages of using simulations, is that we can track the excited electron configuration at all times. The following sections present the analysis and results of the electronic populations for the ensemble.

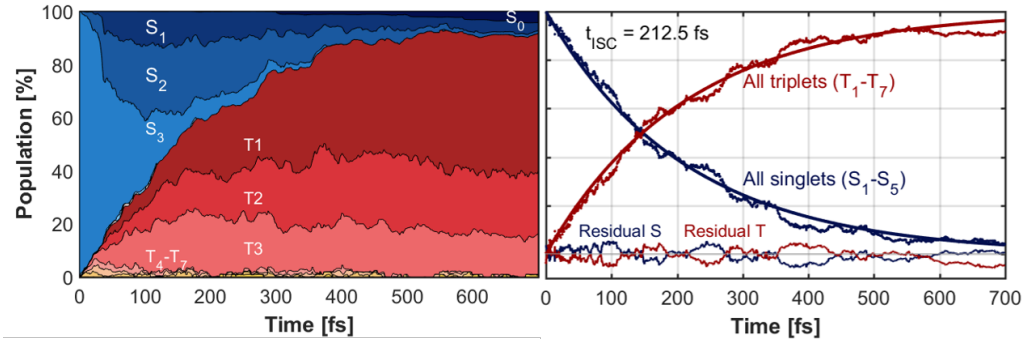

Figure 6.11: Time dependent electronic populations from the dynamics simulations. The left plot shows the MCH electronic populations in a stacked area plot. The right plot shows the total singlet (in blue) and triplet (in red) populations, along with a mono-exponential kinetic fit, and the residuals between data and fit below.

The method for analysis of the MCH electronic populations was described in Chapter 4. Figure 6.12 presents the MCH populations in a stacked area plot in the left panel, and the total singlet and triplet populations summed, shown in the right panel.

In the stacked area plot, each colored area shows the contribution to the total population, with blue colors for the singlets and red for the triplets. Directly upon excitation and at early times, all trajectories populate the S_3 state, which decreases to less than 30 % within the first 100 fs, followed by an increase in population of mainly the lower singlets S_2, S_1 to about 40 % and the triplets T_1, T_2, T_3 to about 35 % in total. More than 50 % of the population is in a triplet state within ~150 fs. By the end of the simulated 700 fs time-frame, most of the population resides in the T_1 state (~55 %), but also with contributions from the T_2 (~25 %) and T_3 (~15%) states. The higher lying singlets S_4, S_5 and triplets T_4, T_5, T_6, T_7 do not play a dominant role throughout the simulations. The observations indicate that the system follows a relaxation pathway with internal conversion (IC) $S_3 \rightarrow S_2 \rightarrow S_1$ on similar time scales as ISC to the triplet states.

The panel to the right in Figure 6.11 shows the summed populations for all singlets (blue) and all triplets (red), as well as the results of a mono-exponential kinetic model fit. In addition, the residual between data and fit are shown oscillating around zero. The time of the ISC from the kinetic fit was found to be 0.21±0.02 ps.

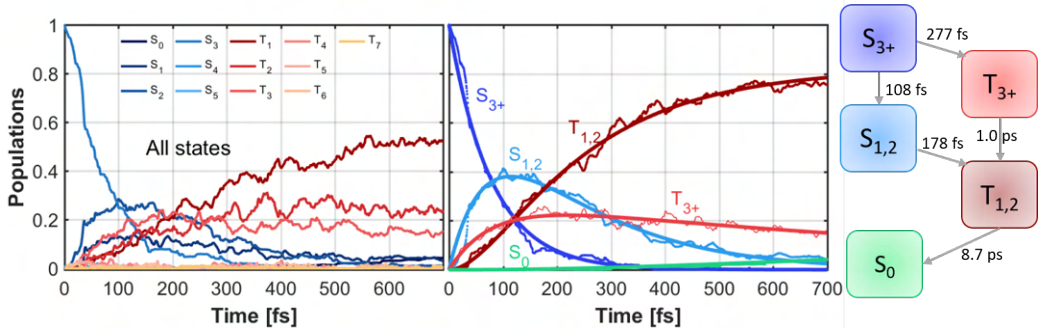

Figure 6.12: Left: Time dependent electronic populations of all states. Right: populations and kinetic model from summed singlet states $S_5, S_4, S_3 \Rightarrow S_{3+}$, and $S_1, S_2 \Rightarrow S_{1,2}$ and triplet states according to $T_1, T_2 \Rightarrow T_{1,2}$ and $T_3, T_4, T_5, T_6, T_7 \Rightarrow T_{3+}$. The right plot also shows the results from fitted kinetics according to the model next to the plot in a schematic way.

Analysis of the underlying electron transfer trends are difficult due to the high number of states that are all close energetically. Building a kinetic model using all six singlets and seven triplets, is unwieldy. Instead, we sum several states and build a simpler model. We combined the singlets into $S_5, S_4, S_3 \Rightarrow S_{3+}$, and $S_1, S_2 \Rightarrow S_{1,2}$, and the triplets according to $T_1, T_2 \Rightarrow T_{1,2}$ and $T_3, T_4, T_5, T_6, T_7 \Rightarrow T_{3+}$. Figure 6.12 shows the result after summation of the selected states, along with the results of a kinetic global fit, and a schematic to the right with the time constants. Based on the kinetic fits, the IC from $S_{3+} \rightarrow S_{1,2}$ decays with a time constant 0.11±0.01 ps, whereas for the triplets $T_{3+} \rightarrow T_{1,2}$ it is much slower, 1.0±114 ps. The very large uncertainty shows the instability of the fit, likely from lack of statistics due to the long lifetime. Likewise, the decay constant to the ground state, $T_{1,2} \rightarrow S_0$ shows a very large uncertainty, $\tau_{GS} = 8.7 \pm 101$ ps. The ISC from both higher $S_{3+} \rightarrow T_{3+}$ and lower states $S_{1,2} \rightarrow T_{1,2}$ occurs on timescales of 0.28±0.047 ps and 0.178±0.012 ps, respectively. However, this was just one model, and another model might give other results, depending on which states are summed.

The observation that IC and ISC occur on similar time scales or that ISC is even faster than IC is already reported for other transition metal complexes. Recent surface hopping simulations of an iron-carbene system, $[Fe(tpy)(pyz\text{-}NHC)]^{2+}$ [228] report an ISC time constant of 55±5 fs and IC of 276±64 fs (from high lying singlets S_N to S_0). The time constant reported for high lying singlets S_N to S_1 was 173±21 fs.

The ISC of $[Fe(bpy)_3]^{2+}$, was reported to be extremely fast (20 ± 5 fs) [38] based on fluorescence up-conversion with femtosecond broad-band transient absorption measurements. Also, for more heavy atom systems such as $[Ru(bpy)_3]^{2+}$ [154, 153] and the $[Re(CO)_3(im)(phen)]^{+}$ complex [213], studies report extremely fast ISC of only few fs. A computational study [154] on $[Ru(bpy)_3]^{2+}$ suggests that ISC is more of a "horizontal" process between high-lying singlets and triplets, followed by additional relaxation within the triplet states. Likewise, the studies on the rhenium complex, [213] suggest an unconventional ISC mechanism in which an ultrafast (~ 8 fs) equilibrium occurs between the singlets and triplets (25:75), which also occurs with frozen nuclear geometry, followed by a slower relaxation towards pure triplets assisted by nuclear motion.

The current case of $[Fe(bpy)(CN)_4]^{2-}$ appears to follow a more traditional relaxation pathway, in which IC in the singlet manifold is faster than ISC, however, the triplets are still populated relatively fast on ultrafast time scales.

Comparison to experiments

The results on the electronic populations presented here show that at least six ($S_1 - S_3$ and $T_1 - T_3$) excited states are involved in the relaxation pathway of the excited state dynamics. Thus, building a reliable kinetic model is difficult. Nonetheless, experimental results do not (yet) have the sensibility to distinguish the many singlet and triplet states in such great detail, which makes comparison to experiments challenging. However, time-resolved X-ray scattering experiments, often find a local heating of the solvent [41, 166], which is interpreted as a result of energy transfer from the solute to the nearest solvent, and hence related to IC and vibrational relaxation of the solute. Therefore, the estimated IC (0.11 ± 0.01 ps) within the singlets is expected to give rise to an almost immediate effect on the observed solvent heating from an X-ray scattering experiment that holds a time resolution of ≤ 100 fs.

Furthermore, experimental methods most often present the results in terms of e.g. MLCT and MC states. We note that the electronic populations presented here in the MCH representation give no information about the electronic charge transfer character. Therefore, the next step concerns the charge transfer analysis associated with the electronic transitions.

6.3.5 Charge transfer character analysis and results

The electronic population analysis, gives information about the spin, i.e. singlet or triplet, but not the charge transfer character e.g. MLCT or MC. Since the simulations are carried out within the adiabatic/MCH framework, as described in Part II, section 3.5.3, a given state might change charge transfer character within the simulated time. As a tool to investigate the charge transfer character at each time point, we employ the automated analysis software, TheoDORE [132, 133, 134]. The following sections present the charge transfer analysis and results from the simulations.

TheoDORE population analysis example

The TheoDORE program performs a population analysis of the one-electron transition density matrix (1TDM) of each excited state, as described Part II, section 4.2. Population analysis of the 1TDM gives a quantitative description of the electronic wave function character of each state and for each time step of the simulations.

The method involves division of the $[Fe(bpy)(CN)_4]^{2-}$ system into fragments, and analysis of the charge transfer changes between the fragments. In order to analyze a given charge transfer in detail, we chose each atom as a fragment, except for the H-atoms which we combined with the nearest C-atom as one fragment. The division results in 21 different fragments of the iron complex. With 21 fragments, we obtain one 21x21 matrix for each of the excited states (27), for each time step (1400), for each trajectory (99). An example of such a matrix for the S_1 state is shown in Figure 6.13.

The matrix is organized such that the top row describes the excited electron position, and first column is the electron hole position for the charge transfer. The values in the matrix are colored according to either high (green), medium (yellow) or low (red) contribution. The fragments are numbered and colored according to the illustration in Figure 6.14. As an example of how to read the matrix, the excitation from the ground state to the S_1 state, is characterized by a ∼8.6 % charge transfer from the iron center to a nitrogen atom located on the bipyridine ligand ($Fe \rightarrow N_{bpy}$). Observed from the mostly yellow and red colors, each of the matrix elements show rather small values showing that the charge transfer is spread over several fragments. To find the total charge transfer from e.g. the iron center to the bipyridine ligand, we can sum several fragments.

S1	Fe	C (eq)	N (eq)	C (ax)	N (ax)	C (ax)	N (ax)	C (eq)	N (eq)	Nbpy	CHbp	CHbp	CHbp	CHbp	Cbpy	Cbpy	CHbp	CHbp	CHbp	CHbp	Nbpy	Sum
Fe [21]	5,17	0,02	0,01	0,59	0,09	0,43	0,09	0,08	0,06	8,56	0,91	6,35	4,24	2,63	7,52	9,74	0,88	8,93	6,80	2,07	14,21	79,38
C (eq) [22]	0,04	0,00	0,00	0,01	0,00	0,00	0,00	0,00	0,00	0,07	0,01	0,05	0,03	0,02	0,06	0,08	0,01	0,08	0,06	0,02	0,12	0,66
N (eq) [23]	0,30	0,00	0,00	0,03	0,01	0,03	0,01	0,00	0,00	0,48	0,05	0,37	0,24	0,16	0,43	0,59	0,05	0,57	0,42	0,13	0,87	4,74
C (ax) [24]	0,04	0,00	0,00	0,01	0,00	0,00	0,00	0,00	0,00	0,07	0,01	0,05	0,03	0,02	0,06	0,08	0,01	0,07	0,05	0,01	0,11	0,62
N (ax) [25]	0,24	0,00	0,00	0,03	0,01	0,02	0,01	0,01	0,00	0,43	0,04	0,33	0,22	0,13	0,38	0,49	0,04	0,45	0,35	0,10	0,71	3,99
C (ax) [26]	0,05	0,00	0,00	0,01	0,00	0,00	0,00	0,00	0,00	0,08	0,01	0,06	0,04	0,02	0,07	0,09	0,01	0,08	0,06	0,02	0,13	0,73
N (ax) [27]	0,27	0,00	0,00	0,03	0,01	0,03	0,01	0,00	0,00	0,47	0,05	0,36	0,23	0,15	0,41	0,53	0,05	0,50	0,38	0,11	0,78	4,37
C (eq) [28]	0,01	0,00	0,00	0,00	0,00	0,00	0,00	0,00	0,00	0,02	0,00	0,01	0,01	0,01	0,01	0,02	0,00	0,01	0,01	0,00	0,03	0,14
N (eq) [29]	0,06	0,00	0,00	0,01	0,00	0,01	0,00	0,00	0,00	0,10	0,01	0,08	0,05	0,03	0,09	0,11	0,01	0,09	0,08	0,02	0,15	0,90
Nbpy [12]	0,01	0,00	0,00	0,00	0,00	0,00	0,00	0,00	0,00	0,02	0,00	0,02	0,01	0,01	0,02	0,03	0,00	0,03	0,02	0,01	0,04	0,22
CHbp [3,15]	0,04	0,00	0,00	0,00	0,00	0,00	0,00	0,00	0,00	0,05	0,01	0,04	0,03	0,02	0,05	0,06	0,00	0,07	0,04	0,02	0,10	0,53
CHbp [9,17]	0,01	0,00	0,00	0,00	0,00	0,00	0,00	0,00	0,00	0,02	0,00	0,01	0,01	0,01	0,02	0,03	0,00	0,02	0,02	0,00	0,03	0,18
CHbp [8,14]	0,04	0,00	0,00	0,01	0,00	0,00	0,00	0,00	0,00	0,05	0,01	0,04	0,02	0,03	0,05	0,08	0,01	0,09	0,06	0,02	0,13	0,64
CHbp [7,13]	0,01	0,00	0,00	0,00	0,00	0,00	0,00	0,00	0,00	0,01	0,00	0,01	0,01	0,00	0,01	0,01	0,00	0,01	0,01	0,00	0,01	0,09
Cbpy [4]	0,04	0,00	0,00	0,01	0,00	0,00	0,00	0,00	0,00	0,06	0,01	0,05	0,03	0,03	0,06	0,10	0,01	0,09	0,06	0,02	0,13	0,70
Cbpy [5]	0,04	0,00	0,00	0,01	0,00	0,00	0,00	0,00	0,00	0,09	0,01	0,08	0,05	0,03	0,10	0,08	0,01	0,05	0,07	0,01	0,10	0,73
CHbp [6,18]	0,01	0,00	0,00	0,00	0,00	0,00	0,00	0,00	0,00	0,01	0,00	0,01	0,00	0,00	0,01	0,01	0,00	0,01	0,01	0,00	0,01	0,08
CHbp[10,19]	0,04	0,00	0,00	0,00	0,00	0,00	0,00	0,00	0,00	0,08	0,01	0,07	0,05	0,03	0,08	0,07	0,01	0,04	0,05	0,01	0,09	0,63
CHbp [2 16]	0,00	0,00	0,00	0,00	0,00	0,00	0,00	0,00	0,00	0,01	0,00	0,01	0,01	0,00	0,01	0,01	0,00	0,00	0,01	0,00	0,01	0,07
CHbp [1,20]	0,03	0,00	0,00	0,00	0,00	0,00	0,00	0,00	0,00	0,05	0,01	0,04	0,03	0,01	0,04	0,05	0,00	0,05	0,04	0,01	0,07	0,43
Nbpy [11]	0,01	0,00	0,00	0,00	0,00	0,00	0,00	0,00	0,00	0,02	0,00	0,02	0,01	0,01	0,02	0,02	0,00	0,01	0,02	0,00	0,02	0,16
Sum	6,46	0,02	0,01	0,75	0,12	0,52	0,12	0,09	0,06	10,75	1,15	8,06	5,35	3,35	9,50	12,28	1,10	11,25	8,62	2,58	17,85	

Figure 6.13: Charge transfer character matrix from the quantitative TheoDORE analysis tools. Example of a 21x21 charge transfer matrix for the S_1 excited state for a given time step and trajectory. The top row shows each fragment and each row give the electron "hole" position. Likewise, the columns give the position of the excited "electron". Each matrix element gives the charge transfer contribution (in %) associated with the given fragments. The elements are colored according to a high contribution (in green), medium (in yellow) or low (in red). Numbering of the fragments are according to the illustration in Figure 6.14.

Figure 6.14 to the right, shows the reduced matrix after combining the fragments of the bipyridine ligand and of the cyanide ligands. The reduced matrix shows a total of ~73 % charge transfer from the Fe-center to the bipyridine, and only ~1 % to the CN ligands, for the given excitation example. The matrix also shows the given excitation corresponds to ~15 % charge transfer from the cyanides to the bipyridine. The charge transfer from Fe to Fe (~5 %) and CN to CN (~0.3 %) is very small. Based on these observations, we would characterize the given electronic transition as primarily an MLCT state since electron density is moving mainly from the metal center to the bipyridine ligand.

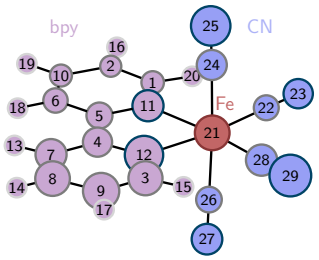

S1	Fe	CN	bpy	sum
Fe	5,2	1,4	72,8	79,4
CN	1,0	0,3	14,9	16,1
bpy	0,3	0,0	4,2	4,5
sum	6,5	1,7	91,8	100,0

Figure 6.14: LEFT: illustration of the assignment of atomic numbering and chosen fragmentation of $[Fe(bpy)(CN)_4]^{2-}$ for the charge transfer analysis. RIGHT: Example of a 3x3 charge transfer matrix, after summation of the matrix elements from fragments associated with bipyridine (bpy, light purple), the cyanides (CN, light blue) or the iron center (Fe, dark red). Each matrix element gives the charge transfer contribution (in %) associated with the given fragments, colored according to a high (green) or low (red) contribution.

Data reduction steps

The above observations are only from one excited state and a single trajectory, and therefore do not describe the general trends of the system. We compute a 21x21 matrix for each of the excited states included in the simulations, (6 singlets and 7 triplets), which gives a total of 27 states, for each of the 1400 time steps (700 fs), in each of the 99 independent trajectories. In total more than a billion matrix elements, which makes representation of the data tricky. Thus, we apply a few steps of data reduction:

1. The first step involves calculating the total charge transfer matrix from the total electronic wave function. Hence, we average over the number of states (27).

2. Next, we average across all trajectories (99) resulting in a single 21x21 matrix per time step.

3. Finally, we sum selected matrix elements into larger fragments (e.g. the 8 atoms of the cyanides into 1 fragment) and the type of transition.

In the following, the calculations from each step is elaborated. Calculation of the total charge transfer matrix from step 1 starts with a calculation of an average matrix, $\Omega_{AB}^{\text{traj}}(t)$ over all 27 states, which gives one 21x21 matrix for each time step t, in each trajectory.

We compute the total charge transfer matrix, $\Omega_{AB}^{\text{traj}}$, for the total electronic wave function, according to the expression:

$$\Omega_{AB}^{\text{traj}}(t) = \sum_{i=1}^{N_{\text{MCH}}} \left| \sum_{\alpha=1}^{N_{\text{diag}}} U_{i\alpha}(t)\, c_{\alpha}^{\text{diag}}(t) \right|^2 \Omega_{AB}^{\text{state}\,i}(t) \tag{6.3}$$

where i runs over the number of MCH states, N_{MCH}, and α runs over the number of diagonal states, (diag) such that, $\Omega_{AB}^{\text{state}\,i}(t)$ is an element of the charge transfer matrix for MCH state i. We can also compute the total charge transfer matrix separately over all MCH triplets or all MCH singlets by summation of the respective states, which we also did in the analysis.

Now, $\Omega_{AB}^{\text{traj}}(t)$ is an element in the charge transfer matrix describing charge transfer between the "hole" (element A) and the "electron" (element B) for a given time step t, for a given trajectory. However, this step only reduces the data amount from having a 21x21 matrix for 27 states, for 1400 time steps, for 99 trajectories, i.e. a 441x27x1400x99 problem to a 441x1400x99 problem. Hence, further data reduction is desired, and we compute an average over all trajectories:

$$\Omega_{AB}^{\text{tot}}(t) = \sum_{k=1}^{N_{\text{traj}}} \frac{\Omega_{AB}^{\text{traj}\,k}(t)}{N_{\text{traj}}} \tag{6.4}$$

which results in one 441x1400 data matrix. Finally, we combine several matrix elements, by defining which columns belongs to which fragments (Fe, CN or bpy), making each summation a 1x1400 vector. Examples of the summation of the matrix elements related to the Fe hole is:

$$\begin{aligned} \Omega_{\text{Fe-Fe}}(t) &= \sum_{A\in\text{Fe}} \sum_{B\in\text{Fe}} \Omega_{AB}^{\text{tot}}(t) \\ \Omega_{\text{Fe-CN}}(t) &= \sum_{A\in\text{Fe}} \sum_{B\in\text{CN}} \Omega_{AB}^{\text{tot}}(t) \\ \Omega_{\text{Fe-bpy}}(t) &= \sum_{A\in\text{Fe}} \sum_{B\in\text{bpy}} \Omega_{AB}^{\text{tot}}(t) \end{aligned} \tag{6.5}$$

where $\Omega_{\text{Fe-Fe}}(t)$, $\Omega_{\text{Fe-CN}}(t)$, $\Omega_{\text{Fe-bpy}}(t)$ are the charge transfer vectors for Fe to Fe, to cyanide or to bipyridine, respectively.

We can also choose to sum the matrix elements based on the type of electronic charge transfer transition (MLCT, MC, LMCT or LC):

$$\begin{aligned}
\Omega_{\mathrm{MLCT}}(t) &= \sum_{\substack{A\in \\ \mathrm{Fe,CN}}} \sum_{\substack{B\in \\ \mathrm{bpy}}} \Omega^{\mathrm{tot}}_{AB}(t) \\
\Omega_{\mathrm{MC}}(t) &= \sum_{\substack{A\in \\ \mathrm{Fe,CN}}} \sum_{\substack{B\in \\ \mathrm{Fe,CN}}} \Omega^{\mathrm{tot}}_{AB}(t) \\
\Omega_{\mathrm{LMCT}}(t) &= \sum_{\substack{A\in \\ \mathrm{bpy}}} \sum_{\substack{B\in \\ \mathrm{Fe,CN}}} \Omega^{\mathrm{tot}}_{AB}(t) \\
\Omega_{\mathrm{LC}}(t) &= \sum_{\substack{A\in \\ \mathrm{bpy}}} \sum_{\substack{B\in \\ \mathrm{bpy}}} \Omega^{\mathrm{tot}}_{AB}(t)
\end{aligned} \tag{6.6}$$

where $\Omega_{\mathrm{MLCT}}(t)$ is the charge transfer vector describing the charge transfer from the metal (Fe and each CN) to the ligand fragment (bpy), and so on.

Results on the total wave function character

With the different fragments of the metal complex defined as the Fe center, the cyanides, and the bipyridene ligand, we can analyze the charge transfer between the fragments. Figure 6.15 shows the charge transfer character of the electronic wave function averaged over all trajectories, as a function of the simulated time. The leftmost plot shows the total wave function character, the middle shows the character of only the singlet states, and the rightmost plot shows the contributions from the triplet states only.

The predominant contributions arise from charge transfer between the Fe→bpy (bright red), CN→bpy (yellow) and Fe→Fe (dark red) fragments. Considering only the singlet states, the main charge transfer character arise from the Fe→bpy (bright red) and CN→bpy (yellow) contributions. Assigning the fragments as given by Eq. (6.6), entails that the singlets show almost exclusively MLCT character throughout the simulations. In contrast, the triplet states show a more mixed character with contributions also from the Fe→Fe charge transfers, and thus a mixture of MC and MLCT character.

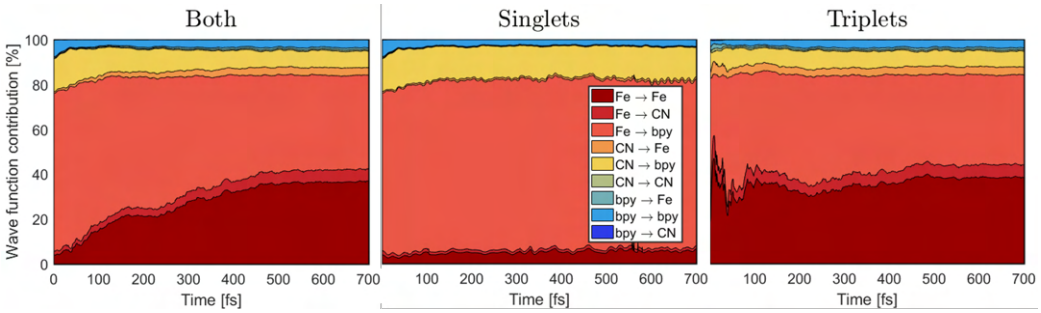

Figure 6.15: Contributions of charge transfer character to the electronic wave function, averaged over all trajectories. The plots show the contributions from the charge transfer between the different fragments (Fe, CN, bpy) to the total wave function (left), to the singlets only (middle), and to the triplets only (right). The contributions are re-normalized to 100 %.

Charge transfer involving the Fe center is expected to dominate, as excitation occurs from mainly Fe located orbitals and for MC related charge transfers, in general. Similarly, we expect the bipyridine to play an important role in the charge transfer related to MLCT states, for this complex.

In comparison to the previously mentioned study [228] of the iron carbene $[Fe(tpy)(pyz\text{-}NHC)]^{2+}$, the singlets also show at least 70 % MLCT character, whereas the triplets only show ∼50 % MLCT and also show ∼20 % MC character (depending on a different choice of dipole moment).

In the following, we analyze the individual fragments in greater detail.

Results from the individual fragments

While, the previous three plots in Figure 6.15 present an overview of the overall trends, additional information is gained by analysis of the individual fragments in terms of ”hole” and ”electron” dynamics. Where hole and electron refers to the extend of the excitation that originates from (the hole) and resides on (the electron) the atomic orbitals of the given fragments involved. From this division, we may analyze the hole and electron dynamics related to each of the fragments as shown in Figure 6.16.

In the figure, the left plot shows the hole and electron dynamics related to the Fe fragment. The total Fe hole dynamics contributes approximately 80% of the total charge transfer throughout the simulations, whereas the Fe electron is less than 5 % increasing to ∼ 40 % during the simulations.

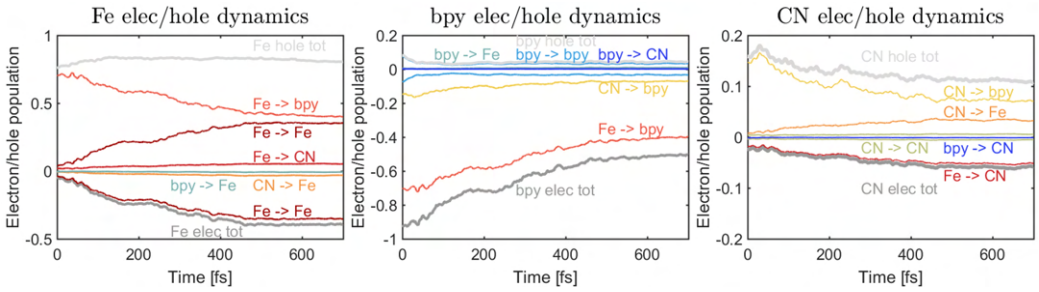

Figure 6.16: Charge transfer dynamics organized into the hole and electron populations, where hole/electron refers to how much of the charge transfer that originates from (the hole) and transfers to (the electron) the atomic orbitals associated with the respective fragment. Positive features show the hole dynamics from either the Fe, CN or bipyridine (bpy) fragments, and negative features show the electron dynamics. Note, the y-axes are different.

The charge transferred *from* the Fe fragment, mainly goes to the bpy fragment and local transitions on Fe. The charge transferred *to* the Fe fragment almost exclusively arise from local transitions on Fe (as in MC states). Interestingly, the temporal evolution of the dominant features of the Fe hole and electron dynamics show an oscillating behavior or 2-step process.

The plot in the middle, shows the hole and electron dynamics related to the bipyridine (bpy) fragment. The bpy hole dynamics only contributes less than ~8% throughout the simulations and within 100 fs it is less than ~5%. Thus, not much charge is transferred *from* the bpy fragment. However, the bpy total electron dynamics contribute more than 90%, at the earliest times, which decreases to ~50% within the 700 fs simulated time frame. Most (~70%) of the charge transfer arise from the Fe fragment, but also about 15% from the CN fragment.

Finally, the plot to the right shows the cyanide hole and electron dynamics. The total CN hole dynamics contribute less than 20% and the transferred charge goes primarily to the bpy fragment and at later time also to Fe. The charge transferred *to* the cyanides contributes less than 6% at all times, and thus the main contribution from the cyanides is the charge transfer to the bipyridine.

Interestingly, the CN fragments show similar trends as the Fe related charge transfers. The charge transfer to the bpy fragment is largest at early times, and the charge transfer to Fe increases with simulated time. Furthermore, the charge transfer of Fe→CN is almost non-existing, espe-

cially at early times. Hence,the cyanides contribute to the charge transfer to bipyridine for this complex, and an assignment of the CN fragments as part of the "metal" is appropriate.

The tendency that small ligands, such as CN or CO, contribute to the charge transfer was observed in the $[Re(CO)_3(im)(phen)]^+$ [213] and the $[Re(Cl)(CO)_3(bpy)]$ [134] complexes. The studies show similar trends with charge transfer both from the carbonyls and the Re center to the phenantroline/bipyrdine for the transitions assigned to show MLCT character.

Results based on the class of charge transfer transition

Based on the observed trends in the charge transfer between the different fragments, we analyze the charge transfer trends, in terms the textbook way of classifying the excited states for transition metal complexes. The traditional classes of excited states for transition metal complexes include MLCT, MC, LMCT and LC. Figure 6.17 presents the time dependent charge transfer dynamics in terms of the four classes. The plot to the left, shows the time dependent charge transfer type from a separation of the electronic wavefunction into singlet and triplet states, and the plot tot the right shows the results from a kinetic model of the main trends.

The left plot, shows that the initial population has ~85 % ^{1}MLCT character, and only small contributions (≤8%) from either ^{1}MC, ^{1}LC or ^{1}LMCT. This was anticipated from the majority of MLCT bright states in the lowest energy band of the absorption spectrum, Figure 6.9. Furthermore, the charge transfer characters that contribute most, at all times of the simulations, are ^{1}MLCT, ^{3}MLCT and ^{3}MC, which describes more than 90% of the population.

The last time point of the simulation, shows less than 5 % singlet ^{1}MLCT character, and ~45 % triplet MC and MLCT character, each. The remaining populations are other types of transitions that each contribute less than 3 % or ground state build up. The total charge transfer (black) decrease about 5 % by the end of the simulations, since it is by definition only describes the excited states. Interestingly, the ^{3}MLCT and ^{3}MC contributions appear as long-lived states.Thus, it is challenging to assign the relaxation pathway with certainty. Based on the first 700 fs of excitation, an overall relaxation mechanism might be described as ^{1}MLCT →^{3}MLCT and ^{3}MC, in a parallel decay mechanism from the ^{1}MLCT state.

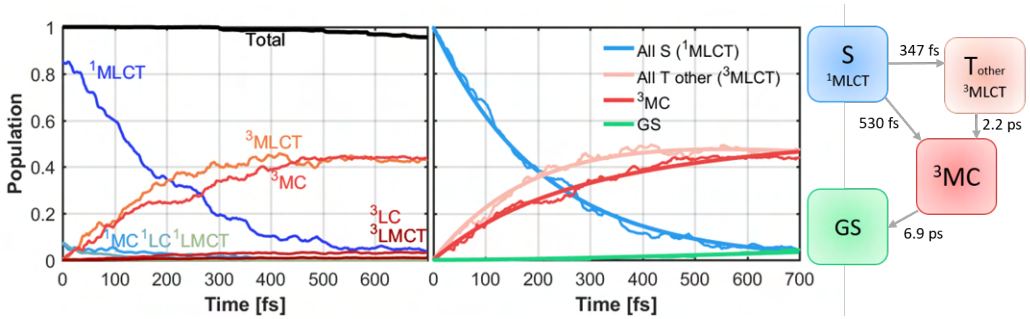

Figure 6.17: Time dependent charge transfer character in terms of the MLCT, MC, LMCT and LC classes. Left: all contributions with ^{1}MLCT, ^{3}MLCT and ^{3}MC most dominant. Right: the results from fits of the kinetic model illustrated next to the plot. Summation of all singlet contributions gives the light blue curve (S), where the ^{1}MLCT is the main contributor. Summation of all triplet contributions except the ^{3}MC contribution gives the rosa curve (T_{other}), where the main contributor is the ^{3}MLCT class. The total charge transfer is not conserved throughout the dynamics, since few trajectories went into the ground state, and thus represents the ground state (GS) build-up.

Kinetic fits of the data using the model illustrated next to the plots in Figure 6.17, give four time decay constants:

1. A decay of 0.35±0.04 ps from the singlets (S) of mainly ^{1}MLCT character to all triplets, except MC, (T_{other}) of mainly ^{3}MLCT character.

2. A parallel decay from the singlets to the states of ^{3}MC character populated with a time constant of 0.53 ± 0.09 ps.

3. A slower population of 2.2 ± 1.5 ps of the ^{3}MC states populated from the other triplet (mainly ^{3}MLCT) states.

4. A slow decay of 6.9±139 ps from the ^{3}MC to the ground state.

The slower decays of several ps show a large uncertainty due to the narrow 700 fs time range of the data used to model ps processes. The ^{3}MC growth is faster than reported from XES experiments (~0.09 ps) [51], however they excite at 400 nm which might lead to a faster ^{3}MC population.

Furthermore, note that the data relative to the fits show hints of oscillations, indicating that the population transfer is beyond a standard kinetic description. Future investigations wish to examine any correlations between certain normal modes or bond lengths and populations of the states, in particular, states of ^{3}MC character.

6.3.6 Structural dynamics

So far, only changes within the solute part of the system was analyzed. However, we are also interested in the solvent effects and the interplay of solute and solvent. Hence, analysis of the radial distribution functions (RDFs) is useful. The RDFs are computed from each time step of the simulations in both the ground and excited state dynamics simulations. The following sections present and discuss the results from the RDFs related to the solute, solvent and solute-solvent cross-term atomic pairs. Each section presents figures that show the averaged RDFs of all 99 excited state trajectories and the corresponding average from ground state trajectories. Furthermore, the RDF differences relative to the averaged ground state, are presented.

RDFs related to atomic pairs on the solute

Figure 6.18 presents the RDFs for selected atomic pairs on the solute. The left column shows the total RDFs averaged over all times before excitation (blue), and after excitation (red), and the difference (green). The right column of the figure shows the difference between the RDF at time t and the average ground state RDF (GS avgr). Red colors refer to a positive peak, and blue is a negative peak. The non-zero differences before time zero, arise from the method of calculating the difference from an average of the whole ground state ensemble, and shows dynamics in the ground state.

The first two rows in Figure 6.18, present the RDFs of the Fe-C_{CN} and Fe-C_{bpy}, solute-solute pairs, which mainly show bond elongations from the metal to the ligands, upon photoexcitation. The Fe-C_{bpy} differences show a significant change in the difference signals directly upon excitation, whereas the Fe-C_{CN} bond elongation grows in more slowly after roughly 100 fs. In addition, the Fe-C_{CN} differences show a broader distribution of bond lengths in the excited state, indicating less tightly bound cyanide ligands. Similar trends are observed in the RDFs for the Fe-N atomic pairs (third row), where the first peak at ~2 Å describes the changes in the bonds between iron and nitrogen from the bipyridine ligand, which shows an immediate change in the difference signals, upon excitation. The second peak at ~3 Å describes the distance to the nitrogen atoms from the cyanides, for which the bond elongation is delayed by ~100 fs.

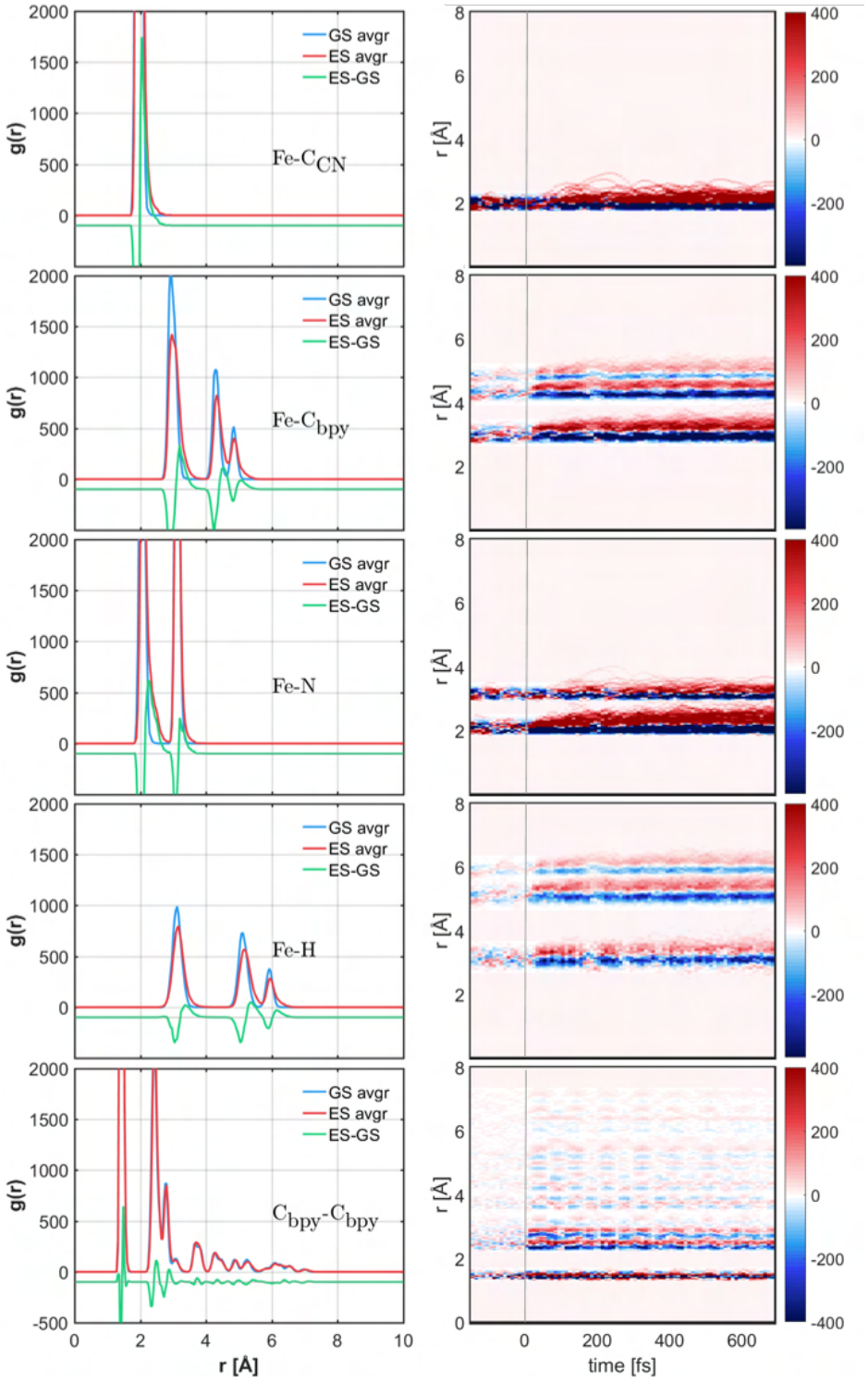

Figure 6.18: RDFs from selected solute-solute atomic pairs. Left: Averaged RDFs over all times below time zero (ground state, GS) and after time zero (excited state, ES). Right: Difference RDFs relative to the average ground state.

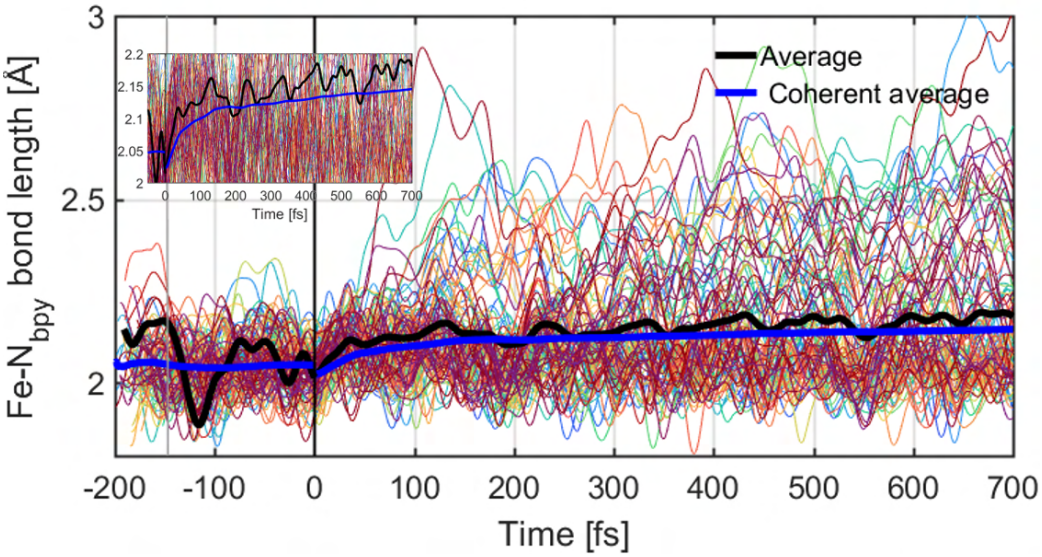

Figure 6.19: Dynamics of the Fe-N_{bpy} bond lengths. Colored curves indicate the specific Fe-N bond lengths for each trajectory (99) in every time step (0.5 fs). The black thick line shows the average over the trajectories for the given time step, and the blue thick line shows the running average of all previous and current time step. The inset shows a zoom of the distances.

From the RDFs of the Fe-H atomic pairs (third row), we observe an overall expansion of the distances between the metal and the bipyridine ligand. In comparison to the results on the $[Ru(bpy)_3]^{2+}$ system, from chapter 5, Figure 5.13, the Ru-H bond elongations were almost non-existing. For the $[Fe(bpy)(CN)_4]^{2-}$ system, differences are observable both at early and later times. Other structural changes on the solute include the C-C bonds within the bipyridine ligand (shown in the last row). From inspection of the differences, we observe only minor structural changes. The plot also shows oscillations with a period of approximately 50-100 fs, which likely arise from activated vibrational modes associated with the bipyridine ligand.

The largest structural changes observed for the $[Fe(bpy)(CN)_4]^{2-}$ system arise from the changes in the Fe-C and Fe-N distances, and these structural changes are expected to be observable in ultrafast time-resolved X-ray scattering experiments, as will be discussed in section 6.3.7.

The dynamics of the Fe-N_{bpy} bonds is also shown in Figure 6.19, for each trajectory (99), at each time step. The plot also shows the average for each time step (black) and the cumulative average (blue), which takes all the previous data points into account. The inset shows a zoom of the distances, where it shows that the Fe-N bonds elongate from ~2.05 Å in the ground state to roughly ~2.10 Å within the first 100 fs followed by a slower continuous grow to roughly ~2.15 Å by the end of the 700 fs time frame. After excitation, the distribution of bond lengths is significantly broader. Future analysis will investigate any correlations with the charge transfer character data, in order to examine if longer bonds are associated with the population of e.g. MC states.

The early structural changes observed in the Fe-bipyridine distances is anticipated, as we predominantly found charge transfer from the Fe to the bipyridine at early times, based on Figure 6.15 from section 6.3.5. The Fe-N_{bpy} bond lengths elongates by roughly ~0.05 Å within the first 100 fs after excitation. The structural changes are therefore small, but small structural changes are expected for MLCT excited states, as reported for similar Fe [231] and Ru [232, 233, 234] based complexes that all show similar ground and $^{1/3}$MLCT state geometries.

The slower Fe-N_{bpy} bond elongations of ~ 0.10 Å, indicate that longer bonds are associated with population of MC states, at later times. Other studies on Fe [231, 166, 235] based complexes confirm that the Fe-ligand structural changes associated with population of ^{3}MC (~ 0.1 Å) and ^{5}MC (~ 0.3 Å) states are larger than for MLCT states (~ 0.02 Å).

In comparison to the RDFs of the $[Ru(bpy)_3]^{2+}$ complex, from chapter 5, Figure 5.13, the largest structural changes also concerned the metal-N_{bpy} bonds with an overall bond elongation of ~0.003 Å. Thus, very small structural changes. Hence, the calculated structural changes of the metal-N_{bpy} bonds are larger for the case of the $[Fe(bpy)(CN)_4]^{2-}$ complex than for the $[Ru(bpy)_3]^{2+}$ complex. However, we should note that the simulations of $[Ru(bpy)_3]^{2+}$ are based on the lowest excited triplet state after thermal equilibration, whereas the current simulations of $[Fe(bpy)(CN)_4]^{2-}$ are far from equilibrium.

In comparison to the $[Fe(bpy)_3]^{2+}$ system, several theoretical studies [236, 237, 238] show that the ^{1,3}MLCT excited states have their energy minimum in the same structural region as the ground state, and thus the structural changes related to populations of the ^{1,3}MLCT states are minimal. However, the potential energy surfaces of the ^{3}MC and ^{5}MC states are located with minima at approximately 0.1 Å and 0.2 Å, longer Fe-N bond lengths, respectively, relative to the ground state equilibrium Fe-N bond length.

Furthermore, a DFT study of $[Ru(bpy)(CN)_4]^{2-}$ [233], reports Ru-N bond elongations of ∼0.05 Å from the ground state to the lowest lying triplet state, with MLCT character, thus in good agreement with our results on the $[Fe(bpy)(CN)_4]^{2-}$ complex at early times.

In summary, the results from the current and previous studies, indicate that the populations of the ^{1,3}MLCT states of $[Ru(bpy)_3]^{2+}$ and $[Fe(bpy)_3]^{2+}$ give rise to basically no structural changes (order of 0.001 Å) with respect to the ground state geometry. However, the populations of the ^{1,3}MLCT states in $[Fe(bpy)(CN)_4]^{2-}$ and $[Ru(bpy)(CN)_4]^{2-}$ lead to minor structural changes on the order of 0.05 Å for the metal-bipyridine bonds. One might speculate that it is likely a consequence of the delocalization of the MLCT excited state over all three bipyridine ligands, which results in almost no change in the bond lengths, whereas the addition of the cyanides to the geometry leads to a more localized MLCT excited state on the single bipyridine unit, leading to slightly larger structural changes. Additionally, even larger structural changes, on the order of 0.1 Å and 0.2 Å, for the metal-bipyridine bonds are observed as a consequence of populations of the ^{3}MC and ^{5}MC excited states, when comparing $[Fe(bpy)(CN)_4]^{2-}$ and $[Fe(bpy)_3]^{2+}$.

RDFs related to solute-solvent atomic pairs

Selected solute-solvent RDFs are shown in Figures 6.20 and 6.21. The difference plots in the right column only shows the distances up to 8 Å, since the main solvent structural changes are observed within roughly 6 Å of the solute. Figure 6.20 shows the RDFs related to the solute Fe and N atoms, relative to the solvent H and O atoms, and Figure 6.21 shows the solute C-atoms relative to the solvent, separated into C-atoms belonging to the bipyridine and cyanide ligands.

General trends in the total averaged RDFs include a decrease in peak height and a peak broadening, in particular, for the lowest distances. However the structural changes in the solvent around the bipyridine ligand is minimal. The general peak broadening from average ground state to excited state indicates less structural order of the nearest solvent molecules.

Iron-solvent interactions: For X-ray scattering experiments, the main contributor to the observed signals are changes related to the iron center, being the part of the molecule with highest electron density. Thus the iron-solvent RDFs are of key interest. The main observations are expansion of the nearest solvent shell located ~6 Å from the iron center, from the average ground to excited state. The difference plots show a fast response from the hydrogen atoms in the solvent directly upon excitation, whereas the Fe-O distances change more slowly. The observed differences are larger in amplitude than observed for the solvated $[Ru(bpy)_3]^{2+}$ system, from Chapter 5, Figure 5.14, where the differences were minimal.

Nitrogen-solvent interactions: The interactions between the nitrogen atoms and the solvent is much stronger observed from the sharp peak at ~1.9 Å, for the N-$H_{solvent}$ RDFs and roughly at 3 Å for the N-$O_{solvent}$ RDFs. This sharp peak is from the nitrogen atoms of the cyanides since they are closer to the solvent than the nitrogens within the bipyridine ligand, that are located close to the metal center. Hence, the sharp peak in the RDFs indicates strong H-bonds between the cyanides (N-atoms) and the solvent (H-atoms), in both the ground and excited state. However, they weaken slightly in the excited state, observed from the decrease in intensity and slight peak broadening.

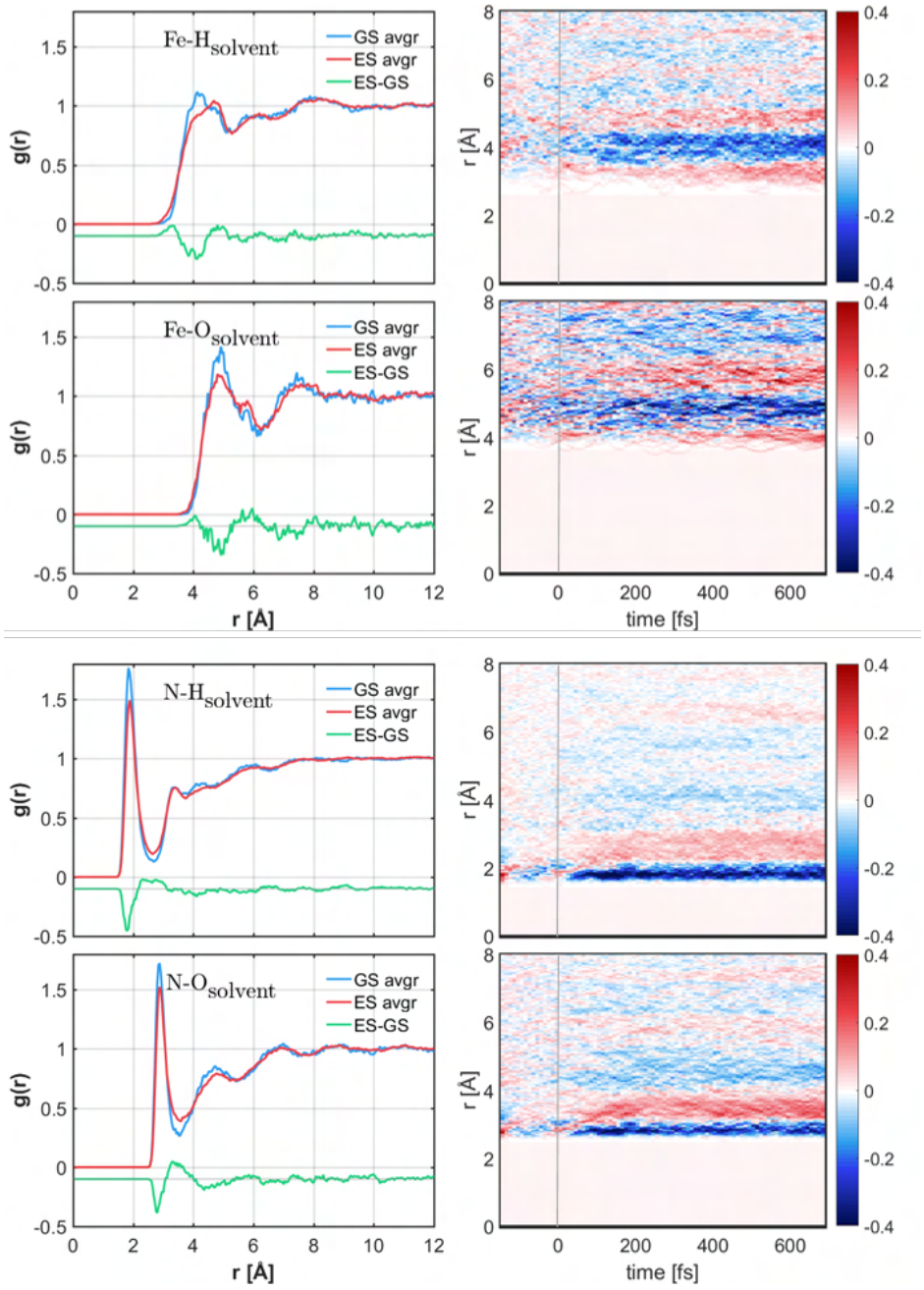

Figure 6.20: RDFs from iron, nitrogen, solute-solvent atomic pairs. Left: Averaged RDFs over all times below time zero (ground state, GS avgr.) and after time zero (excited state, ES avgr.), and the difference shown with an offset. Right: Difference RDFs, from each time step, relative to the average ground state.

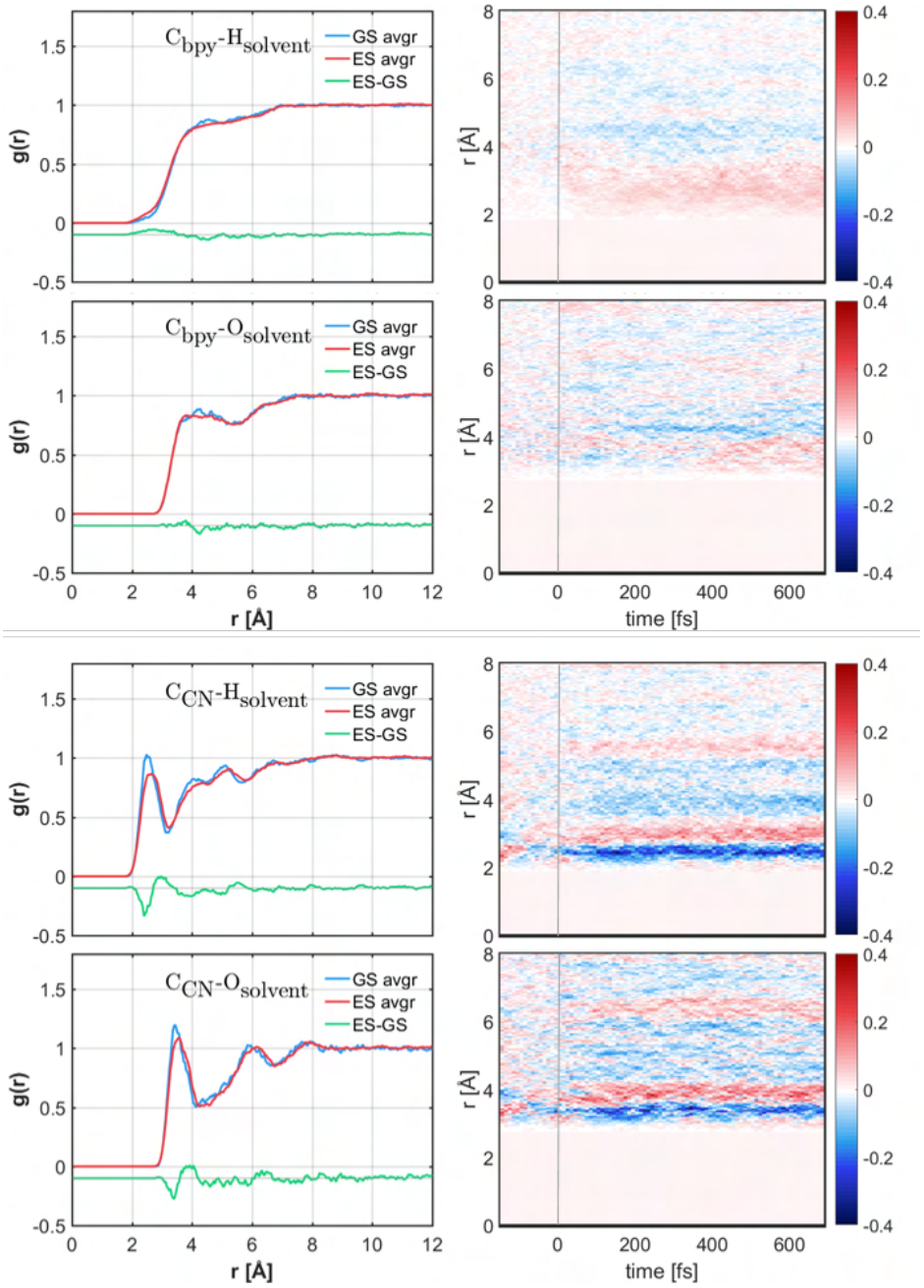

Figure 6.21: RDFs from C atoms from the bipyridine (bpy) or from the cyanides (CN), solute-solvent atomic pairs. Left: Averaged RDFs over all times below time zero (GS avgr.) and after time zero (ES avgr.), and the difference shown with an offset. Right: Difference RDFs, from each time step, relative to the average ground state.

The results of the RDFs of the N-$H_{solvent}$ and N-$O_{solvent}$ atomic pairs are in good agreement with the reported RDFs from a QM/MM MD study [204] on the $[Fe(II)(CN)_6]^{4-}$ and $[Fe(III)(CN)_6]^{3-}$ systems in water. The study also finds strong CN-H bonds located just below 2 Å, closer than the shortest CN-O distances just below 3 Å. Additionally, they observe peak broadening, and thus less solvent structure, for the Fe^{3+} based system, relative to the Fe^{2+} system. The broadening reflects the decreased electrostatic interaction between the cyanides and the solvent in the case of the Fe^{3+} based system. Experiments using 2D IR spectroscopy [239] on the same systems also found that the nearest solvent shell of water was more strongly bound for the case of $[Fe(II)(CN)_6]^{4-}$ than for $[Fe(III)(CN)_6]^{3-}$. From the perspective of the Fe center in the $[Fe(bpy)(CN)_4]^{2-}$ system, populations of MLCT states leads to less charge located on the metal center, and thus less π-backbonding to the cyanides, which might explain the weakening of the cyanide-hydrogen bonds in the excited state.

Carbon-solvent interactions: From the perspective of the C-atoms, we find very different solute-solvent interactions around the cyanides and around the bipyridine. Figure 6.21, top panel, shows the RDFs associated with the C-atoms on the bipyridine, where the structural changes are only minimal. The results are in agreement with the minor structural changes observed for the C-$O_{solvent}$ and C-$H_{solvent}$ for the $[Ru(bpy)_3]^{2+}$ system, shown in Chapter 5, Figure 5.14. From the difference plots on the $[Fe(bpy)(CN)_4]^{2-}$ system, we find slightly different dynamics for the hydrogen and oxygen atoms from the solvent, as in the case of the iron-solvent RDFs. The RDF differences for the C_{bpy}-$H_{solvent}$ pair indicates an almost instantaneous change, with the hydrogen atoms moving slightly closer, whereas the RDF differences for the C_{bpy}-$O_{solvent}$ pair show slightly different features at early times (< 300 fs) than at later times. The small negative features at low distances and early times indicate that the O atoms of the nearest solvent, move slightly away, and move closer at later times, from grow-in of the positive features. This suggests that the nearest water reorganizes as a response to the excitation. The early times are dominated by population of MLCT states, and thus a higher negative charge on the bipyridine ligand, which likely makes the nearest water molecules rotate or simply move away from the ligand. At later times, more of the population transfers to MC states, followed by elongation of most bonds

in the solute, and consequently, the O atoms of the solvent are closer to the bipyridine. However, the overall solvent response around the bipyridine is significantly lower than for the remaining part of the solute.

In contrast to the bipyridine ligand, the C-atoms from the cyanides show much stronger interaction with the nearest solvent with a sharp peak located at roughly 2.5 Å for the C_{CN}-$H_{solvent}$ pair and roughly at 3.5 Å for the C_{CN}-$O_{solvent}$ pair. Both types of pairs show, for the distances below 5 Å, a peak broadening and a shift to larger distances in the excited state indicating that the nearest water molecules move further away from the cyanides and shows less structural order after excitation.

In order to further investigate the dynamics of the H-bonds around the cyanides, we computed Angular Radial Distribution Functions (ARDFs), which allows us to study the "attacking" angle of the water molecules, and the weakening of the solute-solvent H-bonds in greater detail. The ARDFs are discussed in later paragraphs.

A very recent study [203] of the $[Fe(bpy)(CN)_4]^{2-}$ complex, investigates the system using X-ray absorption spectroscopy at the metal $L_{2,3}$-edge along with MD simulations of the system in both water, ethanol and DMSO. Figure 6.22 presents their results of the modeled RDFs between the cyanide N, and the solvent O,H,S atoms, to the left and between the bipyridine H and the solvent O,H,S atoms, to the right. They report strong cyanide-water N-H bonds with a distance of ~1.7 Å in water, based on the maximum of the first peak in the RDF of the N-H pair. Our simulations show a maximum at 1.84 Å from the average ground state and at 1.88 Å from the average of the excited state trajectories, thus in good agreement with their results. Furthermore, they observe a significantly different solvent coordination for the three different solvents. The results show less structure around the cyanides in the case of DMSO than for water and ethanol. Additionally, the solvation structure around the bipyridine ligand is significantly different from the cyanide solvation, with almost no structure, in agreement with our results of the bipyridine-solvent C-H, C-O RDFs.

In conclusion, the observed structural changes from the solute-solvent interactions in the $[Fe(bpy)(CN)_4]^{2-}$ system are expected to be observable in time-dependent X-ray scattering signals within the fs-ps time range, as discussed in the following, in section 6.3.7.

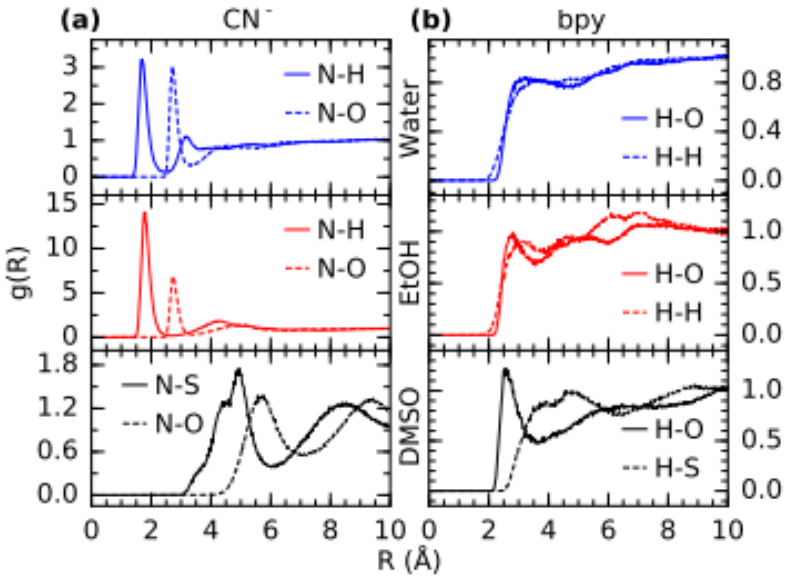

Figure 6.22: Solute-solvent type RDFs from MD simulations of the $[Fe(bpy)(CN)_4]^{2-}$ system in water, ethanol (EtOH) and DMSO, by Jay et al. [203]. Part (a) shows the N-H, N-O, N-S solute-solvent pairs from the cyanide-solvent interactions. Part (b) shows the H-O,H-H, H-S solute-solvent pairs from the bipyridine-solvent interaction.

RDFs related to atomic pairs in the solvent

Figure 6.23 shows solvent-solvent pair RDFs. Note, that the color scale is different from the solute and cross-term plots.

The plots show only minor differences (order of 0.01 Å) from the average ground to the excited state, which indicate that the sampling of the solvent was sufficient, since the solvent is not expected to change much on these time-scales, except through solvent heating as a result of energy transfer from solute to solvent. The general features and shapes of the averaged total signals compares well with combined X-ray and neutron scattering experiments on pure water from literature [182], as indicated by the gray dots. Although, our simulations show a more structured liquid, observed from slightly sharper peaks at low distances. The trends at larger distances are well in agreement with bulk solvent measurements.

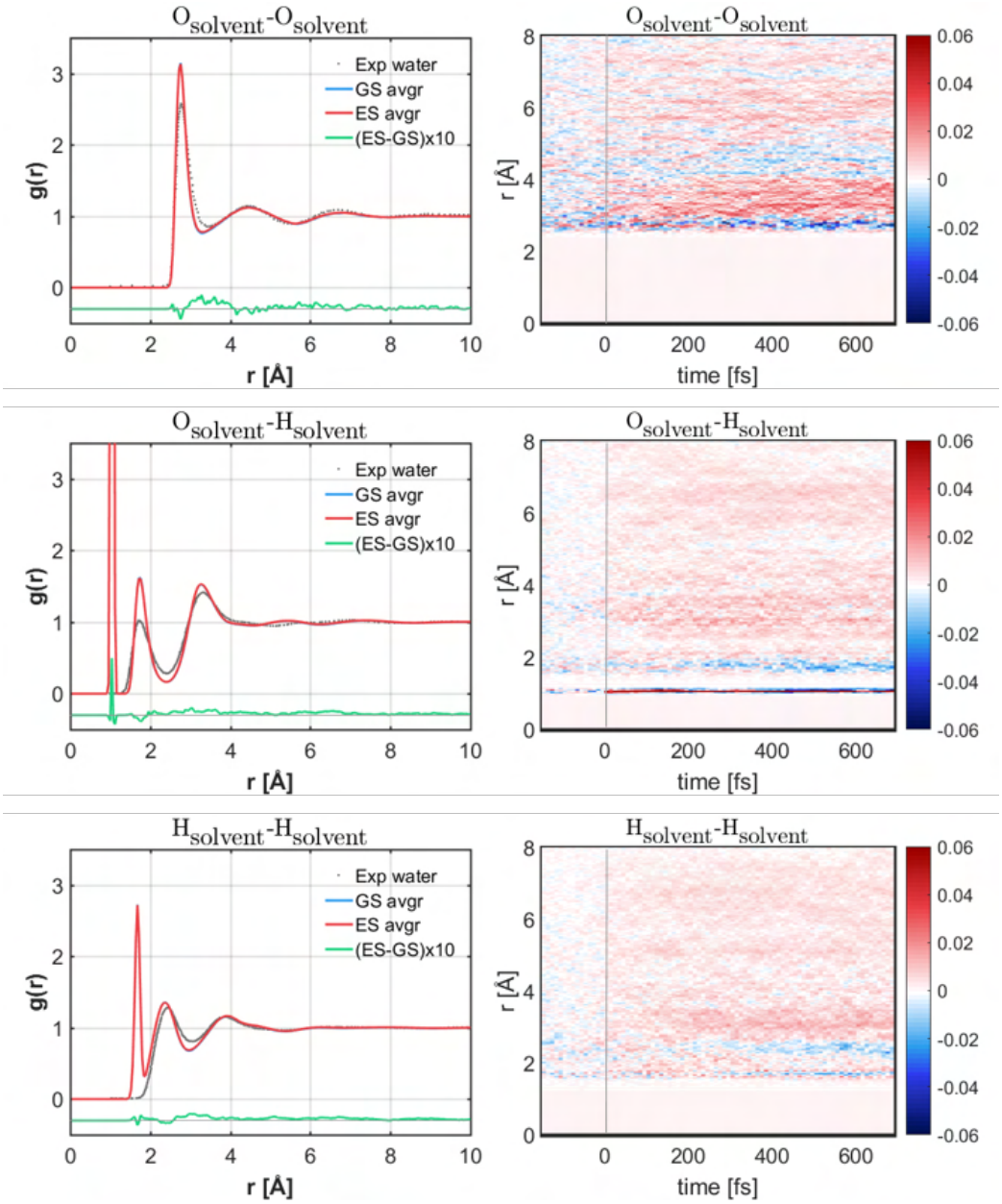

Figure 6.23: RDFs from the solvent-solvent atomic pairs. Left: Averaged RDFs over all times below time zero (ground state, GS) and after time zero (excited state, ES), and the difference enhanced by a factor of ten (ES-GS)x10. Additionally, the gray dots show the RDFs of pure water from experiments [182]. Right: Difference RDFs relative to the average ground state.

The higher order of structure is expected, since the solvent packs around a solute, leading to solvation shells, which are often more ordered than bulk water.

Furthermore, the general features from the ground to excited state are well in agreement with the calculated solvent-solvent RDFs from both the MD (Figure 5.7) and QM/MM MD (Figure 5.15) simulations on the solvated $[Ru(bpy)_3]^{2+}$ system, from Chapter 5. The difference between ground and excited state are less here than for the MD and QM/MM MD simulations, but that might simply be because the solvent did not yet have time to fully equilibrate around the new solute structure within the simulated 700 fs.

The difference plots generally show an overall expansion of solvent, likely as a result of the heat transfer from the solute to the solvent, and from the method of the simulations without periodic boundary conditions. The expansion is mainly observed from the grow-in of the dark blue and red features around distances of 3-4 Å after ~100 fs from excitation. This corresponds well with the observed IC from high-lying singlets, of roughly 100 fs.

Angular Radial Distribution Functions

In order to further investigate the change in the solvent coordination around the cyanide ligands, we calculated combined angular-radial distribution functions (ARDFs), as shown in Figure 6.24. The analysis of the ARDFs was mainly carried out by Sebastian Mai. The ARDF analysis consider the solute-solvent N-O distances, $R_{\text{N-O}}$ relative to the angle, α formed from either the solute cyanide C atom or the solvent H atom, as illustrated below. The analysis also examines the C atom relative to the N-H distance, $R_{\text{N-H}}$. The illustration below shows the relevant distances, R and angles α, for each column in Figure 6.24.

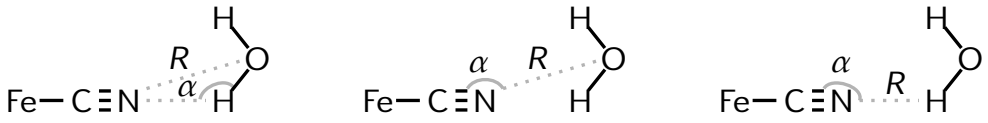

The first row of Figure 6.24 shows the normalized ARDFs, averaged over the ground state trajectories (from -150 to 0 fs). The remaining plots show the difference ARDFs relative to the averaged ground state, at times of 0–50 fs, 100–150 fs, and 650–700 fs. The left halves of all plots present the ARDFs for the axial CN ligands, and the right show the equatorial cyanides. The leftmost column shows the radial distance, $R_{\text{N-O}}$, between solute type N, and solvent type O, relative to the angle $\alpha_{\text{N-H-O}}$ formed with the H atoms in the solvent. These are the main parameters to identify hydrogen bonds around the cyanides, as discussed later. Hence, the first column of plots illustrates how the O-H bond from water points toward the N atom in the cyanide ligands.

From the total ARDF, we observe that strong H-bonds are present at $R_{\text{N-O}} \approx 3.0$ Å distances and CN-H-O angles above 135°, as indicated by the large yellow area. The small yellow areas at lower angles of ∼60-70° arise from the correlated angles of the other hydrogen atom in the nearest water. The differences between the axial and equatorial cyanides are small, but with a slightly higher extend of H-bonding to the axial groups. The differences in the N-H-O angles indicate that the water molecules move further away and towards lower angles. The variation in the shades of blue at longer distances suggests less ordering in the second and third solvation shells.

The second column shows the same N-O distance, $R_{\text{N-O}}$ versus C≡N-O angles, $\alpha_{\text{C-N-O}}$, thus illustrating the solvent oxygen position relative to the cyanides. The total ARDFs show that the water oxygen atoms mainly attack at degrees higher than 90°, which is expected due to the steric hindrance. The main angles of the nearest O atoms, include 90-120 degrees as well as straight angles of 180°, relative to the cyanide group. The difference ARDFs show that the water molecules move slightly away and diffuse towards more straight 180° C≡N-O angles.

The third column presents the solvent hydrogen atoms relative to the cyanides, as the N-H distance, $R_{\text{N-H}}$ versus C≡N-H angles. The total ARDFs, show that strong H-bonds at ∼1 Å, and CN-H angles above 90°. Thus, the H atoms from the water attack from the half sphere around the cyanide group. The difference ARDFs, show at early times a higher extend of H-bonds at the lowest distances, which at later times change. The angles of the closest H-bonds relative to the cyanides increase with time, such that the H-bonds shift towards more straight CN-H angles, as observed from the red area at angles between 90-135° and blue area at higher angles.

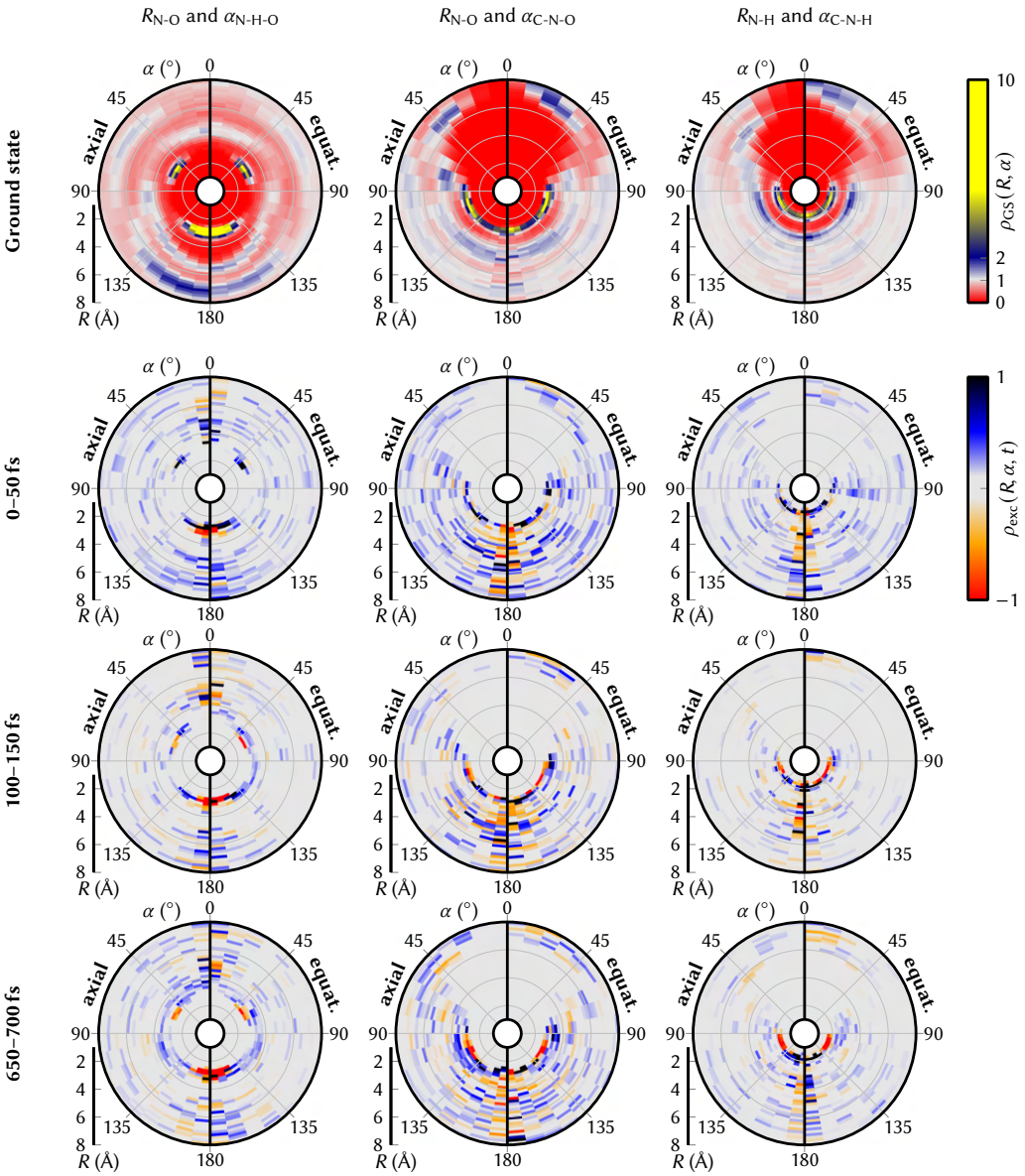

Figure 6.24: Angular-radial distribution functions (ARDFs) of the cyanides relative to the solvent water. The left halves of all plots show the axial cyanides, and the right halves show the equatorial cyanides. The first row presents the total normalized ARDF in the ground state, averaged between -150 and 0 fs. The next three rows present the difference ARDFs (relative to ground state) at 0–50 fs, 100–150 fs, and 650–700 fs. The left column plots the distance $R_{N\text{-}O}$ against the angle $\alpha_{N\text{-}H\text{-}O}$. The second column shows the same distance against the C≡N–O angle. The third column presents the $R_{N\text{-}H}$ distance versus C≡N–H angle. Figure by Sebastian Mai.

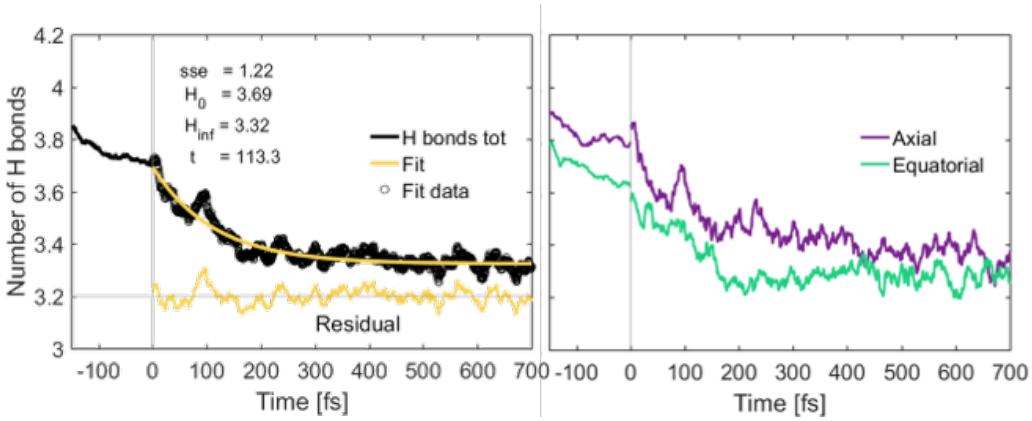

Figure 6.25: Dynamics of the hydrogen bonds around the cyanides. Left plot shows the summed number of H-bonds (black) around all four cyanides and a mono-exponential fit (yellow) of the excited state data. The residual between fit and data is shown below with and offset of 3.2. The model is given by eq. (6.7), with the sum of squared errors shown as sse. Right plot shows the separate contribution when counting only the H-bonds around the axial or equatorial cyanides.

Analysis of the angular dependence of the distances allows us to extract information on the number of hydrogen bonds around the different cyanide ligands. We count the number of H-bonds around the cyanides as how often a distance of $2.45 \leq R_{\text{N-O}} \leq 3.55\,\text{Å}$ and an angle of $135 \leq \alpha_{\text{NHO}} \leq 180°$ occurs.

Counting the number of hydrogen bonds at each time step, allows us to determine the kinetics of the changes in the number of H-bonds, as shown in Figure 6.25. The left plot shows the dynamics of the total number of hydrogen bonds around the cyanides, and the right plot gives the number of hydrogen bonds around the axial and equatorial cyanides, separately. The data before time zero, is based on the ground state dynamics simulations and averaged over the 478 trajectories, whereas the data after time zero is from the excited state dynamics simulations with 99 trajectories. Thus, the statistics are higher for the data before time zero than for the data after time zero. For both data sets, around all four cyanides and only the axial or equatorial, we observe an overall decrease in the number of hydrogen bonds from approximately 3.7 to 3.2, however, slightly higher around the axial (3.9 to 3.3) and less around the equatorial (3.5 to 3.2) cyanides.

The previously mentioned MD study [203] on the $[Fe(bpy)(CN)_4]^{2-}$ system, finds on average slightly less, 2.54±0.41 number of hydrogen bonds around the cyanides. They define the H-bonds from the criteria $r_{N-O} < 3.0$ Å and $\angle NOH < 20°$, as illustrated below, thus slightly different from our definition. They also find a slightly higher number 2.68 ± 0.54 of H-bonds around the axial cyanides than for the equatorial cyanides with 2.40 ± 0.56 hydrogen bonds. Additionally, they find slightly longer (∼ 0.1 Å) and less (1.80±0.42) hydrogen bonds in ethanol than for water.

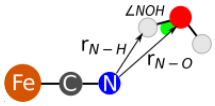

Illustration from [203]

A mono-exponential kinetic fit of the number of H-bonds around all four cyanides, finds a time decay constant of $t = 113 \pm 4.5$ fs. The number of hydrogen bonds at time zero was found to be $H_0 = 3.69 \pm 0.009$, and converging towards $H_\infty = 3.32 \pm 0.003$ for $x \to \infty$. We observe no significant improvement of the fit by introducing a second exponential. The data was fit according to the model:

$$m(x) = H_\infty + (H_0 - H_\infty)e^{(-x/t)} \tag{6.7}$$

A qualitative inspection of Figure 6.25, indicates that the H-bonds around the equatorial cyanides reorganize slightly faster than around the axial cyanides. For future analysis, it would be of interest to compare the H-bond dynamics to the change in charge transfer on the cyanides, and to the overall change of MLCT/MC charge transfer character of the complex.

In summary, we observe strong hydrogen bonds between the cyanides and the nearest water molecules, which mainly attack at CN-H-O angles between 135-180°, and C-N-H angles above 90°, in the ground state. Hence, the hydrogen bonds attack from a half sphere around each cyanide group. Furthermore, we find ∼3.8 number of hydrogen bonds around the cyanides, in the ground state. In the excited state, the hydrogen bonds shift to more straight 180° C-N-H angles, and thus shift to attack more end on towards the cyanides. The number of hydrogen bonds are weakened in the excited state to ∼3.3 which occur on a time scale of 113±4.5 fs.

6.3.7 Calculation of X-ray scattering signals

Based on the radial distribution functions, we can calculate the expected time-dependent wide angle X-ray scattering (WAXS) signals within the earliest 700 fs upon excitation. The method of calculating the scattering from RDFs was described previously in part I, section 2.6. This section presents the results on the calculated scattering from the excited state dynamics simulations.

The current time resolution of TR-WAXS experiments at XFELs goes down to 30-50 fs, pushing into the 10 fs regime [10, 240, 41], however, the time resolution from the simulations of 0.5 fs is currently not experimentally achievable. Therefore, we average signals in time intervals of 10 fs from the simulations to enhance the statistics. Figure 6.27 shows the calculated difference signals from the RDFs of averaged time intervals. The expected scattering signals are cast in terms of contributions from the solute, solvent and cross-term interactions. The figure shows the data in two different ways. The left column shows the calculated difference scattering, ΔS, as a function of the scattering vector,Q , for every 50 fs with the color scale according to the simulated time. The right column shows the calculated data as a function of both Q and time, with the color scale according to the intensity of the difference scattering signals. The plots to the right also show the difference scattering multiplied with Q, in order to enhance the trends at higher Q. The non-zero features in observed before time-zero is a result of the non-zero differences in the RDFs. As discussed previously, it is likely a result of the procedure for calculating the differences, by use of the average ground state RDF. However, the differences from ground to excited state is much larger than the differences within the ground state, and hence we find the results from the excited state trustworthy.

The top row of the figure shows the calculated difference scattering signals from the contribution of the solute structural changes. The solute contribution shows a clear negative feature at $Q \leq 1$ Å^{-1}. For a metal complex as this one, the negative peak at low-Q is consistent with solute bond elongations, associated with population of MC and MLCT states based on comparisons to experiments on $[Fe(bpy)_3]^{2+}$ [41] and an iron carbene system abbreviated $[Fe(bmip)_2]^{2+}$ [58], and to simulations [241] of the same complex.

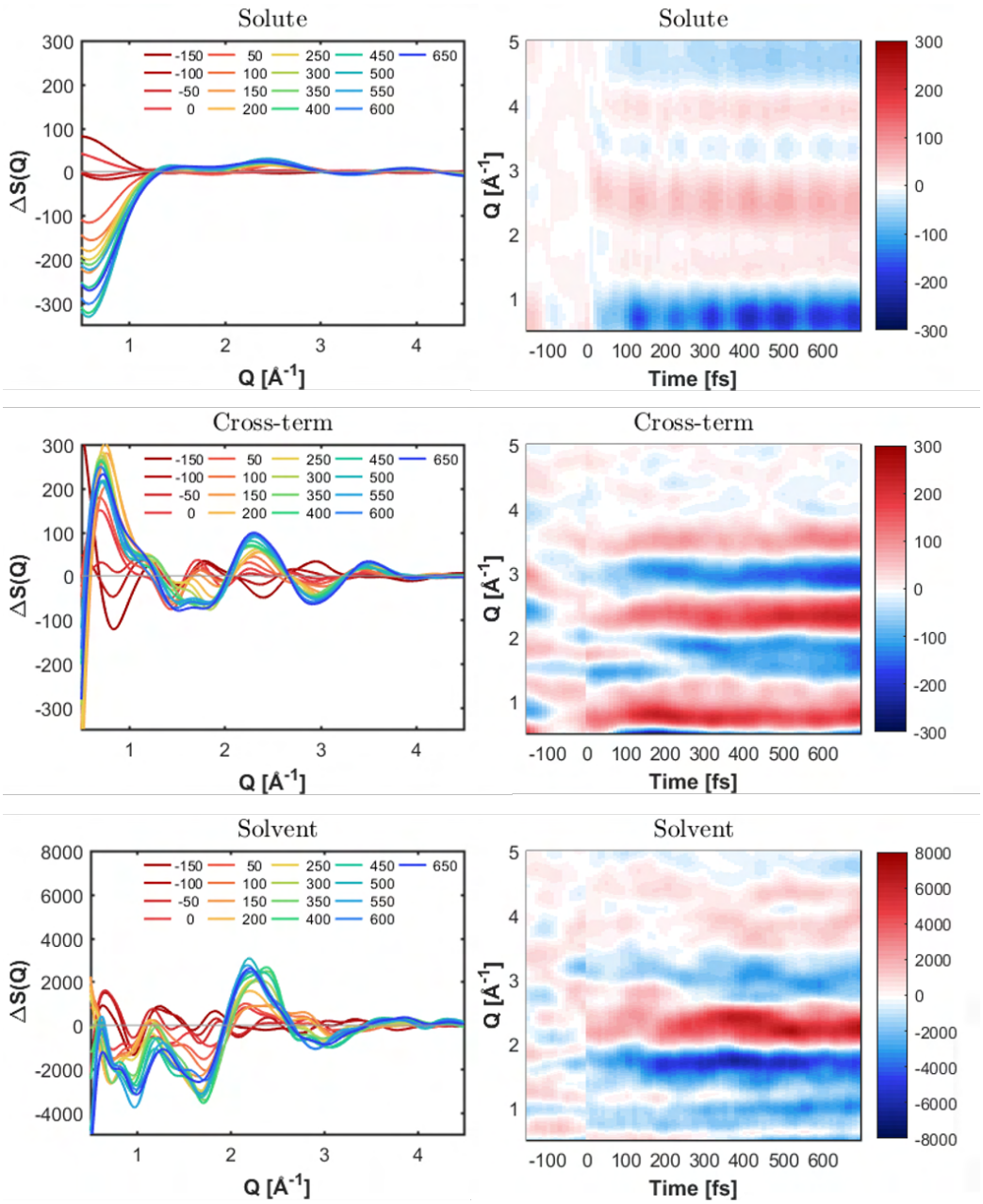

Figure 6.27: Calculated difference time-resolved wide angle X-ray scattering signals in terms of the solute and solute-solvent crossterm and solvent contributions. Left plots, shows every 50 fs on top of each other, whereas right plots show the signals as a function of time and colored according to intensity. The top row shows the solute contributions ($Q\Delta S$ as a function of simulated time and Q), with clear coherent oscillations. The middle part shows the solute-solvent crossterm contributions ($Q\Delta S$). The bottom row shows the solvent contribution.

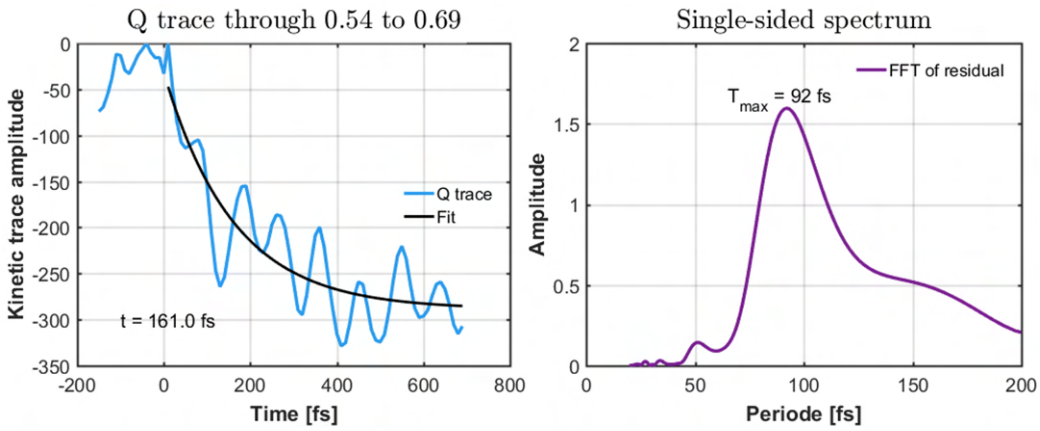

Figure 6.28: Left: an average of the solute data between $0.54 \leq Q \leq 0.69\,\text{Å}^{-1}$, along with a mono-exponential fit of the data after time zero. Right: single-sided spectrum of the Fourier transformed residual between q-trace data and fit.

Additionally, the solute contribution shows oscillating features, and Figure 6.28, shows a plot of the average signal between $0.54 \leq Q \leq 0.69\,\text{Å}^{-1}$, including a mono-exponential fit, along with a Fourier transform of the residual between the data and fit.

The kinetic fit of the solute trace along Q gives a time constant of 161±57 fs. By subtraction of the kinetic fit, and a Fourier Transform of the residual results in a slightly broad peak located with a maximum at 92 fs, as the period of the oscillations. Future analysis of the normal modes will reveal if the oscillation period matches an activated vibrational mode in the solute. An ultrafast time-resolved WAXS experiment with sufficient time resolution (30-50 fs) would be expected to observe the coherent excited state dynamics from the solute.

The middle row of Figure 6.27 shows the solute-solvent cross-term contribution to the calculated scattering signals. Not quite as clear as for the solute, but we also observe hints of oscillating features around $Q = 0.5 - 1.1\,\text{Å}^{-1}$, which is anticipated when the solute shows coherent oscillations. The dominating trend is a positive feature at the lowest Q range, which indicates an overall increase in the distances between solute and solvent, as we saw in the solute-solvent related RDFs.

The last row of Figure 6.27 shows the solvent contribution to the calculated scattering signals. The main features are negative peaks in the region $0.5 \leq Q \leq 2\,\text{Å}^{-1}$ followed by a positive feature around $Q = 2.4\,\text{Å}^{-1}$. The positive feature increases in intensity after ~200 fs. The solvent signals most likely also show minor artifacts observed from the small oscillating features distributed over the Q-range, as a consequence of the very small differences observed in the solvent-solvent related RDFs from Figure 6.23.

In addition, we observe differences within the first ~100-200 fs and the remaining time frame, as for instance, the small negative feature in the cross-term signals that grows in at early time, around $Q = 1.3-1.5\,\text{Å}^{-1}$ and decays after ~200 fs. At the earliest times we mainly populate states with MLCT character, whereas later times populate states with mixed MLCT and MC character, and thus the differences observed at early times are most likely associated with the nearest solvent packing related to population of MLCT states. For example, the increased electron density on the bipyridine ligand might influence the orientation of the nearest solvent molecules towards the bipyridine ligand, and likewise an increased negative charge on the CN groups influences the nearest water molecules. Such small features in the cross-term and solvent contributions, may play an important role in the interpretation of the solvation dynamics as was the case for the bi-metallic complex, $[Ir_2(\text{dimen})_4]^{2+}$ (dimen=diisocyano-para-menthane) [63]. The study by Van Driel et al. compared experimental XFEL scattering data to QM/MM MD simulations, and observed very different dynamics in the solvent contribution to the measured signal at early times (500 fs) and at later times (3 ps). They conclude that the early dynamics corresponds to an initial loss of solvation, in which a solvent acetonitrile molecule, with the methyl part coordinated to the iridium center, shifts to larger distances, followed by the later dynamics in which the nitrogen end of an acetonitrile molecule coordinates to the iridium center.

In conclusion, the calculated scattering from the RDFs clearly show differences between the ground and excited state data for both the solute, solvent and cross-term. The signals also show differences within the earliest 100-200 fs and later times. These differences are expected to be observable in ultrafast time-resolved WAXS experiments with a time resolution of < 150 fs.

6.4 Summary

This chapter presented the analysis and results of the $[Fe(bpy)(CN)_4]^{2-}$ investigations. The following paragraphs summarize the main results from the different sections.

Steady state absorption measurements: The beginning of this chapter presented the steady state absorption results of $[Fe(bpy)(CN)_4]^{2-}$ in water/DMA solvent mixtures. The results from the systematic study of the solvent mixtures showed that it was possible to systematically shift the absorption band associated with MLCT transitions from just below 500 nm to above 700 nm in an approximately linear way, by changing the solvent composition. We observed a slight deviation from linearity for solvent mixtures with less than 50 % DMA, which indicates a preferred solvation towards DMA, and that water molecules remain preferentially in the bulk solvent. We also collected transient absorption data on the solvent mixtures, however, the analysis of the data is ongoing, and the question remains how the solvent mixtures effect the excited state dynamics.

Excited state dynamics simulations with SHARC: The main focus of this chapter is the excited state dynamics simulations of the $[Fe(bpy)(CN)_4]^{2-}$ system solvated in water. In total, we computed 478 trajectories, in which we ran ground state dynamics simulations for randomized lengths between 150 and 200 fs. Following excitation, we ran excited state dynamics simulations of 99 trajectories for 700 fs.

Absorption spectrum: The calculated absorption spectrum shows good agreement with experiment, and thus the initial conditions provides a good starting point for the excited state simulations. Analysis of the electronic character of the states in the absorption spectrum, found that the MC states are very ”dark”, and absorption within the first (∼500 nm) and second (∼ 400 nm) absorption band predominantly populates states of at least 80 % MLCT character. However, based on the high density of states for this complex, several ”dark” states exists of both MLCT and MC character. Especially the second band shows a larger degree of mixed MC/MLCT character. As such, one cannot necessarily expect similar excited state dynamics for excitation at 500 nm and 400 nm.

Electronic populations: A great advantage of using simulations is that it allows us to know the detailed nature of the electronic states at all times. Analysis of the electronic populations found internal conversion (IC) from high lying singlet states (0.11 ± 0.01 ps) on similar time scales as singlet-triplet intersystem crossing (ISC) times (0.21 ± 0.02 ps).

Charge transfer character: Information on the electronic charge transfer character was determined using the TheoDORE analysis tools, described in Chapter 4, section 4.2. These tools find predominant charge transfer involving the Fe center and the bipyridine (bpy) ligand, as expected for metal-to-ligand charge transfer states. Early times are dominated by Fe→bpy charge transfer character, whereas later times showed a mixed Fe→bpy and Fe→Fe character, corresponding to populations of MLCT and MC states. Analysis of the electronic wave function in terms of singlets and triplets separately, shows predominantly Fe→bpy charge transfer character for the singlets, and a mix of both Fe→Fe and Fe→bpy for the triplets, throughout the simulated time. A kinetic model of the charge transfer leads to a branched decay mechanism from initial excited states of predominantly ^{1}MLCT character to triplet states of predominantly ^{3}MLCT (of 0.35 ± 0.04 ps) and ^{3}MC (0.53 ± 0.09 ps) charge tranfer character and also a slower population transfer from ^{3}MLCT to ^{3}MC (of 2.19 ± 1.46 ps).

Structural dynamics: A tool to investigate the structural response of the system following excitation, are radial distribution functions (RDFs), which were presented for both solute-solute, solute-solvent and solvent-solvent type atom pairs. The main structural changes on the solute was a bond elongation of the Fe-N_{bpy} bonds, on the order of $\sim$0.05 Å within the first 100 fs and roughly $\sim$0.1 Å by the end of the simulations. The main observations from the solute-solvent RDFs were the very strong hydrogen bonds between the cyanides and water, at a distance of $\sim$ 1.8 Å in both ground and excited state. The hydrogen bonds weaken following the photoexcitation. In contrast, the nearest solvation around bipyridine showed an unstructured coordination, and not much change during the dynamics simulations. Finally, the solvent-solvent RDFs showed almost no change in structure, only a minor expansion, likely as a consequence of the energy transfer from the solute to the solvent during the excited state dynamics.

Analysis of the angular-RDFs, allowed us to investigate the change in solvation around the cyanides in greater detail. The ARDFs showed that the water molecules mainly "attack" the cyanides at CN-H-O angles of 135-180°, and C-N-H angles above 90° in the ground state. During the excited state dynamics, the angle of "attack" shifts towards more straight 180° angles. Additional analysis showed a decrease in the number of hydrogen bonds around the cyanides from ~3.8 to 3.3 as a result of the excitation. The reorganization of the H-bonds occur on a time scale of 113 ± 4.5 fs.

Calculated X-ray scattering signals: From the RDFs, we computed the expected time-dependent X-ray difference scattering signals, in terms of the solute, cross-term and solvent. The calculated signals arising from the solute showed a strong negative feature in the low-Q region (below $0.7\,\text{Å}^{-1}$), consistent with metal-ligand bond elongations. Additionally, the solute contributions showed coherent excited state dynamics in terms of oscillations of roughly ~100 fs. The calculated cross-term contributions also showed hints of the oscillations in the low-Q region below $1\,\text{Å}^{-1}$. The solvent contributions showed mainly negative features below $Q = 2\,\text{Å}^{-1}$, and a broad positive feature around $Q = 2.4\,\text{Å}^{-1}$, that increases as time progresses in the simulations. Furthermore, the calculated signals, from both the cross-term and solvent term, showed several intermediate features within the simulated excited state dynamics time-frame, which illustrate the reorganizing solvent and changing solute-solvent interactions.

6.5 Main conclusions and discussion

The investigations of the $[Fe(bpy)(CN)_4]^{2-}$ complex concerned the ultrafast excited state dynamics following absorption of visible light using both theory and experiments. In particular, the relationship between electronic, structural and solvent dynamics was studied. We collected experimental steady state absorption spectra, ultrafast transient absorption measurements and time-resolved XFEL scattering signals. However, only the analysis of the steady state absorption spectra were covered in this thesis. Additionally, excited state dynamics simulations of the $[Fe(bpy)(CN)_4]^{2-}$ system in explicit solvation were carried out.

The steady state absorption results on the $[Fe(bpy)(CN)_4]^{2-}$ system in solvent mixtures show that it is possible to modify the energetic landscape simply by changing the solvent, and additionally to do so in a systematic manner from DMA-water solvent mixtures. The trend is approximately linear but with a slight preferential solvation of DMA at low concentrations of DMA in the mixtures. These results confirms existing literature [49] on the type of same study. Whether the excited state dynamics change in a similar systematic manner, is still under investigations from the TA measurements. Previous TA (and XES) investigations [51, 205] on the system in various solvents show that the excited state dynamics are very different depending on solvent. The question remains, how much it is possible to tune the dynamics simply by using solvent mixtures.

The surface hopping simulations from this study act as a major step forward in the excited state dynamics investigations of the $[Fe(bpy)(CN)_4]^{2-}$ complex. To my knowledge, the current literature on the structural effects during the excited state dynamics, from either experiments or simulations, is rather limited. The simulations presented in this thesis are possibly the first consistent excited state simulation study of the coupled electronic, structural and solvent dynamics of an Fe complex. In addition, the simulations do not simply cover the ground and excited state information, but covers the *dynamics* within the simulated 700 fs of excitation, which allows us to extract kinetic time constants of the given processes.

The simulations give information about **(I)** which excited states are populated and how they evolve during the dynamics, **(II)** how the geometry changes as a result of the excitation, **(III)** the influence of the solvent and how the solvent responds to the changes in the solute, **(IV)** how the electronic, structural and solvent dynamics might be correlated or might affect each other. Finally, the simulations allow for comparison with experiments from the calculation of the expected X-ray scattering signals. The following paragraphs present the main conclusions from each part.

(I) electron dynamics:
Excitation in the lowest energy band of the absorption spectrum populates almost exclusively the S_3 singlet excited state. Relaxation via IC ($S_3 \rightarrow S_{1,2}$, 0.11±0.01 ps) and ISC ($S_{\mathrm{All}} \rightarrow T_{\mathrm{All}}, 0.21 \pm 0.02$ ps) occurs on similar time scales, but not as fast as for $[Ru(bpy)_3]^{2+}$

[153, 154] and $[Fe(bpy)]_3^{2+}$ [38] where ISC is even faster (few fs). The longer ISC observed in our simulations, indicates that the cyanide ligands in the geometry influence the ISC time.

Additionally, analysis of the charge transfer character showed an initial population of states with predominantly MLCT character, in agreement with experiments [51]. We also observe a decay from states of MLCT to MC character as in the experiments, but as a parallel decay from the singlet states of predominantly ^{1}MLCT character to triplet states of both ^{3}MC and other triplets of mainly ^{3}MLCT character. Thus, we find a relatively fast (0.53 ± 0.09 ps) population of the ^{3}MC state from the singlet manifold and a slower (2.19 ± 1.46 ps) population of the ^{3}MC state from other triplet states of predominantly ^{3}MLCT character. The population of the ^{3}MC states in the simulations is faster than reported from the XES experiments (~0.09 ps) [51], however they excite at 400 nm (in the second energy band of the absorption spectrum), which might lead to a faster ^{3}MC population growth. In comparison, the MLCT to MC transition in $[Fe(bpy)]_3^{2+}$ is $\leq$ 150 fs [38, 40], while, under debate whether a ^{3}MC state is populated before the ^{5}MC state or not. The $[Fe(bpy)(CN)_4]^{2-}$ system does not populate ^{5}MC states according to experiments [51], which again shows the effect of the cyanides.

A branched decay mechanism from initially excited MLCT states to both ^{3}MLCT and ^{3}MC excited states was also observed experimentally for the iron carbene system, $[Fe(bmip)_2]^{2+}$ [58], in which excitation into states of MLCT character decayed with a time constant of 110 fs into 60 % ^{3}MLCT and 40 % ^{3}MC states.

(II) structural dynamics:

The main structural response are related to changes in the Fe-N_{bpy} bonds, which elongates directly upon excitation. Within the earliest 100 fs the average Fe-N bond lengths elongate by ~0.05 Å, followed by a slower elongation of roughly ~0.1 Å by the end of the simulated 700 fs, relative to the ground state. In comparison to $[Ru(bpy)_3]^{2+}$ (Chapter 5) and $[Fe(bpy)]_3^{2+}$ [236, 237, 238] the structural changes associated with the MLCT states are basically non-existing (order of 0.001 Å), whereas DFT simulations [233] of the structurally similar $[Ru(bpy)(CN)_4]^{2-}$ report Ru-N bond elongations of ~0.05 Å from ground state to the lowest lying triplet state of ^{3}MLCT character.

Thus, the results indicate that the cyanide ligands also influence the structural response related to population of MLCT states. In contrast, the structural response related to the populations of excited states of mainly MC character is found to result in longer Fe-N bonds, based on the simulations of $[Fe(bpy)(CN)_4]^{2-}$ and from a comparison to $[Fe(bpy)]_3^{2+}$ [44, 238] with elongations of ~ 0.2 Å during the relaxation to the high-spin ^{5}MC states [242, 243] and to other Fe-based compounds [231, 235, 166, 244, 245] which show ~ 0.1 Å bond elongations for MC states.

(III) solvent dynamics:
As we already knew before this study, the solvent plays an important role, for this complex of the excited state energetic landscape (in terms of absorption spectrum), and in the change in excited state dynamics depending on solvent [49, 50, 51, 206]. Hence, we included explicit solvation in the simulations, which allows us to observe the (nearest) solvent response directly upon excitation. We collected time dependent RDFs and ARDFs, where we observe the "real-time" response of the solvent.

We confirm, previous studies of $[Fe(bpy)(CN)_4]^{2-}$ [203] and the structurally similar $[Ru(bpy)(CN)_4]^{2-}$ [233], that show a strong interaction of the CN ligands with the solvent, through hydrogen bonds, which are weakened in the excited state. We find a reduction of the number of H-bonds around the cyanides decreasing from ~3.8 to 3.3 after photoexcitation. The decrease in hydrogen bonds decay monoexponentially with a time constant of ~ 110 fs. Also, the decrease in hydrogen bonds is slightly higher around the axial (~3.9 to 3.3) than the equatorial (~3.5 to 3.2) cyanides.

In addition, the results show that the solvent reorganizes around the cyanide ligands such that the H-bonds shift to more straight 180° C-N-H angles and thus ”attack” more end on, within the 700 fs simulated time. As suggested by Toma et. al [49] back in 1983, such a strong solute-solvent interaction allows for a stabilization of the (metal centered) ground state by removal of electron density from the cyanides, and consequently an increase in π-backdonation from the metal. Consequently, the ground state (metal-centered) is stabilized relative to the excited MLCT states, leading to larger excitation energy (shift in absorption spectrum towards shorter wave lengths).

Charge transfer from the metal center to the bipyridine ligand in the excited MLCT state results in less π-backbonding to the cyanides, which likely weakens the cyanide-hydrogen bonds.

(IV) Correlations:

The relationship between electronic populations and structural response, was already discussed above, in terms of the differences in structure based on MLCT or MC character of the excited states. Additional investigations wish to examine if certain bond lengths or normal modes assist the transition from MLCT to MC, since we observed hints of oscillating features in the time dependent populations with a period of roughly 100 fs. Such a ballistic mechanism was also observed in recent experiments of $[Fe(bpy)]_3^{2+}$ [41] for the ^{3}MC to ^{5}MC transition and in excited state simulations [241] of an iron carbene $[Fe(bmip)_2]^{2+}$ complex in the population from MLCT to MC states. In addition, we observed coherent dynamics from the solute contribution in the calculated scattering signals, as a consequence of the excitation.

The electron-solvent relationship was mainly observed from the change in the observed maximum of the lowest absorption band simply by changing the solvent from the steady state experiments. In addition, our studies show that the solvent response occur directly upon excitation, and reorganizes as a consequence of the change in the electronic wave function. Previous studies [51] of the complex in implicit and 4 explicit water molecules indicate that the excited state energy change upon including the specific solvation. They report that all states are destabilized relative to the ground state, however the effect is largest for the lowest ^{3}MLCT state than for the ^{3}MC state. Hence, the large solvent effect is presumably not based on electronic effects but rather direct hydrogen bonding effects, as confirmed by our study.

The coupling between structure and solvent is most evident from the calculated scattering signals, in which the oscillations from the solute, is also present in the solute-solvent cross-term signals. However, a deeper understanding of any couplings between structure and solvent dynamics require investigations in other solvents as well.

6.6 Outlook

The main work of this thesis, regarding the $[Fe(bpy)(CN)_4]^{2-}$ complex concerns the excited state dynamics simulations, and thus the obvious next step would be to compare the simulations to experiments. We already collected data from combined ultrafast time-resolved X-ray emission and X-ray scattering measurements from an XFEL. However, as discussed in the previous chapters, data reduction and analysis is a non-trivial task, and thus the analysis of the data is still under way. From the X-ray emission data, we observe the change in the electronic density on the Fe center, which we could compare to the simulated electronic populations and charge transfer analysis. The time-resolved X-ray scattering data gives us information on the structural response of the solute, and the response of the solvent. We computed the expected time-dependent X-ray scattering signals, which allows for a direct comparison to experiment. The measured scattering data is briefly presented in the next paragraph, however, the analysis of the data is still under way.

In terms of simulations, relevant future studies concern excited state dynamics simulations in various solvents, and potentially in solvent mixtures. In particular, solvents of interest include a weak Lewis acid, such as acetonitrile (MeCN), Dimethylsulfoxid (DMSO), Dimethylformamide (DMF) or dimethylacetamide (DMA). These solvents show the most different absorption spectrum of $[Fe(bpy)(CN)_4]^{2-}$ relative to the absorption spectrum measured in water. In order to investigate the hydrogen bonding between the solute and solvent in greater detail, it would be of interest to study other H-bonding solvents such as methanol (MeOH) or ethanol (EtOH). Furthermore, a computational study in solvent mixtures of water and DMA would allow for a comparison to the measured transient absorption data. In particular, a deeper study of the preferential solvation in solvent mixtures, and the effect on the excited state dynamics is of interest.

Brief presentation of the XFEL scattering data

Figure 6.29 shows the measured X-ray scattering difference signals collected at the X-ray Correlation Spectroscopy, XCS instrument at the LCLS, located in California at SLAC National Accelerator Laboratory. The necessary data reduction and filtering was carried out by the graduate student Kathryn Ledbetter, from the group of Kelly Gaffney, as one of the collabo-

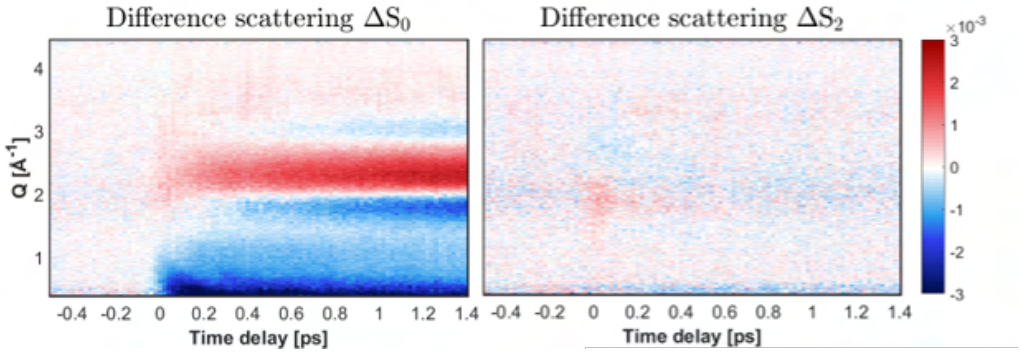

Figure 6.29: Measured time-resolved wide angle X-ray difference scattering signals ΔS as a function of the scattering vector Q, and time delays from -0.5 to 1.4 ps, of the $[Fe(bpy)(CN)_4]^{2-}$ complex in water. Left: The isotropic contribution, ΔS_0. Right: The anisotropic contribution, ΔS_2.

rating partners located at the facility. The data is not yet scaled according to the sample concentration, hence the amplitude of the measured signals should only be considered relative to each other. The left plot of the figure shows the isotropic difference scattering signals, ΔS_0, and the right plot shows the anisotropic contribution, ΔS_2.

The anisotropic contribution mainly shows the ultrafast response from the solvent, as we found in the case of $[Ru(bpy)_3]^{2+}$ in water, discussed in chapter 5, section 5.2.2.

The isotropic contribution shows a clear response after time zero, with mainly a negative feature at $Q < 1\,\text{Å}^{-1}$. Such a negative feature is well in agreement with the calculated scattering from the contribution of the structural changes in the solute, based on a qualitative comparison of figure 6.27. Furthermore, the isotropic contribution shows the feature of heated water with the positive signal around $Q = 2.2\,\text{Å}^{-1}$, with negative features on both sides. This feature shows a slower grow-in after few hundreds of fs, and is in qualitative agreement with the calculated features observed from the cross-term and solvent contributions.

Future analysis includes further comparisons of the simulated and calculated scattering data.

Chapter 7

Publications and Other work

This chapter gives an overview of the work during the Ph.D. studies that let to a publication, along with a brief description of each paper and other work carried out during the studies.

7.1 Publications and contributions

Paper I **Excited-state solvation structure of transition metal complexes from molecular dynamics simulations and assessment of partial atomic charge methods**
Mostafa Abedi, Gianluca Levi, **Diana B. Zederkof**, Mátyás Pápai and Klaus B. Møller. *Phys. Chem. Chem. Phys.*,vol. 21, no. 7, pp. 4082-4095. 2019.
https://doi.org/10.1039/C8CP06567E.
Contributions: Contributed to the pre-analysis related to the $[Ru(bpy)_3]^{2+}$ complex, by carrying out preliminary MD simulations showing contradictory results depending on type of partial charge, which let to the idea of a more comprehensive, systematic study. Analyzed the differences between few types of partial charges for the $[Ru(bpy)_3]^{2+}$ complex. Contributed to the scientific discussions using different types of partial charges. Revision of the manuscript two times through internal review.

Paper II **Excited state charge distribution and bond expansion of ferrous complexes observed with femtosecond valence-to-core x-ray emission spectroscopy**
Kathryn Ledbetter, Marco E. Reinhard, Kristjan Kunnus, Alessandro Gallo, Alexander Britz, Elisa Biasin, James M. Glownia, Silke Nelson, Tim B. Van Driel, Clemens Weninger, **Diana B. Zederkof**, Kristoffer Haldrup, Amy A. Cordones, Kelly J. Gaffney, Dimosthenis Sokaras and Roberto Alonso-Mori. *J. Chem. Phys.*, vol. 152, no. 7, pp. 074203 (2020).
https://doi.org/10.1063/1.5139441
Contributions: Participated in the XFEL experiment and data collection of the measurements on the $[Fe(bpy)(CN)_4]^{2-}$ complex. Revising the manuscript through two iterations.

Paper III **Observing the structural evolution in the photodissociation of diiodomethane with femtosecond solution X-ray scattering**
Matthijs R. Panman, Elisa Biasin, Oskar Berntsson, Markus Hermann, Stephan Niebling, Ashley J. Hughes, Joachim Kubel, Kalina Atkovska, Emil Gustavsson, Amke Nimmrich, Asmus O. Dohn, Mads Laursen, **Diana B. Zederkof**, Alireza Honarfar, Kensuke Tono, Tetsuo Katayama, Shigeki Owada, Tim B. van Driel, Kasper Kjær, Martin M. Nielsen, Jan Davidsson, Jens Uhlig, Kristoffer Haldrup, Jochen S. Hub and Sebastian Westenhoff. Phys. Rev. Lett. 125, 226001.
https://doi.org/10.1103/PhysRevLett.125.226001.
Contributions: Participated in the experiments both at SACLA and LCLS, and was co-responsible for the data collection of the X-ray scattering measurements on diiodomethane. Revising the manuscript through several iterations.

Each of the papers present investigations of different types of studies and molecular systems. The following sections give a brief summary of the work related to each paper.

7.2 MD simulations of solvation structure

Part of the work related to the structural dynamics investigations on the $[Ru(bpy)_3]^{2+}$ system, led to the publication, **Paper I**, as previously discussed in Chapter 5. In addition, the investigations concern simulations of the ground and excited state solvation structure of several transition metal complexes, namely the structurally similar $[Fe(bpy)_3]^{2+}$ complex, an iron carbene system, $[Fe(bimp)_2]^{2+}$ and a copper-based system, $[Cu(phen)_2]^{+}$. The studies evaluate the performance of several of the most popular partial atomic charge (PAC) methods for the description of the charge distribution of the solute, applied in classical molecular dynamics (MD) simulations of the metal complexes in solution. The various PACs were evaluated against higher theoretical level mixed quantum mechanics/molecular mechanics (QM/MM) Born-Oppenheimer MD simulations, based on collected radial distribution functions (RDFs) from both methods.

The motivation for employing pure classical MD simulations is the desire for computational tools that allow for simulations of large systems containing thousands of solvent molecules, and long simulations for good statistics. In particular, the interpretation of the structural dynamics related to the solvent from X-ray scattering experiments are often challenging, and thus simulation tools are desired for the assistance of interpretation.

The results show that choice of the most suitable PAC method depends on the type of ligands and how much space between the ligands is available in order for the solvent to approach the metal center of the given complex. For the four complexes studied, the overall results show that the ChelpG/RESP or CM5 type PACs prodcued RDFs closest to those obtained from QM/MM MD simulations.

7.3 Ultrafast Valence-to-Core X-ray Emission Spectroscopy

As part of the XFEL experiments on combined X-ray Emission Spectroscopy (XES) and X-ray scattering measurements on the $[Fe(bpy)(CN)_4]^{2-}$ system, we also measured Valence-to-Core X-ray Emission Spectroscopy (VtC XES). The time-resolved VtC XES technique is an emerging tool to study transition metal complexes, in particular, iron-based complexes. The spectral region of "traditional" hard X-ray XES concerns the radiative decay associated with 2p-1s (K_α) and 3p-1s (K_β) transitions, whereas VtC XES concerns the decay from valence electrons to the metal core (3d-1s). Hence, VtC XES is sensitive to changes in the local bonding and chemical environment of the metal.

Extension of the technique to the ultrafast regime is still a relatively new tool, and requires sufficient photon flux and very sensitive spectrometers. The measured VtC XES data, was used to demonstrate the potential of the technique, and let to the publication, **Paper II**, written in collaboration by Kathryn Ledbetter and co-workers. I participated in the experiment carried out at the LCLS on the $[Fe(bpy)(CN)_4]^{2-}$ system. Extending the VtC XES technique to the ultrafast regime makes it a promising tool to study changes in local geometry, ligand environment and oxidation states following photoexcitation. The VtC XES spectra are sensitive to both electronic and geometric changes making them promising tools to study ultrafast coupled electronic-nuclear excited state dynamics.

In the work related to the paper, the data from three iron complexes was compared, the $[Fe(CN)_6]^{4-}$, $[Fe(bpy)(CN)_4]^{2-}$ and $[Fe(bpy)_2(CN)_2]$ systems. Comparisons of the measured spectra with ground state DFT calculated spectra revealed signatures of changes associated with bond lengths and oxidation state. Furthermore, the simulated spectra VtC XES spectra of the same type of excited state (e.g. ^{5}MC) show different features, depending on the molecular system, which shows the sensitivity to chemical structure. The excited VtC spectrum associated with $[Fe(bpy)(CN)_4]^{2-}$ showed most resemblance with the simulated spectrum for a ^{3}MC state, and not a ^{5}MC state, and thus the method also shows sensitivity of local spin-state on the absorbing metal. Furthermore, for the $[Fe(bpy)(CN)_4]^{2-}$ complex, the population of a triplet metal centered excited state instead of a quintet state also confirms previous studies using K_β XES [51].

7.4 X-ray scattering on the diiodomethane system

Before my Ph.D. studies, I was invited to participate in an XFEL scattering experiment on the photo-dissociation of diiodomethane (CH_2I_2) in solution at the SACLA facility. Later the proposed study was also accepted at the LCLS facility, where I also participated very early in my Ph.D. studies. The results presented in **Paper III** are focused on the measurements at the LCLS experiment due to increased time-resolution. My involvement in the project mainly concerns the two experiments, where I was co-responsible for the data-handling of the large amounts of scattering data.

Paper III presents the ultrafast time-resolved wide angle X-ray scattering measurements of CH_2I_2 dissociating into the two radicals $CH_2I^{\bullet}$ and $I^{\bullet}$. Through a fitting procedure of a model based on classical MD simulations to the experimental data, the time-dependent structural dynamics was extracted. The results show the dissociation process and how the radicals collide with the nearest solvent and later form the photo-isomer CH_2I-I. The photo-dissociation process act as model system to study elementary chemical events.

7.5 Other experiments at XFELs

During the Ph.D. studies, I have participated in several "beamtimes" at either the Linac Coherent Light Source (LCLS) [246, 10] located in California, the SPring-8 Angstrom Compact free electron LAser (SACLA) [11, 247] located in Japan, or the European-XFEL located in Hamburg. The time frame of the Ph.D. studies have been particularly exciting for the hard XFEL community due to the commissioning of not just one but three new hard XFELs, producing light with wavelengths on the order of Å. Both the European-XFEL, the Swiss-FEL [248, 249] in Switzerland and the PAL-XFEL [250] in Korea have been commissioned, and furthermore the upcomming high-energy upgrade at the LCLS [196], makes the future studies involving XFELs very exciting.

Particularly, at the European-XFEL, our group has participated in several of the early user experiments at the FXE instrument during the Ph.D. studies. With several collaborators, we measured the Cu-based complex $[Cu_4(PCP)_3]^{3+}$ complex, at the second user assisted experiment at the FXE

instrument. We also measured the combined X-ray scattering and emission of the $[Fe(bpy)(CN)_4]^{2-}$ complex in various solvents. However, the experiments at the FXE instrument have proven particularly challenging, and the instrument is still under constant development.

Additionally, during the Ph.D. studies, I participated in five different X-ray scattering and emission experiments at the LCLS measuring the photoinduced dynamics in diiodomethane (**Paper III**), Fe-based nanoparticles, the previously discussed measurements on the $[Fe(bpy)(CN)_4]^{2-}$ system (**Paper II**), the structurally similar iron-based, $[Fe(terpy)_2]^{2+}$ system, and the bi-metallic iridium-based $[Ir_2(dimen)_4]^{2+}$ complex. My main contributions to the work was to assist the data collection and reduction process during the experiments. The data from most of these experiments are not yet published, due to the large amount of necessary data analysis, which is still ongoing.

At the SACLA facility, I participated in two experiments during my Ph.D. studies, measuring different iron-carbene systems, and bromoform ($CHBr_3$) in various solvents. Again, my contributions to the work was to assist the data collection and reduction process during the experiments. The analysis of the data from these beamtimes is still ongoing.

All investigations using XFEL experiments, have relied on large international collaborations, and require a lot of manpower in terms of developing and running the XFEL instruments, handling the large amounts of data, and analysis of the data. Thus, the pathway to publications is often long, since the ultrafast dynamics studies employing X-ray scattering is truly a field that requires a great team effort.


SACLAとSPring-8がつながれば、
もっとたくさんの人が、もっと小さな世界を見ることができます。
SACLA
SPring-8
SACLA x SPring-8

Chapter 8

Summary and Conclusions

8.1 Summary

This section gives a summary of the thesis with a short description of each part and chapter.

Chapter 1
The first chapter gave an introduction to the field, and the motivation for the study. The topic of interest is ultrafast excited state dynamics of solvated transition metal complexes. These molecular complexes are of particular interest due to their ability to absorb visible light, and the potential of fine-tuning their excited state properties by adjustment of the chemical structure and local environment. This thesis concerns the two model systems referred to as $[Ru(bpy)_3]^{2+}$ and $[Fe(bpy)(CN)_4]^{2-}$.

Following the introduction, the thesis was divided into three parts.

Part I The first part was focused on the experimental background information, in particular the use of X-ray scattering as a probe for ultrafast dynamics studies.

Part II The second part presented the basics of the theoretical background related to the computational studies of this thesis.

Part III The last part described the analysis and results on the $[Ru(bpy)_3]^{2+}$ and the $[Fe(bpy)(CN)_4]^{2-}$ systems, along with a brief description of other work during the Ph.D. studies.

Chapter 2
The second chapter of the thesis described how X-ray scattering, is a useful technique to study molecular structure, and that the use of X-ray Free Electron Lasers (XFELs) allow for measurements of the molecular dynamics by use of fs-time-resolved X-ray scattering. The experimental setup employs an optical pump, X-ray probe setup with the sample in a free flowing jet, and the scattering collected by advanced detectors. Each detected image requires Megabytes of space, and thus the collected set of images throughout the experiment require substantial treatment in terms of data reduction and additionally undergo corrections and filters before the data is ready for analysis. Finally, the chapter described the advantage of analyzing *difference* scattering signals, and that scattering is a global probe, measuring both the structural changes of the solute and the solvent.

Chapter 3
In the third chapter, it was described how computer simulations act as a useful tool to study the electronic structure of different types of systems. Hence, the chapter described the basics of Density Functional Theory (DFT), which is a popular method since it provides a good balance between fast and accurate results. Additionally, the time-dependent variant TD-DFT was employed to study the excited state landscape. Furthermore, the chapter introduced classical and mixed quantum-classical methods, which are particularly useful when including the solvent in the simulations. Finally, the chapter described how to describe the nuclei dynamics of the molecular systems either by pure classical methods or by surface hopping methods, as applied in this work.

Chapter 4
Chapter four of the thesis described some of the useful tools applied for the analysis of the computational results. The basic principles of the calculation of the electronic populations was described. The TheoDORE analysis tools are particularly useful to study the charge transfer character of each excited state, and provides a quantitative description of the localization of the excited charge.

Chapter 5
The next chapter presented the analysis and results on the $[Ru(bpy)_3]^{2+}$ system. Ultrafast time-resolved X-ray difference scattering signals obtained at an XFEL, were presented. The data was modeled by use of classical molecular dynamics (MD), and mixed quantum-mechanics/molecular mechanics (QM/MM) MD simulations. The chapter presented the analysis of the measured anisotropic scattering signals. A small feature was assigned to the ultrafast response of the water molecules to the polarization of the optical laser. It was presented how to use the anisotropic signal to determine the instrument response function of ∼160 fs. The isotropic part was analyzed using radial distribution functions (RDFs) from dynamics simulations, in which the mixed QM/MM MD results were in better agreement with the experimental data than the classical MD results.

Chapter 6
This chapter presented the analysis and results on the $[Fe(bpy)(CN)_4]^{2-}$ system. The metal complex was studied using optical absorption measurements in solvent mixtures of water and dimethylacetamide (DMA), which showed an approximately linear shift in the absorption maximum of the lowest energy band from just below 500 nm to roughly 725 nm, by changing the solvent water/DMA composition.

Additionally, the chapter presented results from excited state dynamics simulations for the earliest 700 fs upon excitation of the $[Fe(bpy)(CN)_4]^{2-}$ system in explicit water. Key results find the decay mechanism from the singlet S_3 excited state to lower lying singlet states ($S_{1,2}$) occur on similar time scales (0.11±0.01 ps) as intersystem crossing (ISC) to triplet states (0.21±0.02 ps). The triplet excited states showed a mixture of states of mainly ^{3}MLCT or ^{3}MC charge transfer character, which are both populated from the initial ^{1}MLCT excited states. Results on the structural dynamics mainly concerned Fe-bipyridine bond elongations, and a strong solute-solvent interaction between the (cyanide-water) nitrogen-hydrogen atoms, weakened in the excited state.

Chapter 7
After the main chapters of analysis and results, the next chapter presented an overview of co-authored publications written during the Ph.D. studies, along with a brief description of other work carried out during the studies. At the time of submission of this thesis, I co-authored 3 publications.

8.2 Conclusions

The work presented in this thesis describes the ultrafast excited state dynamics of solvated metal complexes, in particular the $[Ru(bpy)_3]^{2+}$ and $[Fe(bpy)(CN)_4]^{2-}$ systems. Key investigations concerned the structural dynamics related to populations of MLCT excited states, and the influence of solvation. Methods of investigation were both experiments and theory, in terms of TR-WAXS measurements and several types of simulations of the molecular dynamics.

The $[Ru(bpy)_3]^{2+}$ investigations: The advantages and challenges of both theory and experiments was evident in the $[Ru(bpy)_3]^{2+}$ investigations, where the measured TR-WAXS signals clearly show a response of the system upon photoexcitation, however the interpretation of the measured difference signals required assistance from simulations. The explanation of why the classical methods fail, might be a result of two main factors. Firstly, that the methods mainly show good results of the solvent response as a consequence of structural changes of the solute, however, the structural changes within the $[Ru(bpy)_3]^{2+}$ complex from ground state to ^{3}MLCT excited state are minimal (~ 0.001 Å). Secondly, the methods fail to describe the electronic interactions. Since, the excited state shows MLCT character, which involves the bipyridines, the solute-solvent interaction is more direct and likely larger, than for excited states of predominantly MC character.

A model based on higher level QM/MM MD simulations of the solvated system in the electronic ground state and the lowest excited triplet state of MLCT character, was in better agreement with the experimental scattering data. However, the second model was also in poor agreement with data at the earliest time delays (below 1 ps). The discrepancy at early times was assigned to the model missing the relaxation of the nearest solvent, since the model was based on simulations of averaged structural dynamics after solvent equilibration. In conclusion, caption of the earliest dynamics calls for excited state dynamics simulations of both the solute and solvent, in order to directly capture the immediate response of the system.

The $[Fe(bpy)(CN)_4]^{2-}$ investigations: Excited state dynamic simulations were carried out for the $[Fe(bpy)(CN)_4]^{2-}$ system in explicit water. From analysis of the electronic populations, the excited state relaxation of the $[Fe(bpy)(CN)_4]^{2-}$ system undergoes a larger degree of branched decay than the $[Ru(bpy)_3]^{2+}$ system within the earliest 700 fs after photoexcitation. Both systems show an initial population of states of predominantly MLCT character. However, in contrast to the $[Ru(bpy)_3]^{2+}$ system, the simulations on $[Fe(bpy)(CN)_4]^{2-}$ show populations of metal-centered states within 0.53 ± 0.09 ps. The population mainly occurs from MLCT states from both the singlet and triplet manifold. The results find an overall time of intersystem crossing (ISC) of 0.21 ± 0.02 ps, hence ISC is faster for $[Ru(bpy)_3]^{2+}$ [153, 154] and for $[Fe(bpy)_3]^{2+}$ [38] (within few fs) than for the $[Fe(bpy)(CN)_4]^{2-}$ complex.

In terms of structural response, the main effects are related to the metal-ligand bonds. The Fe-bipyridine bonds elongate after photoexcitation on two times scales. A fast elongation within the first 100 fs of ~0.05 Å on average followed by a slower elongation of roughly ~0.1 Å by the end of the simulated 700 fs, relative to the ground state distance. The fast elongation is likely a direct response to the excitation and population of mainly MLCT excited states, whereas the slow elongation is the structural response to the increasing population of MC excited states.

The $[Fe(bpy)(CN)_4]^{2-}$ system shows a strong interaction with the solvent, observed from the strong solvatochromism of the steady state absorption spectrum. The lowest energy band shift approximately linearly from ~485 nm (pure water) to ~725 nm (pure DMA) in water/DMA solvent mixtures. For low concentrations of DMA, the observed shift is larger than expected from a linear trend, indicating a preferential solvation of DMA. We speculate that DMA preferentially solvates the bipyridine unit, and the water mostly interacts with the cyanide ligands. The strong cyanide-water interaction was confirmed by the excited state dynamics simulations, for both ground and excited states. The strong cyanide-hydrogen bond was slightly weakened following photoexcitation, based on a reduction in the number of nearest hydrogen bonds from 3.8 to 3.3, with a decay constant of ~ 0.11 ps.

General conclusions:

1. Based on the investigations of the $[Ru(bpy)_3]^{2+}$ and $[Fe(bpy)(CN)_4]^{2-}$

complexes, this study confirms that the structural changes as a response to populations of excited MLCT states are minimal.

2. The cyanide ligands strongly influence the ultrafast excited state dynamics and thus the structural response.

For the case of $[Ru(bpy)_3]^{2+}$ and $[Fe(bpy)_3]^{2+}$ the structural changes associated with MLCT states are on the order of ∼0.001 Å [236, 237, 238], whereas simulations on the $[Fe(bpy)(CN)_4]^{2-}$ and $[Ru(bpy)(CN)_4]^{2-}$ [233] report structural changes on the order of ∼ 0.05 Å for the metal-bipyridine bonds. Since, the cyanide ligand, is a very strong-field type ligand it binds very tightly to the metal, which changes the electronic structure by allowing π-backbonding from the metal. Hence, the bipyridine and cyanides are very different types of ligands. Additionally, our simulations on the $[Fe(bpy)(CN)_4]^{2-}$ system show that, especially at early times, the cyanides participate in the charge transfer from "metal" to the bipyridine and thus participate in the "metal-to-ligand" charge transfer. Hence, this study concludes that the cyanides play an important role related to charge transfer and thereby also influence the structural response from the excitation into MLCT excited states.

3. For both systems, the solvent plays an important role for the excited state dynamics.

4. The interaction with the solvent is very different for the bipyridine and cyanide ligands. The water solvent shows only minor interaction with the bipyridine ligands, whereas the cyanides strongly interact and form hydrogen bonds to the nearest water molecules.

5. The solvent responds instantly to the excitation in terms of change in solute-hydrogen (from water) distances/bonds, and additionally shows a slower response in terms of diffusion of water molecules (based on solute-water (oxygen) distances).

In terms of solvent effects, both systems, but in particular the $[Fe(bpy)(CN)_4]^{2-}$ system, show different excited state properties such as the position of the lowest energy band in the absorption spectrum, MLCT lifetimes and structural changes depending on the nature and type of solvent. Considering the solute-solvent interactions, the cyanide ligands also play an important

role, based on the observed strong CN-H bonds formed with the nearest water molecules in the case of the $[Fe(bpy)(CN)_4]^{2-}$ complex in aqueous solution. In contrast, the interactions between the bipyridine ligand and water are minimal and do not show much change from ground to excited state for both the $[Ru(bpy)_3]^{2+}$ and $[Fe(bpy)(CN)_4]^{2-}$ complexes.

Considering the time scales, the solvent shows a direct response upon excitation, mainly in the form of shifts to larger distances and weakened hydrogen bonds of CN-H. From the iron-solvent difference RDFs, a small change in Fe-H distances is instant whereas the Fe-O distances increase slower. The results indicate that the solvent responses directly to the change in charge distribution rather than to the the structural changes of the solute, (which likely give a response on longer time scales).

6. Calculated scattering from pure classical molecular dynamics simulations were not in agreement with experimental data, for the case of $[Ru(bpy)_3]^{2+}$.

7. Excited state dynamics simulations including solvation is likely the way forward in terms of understanding the earliest solvent response observed from ultrafast time-resolved X-ray scattering measurements.

8. Computational and experimental techniques continuously complement each other in ultrafast electronic and coupled electronic-nuclear excited state dynamics studies of solvated transition metal complexes.

Finally, this study found that pure classical dynamics simulations were not accurate enough (from comparison to experiment) for the description of the solvent structural changes upon photoexcitation into the MLCT manifold, in the $[Ru(bpy)_3]^{2+}$ system, and possibly for solvent dynamics concerning MLCT states in general. Mixed QM/MM MD simulations of the Ru-system in the lowest ^{3}MLCT excited state, was in better agreement with experimental data at longer time delays (1 ps), indicating that the early solvent dynamics is very different from the simulations of the solvent after re-equilibration. Furthermore, such type of simulations of the solute and solvent response, becomes more challenging when the systems show a branching decay mechanism from the initially excited states, as was found for the $[Fe(bpy)(CN)_4]^{2-}$ system.

8.3 Outlook

Minor structural changes associated with MLCT states: In order to investigate in greater detail, whether MLCT excited states of potential photosensitizers in general leads to only minor structural changes, one could make a more systematic study of several compounds that show relatively long-lived (ps) MLCT excited states. However, currently the number of existing metal complexes based on earth-abundant metals, and showing long-lived MLCT excited states is rather limited and is therefore also the type of complex, which is desirable to design.

Solvent response using classical methods: The conclusion that the purely classical methods are not accurate enough to describe the dynamics and solvent response related to MLCT excited states requires additional investigations of other metal complexes showing excited state dynamics involving MLCT states. Whether the trajectory surface hopping simulations are accurate enough still requires a comparison to the experimentally obtained difference scattering signals, which is an obvious next step for the case of the $[Fe(bpy)(CN)_4]^{2-}$ system. Similarly, excited state dynamics simulations of $[Ru(bpy)_3]^{2+}$ including solvation might also reveal if the early dynamics observed experimentally can be explained from simulations.

Affect of cyanides: In terms of the influence of the cyanide ligands, it would be of interst to compare metal-bipyridine-based compounds with cyanides (CN^-), carbonyls (CO), and nitrosyls (NO^+), which are all isoelectronic, but with different charge and donor/acceptor abilities. Such an investigation could deepen the understanding of the interaction between the metal center and these tightly bound ligands, in particular the effect of π-backbonding from the metal to these type of ligands. Additionally, how the ligands effect the interaction with the solvent, and the excited state dynamics.

Affect of solvent: In order to investigate the solvent influence in greater detail, the obvious next step is to study the $[Ru(bpy)_3]^{2+}$ and $[Fe(bpy)(CN)_4]^{2-}$ systems in other solvents, and perhaps also in solvent mixtures. Such investigations are already planned in terms of experiments, but would also be of interest in terms of simulations. The fact that the solvent alone is capable of changing the excited state structural dynamics is a new frontier and has the opportunity to play an important role in future developments of materials for light absorption applications.

Experiments vs. simulations: Experimental observations have the advantage of often being considered as the most trustworthy observation. Thus, simulations are often benchmarked against experimental results. On the other hand, experiments often provide highly correlated information, and do not always give a simple answer. The results from the experimental TR-WAXS difference signals are particularly useful to answer questions on the dynamics of the molecular structure. However, at the same time, the measured signals show the structural changes in a global perspective such that the signals show contributions from changes within both the solute and solvent, which are highly correlated. In contrast, simulations give unprecedented detail down to the electronic and atomic level. Hence, we can observe exactly which chemical bonds change and how. However, simulations might have difficulties describing larger metal complexes containing heavy atoms or several metal atoms, or complicated systems in terms of solvent e.g. systems in solvent mixtures. Furthermore, regardless of the level of detail, if a given simulation, strongly disagrees with experiments, it is often considered worthless. Likewise, the analysis of TR-WAXS signals often depends on simulations for the interpretation of the results. Hence, both methods complement and depend on each other.

Future perspectives of the methods: For the future development of new photosensitizer systems, and with the increasing time-resolution found in experiments, the way forward relies on a higher demand of simulations of a higher level of accuracy in terms of solute-solvent interactions. Hence, excited state dynamics simulations including explicit solvation is a way forward in terms of understanding the direct response of both the solute, the solvent and their coupling. Additionally, ultrafast time-resolved X-ray scattering experiments continuously develop the resolution in both space (Q-region) and time domain, making it a particularly useful tool to study solvation dynamics related to photoabsorption processes, but still relies on simulations for interpretation of the solvent response.

Appendix A

Paper I

View Article Online
DOI: 10.1039/C8CP06567E

PCCP

ARTICLE TYPE

Cite this: DOI: 10.1039/xxxxxxxxxx

Excited-State Solvation Structure of Transition Metal Complexes from Molecular Dynamics Simulations and Assessment of Partial Atomic Charge Methods†

Mostafa Abedi,[a] Gianluca Levi,‡[a] Diana B. Zederkof,[b] Niels E. Henriksen,[a] Mátyás Pápai,[ac] and Klaus B. Møller*[a]

Received Date
Accepted Date

DOI: 10.1039/xxxxxxxxxx

www.rsc.org/journalname

In this work, we investigate the excited-state solute and solvation structure of $[Ru(bpy)_3]^{2+}$, $[Fe(bpy)_3]^{2+}$, $[Fe(bmip)_2]^{2+}$ and $[Cu(phen)_2]^{+}$ (bpy=2,2'-pyridine; bmip=2,6-bis(3-methyl-imidazole-1-ylidine)-pyridine; phen=1,10-phenanthroline) transition metal complexes (TMCs) in terms of solute-solvent radial distribution functions (RDFs) and evaluate the performance of some of the most popular partial atomic charge (PAC) methods for obtaining these RDFs by molecular dynamics (MD) simulations. To this end, we compare classical MD of a frozen solute in water and acetonitrile (ACN) with quantum mechanics/molecular mechanics Born-Oppenheimer molecular dynamics (QM/MM BOMD) simulations. The calculated RDFs show that the choice of a suitable PAC method is dependent on the coordination number of the metal, denticity of the ligands, and type of solvent. It is found that this selection is less sensitive for water than ACN. Furthermore, a careful choice of the PAC method should be considered for TMCs that exhibit a free direct coordination site, such as $[Cu(phen)_2]^{+}$. The results of this work show that fast classical MD simulations with ChelpG/RESP or CM5 PACs can produce RDFs close to those obtained by QM/MM MD and thus, provide reliable solvation structures of TMCs to be used, e.g. in the analysis of scattering data.

1 Introduction

Transition metal complexes (TMCs) have been used broadly in solar energy conversion and photocatalysis applications due to their excited-state photophysical and photochemical properties.[1] The advent and development of ultrafast spectroscopy in recent years has made it feasible to study and unravel mechanisms of ultrafast excited-state dynamics of TMCs in solution.[2–4] The experiments reveal that excited-state photophysical and photochemical properties can be strongly affected by the molecular environment in solution leading to significant changes in relaxation rates and products.[5–12] Therefore, in order to get a deep understanding of such processes, a detailed insight into the effect and role of the solvent is essential. By utilizing time-resolved X-ray diffuse scattering (TRXDS) and extended X-ray absorption fine structure (EXAFS) spectroscopy, one can obtain information about the solvent structure.[13–17] However, the complicated ultrafast excited-state dynamics of TMCs and, in particular, the nearest surrounding solvation make the interpretation of the observed experimental features difficult. In this regard, computational chemistry tools play an essential role for comprehensive interpretation and understanding.

There are two commonly used theoretical approaches for considering solvent effects: methods that treat the solvent explicitly and implicit models. In the implicit solvent treatment, also known as continuum solvation models,[18–20] the solvent molecules are approximated by a homogeneous medium. The polarizable continuum model (PCM)[18] is a well-known implicit solvent model. Implicit models do not provide information about the structure of the solvent. Solvent structure can only be simulated using explicit solvent methods, in which the interaction between all solute-solvent pairs is explicitly considered. The explicit solvent treatment is usually employed in classical molecular dynamics (MD), *ab initio* MD (AIMD) or hybrid quantum mechanics/molecular mechanics (QM/MM) MD simulation approaches. In classical MD simulations, the forces are obtained from predetermined molecular mechanics (MM) force fields, while in AIMD an electronic

[a]*Department of Chemistry, Technical University of Denmark, 2800 Kongens Lyngby, Denmark; E-mail: kbmo@kemi.dtu.dk*
‡ *Present address: Faculty of Physical Sciences, University of Iceland, 107 Reykjavík, Iceland*
[b]*Department of Physics, Technical University of Denmark, 2800 Kongens Lyngby, Denmark*
[c]*Wigner Research Center for Physics, Hungarian Academy of Sciences, P.O. Box 49, H-1525 Budapest, Hungary*

† Electronic Supplementary Information (ESI) available: See DOI: 10.1039/cXCP00000x/

View Article Online
DOI: 10.1039/C8CP06567E

structure method is used for calculating the forces on-the-fly; in QM/MM MD, a hybrid scheme of these two approaches is applied. Classical MD simulations are among the most popular methods for studying chemical processes of medium- to large-size systems in condensed phases. One of the main challenges in classical MD is the specification of suitable empirical models for the forces between the atoms. These force fields are parametrized by fitting to experimental data or high-level *ab initio* calculations. A major limitation of this method is that the model is not transferable to any type of reaction or chemical process and often needs to be re-parameterized. On the other hand, classical MD simulations are fast and easy to handle. AIMD addresses the limitation of force fields in MD simulations. In this method, the forces are calculated "on the fly", i.e. during the MD propagation, from electronic structure calculations, typically using density functional theory (DFT). Because the electronic structure calculation is performed at every time step of the simulation, the AIMD method is computationally very demanding. The computational cost can be reduced by density functional tight binding (DFTB),[21] which is much faster than DFT but less accurate[22] or by QM/MM MD, in which the most important part of the system is described by a suitable (high-level) quantum chemistry method and the rest by molecular mechanics using a force field[23–26].

Solvation structure can be obtained from explicit solvent methods through the evaluation of solute-solvent radial distribution functions (RDFs), which can be used for calculations of XDS[27] and EXAFS[28] signals. Classical MD simulations have been extensively applied for calculating RDFs and gaining information about the solvation structure around TMCs in both ground and excited states.[11,29–35] However, standard available force fields are particularly developed for ground-state (GS) MD simulations. This rises a serious problem when performing MD simulations in the excited state: the force fields essentially are required to be re-parametrized. The pairwise electrostatic interactions between solute and solvent atoms, which rely on the choice of partial atomic charges (PACs), play a key role in the determination of solvent configurations in MD simulations. In this work, we explore the idea of using PACs of the excited state of the solute from DFT calculations in MD simulations while keeping the GS van der Waals (vdW) parameters, to develop an approximate excited-state force field. For polar solvents like water and ACN this is justified by the fact that the contribution of vdW terms (non-electrostatic non-bonded interactions) is significantly smaller than those of electrostatic interactions in the potential energy of the system.[36] Therefore, using the GS vdW parameters for the excited-state simulations should not result in a notable error.

In the present work, we perform classical MD simulations and assess the performance of several of the most popular PAC methods (see Theoretical Methods part) in the description of the solvation structure of four prototypical polypyridine TMCs including two *tris*-bidentate TMCs $[Ru(bpy)_3]^{2+}$ and $[Fe(bpy)_3]^{2+}$, a *bis*-tridentate TMC $[Fe(bmip)_2]^{2+}$ and a *bis*-bidentate TMC $[Cu(phen)_2]^{+}$ (bpy=2,2'-pyridine; bmip=2,6-bis(3-methyl-imidazole-1-ylidine)-pyridine; phen=1,10-phenanthroline) (see Fig. 1). The excited-state dynamics of these TMCs have been extensively investigated.[4,11,32,34,37–42] These TMCs represent a comprehensive set exhibiting a range of possibilities for solvent molecules to approach the metallic center depending on the coordination number of the metal and denticity of the ligands. We assess the performance of the various PAC methods by contrasting the RDFs simulated by classical MD with frozen solute to those obtained by QM/MM Born-Oppenheimer molecular dynamics (BOMD) simulations of a non-rigid solute carried out in the present work or taken from the literature (QM/MM MD and AIMD). In this work, we seek suitable PAC methods, which enable us to perform classical MD simulations (with frozen solute) without need of force field reparameterization to provide reliable RDFs. These results can be used to complement and assist experimental determinations. The QM/MM BOMD and classical MD simulations are performed in water for $[Ru(bpy)_3]^{2+}$ and $[Fe(bpy)_3]^{2+}$ and in acetonitrile (ACN) for $[Fe(bmip)_2]^{2+}$ and $[Cu(phen)_2]^{+}$; these two solvents are the most popular ones in experimental studies of such TMCs.

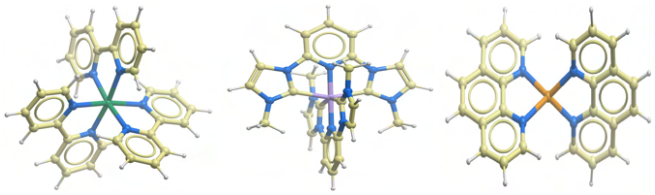

(a) $[Ru/Fe(bpy)_3]^{2+}$ **(b)** $[Fe(bmip)_2]^{2+}$ **(c)** $[Cu(phen)_2]^{+}$

Fig. 1 Schematic molecular structures of the investigated TMCs. Color codes: Nitrogen–blue; Carbon–yellow; Hydrogen–white; Ruthenium–green; Iron–violet; Copper–orange.

2 Theoretical Methods

2.1 Partial Atomic Charges

As PACs are not quantum mechanical observables, many different methods have emerged to calculate them. In the present work, seven common PAC methods have been chosen: Mulliken population analysis (MPA)[43], natural population analysis (NPA)[44], charges from electrostatic potentials using a grid based method (ChelpG)[45], restrained electrostatic potential (RESP)[46], atoms in molecules (AIM)[47], Hirshfeld[48] and charge model 5 (CM5)[49].

MPA and NPA are methods based on partitioning the molecular electronic wave function. MPA, due to its simplicity, is the most straightforward method for assigning PACs and almost all quantum chemistry programs provide it as default population analysis. However, this method suffers from basis-set dependency and lack of convergence of atomic charges with increasing basis-set size. NPA was developed by Reed *et al.*[44] as an alternative to overcome the problems with MPA. This method works based on natural atomic orbitals on each atomic center which are orthogonal and less sensitive to the basis set. The NPA method is usually recommended for characterization of the electron distribution in systems that have high ionic character.[44]

ChelpG and RESP, in which PACs are derived through a fitting procedure to reproduce the molecular electrostatic potential (ESP), a real physical observable, are among the most popular methods for assigning atomic charges. The ESP at a given point *i*

View Article Online
DOI: 10.1039/C8CP06567E

is computed by eqn (1):

$$\Phi_{ESP}(\boldsymbol{r}_i) = \sum_{\alpha}^{M} \frac{Z_\alpha}{|\boldsymbol{R}_\alpha - \boldsymbol{r}_i|} - \sum_{j}^{L} \frac{\rho(\boldsymbol{r}_j)}{|\boldsymbol{r}_j - \boldsymbol{r}_i|} V_p \quad (1)$$

where Z_α and $\boldsymbol{R}_\alpha$ are respectively the charge and position of nucleus α and M is the total number of nuclei. The electron density of the molecule at point j is denoted by $\rho(\boldsymbol{r}_j)$, where $\boldsymbol{r}_j$ is the grid point coordinate. V_p is the volume per grid point and L is the total number of grid points. The first term in eqn (1) is straightforward to calculate. But for the molecular electron density, quantum chemistry calculations are required. Atomic charges Q_α are obtained by least squares fitting of the molecular ESP. The best fit is achieved by minimization of an error function, F_{error}^{ESP}, (eqn (2)) so that the ESP predicted by the Q_α is as close as possible to Φ_{ESP}.

$$F_{error}^{ESP} = \sum_{i}^{N} \left[\Phi_{ESP}(\boldsymbol{r}_i) - \sum_{\alpha}^{M} \frac{Q_\alpha}{|\boldsymbol{R}_\alpha - \boldsymbol{r}_i|} \right]^2 \quad (2)$$

Here, N is the total number of ESP points. The Q_α (α=1, ..., M) can be found by solving eqn (3):

$$\frac{\partial F_{error}^{ESP}}{\partial Q_\alpha} = -\sum_{i}^{N} \frac{2}{|\boldsymbol{R}_\alpha - \boldsymbol{r}_i|} \left[\Phi_{ESP}(\boldsymbol{r}_i) - \sum_{\alpha}^{M} \frac{Q_\alpha}{|\boldsymbol{R}_\alpha - \boldsymbol{r}_i|} \right] = 0 \quad (3)$$

In the ChelpG method, a cubic box is designed and the molecular ESP points are generated between 0-2.8 Å from the vdW surface of the molecule. A well-known issue that affects ChelpG is the poor prediction of the atomic charges of deeply buried atoms, such as metals in TMCs. This is because during the fitting procedure the molecular ESP points are far from the buried atoms. This problem is addressed by the RESP method by utilizing a penalty function in eqn (2), which enables us to introduce target charges and the possibility to fix them during the fitting. Moreover, this method ensures that atoms with the same chemical environment possess identical partial charges. Here, we use a hyperbolic penalty function. Bayly *et al.*[46] have found that a hyperbolic restraint function determines charges better than a quadratic function. Eqn (4) shows the modified error function for the calculation of the RESP charges:

$$F_{error}^{RESP} = \sum_{i}^{N} \left[\Phi_{ESP}(\boldsymbol{r}_i) - \sum_{\alpha}^{M} \frac{Q_\alpha}{|\boldsymbol{R}_\alpha - \boldsymbol{r}_i|} \right]^2 + \beta \sum_{\alpha}^{M} \left[\sqrt{(Q_{0\alpha} - Q_\alpha)^2 + b^2} - b \right] \quad (4)$$

Here, β is a quantity for setting the strength of the restraint, $Q_{0\alpha}$ is the target charge and b is the tightness of the hyperbola around its minimum. The RESP charges can be obtained by solving eqn (5):

$$\frac{\partial F_{error}^{RESP}}{\partial Q_\alpha} = -\sum_{i}^{N} \frac{2}{|\boldsymbol{R}_\alpha - \boldsymbol{r}_i|} \left[\Phi_{ESP}(\boldsymbol{r}_i) - \sum_{\alpha}^{M} \frac{Q_\alpha}{|\boldsymbol{R}_\alpha - \boldsymbol{r}_i|} \right] - \beta \frac{(Q_{0\alpha} - Q_\alpha)}{\sqrt{(Q_{0\alpha} - Q_\alpha)^2 + b^2}} = 0 \quad (5)$$

The basis of the AIM and Hirshfeld methods is to partition the electron density into atomic domains. In the AIM method, topological analysis of the electron density is used to find the electron density maxima (which often occur at the nuclei) and minima. The atomic domains (also known as Bader regions) are obtained by following the density gradients. The border between regions, which is called the zero flux surface, is placed where the density gradient is zero. The partial charges are then obtained by integration of the electron density in each atomic domain. The Hirshfeld method is similar to AIM except that the atomic domains are defined based on a weight factor, which is the ratio of the electron densities of isolated atoms and the density constructed from a sum of atomic densities (the so-called promolecular density). The main disadvantages of the AIM method are its computational cost and the overestimation of partial charges for polar bonds[50], similarly to the NPA method[51], while the Hirshfeld method frequently underestimates these charges[52]. Finally, CM5 is a parametrized method that uses gas-phase Hirshfeld charges as input and derives PACs to reproduce the molecular dipole moment. The charges derived by dividing the electron density are less sensitive to the basis set size and usually yield more reasonable PACs for the buried atoms.

2.2 Computational Details

In this section, we provide the computational details for the methods used in this work. Section 2.2.1 covers the geometry optimizations and PAC calculations of the chosen TMCs using density functional theory (DFT) in gas phase. In section 2.2.2, we discuss the classical MD simulations utilizing the optimized structures and PACs obtained from DFT calculations. Finally, a detailed description of the QM/MM MD simulations is given in section 2.2.3.

2.2.1 Electronic Structure Calculations: Optimizations and PAC Calculations

The structures of the four selected TMCs were optimized using DFT with the B3LYP* hybrid exchange-correlation functional[53,54] in combination with a triple zeta valence quality basis set augmented by polarization functions (Def2TZVP)[55]. The B3LYP* functional has been benchmarked for the structural and energetic characteristics of TMCs against high-level quantum chemical methods and experimental results and shown reliable performance.[56–60] D_{2d} and C_2 symmetries are used for $[Fe(bmip)_2]^{2+}$ in its ground and excited states, respectively, and C_1 for the other TMCs (geometry optimizations and PAC calculations for classical MD simulations).

For the GS calculations, the total spin angular momentum quantum number was set to zero (S=0) for all structures while unrestricted open-shell calculations were performed for the low-lying triplet metal-to-ligand charge-transfer (^{3}MLCT) state (for $[Ru(bpy)_3]^{2+}$ and $[Cu(phen)_2]^{+}$) and low-lying quintet metal-centered, ^{5}MC (high-spin; HS) state (for $[Fe(bpy)_3]^{2+}$), applying S=1 and S=2, respectively. It should be noted that the very high density of low-lying electronic states in $[Fe(bmip)_2]^{2+}$ leads to several conical intersections between the ^{3}MLCT and ^{3}MC states[42,61] which prevents us from performing state-specific QM/MM BOMD

View Article Online
DOI: 10.1039/C8CP06567E

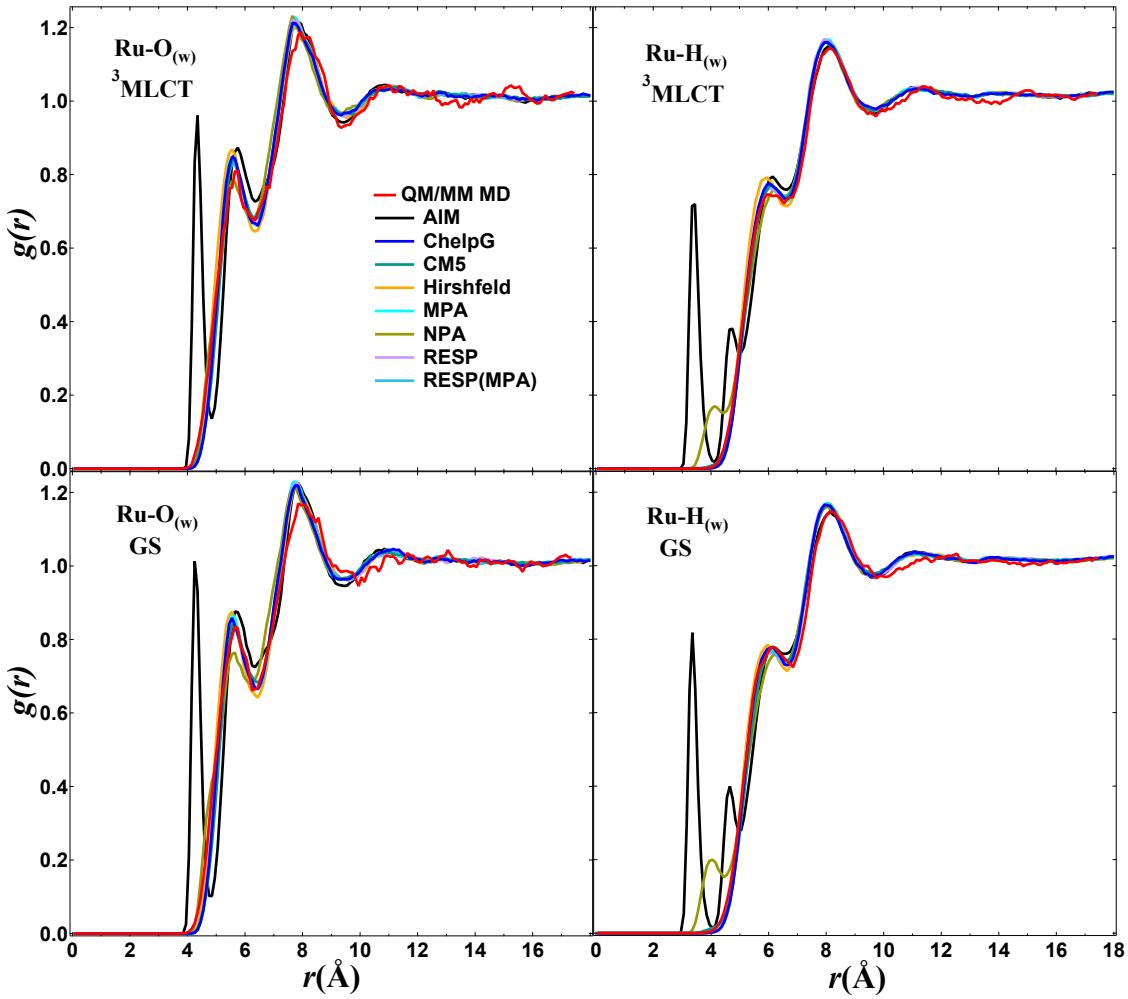

Fig. 2 The RDFs, $g(r)$, of $[Ru(bpy)_3]^{2+}$ in water for the Ru-O_w and Ru-H_w pairs obtained from the classical MD and QM/MM MD (red lines) simulations in the GS and ^{3}MLCT state.

simulations in the excited state. Therefore, for $[Fe(bmip)_2]^{2+}$ we only compare the GS RDFs obtained from the classical MD simulations with the QM/MM BOMD ones. The Cartesian coordinates of the GS DFT optimized structures of all TMCs are provided in the ESI. The geometry optimization as well as the calculation of MPA, NPA, ChelpG, Hirshfeld and CM5 charges were performed in gas phase using the GAUSSIAN 16 Rev A.03 suite of program[62]. Scalar-relativistic effects were taken into account for all calculations using the second-order Douglass-Kroll-Hess (DKH2) method.[63,64] We compared the gas-phase and PCM-calculated PACs (computed at geometries re-optimized in PCM) and the results have shown that the solvent effect on the PACs is negligible, and henceforth we use gas-phase calculations for solute structure and PACs. The AIM charges were computed with the Multiwfn program[65] using the wave function file (.wfx file) obtained from the DFT calculations. A high density grid is required for accurate numerical representation of the electron density to ensure convergence of the calculated AIM charges. In present work, this convergence was achieved at a grid spacing of 0.02 Å. For the calculation of ChelpG charges, the vdW radii of 2.17 Å, 2.02 Å and 1.81 Å were used for Ru^{2+}, Fe^{2+} and Cu^{+} metal ions in their ground states, respectively, which were taken from the literature.[66] In the excited states the above-mentioned vdW radii might no longer be adequate. Therefore, we also investigate the effect of different vdW radii of the metals on the ChelpG PACs and solvation structures. To obtain accurate ESP values, a high point density for the fitting procedure is necessary. Sigfridsson and Ryde[67] have suggested to use at least 2000 ESP points per atom. In this work, the grid spacing was set to 0.15 Å and employed ca. 4000 ESP points per atom in order to ensure that the charges are well-determined. The RESP charges were calculated using the two-stage RESP algorithm implemented in the Antechamber package[68,69] which is part of AmberTools. The default value of 0.1 *e* was used for the *b* term and the values of 0.0005 *e* and 0.001 *e* were set for the β term for the first and second stage, respectively (see eqn (5)). We have performed two sets of RESP calculations. In the first set we have only restricted atoms with the same chemical environment to have the same partial charges, while in the second set we have used additionally the MPA charges as target charges for the metal atoms and fixed them during the fitting procedure (calculations tagged by RESP(MPA)). The computed PACs of the four TMCs using different methods are reported in Figs S1-S4 of the ESI.

View Article Online
DOI: 10.1039/C8CP06567E

2.2.2 Classical Molecular Dynamics Simulations

All classical MD simulations were carried out with the Desmond software package[70] at constant-temperature and volume (NVT). The DFT-optimized geometries of the selected TMCs were solvated in water (four-site TIP4P model)[71] for $[Ru(bpy)_3]^{2+}$ and $[Fe(bpy)_3]^{2+}$ and in ACN solvent for $[Fe(bmip)_2]^{2+}$ and $[Cu(phen)_2]^{+}$. The three-site model of Guàrdia *et al.*[72] was adopted for ACN. The selection of these solvents was made to match the experimental conditions of the time-resolved scattering and spectroscopic measurements performed on the investigated TMCs.[14,41,73,74] Chloride (Cl^-) counterions were added for neutralization of the total charge. The standard OPLS 2005[75] Lennard-Jones (LJ) parameters were used to model the nonbonded dispersion and exchange repulsion interactions between the atoms of the solute and the solvent. The ground- and excited-state PACs used in classical MD simulations are obtained from the DFT calculations described in the previous section and are kept fixed during the simulations.

The MD simulations were performed in a cubic box with size length of 35 Å under periodic boundary conditions (PBCs). To speed up the calculation of forces, the multistep RESPA integrator[76] was used, where the nonbonded-near and nonbonded-far (long-range electrostatic) interactions were updated every 1 fs and 3 fs, respectively. A distance cut-off of 9 Å was applied to separate short- and long-range Coulombic interactions, for the latter, the particle mesh Ewald (PME) was used. For the equilibration of the system, the default protocol in Desmond was used, which consists of three stages: 1) A 100 ps constant-NVT simulation in Brownian regime at a temperature of 10 K and restraining solute heavy atoms with a force constant of 50 kcal mol^{-1} $Å^{-2}$. 2) A 12 ps constant-NVT simulation with the same temperature and restrains as stage 1. 3) A 24 ps constant-NVT simulation with the temperature increased to 300 K and no restraints. The Berendsen thermostat[77] was applied in the equilibration. Finally, a 2 ns NVT production simulation was run by applying restraints on all solute atoms with a harmonic force constant of 1000 kcal mol^{-1} $Å^{-2}$ and the trajectory was recorded every 50 fs. The bond lengths involving hydrogen atoms in the solute were constrained using the M-SHAKE algorithm[78] implemented in Desmond. The counterions were placed away from the solute and restrained with the same force constant to avoid any coordination with the solute. The system temperature was maintained at 300 K using the Noše-Hoover thermostat[79,80]. The structure and configuration input files were generated with the Maestro program (Schrödinger, LLC).

2.2.3 QM/MM MD Simulations

The QM/MM MD simulations were performed using the MD tools of the Atomic Simulation Environment (ASE)[81,82] and the implementation of QM/MM electrostatic embedding[83,84] that interfaces ASE built-in classical force fields with the GPAW DFT code[85,86]. For all four TMCs, the simulations employed a fixed QM/MM partitioning scheme, in which the complex (QM part) is entirely described with GPAW and the MM solvent is modeled through a fixed point-charge force field. The Kohn-Sham orbitals within the GPAW simulation cell for the QM solute were represented in a basis of linear combination of atomic orbitals (LCAO)[87], using TZP basis set[87] for the metal and DZP basis set[87] for the rest of the atoms. We assessed the performance of the selected mixed basis set against TZP basis set for all atoms in predicting the charge transfer in the MLCT state. The results show very similar charge transfer. The grid spacing of the cell was set to 0.18 Å; this value was found to ensure convergence with respect to structural parameters of TMCs[88]. Since forces for hybrid functionals are not yet implemented in GPAW, the BLYP functional, which is the GGA precursor of the hybrid functional B3LYP*, was used for describing all TMCs except $[Ru(bpy)_3]^{2+}$ where the GGA DFT functional BP86[89,90] was applied. The BLYP has been used in previous studies.[39,91,92] The BP86 functional is known from previous DFT studies of this complex[35,93], to give a GS structure and an energy separation between the lowest ^{3}MLCT excited state and the GS in good agreement with the X-ray crystal structure and optical spectroscopic measurements, respectively.

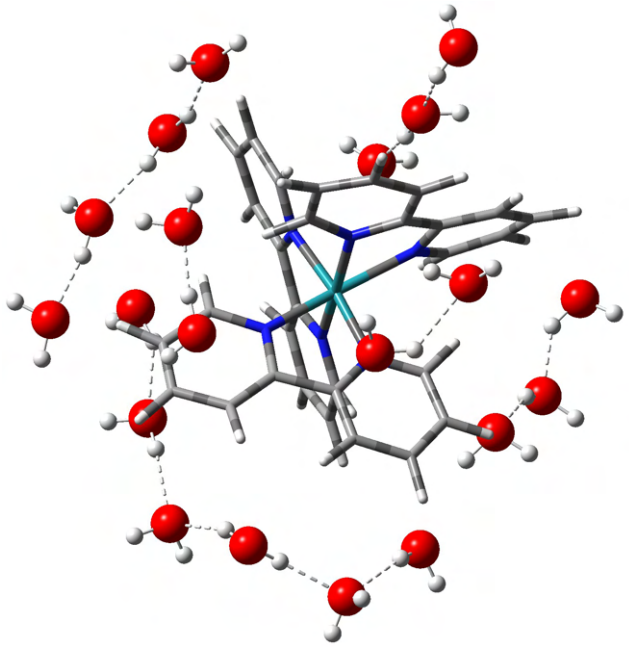

Fig. 3 Graphical representation of the chain of hydrogen-bonded water molecules around $[Ru(bpy)_3]^{2+}$ obtained from a snapshot of a QM/MM MD trajectory in the GS.

In the following, we applied the same parameters as in the classical MD simulations described above, if not specified otherwise. The ACN force field was implemented in a development branch of ASE based on the parametrization of Ref. 67 and on the scheme for holonomic constraints of rigid triatomic molecules from Ref. 62. For the nonbonded interactions, a standard LJ potential was used, in which LJ parameters for the atoms of the complex were taken from the universal force field (UFF)[94]. The QM/MM MD data in a solvent bath at 300 K were obtained for the GS of all four TMCs and for the excited state of $[Ru(bpy)_3]^{2+}$, $[Fe(bpy)_3]^{2+}$ and $[Cu(phen)_2]^{+}$. The procedure that we employed for each of the four systems is the following. First, the GS geometry of the complex was optimized with GPAW in vacuum using a quasi-Newton local optimization algorithm implemented in ASE. Then, the GS

View Article Online
DOI: 10.1039/C8CP06567E

optimized geometry was centered in a box of solvent molecules pre-equilibrated in the NVT ensemble at 300 K. After solvating the complex, the QM/MM simulation box was equilibrated in the NVT ensemble to 300 K employing a time step of 1 fs. The Equilibration was carried out with the ASE Langevin thermostat applied to the atoms of the solvent. PBCs were treated according to the minimum image convention.[95]

During these simulations the solute geometry is flexible and in order to eliminate the fastest vibrational motions and thus reduce the computational time in the QM/MM MD simulations, we enforced two bond length constraints per hydrogen atom in the complex using the RATTLE algorithm[96] as implemented in ASE. Following thermal equilibration of the solvent, QM/MM MD data were collected for at least 18 ps with a time step of 2 fs. From this first equilibrated trajectory, a set of other 20-45 QM/MM trajectories were started to accelerate the data collection. The starting MD frames were spaced by at least 0.5 ps from each other. Moreover, to further minimize the correlation between them, the velocities of the atoms of each of the starting frames were randomized by imposing a Maxwell-Boltzmann distribution at 300 K. Overall, we collected between 150 and 400 ps of 300 K equilibrated QM/MM MD data for the GS of each of the four complexes.

For $[Ru(bpy)_3]^{2+}$, $[Fe(bpy)_3]^{2+}$ and $[Cu(phen)_2]^{+}$, we further generated QM/MM MD data in the same excited states as considered in the classical MD investigation. This was achieved by starting excited-state QM/MM trajectories from a set of representative configurations of each of the equilibrated GS trajectories. The excited states were described using a recent implementation of ΔSCF in GPAW[88], based on fixing the electronic configuration of the system with Gaussian smeared constraints on the orbital occupation numbers. The Gaussian smearing ensures stable convergence of the electronic density at each step during the QM/MM MD propagation. We used a flexible width for the Gaussian functions controlling the extent of the smearing during the SCF cycle. Starting from an initial value of 0.01 Å, the width was increased by 0.01 Å at each 120 SCF steps until convergence of the density. In most of the cases, convergence of the SCF cycle took place within the first 120 steps. The ΔSCF-QM/MM trajectories were propagated with a time step of 2 fs, with the Langevin thermostat applied to the solvent. In total, we collected between 100 and 200 ps of excited-state ΔSCF-QM/MM trajectories for each of the three TMCs. In the cases of $[Fe(bpy)_3]^{2+}$ and $[Cu(phen)_2]^{+}$, we observe that the solvation shell and solute structure relax within 3 ps. In $[Cu(phen)_2]^{+}$, as copper is tetracoordinated, the planes of the two ligands are perpendicular in the GS and due to a pseudo Jahn-Teller distortion, flat in the ^{3}MLCT state. The average atomic Cartesian coordinates and significant internal structural parameters of the solvated TMCs obtained as averages from the equilibrated parts of the QM/MM MD trajectories are reported in Tables S1-14 of the ESI. For a comparison, structural information from the gas-phase DFT optimizations using the Gaussian 16 and GPAW programs are also reported.

In terms of computational efficiency, our simulations indicate that the QM/MM MD simulations, using 16 CPU cores, are 4 orders of magnitude slower than the classical MD simulations.

2.2.4 Analysis of Solvation Structure

Solute-solvent RDFs, *g(r)*, from the ground- and excited-state classical MD and QM/MM MD simulations were computed using the VMD software[97] with a bin size of 0.1 Å for the radial sampling. For the excited state simulations, we ensured that the RDFs reflected equilibrium distributions by checking the convergence with respect to the amount of sampled configurations included in the computation of the RDFs. Furthermore, the running solvent coordination number (*cn*), as shown in eqn (6), was used to obtain information about the solvent organization and orientation around the complex.

$$cn(R) = 4\pi\rho \int_0^R r^2 g_{\mathrm{m-s}}(r) dr \qquad (6)$$

Here, ρ is the density of the bulk solvent. $cn(R)$ gives the number of *s* solvent atoms in a sphere with radius *R* around the transition metal center m.

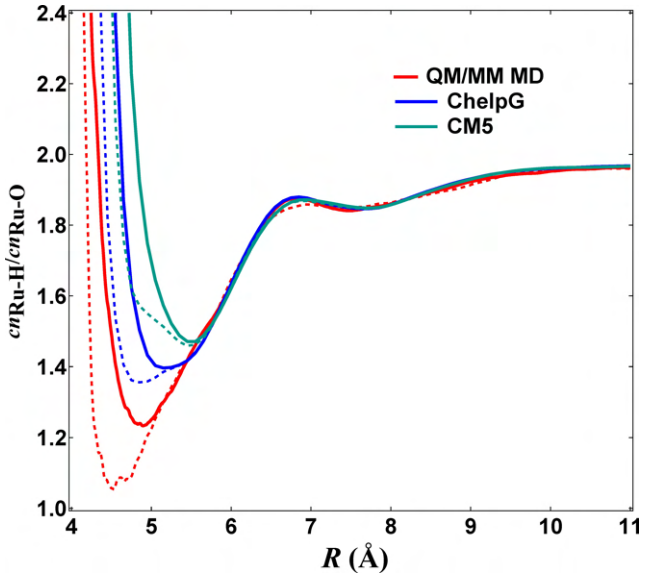

Fig. 4 Plot of the coordination number ratio $cn_{\mathrm{Ru-H_w}}/cn_{\mathrm{Ru-O_w}}$ as a function of the distance from the Ru atom for $[Ru(bpy)_3]^{2+}$ in water obtained from the classical MD simulations, using the ChelpG and CM5 methods, and QM/MM MD simulations. The solid and dashed lines correspond to the ground and ^{3}MLCT states, respectively.

3 Results

Fig. 2 shows the RDFs of $[Ru(bpy)_3]^{2+}$ in water for the $Ru-O_w$ and $Ru-H_w$ pairs, which are labeled by $g_{\mathrm{Ru-O_w}}(r)$ and $g_{\mathrm{Ru-H_w}}(r)$. The first peak of the $g_{\mathrm{Ru-O_w}}(r)$ bears important information about the first solvation shell. As seen in Fig. 2, left panels, for the results of QM/MM MD in either GS or ^{3}MLCT state, this peak is located at 5.5 Å and is followed by a valley at 6.45 Å. The $cn_{\mathrm{Ru-O_w}}$ shows that this shell carries an approximate number of 15 water molecules for both the GS and ^{3}MLCT state and contains a chain of hydrogen-bonded water molecules intercalated between the bpy ligands (Fig. 3). Moret *et al.*[35,37] using MD simulations in the GS and QM/MM MD simulations in the ^{3}MLCT state, and also Tavernelli *et al.*[98] for the ^{1}MLCT state by QM/MM

View Article Online
DOI: 10.1039/C8CP06567E

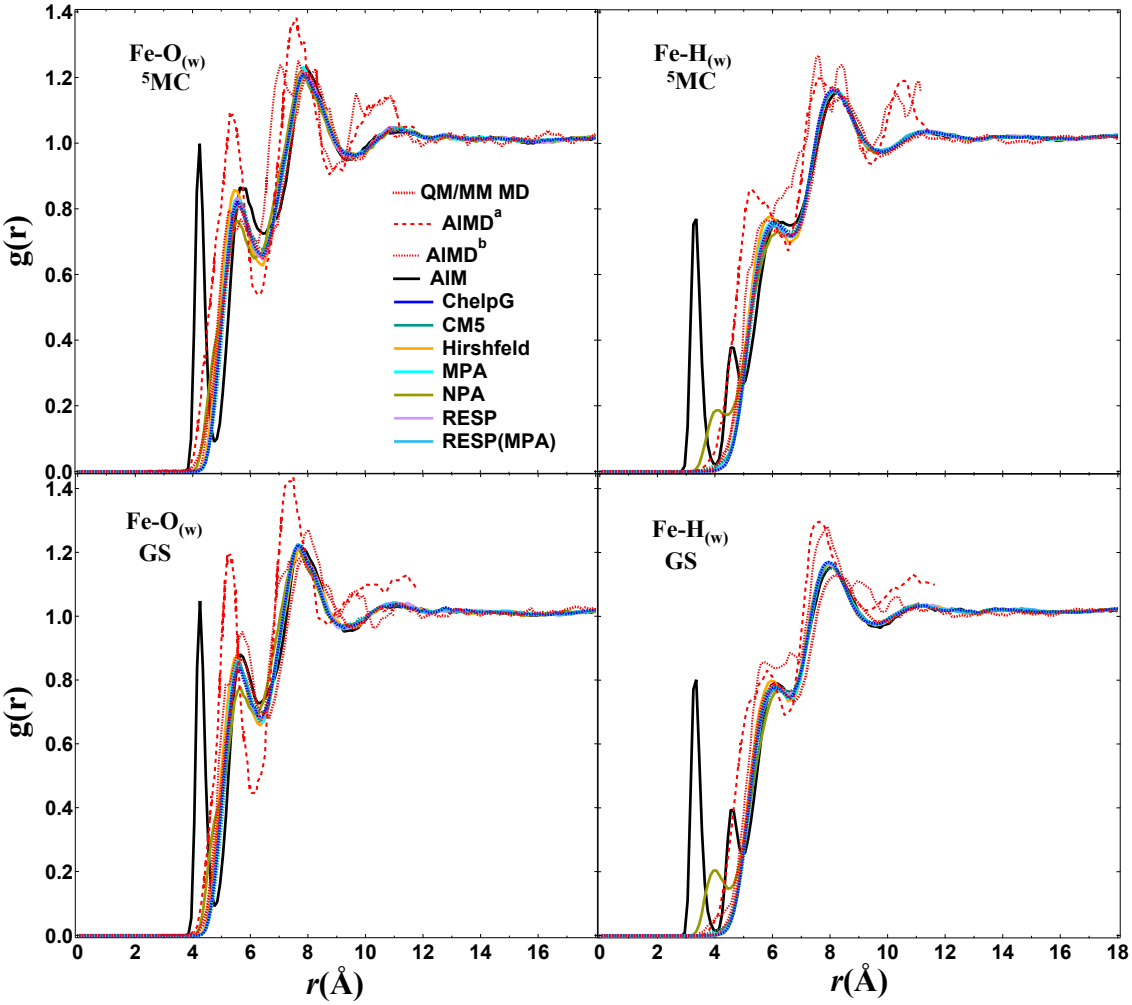

Fig. 5 The RDFs, $g(r)$, of $[Fe(bpy)_3]^{2+}$ in water for the Fe-O_w and Fe-H_w pairs obtained from the classical MD and QM/MM MD (solid red lines) simulations in the GS and ^{5}MC state. It is also shown the AIMD data from the literature: ^{a} Refs. 91 and ^{b} Refs. 39. The AIMD data (dashed and dotted lines) are available until 12 Å.

MD simulations, observed the same solvation structure. The red lines in Fig. 4 show plots of the coordination number ratio $n_{HO}(r) = cn_{Ru-H_w}(r)/cn_{Ru-O_w}(r)$ obtained from the QM/MM MD simulations in the GS (solid line) and the ^{3}MLCT state (dashed line). At short distances from the Ru center (below 4 Å, not shown in Fig. 4), very large n_{HO} values reveal that only water H atoms can approach the Ru atom. The n_{HO} falls down below 2 between 4.3 Å and 6.6 Å, which indicates that the oxygen atoms of water orient toward Ru in the first solvation shell. Thereafter, n_{HO} then converges toward 2 reflecting the random orientation of water in the bulk solvent. Having fairly different n_{HO} for the GS and the excited state, despite negligible changes in the corresponding RDFs (Fig. 2), reflects the high sensitivity of this parameter to the small changes in solvent organization. By comparing the minima of the ratios in the case of the QM/MM MD, it is found that upon transition from the GS to the ^{3}MLCT state, water molecules prefer to re-orient through the oxygen atoms toward the Ru^{2+} cation at ~0.35 Å shorter distance.

The results obtained from the classical MD simulations show that the RDFs from the ChelpG, CM5, Hirshfeld, MPA, RESP and RESP(MPA) methods reproduce the QM/MM MD RDFs very well. The NPA method, except small shoulders at ~4 Å in $g_{Ru-H_w}(r)$, also predicts the RDFs in good agreement with the QM/MM MD ones but AIM fails. Fig. S1 shows that the AIM method predicts large positive charge (+1.2 *e*) for the Ru and large negative charges (-1.1 *e*) for the nitrogen atoms bonded to Ru, which causes larger charge separations in the bpy ligands, compared to the other PAC methods (see Fig. S6). The large negative charges and more accessibility of the nitrogen atoms with respect to Ru, provide a condition for intercalation of three water molecules between the bpy ligands and hydrogen bonding with the hydrogen atoms of water.

For the ChalpG charges in the ^{3}MLCT state, we studied the effect of different vdW radii for Ru on the charges and RDFs. The vdW radii of 2.17 Å, 1.80 Å and 1.20 Å have been used for the Ru atom in the calculation of ChelpG charges and their corresponding RDFs are shown in Fig. S7. The results show that although different vdW radii can affect the PACs significantly, this has no considerable effect on the RDFs. Fig. 4 and S8 present a comparison between the n_{HO} obtained from the QM/MM MD and classical MD simulations. The results show that the ChelpG, RESP, RESP(MPA) and Hirshfeld methods successfully reproduce

View Article Online
DOI: 10.1039/C8CP06567E

the n_{HO} ratio of QM/MM MD while the AIM and NPA and MPA methods fail. Upon going from the GS to the ^{3}MLCT state, the differences between RDFs are very small indicating that the amount of charge transfer from the Ru to the bpy ligands is not sufficient to change the equilibrium solvation structure in the ^{3}MLCT state. Fig. S6 supports this observation by showing the same charge separations of the bpy ligands for the GS and the ^{3}MLCT state.

The charge localization in the excited state of $[Ru(bpy)_3]^{2+}$ in water from the QM/MM MD simulations has also been investigated. The DFT gas-phase calculations give charge distribution and, thus, PACs distributed equally over the three bpy ligands. Fig. S5 illustrates spin densities calculated from different snapshots along a single QM/MM MD trajectory in the 3MLCT state. During the first ps, the charge oscillates between all ligands and then it localizes over at most two bpy ligands, with the pair carrying the charge changing during the dynamics. These results are in good agreement with the observation of Moret *et al.*[37]. We note that using fixed equally distributed charges in classical MD simulations does not seem to affect the RDFs compared to the QM/MM MD ones. This can be attributed to the small magnitude of the charge transfer upon excitation (0.1-0.3 e, as obtained from different PAC methods), which can also be seen from very similar RDFs for the ground and excited states.

Fig. 5 illustrates the $g_{Fe-O_w}(r)$ and $g_{Fe-H_w}(r)$ of $[Fe(bpy)_3]^{2+}$ extracted from the QM/MM MD and classical MD simulations in water. As expected from the similarity between the ground state ligand structure of $[Ru(bpy)_3]^{2+}$ and $[Fe(bpy)_3]^{2+}$ and type of solvent, the same trends in the RDFs of these two complexes are observed. Lawson Daku *et al.*[39,91] have investigated $[Fe(bpy)_3]^{2+}$ utilizing AIMD simulations. The red dotted and dashed lines in Fig. 5 are the AIMD RDFs. The dotted one[39] was obtained using the BLYP functional within the Car-Parinello MD (CPMD) scheme and the simulations were performed for 24.5 and 4 ps for the GS and the ^{5}MC state, respectively. Their results have shown that upon going from the GS to the ^{5}MC states, two water molecules are expelled from the first solvation shell (∼17 in the GS and ∼15 in the ^{5}MC). The dashed lines[91] correspond to RDFs obtained by applying the dispersion-corrected BLYP-D3 functional in the BOMD approach, in order to describe long-range dispersion interactions, and calculated for longer simulation times, 76.6 ps for the GS and 67.2 ps for the ^{5}MC state. The new study[91] revealed that the number of water molecules in the first shell actually increases from ∼15 in the GS state to ∼17 in the ^{5}MC state. The RDFs and the resulting cn_{Fe-O_W} value obtained from our QM/MM MD, by going from the GS to the ^{5}MC state, show that around 0.7 water molecule is expelled from the first coordination shell into the bulk solvent. The expulsion of water molecules from the first solvation shell is consistent with the increase in the density of bulk solvent by 0.2% upon formation of the ^{5}MC state, as measured by Haldrup *et al.* using XDS.[13] The RDFs extracted from classical MD simulations for all PAC methods, except AIM, are in good agreement with the QM/MM MD and show the same trend: a decrease in the number of water molecules in the first shell upon the GS → ^{5}MC transition. We investigated the effect of changing the vdW radii of Fe on the excited-state ChelpG charges and RDFs. As for $[Ru(bpy)_3]^{2+}$, we did not see any effect on the RDFs by using vdW radii of 2.02 Å and 1.2 Å (see Fig. S9 in ESI).

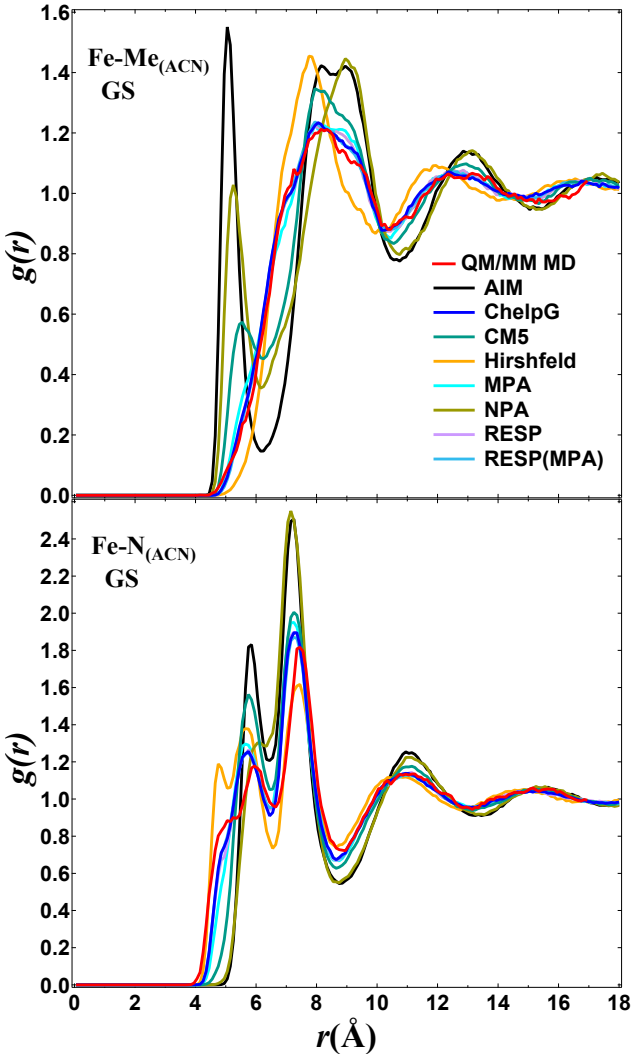

Fig. 6 The RDFs, $g(r)$, of $[Fe(bmip)_2]^{2+}$ in ACN for the Fe-$N_{(ACN)}$ and Fe-$Me_{(ACN)}$ pairs obtained from the classical MD and QM/MM MD (red lines) simulations in the GS. Note that some curves are overlapped with each other.

From the $[Ru(bpy)_3]^{2+}$ and $[Fe(bpy)_3]^{2+}$ RDF results, it can be concluded that the structure of the three bidentate bpy ligands prevent the solvent molecules to coordinate *directly* to the metals and be affected by their charges. This shows that the ligand charges have a more important role than the metal charges in the determination of the solvation structure in such TMCs. However, the charges of the metals have an *indirect* effect on the solvation structure by changing the charges of the neighboring nitrogen atoms.

Fig. 6 shows the $g_{Fe-N_{(ACN)}}(r)$ and $g_{Fe-Me_{(ACN)}}(r)$ for the GS of $[Fe(bmip)_2]^{2+}$ in ACN. As mentioned before (Section 2.2.1), the existence of several conical intersections between the low-lying triplet MLCT and MC excited states did not allow us to carry out state-specific QM/MM MD simulations for the ^{3}MLCT state of $[Fe(bmip)_2]^{2+}$. $[Fe(bmip)_2]^{2+}$ has two tridentate bmip ligands and gives the possibility to the solvent molecules (ACN) to approach the metal atom in the simulations. This is reflected in the

View Article Online
DOI: 10.1039/C8CP06567E

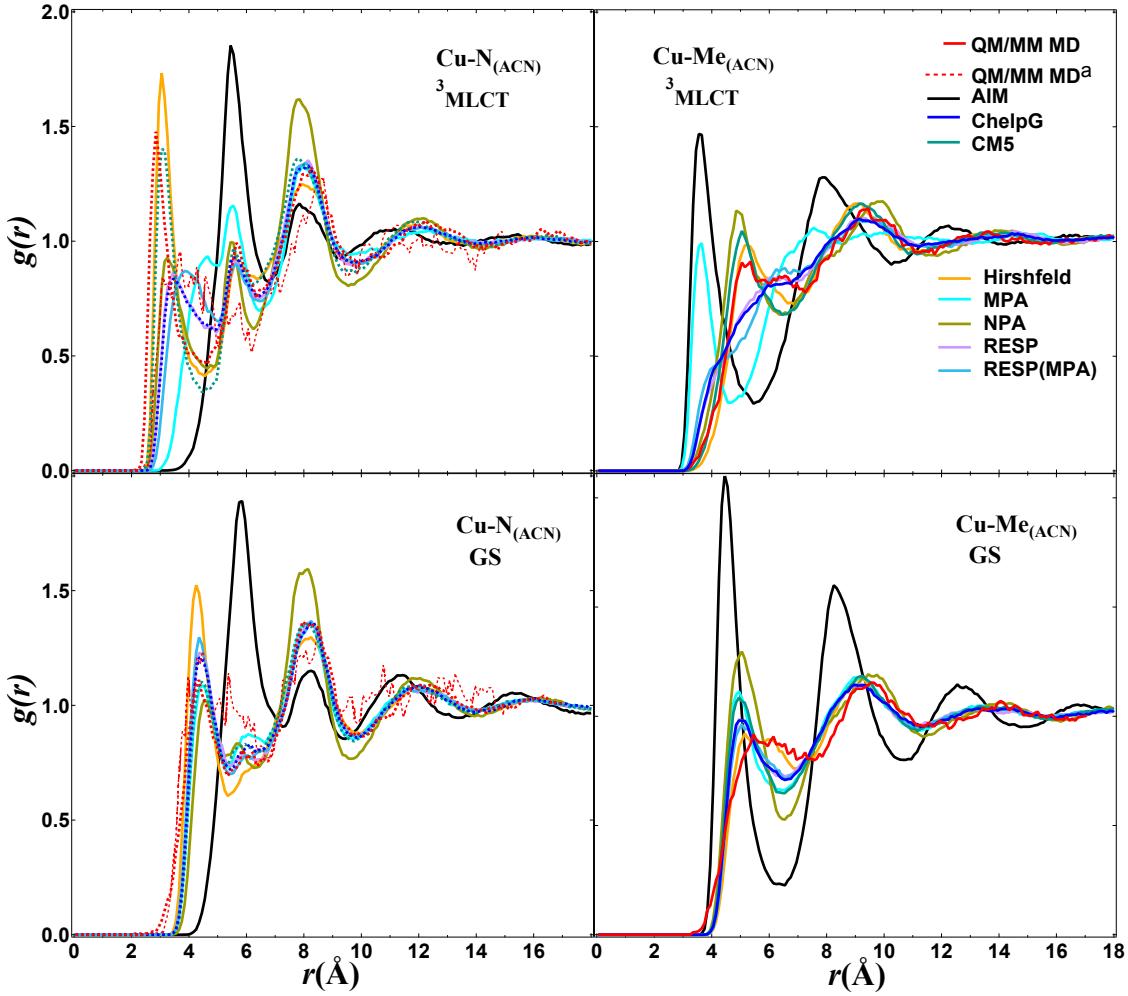

Fig. 7 The RDFs, $g(r)$, of $[Cu(phen)_2]^+$ in ACN for the Cu-$N_{(ACN)}$ and Cu-$Me_{(ACN)}$ pairs obtained from the classical MD and QM/MM MD (red lines) simulations in the GS and ^{3}MLCT state. Also shown are the QM/MM MD data from the literature: [a]Ref. 19.

larger differences of the RDFs in $[Fe(bmip)_2]^{2+}$ compared to the two previous cases. The AIM and NPA methods, similarly to the cases of $[Ru(bpy)_3]^{2+}$ and $[Fe(bpy)_3]^{2+}$, exaggerate the negative charges of the nitrogen atoms (see Fig. S3), leading to attraction of the methyl groups of the ACN molecules. These electrostatic attractive interactions are reflected in the structured peaks centered at 5 Å and 5.2 Å in the $g_{Fe-Me_{(ACN)}}(r)$ corresponding to the AIM and NPA methods, respectively (see Fig. 6, top panel). However, here the peaks are located at longer distances. This is due to the bulky structure of the ACN molecules, compared to water, which prevents them from intercalating between the ligands and getting close to Fe. Among the applied PAC methods, the MPA, ChelpG, RESP and RESP(MPA) methods provide RDFs close to the QM/MM MD ones. Although, we do not have QM/MM MD results for the ^{3}MLCT state of $[Fe(bmip)_2]^{2+}$ to compare with, for the reason explained above, we have, for the sake of completeness, included the $g_{Fe-N_{(ACN)}}(r)$ and $g_{Fe-Me_{(ACN)}}(r)$ obtained from classical MD simulations in the ESI (see Fig. S10).

The last case that we have considered for this study is $[Cu(phen)_2]^+$ in ACN. The main reason for choosing this TMC is its unique ligand structure that offers the possibility of direct coordination of solvent molecules to the copper. This enables us to study the *direct* effect of the metal charge on the calculated RDFs using different PAC methods. Fig. 7 displays the $g_{Cu-N_{(ACN)}}(r)$ and $g_{Cu-Me_{(ACN)}}(r)$ for $[Cu(phen)_2]^+$ in the GS and ^{3}MLCT state in ACN. The red dashed lines in Fig. 7 show QM/MM MD RDFs, which were taken from Ref. 19 and were calculated from ~20 ps simulations using the CPMD scheme. Owing to the flattened geometry of $[Cu(phen)_2]^+$ in the ^{3}MLCT state, we are able to assess the performance of each PAC method more precisely. By inspection of the coordination number of the first solvation shell in the QM/MM MD $g_{Cu-N_{(ACN)}}(r)$ it is realized that upon transition from the GS to the ^{3}MLCT state this shell shifts to a shorter distance by 1.5 Å. This is showing an increased Cu-N coordination and, at the same time, a decrease in the number of ACN molecules from 4.2 in the GS to 2.6 in the ^{3}MLCT state, i.e., a shift of ~1.5 ACN molecules to the second shell upon transition to the ^{3}MLCT state. Among the applied PAC methods in classical MD simulations, for the GS all of them, except AIM and NPA, reproduce the QM/MM MD RDFs reasonably well. On the other hand, in the ^{3}MLCT state, only CM5 along with Hirshfeld, which predict large positive charges on Cu (see Fig. S4), provide RDFs relatively close

View Article Online
DOI: 10.1039/C8CP06567E

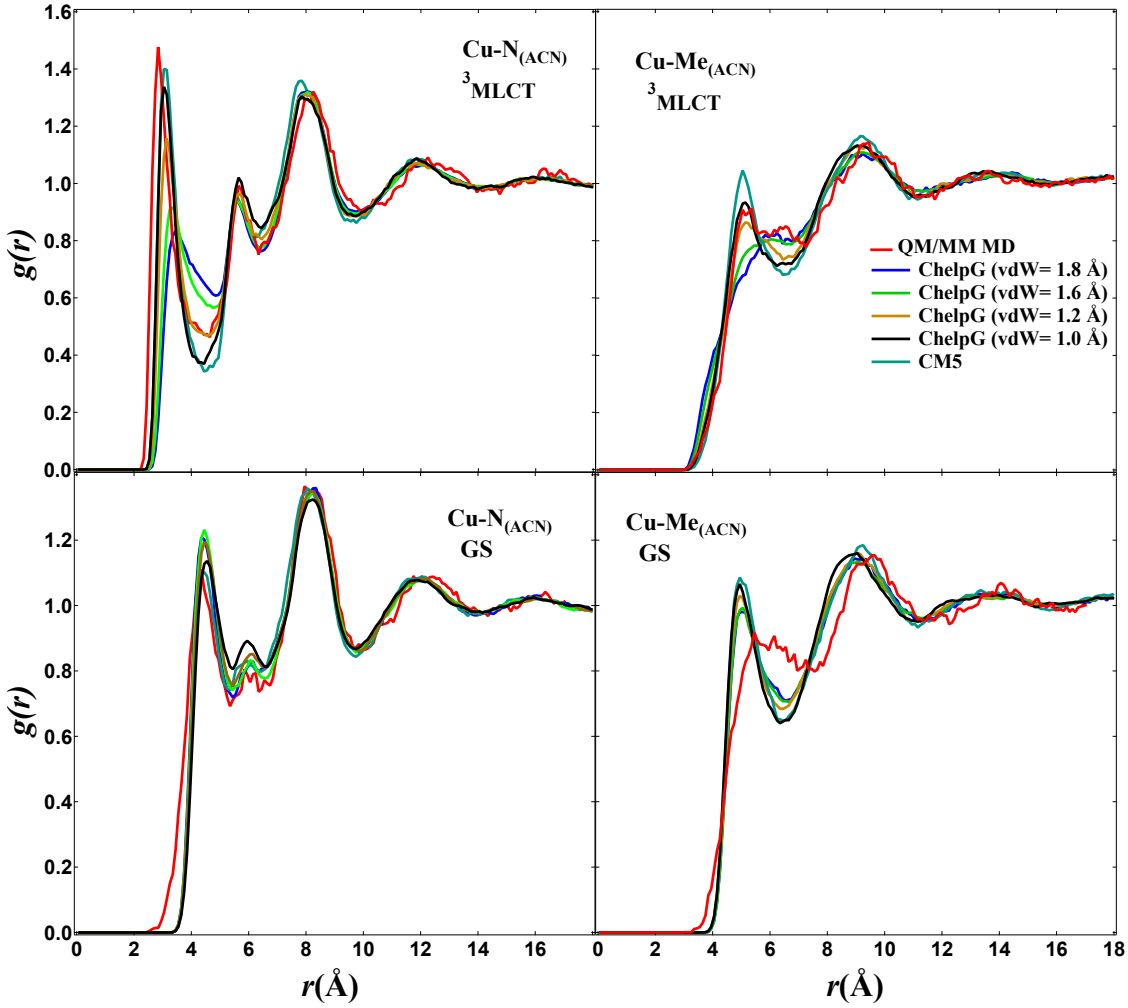

Fig. 8 The RDFs, $g(r)$, of $[Cu(phen)_2]^+$ in ACN for the Cu-$N_{(ACN)}$ and Cu-$Me_{(ACN)}$ pairs obtained from the classical MD, using the ChelpG method with different vdW radii of Cu, and QM/MM MD (red lines) simulations in the GS and ^{3}MLCT state.

to the QM/MM MD ones. Note that although AIM and NPA provide large positive charges on Cu, the negative charges on the nitrogen atoms cause repulsive forces between the complex and the ACN molecules. In case of the GS $g_{Cu-N_{(ACN)}}(r)$, none of the PAC methods can reproduce the tail in the QM/MM MD RDF at short distance (r<3 Å). This may be attributed to the flexibility of the solute not included in the classical MD simulations (see Fig. S16).

Similar to $[Ru(bpy)_3]^{2+}$, we study the effect of the vdW radius of Cu on the excited-state ChelpG PACs and RDFs. The values of 1.80 Å, 1.60 Å, 1.20 Å and 1.00 Å were used in computing the ChelpG charges. The calculated PACs reveal that by decreasing the vdW radius, the charges of Cu and N atoms become more positive and negative, respectively, i.e., the ionic character is increased. As seen in Fig. 8, top panels, the RDF results in the ^{3}MLCT state show that using different vdW radii in ChelpG PACs calculations leads to remarkable changes in the RDFs. This is ascribed to the significant effect of the charges of Cu and N atoms on the calculated RDFs of $[Cu(phen)_2]^+$. However, according to Fig. 8, bottom panels, the GS RDFs are much less sensitive to the chosen vdW radius. The results show that applying vdW radii of 1.20 Å or 1.00 Å for Cu in the excited-state ChelpG calculations can provide RDFs fairly close to the CM5 and QM/MM MD.

4 Discussion and Conclusions

In this work, utilizing the RDF, which is a powerful tool for characterizing the solvation structure, we have evaluated the performance of several most-used PAC methods in classical MD simulations aimed at describing ground- and excited-state solvation structures. Several PAC methods have been considered for this study including MPA, NPA, ChelpG, RESP, RESP(MPA), AIM, Hirshfeld and CM5. For this purpose, four popular polypyridine TMCs have been chosen: $[Ru(bpy)_3]^{2+}$, $[Fe(bpy)_3]^{2+}$, $[Fe(bmip)_2]^{2+}$ and $[Cu(phen)_2]^+$. We analyse the RDFs obtained from classical MD simulations using fixed charges and frozen solute structure, and compare them to more accurate QM/MM MD RDFs where both the electronic and nuclear structures are allowed to evolve. These results show that for the four investigated TMCs, the AIM and NPA methods are not suitable to characterize the solvation structure of TMCs that possess ionic character. This is not surprising because these methods suffer from overestimation of PACs for atoms in ionic bonds.[50,51] Depending

View Article Online
DOI: 10.1039/C8CP06567E

on the ligand structure, the ChelpG, RESP, RESP(MPA) and CM5 methods are well-suited to describe the solvation structure. For $[Ru(bpy)_3]^{2+}$ and $[Fe(bpy)_3]^{2+}$, the three bidentate bpy ligands do not allow the solvent molecules to feel the charge of the metal directly. For such TMCs like $[Ru(bpy)_3]^{2+}$ and $[Fe(bpy)_3]^{2+}$, with exclusion of AIM, one can apply any other PAC method of this work in classical MD simulations and obtain RDFs as accurate as those provided by QM/MM BOMD in water. In $[Fe(bmip)_2]^{2+}$ and especially $[Cu(phen)_2]^{+}$, more space is available between the ligands which enables the solvent molecules to approach the metals. In such cases, our results in ACN indicate that a careful selection of the PAC method is required. Thus, the selection of PAC method is dependent on the coordination number of the metal and the denticity of the ligands.

To extend our conclusion, we also studied the effect of the type of the solvent. To do so, we have repeated the classical MD simulations for $[Ru(bpy)_3]^{2+}$ and $[Fe(bpy)_3]^{2+}$ in ACN solvent and for $[Fe(bmip)_2]^{2+}$ and $[Cu(phen)_2]^{+}$ in water; Figs. S11-S14 present their corresponding RDFs. The results show that the RDFs simulated in ACN are more sensitive to the choice of the applied PAC methods than in water, particularly in the cases of $[Fe(bmip)_2]^{2+}$ and $[Cu(phen)_2]^{+}$ for which more space is accessible between the ligands. These results might be due to the nearly twice as large dipole moment of ACN (3.96 D) compared to the one of water (2.18 D), as computed from the applied force fields[72,99]. Hence, in addition to the ligand denticity and metal coordination number dependency, the selection of PAC method is also solvent-dependent. The effect of the vdW radius of the metals on ChelpG PACs and resulting RDFs for the GS and ^{3}MLCT state of $[Ru(bpy)_3]^{2+}$ and $[Cu(phen)_2]^{+}$ in ACN was also studied. By decreasing this parameter, the charge of the metal becomes more positive while the bonded N atoms get more negative and leading to a higher ionic character. For $[Ru(bpy)_3]^{2+}$, no changes are observed in the RDFs obtained using different vdW radii. However, the excited state of $[Cu(phen)_2]^{+}$ is found to be highly sensitive on the vdW radius. Our calculations show that by using vdW radii of 1.20 or 1.00 Å for the Cu atom in the ChelpG calculations, we can produce RDFs in good agreement with the QM/MM MD. Furthermore, for the ^{3}MLCT state of $[Cu(phen)_2]^{+}$, we studied this effect in water. These results show that the obtained RDFs (see Fig. S15) are more sensitive to changing the vdW radius in ACN than water. This leads to the conclusion that the application of ChelpG PACs for such cases requires the optimization of the vdW radius of the metal by further benchmarking.

According to the RDF results, only PAC methods derived from physical observables, the ESP for the ChelpG, RESP, and RESP(MPA) methods and the molecular dipole moment for the CM5 method, enable us to produce RDFs as close as those from QM/MM MD. As mentioned in Section 2.1, the RESP method is designed to overcome the problem of charge prediction of deeply buried atoms in the ChelpG method. However, in all four cases in this work, the results have demonstrated almost identical RDFs for the ChelpG and the RESP/RESP(MPA) methods. Among the applied PAC methods, the ChelpG/RESP and the CM5 PAC methods can characterize the solvation structure around TMCs using fast classical MD simulations with an accuracy approaching the one of QM/MM MD simulations.

Conflicts of interest

There are no conflicts to declare.

Acknowledgements The research leading to the presented results has received funding from the People Programme (Marie Curie Actions) of the European Union's Seventh Framework Programme (FP7/ 2007-2013) under REA Grant Agreement No. 609405 (COFUNDPostdocDTU), the Danish Council of Independent Research Grant No. 4002-00272, the Independent Research Fund Denmark Grant No. 8021-00347B, and was also supported by the "Lendület" (Momentum) Program of the Hungarian Academy of Sciences (LP2013-59). GL thanks the Icelandic Research Fund for financial support.

References

1 V. Balzani, G. Bergamini, S. Campagna and F. Puntoriero, in *Photochemistry and Photophysics of Coordination Compounds I*, ed. V. Balzani and S. Campagna, Springer Berlin Heidelberg, Berlin, Heidelberg, 2007, pp. 1–36.

2 M. Chergui, *Acc. Chem Res.*, 2015, **48**, 801–808.

3 J. K. McCusker, *Acc. Chem. Res.*, 2003, **36**, 876–887.

4 M. Iwamura, S. Takeuchi and T. Tahara, *Acc. Chem. Res.*, 2015.

5 T. J. Penfold, B. F. E. Curchod, I. Tavernelli, R. Abela, U. Rothlisberger and M. Chergui, *Phys. Chem. Chem. Phys.*, 2012, **14**, 9444–9450.

6 A. E. Nahhas, A. Cannizzo, F. v. Mourik, A. M. Blanco-Rodríguez, S. Záliš, A. Vlček Jr. and M. Chergui, *J. Phys. Chem. A*, 2010, **114**, 6361–6369.

7 A. O. Dohn, K. S. Kjær, T. B. Harlang, S. E. Canton, M. M. Nielsen and K. B. Møller, *Inorg. Chem.*, 2016, **55**, 10637–10644.

8 K. S. Kjæer, K. Kunnus, T. C. B. Harlang, T. B. Van Driel, K. Ledbetter, R. W. Hartsock, M. E. Reinhard, S. Koroidov, L. Li, M. G. Laursen, E. Biasin, F. B. Hansen, P. Vester, M. Christensen, K. Haldrup, M. M. Nielsen, P. Chabera, Y. Liu, H. Tatsuno, C. Timm, J. Uhlig, V. Sundstom, Z. Nemeth, D. S. Szemes, E. Bajnoczi, G. Vanko, R. Alonso-Mori, J. M. Glownia, S. Nelson, M. Sikorski, D. Sokaras, H. T. Lemke, S. E. Canton, K. Warnmark, P. Persson, A. A. Cordones and K. J. Gaffney, *Phys. Chem. Chem. Phys.*, 2018, **20**, 4238–4249.

9 M. A. Chagas and W. R. Rocha, *Chem. Phys. Lett.*, 2014, **612**, 78–83.

10 F. Ma, M. Jarenmark, S. Hedstrom, P. Persson, E. Nordlander and A. Yartsev, *RSC Adv.*, 2016, **6**, 20507–20515.

11 D. A. Hoff, R. Silva and L. G. C. Rego, *J. Phys. Chem. C*, 2011, **115**, 15617–15626.

12 A. Agena, S. Iuchi and M. Higashi, *Chem. Phys. Lett.*, 2017, **679**, 60–65.

13 K. Haldrup, W. Gawelda, R. Abela, R. Alonso-Mori, U. Bergmann, A. Bordage, M. Cammarata, S. E. Canton, A. O. Dohn, T. B. van Driel, D. M. Fritz, A. Galler, P. Glatzel, T. Har-

View Article Online
DOI: 10.1039/C8CP06567E

lang, K. S. Kjær, H. T. Lemke, K. B. Møller, Z. Németh, M. Pápai, N. Sas, J. Uhlig, D. Zhu, G. Vankó, V. Sundström, M. M. Nielsen and C. Bressler, *J. Phys. Chem. B*, 2016.

14 K. Haldrup, G. Vankó, W. Gawelda, A. Galler, G. Doumy, A. M. March, E. P. Kanter, A. Bordage, A. Dohn, T. B. van Driel, K. S. Kjær, H. T. Lemke, S. E. Canton, J. Uhlig, V. Sundström, L. Young, S. H. Southworth, M. M. Nielsen and C. Bressler, *J. Phys. Chem. A*, 2012, **116**, 9878–9887.

15 E. Biasin, T. B. van Driel, K. S. Kjær, A. O. Dohn, M. Christensen, T. Harlang, P. Chabera, Y. Liu, J. Uhlig, M. Pápai, Z. Németh, R. Hartsock, W. Liang, J. Zhang, R. Alonso-Mori, M. Chollet, J. M. Glownia, S. Nelson, D. Sokaras, T. A. Assefa, A. Britz, A. Galler, W. Gawelda, C. Bressler, K. J. Gaffney, H. T. Lemke, K. B. Møller, M. M. Nielsen, V. Sundström, G. Vankó, K. Wärnmark, S. E. Canton and K. Haldrup, *Phys. Rev. Lett.*, 2016, **117**, 013002.

16 T. B. van Driel, K. S. Kjær, R. W. Hartsock, A. O. Dohn, T. Harlang, M. Chollet, M. Christensen, W. Gawelda, N. E. Henriksen, J. G. Kim, K. Haldrup, K. H. Kim, H. Ihee, J. Kim, H. Lemke, Z. Sun, V. Sundström, W. Zhang, D. Zhu, K. B. Møller, M. M. Nielsen and K. J. Gaffney, *Nat. Commun.*, 2016, **7**, 13678.

17 S. E. Canton, K. S. Kjær, G. Vankó, T. B. van Driel, S.-i. Adachi, A. Bordage, C. Bressler, P. Chabera, M. Christensen, A. O. Dohn, A. Galler, W. Gawelda, D. Gosztola, K. Haldrup, T. Harlang, Y. Liu, K. B. Møller, Z. Németh, S. Nozawa, M. Pápai, T. Sato, T. Sato, K. Suarez-Alcantara, T. Togashi, K. Tono, J. Uhlig, D. A. Vithanage, K. Wärnmark, M. Yabashi, J. Zhang, V. Sundström and M. M. Nielsen, *Nat. Commun.*, 2015, **6**, 6359.

18 J. Tomasi, B. Mennucci and R. Cammi, *Chem. Rev.*, 2005, **105**, 2999–3093.

19 C. J. Cramer and D. G. Truhlar, *Chem. Rev.*, 1999, **99**, 2161–2200.

20 O. Andreussi and G. Fisicaro, *International Journal of Quantum Chemistry*, **119**, e25725.

21 M. Elstner, D. Porezag, G. Jungnickel, J. Elsner, M. Haugk, T. Frauenheim, S. Suhai and G. Seifert, *Phys. Rev. B*, 1998, **58**, 7260–7268.

22 A. W. Sakti, Y. Nishimura, C.-P. Chou and H. Nakai, *J. Phys. Chem. A*, 2018, **122**, 33–40.

23 A. Warshel and M. Levitt, *J. Mol. Biol.*, 1976, **103**, 227 – 249.

24 M. J. Field, P. A. Bash and M. Karplus, *Journal of Computational Chemistry*, **11**, 700–733.

25 G. Groenhof, *Introduction to QM/MM Simulations*, Humana Press, Totowa, NJ, 2013, pp. 43–66.

26 H. M. Senn and W. Thiel, *Angew. Chem. Int. Ed.*, **48**, 1198–1229.

27 A. O. Dohn, E. Biasin, K. Haldrup, M. M. Nielsen, N. E. Henriksen and K. B. Møller, *J. Phys. B: At. Mol. Opt. Phys.*, 2015, **48**, 244010.

28 P. D'Angelo, A. D. Nola, A. Filipponi, N. V. Pavel and D. Roccatano, *J. Chem. Phys.*, 1994, **100**, 985–994.

29 I. Josefsson, S. K. Eriksson, H. Rensmo and M. Odelius, *Struct. Dyn.*, 2016, **3**, 23607.

30 J. J. Szymczak, F. D. Hofmann and M. Meuwly, *Phys. Chem. Chem. Phys.*, 2013, **15**, 6268–6277.

31 A. K. Das, R. V. Solomon, F. Hofmann and M. Meuwly, *J. Phys. Chem. B*, 2016, **120**, 206–216.

32 S. Iuchi and N. Koga, *Phys. Chem. Chem. Phys.*, 2016, **18**, 4789–4799.

33 T. J. Penfold, S. Karlsson, G. Capano, F. A. Lima, J. Rittmann, M. Reinhard, M. H. Rittmann-Frank, O. Braem, E. Baranoff, R. Abela, I. Tavernelli, U. Rothlisberger, C. J. Milne and M. Chergui, *J. Phys. Chem. A*, 2013, **117**, 4591–4601.

34 G. Capano, U. Rothlisberger, I. Tavernelli and T. J. Penfold, *J. Phys. Chem. A*, 2015, **119**, 7026–7037.

35 M.-E. Moret, I. Tavernelli and U. Rothlisberger, *J. Phys. Chem. B*, 2009, **113**, 7737–7744.

36 J. J. Nogueira and L. González, *Annu. Rev. Phys. Chem.*, 2018, **69**, 473–497.

37 M.-E. Moret, I. Tavernelli, M. Chergui and U. Rothlisberger, *Chem. Eur. J.*, 2010, **16**, 5889–5894.

38 A. J. Atkins and L. González, *J. Phys. Chem. Lett.*, 2017, **8**, 3840–3845.

39 L. M. Lawson Daku and A. Hauser, *J. Phys. Chem. Lett.*, 2010, **1**, 1830–1835.

40 G. Auböck and M. Chergui, *Nat. Chem.*, 2015, **7**, 629.

41 Y. Liu, T. Harlang, S. E. Canton, P. Chábera, K. Suárez-Alcántara, A. Fleckhaus, D. A. Vithanage, E. Göransson, A. Corani, R. Lomoth, V. Sundström and K. Wärnmark, *Chem. Commun.*, 2013, **49**, 6412–6414.

42 M. Pápai, G. Vankó, T. Rozgonyi and T. J. Penfold, *J. Phys. Chem. Lett.*, 2016.

43 R. S. Mulliken, *J. Chem. Phys.*, 1955, **23**, 1833–1840.

44 A. E. Reed, R. B. Weinstock and F. Weinhold, *J. Chem. Phys.*, 1985, **83**, 735–746.

45 C. M. Breneman and K. B. Wiberg, *J. Comput. Chem.*, 1990, **11**, 361–373.

46 C. I. Bayly, P. Cieplak, W. Cornell and P. A. Kollman, *J. Phys. Chem.*, 1993, **97**, 10269–10280.

47 R. F. W. Bader, *Chem. Rev.*, 1991, **91**, 893–928.

48 F. L. Hirshfeld, *Theor. Chim. Acta*, 1977, **44**, 129–138.

49 A. V. Marenich, S. V. Jerome, C. J. Cramer and D. G. Truhlar, *J. Chem. Theory Comput.*, 2012, **8**, 527–541.

50 S. M. Bachrach, in *Reviews in Computational Chemistry*, Wiley-Blackwell, 2007, ch. Volume 5, pp. 171–228.

51 A. B. Sannigrahi, P. K. Nandi and P. R. Schleyer, *Chem. Phys. Lett.*, 1993, **204**, 73–79.

52 E. R. Davidson and S. Chakravorty, *Theor. Chim. Acta*, 1992, **83**, 319–330.

53 M. Reiher, O. Salomon and B. Artur Hess, *Theor. Chem. Acc.*, 2001, **107**, 48–55.

54 M. Reiher, *Inorg. Chem.*, 2002, **41**, 6928–6935.

55 F. Weigend and R. Ahlrichs, *Phys. Chem. Chem. Phys.*, 2005, **7**, 3297–3305.

56 M. Pápai, G. Vankó, C. de Graaf and T. Rozgonyi, *J. Chem. Theory Comput.*, 2013, **9**, 509–519.

View Article Online
DOI: 10.1039/C8CP06567E

57 D. Leshchev, T. C. B. Harlang, L. A. Fredin, D. Khakhulin, Y. Liu, E. Biasin, M. G. Laursen, G. E. Newby, K. Haldrup, M. Nielsen, K. Warnmark, V. Sundstrom, P. Persson, K. S. Kjaer and M. Wulff, *Chem. Sci.*, 2018, **9**, 405–414.

58 L. M. Lawson Daku, A. Vargas, A. Hauser, A. Fouqueau and M. E. Casida, *ChemPhysChem*, 2005, **6**, 1393–1410.

59 M. Reiher, *Inorg. Chem.*, 2002, **41**, 6928–6935.

60 H. Paulsen, V. Schünemann and J. A. Wolny, *Progress in electronic structure calculations on spin-crossover complexes*, 2013.

61 L. A. Fredin, M. Pápai, E. Rozsályi, G. Vankó, K. Wärnmark, V. Sundström and P. Persson, *J. Phys. Chem. Lett.*, 2014, **5**, 2066–2071.

62 M. J. Frisch, G. W. Trucks, H. B. Schlegel, G. E. Scuseria, M. A. Robb, J. R. Cheeseman, G. Scalmani, V. Barone, G. A. Petersson, H. Nakatsuji, X. Li, M. Caricato, A. V. Marenich, J. Bloino, B. G. Janesko, R. Gomperts, B. Mennucci, H. P. Hratchian, J. V. Ortiz, A. F. Izmaylov, J. L. Sonnenberg, D. Williams-Young, F. Ding, F. Lipparini, F. Egidi, J. Goings, B. Peng, A. Petrone, T. Henderson, D. Ranasinghe, V. G. Zakrzewski, J. Gao, N. Rega, G. Zheng, W. Liang, M. Hada, M. Ehara, K. Toyota, R. Fukuda, J. Hasegawa, M. Ishida, T. Nakajima, Y. Honda, O. Kitao, H. Nakai, T. Vreven, K. Throssell, J. A. Montgomery Jr., J. E. Peralta, F. Ogliaro, M. J. Bearpark, J. J. Heyd, E. N. Brothers, K. N. Kudin, V. N. Staroverov, T. A. Keith, R. Kobayashi, J. Normand, K. Raghavachari, A. P. Rendell, J. C. Burant, S. S. Iyengar, J. Tomasi, M. Cossi, J. M. Millam, M. Klene, C. Adamo, R. Cammi, J. W. Ochterski, R. L. Martin, K. Morokuma, O. Farkas, J. B. Foresman and D. J. Fox, *Gaussian16 Revision A.03*, 2016.

63 M. Douglas and N. M. Kroll, *Ann. Physics*, 1974, **82**, 89–155.

64 B. A. Hess, *Phys. Rev. A: At. Mol. Opt. Phys.*, 1986, **33**, 3742–3748.

65 T. Lu and F. Chen, *J. Comput. Chem.*, 2012, **33**, 580–592.

66 S. Nag, K. Banerjee and D. Datta, *New J. Chem.*, 2007, **31**, 832–834.

67 E. Sigfridsson and U. Ryde, *J. Comput. Chem.*, 1998, **19**, 377–395.

68 J. Wang, W. Wang, P. A. Kollman and D. A. Case, *J. Mol. Graph. Model.*, 2006, **25**, 247–260.

69 J. Wang, R. M. Wolf, J. W. Caldwell, P. A. Kollman and D. A. Case, *J. Comput. Chem.*, 2004, **25**, 1157–1174.

70 K. J. Bowers, D. E. Chow, H. Xu, R. O. Dror, M. P. Eastwood, B. A. Gregersen, J. L. Klepeis, I. Kolossvary, M. A. Moraes, F. D. Sacerdoti, J. K. Salmon, Y. Shan and D. E. Shaw, SC 2006 Conference, Proceedings of the ACM/IEEE, 2006, p. 43.

71 W. L. Jorgensen, J. Chandrasekhar, J. D. Madura, R. W. Impey and M. L. Klein, *J. Chem. Phys.*, 1983, **79**, 926–935.

72 E. Guàrdia, R. Pinzón, J. Casulleras, M. Orozco and F. J. Luque, *Mol. Simul.*, 2001, **26**, 287–306.

73 N. H. Damrauer, G. Cerullo, A. Yeh, T. R. Boussie, C. V. Shank and J. K. McCusker, *Science*, 1997, **275**, 54–57.

74 M. Iwamura, S. Takeuchi and T. Tahara, *J. Am. Chem. Soc.*, 2007, **129**, 5248–5256.

75 W. L. Jorgensen, D. S. Maxwell and J. Tirado-Rives, *J. Am. Chem. Soc*, 1996, **118**, 11225–11236.

76 D. D. Humphreys, R. A. Friesner and B. J. Berne, *J. Phys. Chem.*, 1994, **98**, 6885–6892.

77 H. J. Berendsen, J. P. Postma, W. F. Van Gunsteren, A. Dinola and J. R. Haak, *J. Chem. Phys.*, 1984.

78 V. Kräutler, W. F. van Gunsteren and P. H. Hünenberger, *Journal of Computational Chemistry*, **22**, 501–508.

79 S. Nosé, *J. Chem. Phys.*, 1984, **81**, 511–519.

80 W. G. Hoover, *Phys. Rev. A: At. Mol. Opt. Phys.*, 1985, **31**, 1695–1697.

81 A. H. Larsen, J. J. Mortensen, J. Blomqvist, I. E. Castelli, R. Christensen, M. Dułak, J. Friis, M. N. Groves, B. Hammer, C. Hargus, E. D. Hermes, P. C. Jennings, P. B. Jensen, J. Kermode, J. R. Kitchin, E. L. Kolsbjerg, J. Kubal, K. Kaasbjerg, S. Lysgaard, J. B. Maronsson, T. Maxson, T. Olsen, L. Pastewka, A. Peterson, C. Rostgaard, J. Schiøtz, O. Schütt, M. Strange, K. S. Thygesen, T. Vegge, L. Vilhelmsen, M. Walter, Z. Zeng and K. W. Jacobsen, *J. Phys. Condens. Matter*, 2017, **29**, 273002.

82 S. R. Bahn and K. W. Jacobsen, *Comput. Sci. Eng.*, 2002, **4**, 55.

83 A. O. Dohn, E. ö. Jónsson, G. Levi, J. J. Mortensen, O. Lopez-Acevedo, K. S. Thygesen, K. W. Jacobsen, J. Ulstrup, N. E. Henriksen, K. B. Møller and H. Jónsson, *J. Chem. Theory Comput.*, 2017, **13**, 6010–6022.

84 A. O. Dohn, E. Ã. JÃşnsson, K. S. KjÃęr, T. B. van Driel, M. M. Nielsen, K. W. Jacobsen, N. E. Henriksen and K. B. MÃÿller, *The Journal of Physical Chemistry Letters*, 2014, **5**, 2414–2418.

85 J. Enkovaara, C. Rostgaard, J. J. Mortensen, J. Chen, M. Dulak, L. Ferrighi, J. Gavnholt, C. Glinsvad, V. Haikola, H. A. Hansen, H. H. Kristoffersen, M. Kuisma, A. H. Larsen, L. Lehtovaara, M. Ljungberg, O. Lopez-Acevedo, P. G. Moses, J. Ojanen, T. Olsen, V. Petzold, N. A. Romero, J. Stausholm-Møller, M. Strange, G. A. Tritsaris, M. Vanin, M. Walter, B. Hammer, H. Häkkinen, G. K. H. Madsen, R. M. Nieminen, J. K. Nørskov, M. Puska, T. T. Rantala, J. Schiøtz, K. S. Thygesen and K. W. Jacobsen, *J. Phys. Condens. Matter*, 2010, **22**, 253202.

86 J. J. Mortensen, L. B. Hansen and K. W. Jacobsen, *Phys. Rev. B: Condens. Matter*, 2005, **71**, 35109.

87 A. H. Larsen, M. Vanin, J. J. Mortensen, K. S. Thygesen and K. W. Jacobsen, *Phys. Rev. B*, 2009, **80**, 195112.

88 G. Levi, M. Pápai, N. E. Henriksen, A. O. Dohn and K. B. Møller, *J. Phys. Chem. C*, 2018, **122**, 7100–7119.

89 A. D. Becke, *Phys. Rev. A: At. Mol. Opt. Phys.*, 1988, **38**, 3098.

90 J. P. Perdew, *Phys. Rev. B*, 1986, **33**, 8822–8824.

91 L. M. Lawson Daku, *Phys. Chem. Chem. Phys.*, 2018, **20**, 6236–6253.

92 L. M. Lawson Daku, *Phys. Chem. Chem. Phys.*, 2019, **21**, 650–661.

93 M. Buchs and C. Daul, *CHIMIA*, 1998, **52**, 163–166.

94 A. K. Rappe, C. J. Casewit, K. S. Colwell, W. A. G. III and W. M. Skiff, *J. Am. Chem. Soc*, 1992, **114**, 10024–10035.

95 M. P. Allen and D. J. Tildesley, *Computer Simulation of Liquids*,

View Article Online
DOI: 10.1039/C8CP06567E

Oxford University Press, 2nd edn., 1989.
96 H. C. Andersen, *J. Comput. Phys.*, 1983, **52**, 24.
97 W. Humphrey, A. Dalke and K. Schulten, *J. Mol. Graphics*, 1996, **14**, 33–38.
98 I. Tavernelli, B. F. E. Curchod and U. Rothlisberger, *Chem. Phys.*, 2011, **391**, 101–109.
99 M. W. Mahoney and W. L. Jorgensen, *J. Chem. Phys.*, 2000, **112**, 8910–8922.

Appendix B

Paper II

Excited State Charge Distribution and Bond Expansion of Ferrous Complexes Observed with Femtosecond Valence-to-Core X-ray Emission Spectroscopy

Kathryn Ledbetter,[1,2] Marco E. Reinhard,[2] Kristjan Kunnus,[2] Alessandro Gallo,[3,4] Alexander Britz,[2,5] Elisa Biasin,[2] James M. Glownia,[5] Silke Nelson,[5] Tim B. Van Driel,[5] Clemens Weninger,[5] Diana B. Zederkof,[6] Kristoffer Haldrup,[6] Amy A. Cordones,[2] Kelly J. Gaffney,[2, a)] Dimosthenis Sokaras,[7, a)] and Roberto Alonso-Mori[5, a)]

[1)] *Department of Physics, Stanford University, Stanford, California 94305, USA.*

[2)] *Stanford PULSE Institute, SLAC National Accelerator Laboratory, Menlo Park, California 94025, USA.*

[3)] *SUNCAT Center for Interface Science and Catalysis, SLAC National Accelerator Laboratory, Menlo Park, California 94025, USA*

[4)] *Department of Chemical Engineering, Stanford University, 443 Via Ortega, Stanford, CA 94305, USA*

[5)] *LCLS, SLAC National Accelerator Laboratory, Menlo Park, California 94025, USA.*

[6)] *Department of Physics, Technical University of Denmark, 2800 Kongens Lyngby, Denmark.*

[7)] *SSRL, SLAC National Accelerator Laboratory, Menlo Park, California, 94025, USA.*

(Dated: 14 January 2020)

Valence-to-core x-ray emission spectroscopy (VtC XES) combines the sample flexibility and element specificity of hard x-rays with the chemical environment sensitivity of valence spectroscopy. We extend this technique to study geometric and electronic structural changes induced by photoexcitation in the femtosecond time domain via laser-pump, x-ray probe experiments at an x-ray free electron laser. The results of time-resolved VtC XES on a series of ferrous complexes $[Fe(CN)_{2n}(2,2'\text{-bipyridine})_{3-n}]^{-2n+2}$, $n = 1, 2, 3$ are presented. Comparisons with spectra obtained from ground state density functional theory calculations reveal signatures of excited state bond length and oxidation state changes. An oxidation state change associated with a metal-to-ligand charge transfer state with a lifetime of less than 100 femtoseconds is observed, as well as bond length changes associated with metal-centered states with lifetimes of 13 and 250 picoseconds.

[a)]Corresponding authors. E-mail: kgaffney@slac.stanford.edu; dsokaras@slac.stanford.edu; robertoa@slac.stanford.edu

I. INTRODUCTION

Valence-to-core x-ray emission spectroscopy (VtC XES) is an emerging technique for the study of inorganic 3d metal based molecular systems. In the VtC spectral region (Kβ'' and K$\beta_{2,5}$), emission arises from the radiative decay of valence electrons to the metal 1s core hole created by an x-ray absorption process. Such transitions gain dipole-allowed intensity via the mixing of metal np character into the valence orbitals. Therefore, VtC XES is sensitive to bonding and chemical environment of the absorbing atom, but retains specificity to the absorbing atom. Static VtC XES studies have demonstrated the technique's sensitivity to ligand environment, including protonation, as well as oxidation state and bond lengths.[1–8]

Extending VtC XES to ultrafast time-resolved experiments holds promise as a tool to probe local geometry, ligand environment, and oxidation state of transient species. The goal of understanding chemical reaction dynamics and mechanisms requires resolution on femtosecond and picosecond time scales and sensitivity to the geometric and electronic structure of transient species. VtC XES spectra are sensitive to both electronic and geometric structure, and have proven straightforward to model: ground state DFT calculations of single-electron transitions are found to agree well with experimental VtC data, in contrast to the many-electron approaches necessary to model K$\beta_{1,3}$ transitions.[3,5]

Time-resolved XES in the 2p-1s (Kα) and 3p-1s (K$\beta_{1,3}$) main line regions has already been used to uncover the spin state of short-lived intermediates and track the population of optically dark metal-centered states in a variety of molecules, including proteins.[9–14] XES has the advantage of being element-specific, and working in the hard x-ray regime allows considerable flexibility in sample environments, including solids and liquids at variable temperatures and conditions. The VtC region's sensitivity to the local structure and oxidation state, in conjunction with the simplicity of modeling the spectrum, makes it an attractive addition to transient Kα and K$\beta_{1,3}$ XES experiments to concurrently monitor spin, geometric and oxidation state changes. In terms of geometric sensitivity, other methods such as time-resolved x-ray solution scattering (XSS) and extended x-ray absorption fine structure (EXAFS) access geometric information directly; however, XSS is complex to interpret, and EXAFS requires scanning of the incident monochromatic photon energy, making this method less amenable to x-ray laser sources. In contrast to EXAFS, full XES spectra can be measured on a shot-by-shot basis using dispersive spectrometers,[15] and can be combined with

XSS in a single experiment, providing complementary information and taking advantage of the total flux of the XFEL SASE pulses.

A major challenge in implementing time-resolved VtC XES is the very small signal magnitude, since the $K\beta_{2,5}$ emission is 50-100 times less intense than the $K\beta_{1,3}$ main line. Time-resolved VtC XES studies at the Advanced Photon Source light source observed transient species on the 100 ps timescale,[16–18] taking advantage of the MHz repetition rate of the light source to obtain difference spectra at high photon flux ($> 10^{15}$ ph/s).[18,19] With the application of time-slicing methods, the timescales available at synchrotrons can be improved to the tens of ps regime.[20] In comparison, x-ray free-electron laser (XFEL) sources such as the Linac Coherent Light Source (LCLS) combine high photon flux ($> 10^{14}$ ph/s) with femtosecond time resolution. Thus, XFEL experiments could ideally be used to record a two-dimensional map of VtC changes with high resolution in both emission energy and time.

This study demonstrates femtosecond resolution VtC XES at the LCLS. Although the signal-to-noise of the data presented here precludes robust two-dimensional mapping of the VtC difference spectra, energy-resolved difference spectra integrated over tens of picoseconds and femtosecond time-resolved difference spectra integrated over a few eV are shown to provide information about geometric and electronic structure of transient species. Pump-probe VtC XES was performed on a series of ferrous complexes: $[Fe(CN)_6]^{4-}$, $[Fe(CN)_4(bpy)]^{2-}$ (bpy = 2, 2′-bipyridine), and $[Fe(CN)_2(bpy)_2]$. Our measurements focused on demonstrating the ability of VtC to characterize the properties of short-lived intermediates formed following ultrafast internal conversion, intersystem crossing, charge transfer, and ligand rearrangement. Experimental difference spectra were compared to theoretical spectra extracted from ground state DFT calculations of the expected species to demonstrate sensitivity to bond length expansion in the triplet excited state of $[Fe(CN)_4(bpy)]^{2-}$ and quintet excited state of $[Fe(CN)_2(bpy)_2]$. Time traces of a difference spectrum of $[Fe(CN)_4(bpy)]^{2-}$ with ≈ 100 fs resolution show sensitivity to Fe oxidation state that allow a short-lived charge-transfer state to be observed.

II. METHODS

A. Experimental

Optical laser pump/x-ray probe measurements on solution samples were carried out at the XCS hutch[21] of the LCLS. The samples were delivered in a 50 μm round liquid jet in a helium environment. $[Fe(CN)_6]^{4-}$ and $[Fe(CN)_4(bpy)]^{2-}$ were dissolved in water at 50 and 33 mM concentrations, respectively, while $[Fe(CN)_2(bpy)_2]$ was dissolved in methanol at 15 mM concentration, to maintain an optical density (OD) of ≈ 0.5 at the pump wavelength in the jet. For $[Fe(CN)_4(bpy)]^{2-}$ and $[Fe(CN)_2(bpy)_2]$, the sample was pumped with 495 nm laser pulses generated from a Ti:sapphire laser and optical parametric amplifier described elsewhere.[22] The optical pulse duration was less than 70 fs. The optical pulse energy was 7 μJ (spot size 170 x 360 μm; 5 mJ/cm^2) for all plotted data sets, except for the data shown in Figure 1**b**, where the pulse energy varied from 7-17 μJ among averaged data runs. For $[Fe(CN)_6]^{4-}$, the sample was pumped with 266 nm light using the third harmonic of the same Ti:sapphire laser, with a pulse energy of 13.5 μJ (spot size and fluence on the order of 100 x 100 μm; 100 mJ/cm^2).

The sample was probed with pink x-ray pulses centered at 9450 eV ($[Fe(CN)_4(bpy)]^{2-}$and $[Fe(CN)_2(bpy)_2]$) or 8000 eV ($[Fe(CN)_6]^{4-}$), with a spectral width $\Delta E/E$ of 1×10^{-3}, pulse duration of 50 fs, and 120 Hz repetition rate.[21] The x-ray pulse energy on sample was ∼0.75 mJ/pulse. The incident x-rays were focused by compound refractive beryllium lenses with a ∼4 m focal length to a round beam size of 20 x 20 μm. The full Fe Kβ XES spectra (from 7025 to 7115 eV) were collected using a four-crystal von Hamos spectrometer[15] in a shot-by-shot mode. Four cylindrically bent Ge(620) crystal analyzers with a 250 mm bending radius were used. The crystal analyzers are 110 x 25 mm and the spectrometer collects a total solid angle of $\approx 1.4\%$ of the sphere. The energy resolution is estimated to be 0.6 eV, including major geometrical contributions and the intrinsic energy resolution of the crystal analyzer (Darwin width and broadening associated with stress induced in the lattice planes when the analyzer is bent). The spectrum was collected on an ePix100 detector.[23] A helium bag was used between the sample, crystals, and detector to minimize attenuation of the fluorescence and to reduce background from diffuse scattered radiation. The spectrometer was calibrated to the spectrum of a reference sample ($[Fe(CN)_6]^{4-}$ in water, 350 mM concentration).

The time delay between laser pump and x-ray probe pulses was scanned continuously with an encoded delay stage.[24] A spectrally encoding timing tool[25] was used to measure x-ray arrival time relative to the optical pump pulse by probing the x-ray induced change in refractive index of a thin crystal (Si_3N_4 for all datasets except the data shown in Figure1**b**, which contains data taken with both Si_3N_4 and Ce:YAG timing tools) with chirped white-light pulses derived from the optical laser. Sorting the single shot XES spectra by the measured probe arrival time eliminates the majority of the pump-probe time delay jitter and leads to a time resolution of ≈ 100 fs.

Every seventh x-ray shot was taken without the optical laser, and these were averaged to form a laser-off spectrum. The laser-on spectra were binned by time delay. Background scatter was removed from the spectrum by subtracting an average signal from regions of the area detector on either side of the spectrum. All averaged, background-subtracted spectra were normalized to the area under the $K\beta_{1,3}$ main line (7025-7092 eV) to allow intensity changes to be reliably measured. Examples of pre-normalization laser-off and laser-on spectra are shown in the Supplementary Material. For the calculation of area under the VtC spectrum, the signal due to the tail of the $K\beta_{1,3}$ main line was removed by subtracting a single pseudo-Voigt lineshape (variable-weighted sum of Gaussian and Lorentzian functions) fitted to the $K\beta_{1,3}$ main line, as shown in the Supplementary Material. In all cases, about 10% of x-ray shots were removed from the analysis due to very low counts on one or more detectors. Therefore, the laser-off spectra (one-seventh of x-ray shots) represent the statistics possible from an x-ray flux of $\sim 1 \times 10^{13}$ photons/s. The spectra shown in Figure 1 are the result of 50 min ($[Fe(CN)_6]^{4-}$), 260 min ($[Fe(CN)_4(bpy)]^{2-}$), and 100 min ($[Fe(CN)_2(bpy)_2]$) integration times, corresponding to doses ranging from 10^{16} to 10^{17} x-ray photons for the laser-off spectra. The data used to calculate VtC difference areas for $[Fe(CN)_4(bpy)]^{2-}$ and $[Fe(CN)_2(bpy)_2]$ in Table I were integrated for 80 and 40 minutes, respectively. The data shown in Figure 4 is the result of 80 min of integration time.

B. Computational

Density functional theory calculations were carried out with the ORCA 4.1.2 package.[26] Geometries in various spin states were optimized using the B3LYP functional and def2-TZVP[27] basis set using the DFT-D3 approach with Becke-Johnson damping.[28,29] The B3LYP

functional has been shown to match metal-ligand bond lengths from crystal structures for these complexes with error of less than 3%.[30] The effect of the solvent (water for $[Fe(CN)_6]^{4-}$ and $[Fe(CN)_4(bpy)]^{2-}$; methanol for $[Fe(CN)_2(bpy)_2]$) was simulated using the conductor-like polarizable continuum model (CPCM).[31]

X-ray emission spectra were calculated using the one-electron approach described by Lee *et al.*,[3] wherein ground state DFT calculations are used to determine the energetics of the occupied valence orbitals which participate in VtC transitions. Only electric dipole transitions were included in the spectrum. The B3LYP functional and def2-TZVP basis set were used, except for the Fe atom, which used the CP(PPP) basis set with a special integration accuracy of 7, as used in several studies for VtC calculations of ferrous complexes.[3,5,16,17] Scalar relativistic effects were included via the zero-order regular approximation (ZORA)[32,33] and the solvent was again modeled using the CPCM method. An input file for the XES calculation is shown in the Supplementary Material. The calculated transitions were broadened by a 3 eV FWHM Gaussian function and shifted by 23 eV to match experiment, as described in the Supplementary Material.

III. RESULTS

The time-resolved VtC spectra of the three complexes are summarized in Figure 1. Panels **a-c** show laser-on, laser-off, and difference (multiplied by a factor of 2) spectra for each complex. Panels **d-f** show calculated spectra of relevant species and their difference spectra multiplied by a factor of 0.5.

Aqueous $[Fe(CN)_6]^{4-}$ was excited with 266 nm light into the charge-transfer-to-solvent (CTTS) band. There are two major deactivation pathways: (1) photo-oxidation resulting in the oxidized species in a doublet state with a nanosecond lifetime[34] and (2) photoaquation following internal conversion and loss of a cyano ligand.[35] Flash photolysis measurements estimated the quantum yield of photo-oxidation at 266 nm to be ≈ 0.5,[34] while the quantum yield of photoaquation was found to be below 0.2 via 2D UV spectroscopy in the range 255-315 nm.[35,36] Optical transient absorption measurements have demonstrated that photo-oxidation and dissociation are complete within the first few hundred femtoseconds.[36,37] The lifetime of the penta-coordinated species resulting from dissociation, prior to coordinating a water molecule, has been measured via time-resolved XANES to be 19 ps.[20] On the 10-50

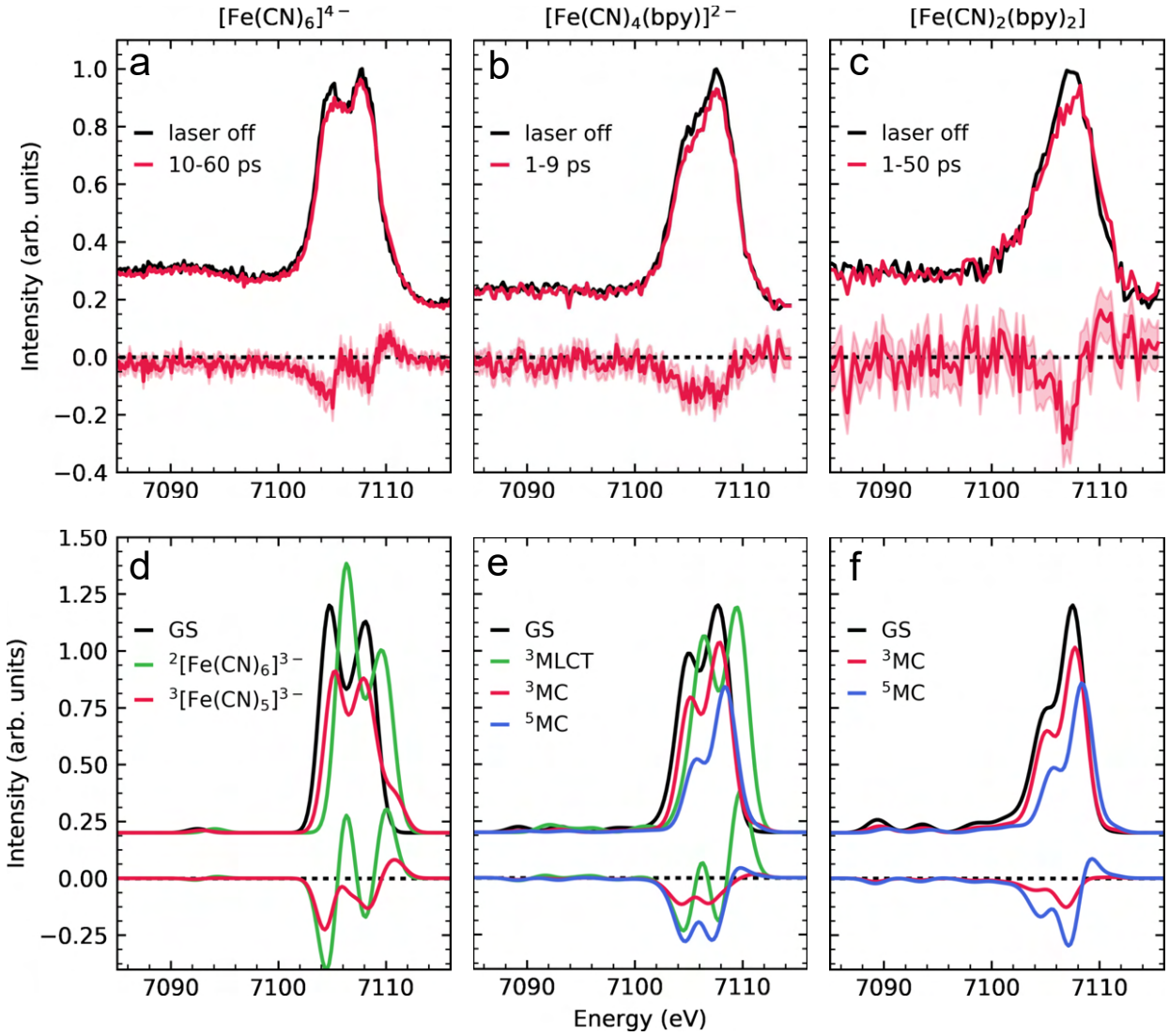

FIG. 1. Measured and calculated VtC spectra for the three complexes. **a-c**: Experimental laser-off (black) and laser-on (red) averaged spectra. Difference signals (red, with shaded error bars) have been multiplied by 2. **d-f**: Calculated spectra and difference signals for relevant states. Difference signals have been multiplied by 0.5.

ps time scale shown in Figure 1, 50% of initially excited molecules are photo-oxidized and 20% have dissociated, with aquation taking place over this time period. Photo-oxidation therefore represents >70% of the photoproduct, with penta-coordinate and aquated species representing the minority decay channels. The current work focuses, in part, on the impact photo-oxidation has on the VtC XES spectra. An in-depth investigation of the multiple species present will be given in an upcoming publication. The VtC difference spectrum,

integrated from 10-60 ps (Figure 1**a**), resembles a shift to higher energy, consistent with the blueshift associated with oxidation in the calculated spectra (**d**) and with previous studies of ferrous and ferric hexacyanide.[3,16,38]

Aqueous $[Fe(CN)_4(bpy)]^{2-}$ was excited with 495 nm light into a bpy-localized metal-to-ligand charge transfer (MLCT) state.[11] Previous ultrafast XES and visible transient absorption (TA) experiments have determined the excited state dynamics of the molecule in water, with the MLCT state relaxing within 100 fs into a metal-centered triplet (^{3}MC) state with a lifetime of 13 ps.[11] The difference signal due to the ^{3}MC state is visible in the transient VtC, integrated from 1-9 ps (Figure 1**b**), and is in good agreement with the calculated difference spectrum (**e**).

$[Fe(CN)_2(bpy)_2]$ in methanol was also excited with 495 nm light into a bpy-localized MLCT state.[39] Previous K$\beta_{1,3}$ XES measurements[39] have determined that the MLCT state decays sequentially to a ^{3}MC state, with time constant 120 fs, then to a metal-centered quintet state (^{5}MC), with time constant 60 fs. The final quintet state has a lifetime of 256 ps. The difference spectrum integrated from 1-50 ps (Figure 1**c**) matches the expected signature of the quintet state from calculation (**f**), but signal-to-noise does not allow isolation of the short-lived triplet difference spectrum on the sub-ps timescale.

IV. DISCUSSION

Photoexcitation of iron complexes leads to multiple changes in the electronic and nuclear structure including charge distribution and oxidation state, spin distribution and total spin moment, and metal-ligand bond lengths, angles, and coordination symmetry. Here, we demonstrate via calculated difference spectra and their comparison to the transient data that ultrafast VtC XES spectroscopy is primarily sensitive to metal-ligand bond lengths and the oxidation state of the iron center. The spectra are found to be only indirectly sensitive to the iron spin moment through the correlation of metal-ligand bond length and spin moment, which results from the occupation of antibonding orbitals in high-spin states.

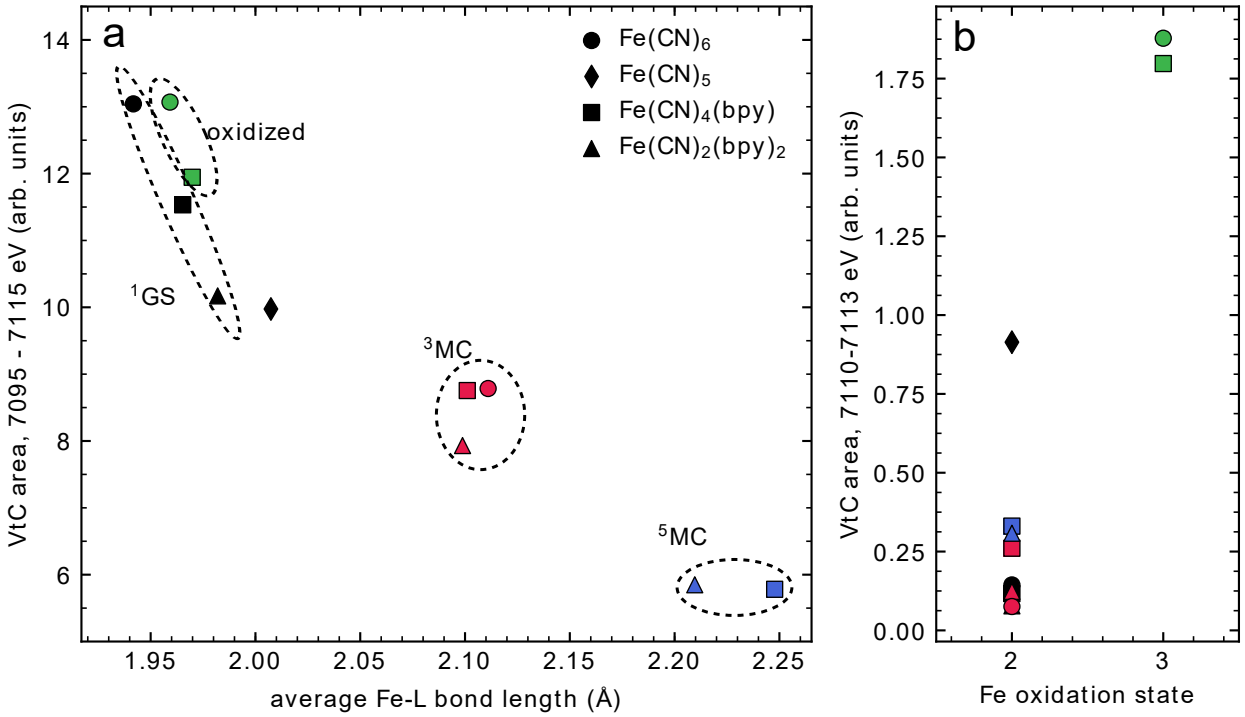

FIG. 2. **a**: Area under simulated VtC spectrum from 7095-7115 eV as a function of Fe-ligand bond lengths for all species shown in Figure 1, as well as $^3[Fe(CN)_6]^{4-}$. States of the same spin group together in both area and bond length. **b**: Area integrated from 7110-7113 eV as a function of iron oxidation state. The blueshift associated with oxidation moves intensity to this region of the spectrum.

A. Structural sensitivity

Figure 2**a** shows the relationship between total area of the simulated VtC spectrum and metal-ligand bond lengths of the optimized structures. The calculated spectrum for each Fe complex was integrated between 7095 and 7115 eV and plotted against the average distance between the iron center and the coordinating ligand atoms (nitrogens of bipyridine ligands or carbons of cyano ligands) in the DFT-optimized geometries. The metal-ligand distance affects the mixing between ligand orbitals and metal np orbitals, for which transitions to the Fe 1s core hole are dipole allowed. A decrease in integrated signal intensity as a function of bond length is observed, especially among structural variants of the same complex. Square pyramidal $^3[Fe(CN)_5]^{3-}$ lies below the trend for $Fe(CN)_6$ species. We assign this effect to the loss of a ligand, which decreases the total orbital overlap. When areas are normalized to the number of coordinating atoms, the penta-coordinated species aligns with the trend

(see Figure S4).

Static VtC measurements of Mn and Fe complexes have found an exponential relationship between the area of the Kβ'' region of the VtC spectrum and metal-ligand bond length,[1,5] and Lee *et al.* find an exponential relationship between total VtC area and metal-ligand bond length for an Fe(III) D_{4h} complex.[3] These studies investigated large ranges of bond lengths, which varied by more than 0.5 Å, in contrast to our case, where the bond lengths vary by less than 0.25 Åbased on DFT calculations; the exponential relationship between calculated VtC area and artificially varied bond lengths in this narrow range is shown in the Supplementary Material, Figure S5.

To demonstrate that the trend of decreasing VtC area is due primarily to bond length changes and not to the population of different metal 3d orbitals in the high-spin state, additional DFT calculations were carried out with low spin electronic configurations on fixed high-spin geometries. This isolates the effects of geometry and spin. Figure 3**a** shows calculated spectra of $[Fe(CN)_2(bpy)_2]$ in singlet, triplet and quintet geometries. The spin state is fixed to both the native value (solid lines) and singlet value (dashed lines). Different spin states on the same geometry (solid vs dashed lines) yield small changes in the ratio between peaks and overall shifts of less than 0.2 eV. The effect of spin state on the integrated area is shown in Figure 3**b** (solid vs open circles). The dominant effect is demonstrated to be geometric, with relatively small area changes associated with spin state.

The appearance of new transitions on the high energy side of the spectrum due to population of new orbitals in the high-spin state, as observed by March *et al.*[17] in $[Fe(terpy)_2]^{2+}$, is dependent on the symmetry of the molecule. From the DFT calculations, for the octahedral $[Fe(CN)_6]^{4-}$, population of new 3d orbitals in the triplet state is not observed in the spectrum, as the iron p and d orbitals do not mix in this symmetry. In $[Fe(CN)_4(bpy)]^{2-}$, which has C_{2v} symmetry in the ground state, p/d mixing causes a new transition at 7111.2 eV, resulting from population of an orbital of primarily Fe d character, to appear in the triplet state. This transition does not appear in the calculated spectrum of the triplet geometry with singlet spin (these spectra are shown in the Supplementary Material, Figure S6). However, this signifier of the spin state is of low intensity and does not appreciably affect the total VtC area. In $[Fe(CN)_2(bpy)_2]$, which has C_2 symmetry in the ground state, no new transitions appear on the high energy shoulder in the high-spin state. This is due to the the lowered symmetry, which causes enough mixing of p and d orbitals that there are

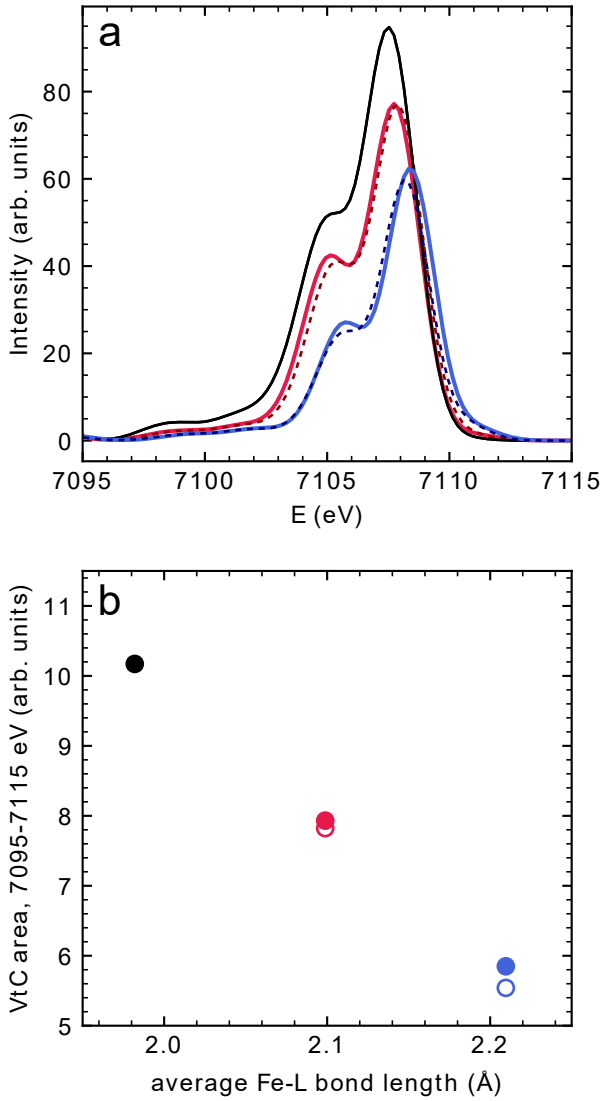

FIG. 3. **a**: Calculated VtC spectra of $[Fe(CN)_2(bpy)_2]$, with ground state (black), triplet (red), and quintet (blue) geometries calculated in native (solid) and singlet (dashed) electronic configuration. **b**: Integrated area under the curves in **a** as a function of average Fe-ligand bond length, with native (solid) and singlet (open) electronic configurations. Change in spin configuration results in minimal change in area and shifts of < 0.2 eV.

no longer any energetically well-separated orbitals of primarily Fe d character.

The sensitivity of the total VtC area to orbital overlap can be used to correlate experimental data to changes in bond length in the excited state. To formulate a quantity that is directly comparable between calculation and experiment, an area ratio is defined as the ratio between total area in the excited state A_{ES} and total area in the ground state A_{GS}.

TABLE I. Ratio of excited-state area A_{ES} to ground-state area A_{GS} under calculated and experimental VtC spectra, integrated from 7095 to 7115 eV. Experimental values have been scaled to unity excitation fraction as described in the text.

molecule	spin mult.	area ratio A_{ES}/A_{GS}	
		experimental	calculated
$[Fe(CN)_4(bpy)]^{2-}$	3	0.7 ± 0.1	0.76
	5	-	0.50
$[Fe(CN)_2(bpy)_2]$	3	-	0.78
	5	0.6 ± 0.1	0.58

Table I reports the areas of calculated spectra for triplet and quintet $[Fe(CN)_4(bpy)]^{2-}$ and $[Fe(CN)_2(bpy)_2]$, divided by the area of the ground-state calculation for each complex.

Comparable area ratios were extracted from experimental data by obtaining a difference area ΔA and a ground state area A_{GS}, and scaling the difference area to represent 100% population in the excited state. The experimental area ratio is given by

$$\frac{A_{ES}}{A_{GS}} = 1 - \frac{1}{\alpha}\frac{\Delta A}{A_{GS}} \tag{1}$$

where α represents the fractional population in the excited state during the time delays integrated to calculate ΔA. ΔA was obtained by integrating the difference spectrum from 7095-7115 eV. A_{GS} was obtained from the ground-state VtC spectrum, background-subtracted as described in Methods, integrated over energy from 7095-7115 eV. Using the known excitation fraction, which is extracted from the $K\beta_{1,3}$ XES data by comparison to model spectra,[11] and the known decay times of the ^{3}MC state of $[Fe(CN)_4(bpy)]^{2-}$ and ^{5}MC state of $[Fe(CN)_2(bpy)_2]$, the excited state population α was calculated for each molecule. For $[Fe(CN)_4(bpy)]^{2-}$ the signal was integrated from 1-9 ps and divided by a factor of $\alpha = 0.20$, accounting for the initial total excited fraction of 0.26, ionization yield of 5%, and 13 ps lifetime of the ^{3}MC state, all obtained from analysis of $K\beta_{1,3}$ XES. For $[Fe(CN)_2(bpy)_2]$ the signal was integrated from 1-60 ps, giving $\alpha = 0.38$ (initial excitation fraction 0.42; lifetime of 256 ps). The resulting area ratios are reported in Table I.

Although the statistical uncertainty is large in these data sets, the area ratios are consistent with the spectral changes predicted by DFT. In future time-resolved experiments

with sufficient signal-to-noise to extract difference spectra at many time points, this method could potentially be used to follow structural dynamics such as vibrations.

B. Oxidation sensitivity

While the area under the VtC spectrum depends primarily on metal-ligand orbital overlap, the position of the spectrum in energy is sensitive to the oxidation state of the iron center. A blueshift is associated with increased oxidation state, which is more pronounced than shifts observed in the $K\beta_{1,3}$ region.[3] A center-of-mass shift of 1.3 and 1.4 eV is observed in the calculated VtC spectra (Figure 1**d-e**) for oxidized $[Fe(CN)_6]^{4-}$ and the ^{3}MLCT state of $[Fe(CN)_4(bpy)]^{2-}$, respectively. This shift moves intensity into the high energy shoulder of the spectrum (7110-7113 eV), as quantified in Figure 2**b** for the calculated spectra. The two calculated states where the iron center is oxidized have more than five times the intensity in this region than any of the hexa-coordinated Fe(II) states. Therefore, the integrated area of the high-energy shoulder of the spectrum has the potential to be used to track local oxidation state of the metal in these complexes.

While there are also energetic shifts associated with metal-ligand bond length and symmetry changes,[8] their effects on the difference intensity in this energy range are comparatively small. The center-of-mass of the triplet state spectra are shifted 0.3-0.4 eV relative to the singlet, and the quintet state spectra are shifted by 1.1-1.2 eV. Because the intensity of the spectrum for high-spin states is considerably smaller, due to loss of overlap between metal and ligand orbitals, even the relatively large shift associated with quintet states does not affect the integrated intensity of the high-energy shoulder to the extent that oxidation state changes do. This allows even large bond length changes to be separated from oxidation state changes. However, the symmetry change associated with the loss of a ligand between $[Fe(CN)_6]^{4-}$ and $^3[Fe(CN)_5]^{3-}$ also has a large effect in this area of the spectrum, indicating that for reactions with both oxidation state changes and coordination changes, more subtle analysis is necessary.

Figure 4 shows experimental time traces of the difference signal for $[Fe(CN)_4(bpy)]^{2-}$ integrated in two regions. The first region, 7103-7110 eV (red), tracks the overall overlap of metal and ligand orbitals as the molecule expands. The second region, 7110-7113 eV (green), tracks the oxidation state of the iron as the molecule is excited into the MLCT

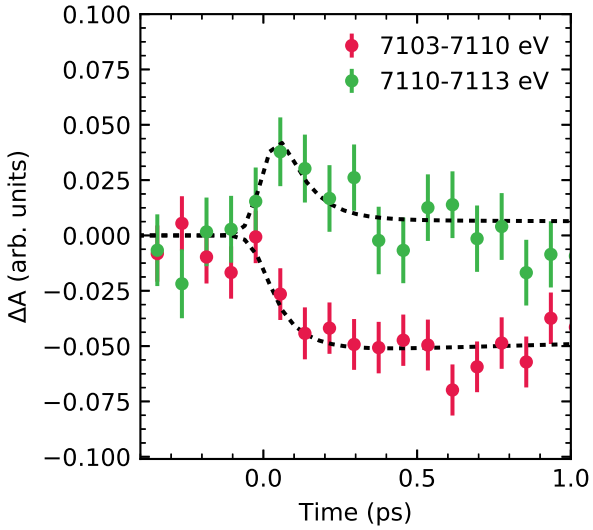

FIG. 4. Time traces of integrated difference intensity in 7103-7110 eV (red) and 7110-7113 eV (green) regions of $[Fe(CN)_4(bpy)]^{2-}$ data. Dashed lines represent expected signal from kinetics extracted from K$\beta_{1,3}$ XES fits and VtC spectra from DFT calculations.

state and then quickly decays into the ^{3}MC state. Overlaid on the plot (dashed lines) is the signal expected from calculated spectra and the lifetimes of the MLCT (90 fs) and ^{3}MC (13 ps) states from K$\beta_{1,3}$ XES.[11] Good agreement between expected and observed signal demonstrates that time-resolved VtC can be used to differentiate charge transfer and metal-ligand bond length changes occurring simultaneously.

V. CONCLUSION

Femtosecond time-resolved VtC XES measurements of three Fe-centered complexes are presented, which demonstrate geometric and oxidation state sensitivity of this method on ultrafast timescales. Calculations indicate that the VtC spectrum is primarily sensitive to geometry, and only indirectly sensitive to spin state via the correlation between spin state and metal-ligand bond lengths. Direct spin sensitivity can instead be achieved with ultrafast K$\beta_{1,3}$ XES, making VtC and K$\beta_{1,3}$ XES complementary approaches to acquiring a more complete characterization of electronic and nuclear excited state dynamics in 3d transition metal complexes. Leveraging the whole Kβ XES spectrum for combined spin, oxidation and geometric information on transient species could be an important method for

the field of ultrafast photochemistry, where electronic and nuclear changes dictate excited state reactivity. K$\beta_{1,3}$ and VtC XES data can be collected concurrently with x-ray solution scattering (XSS), which is also sensitive to structure. The local metal-ligand bond length information available in VtC XES could be used to constrain interpretation of the global structural information given by XSS. The low emission cross-section for VtC XES remains a challenge, but the combination of high-throughput spectrometers like the one used here and the increased repetition rates of superconducting accelerator based x-ray lasers like European XFEL, LCLS-II, and LCLS-II-HE will greatly increase the average x-ray flux and enable robust difference spectra to be measured rapidly, providing the opportunity to track charge distribution and structural dynamics with femtosecond resolution transient VtC XES.

ACKNOWLEDGMENTS

This work is supported by the U.S. Department of Energy, Office of Science, Basic Energy Sciences, Chemical Sciences, Geosciences, and Biosciences Division. Use of the Linac Coherent Light Source (LCLS), SLAC National Accelerator Laboratory, is supported by the U.S. Department of Energy, Office of Science, Office of Basic Energy Sciences under Contract No. DE-AC02-76SF00515. Some of the computing for this project was performed on the Sherlock cluster. We thank Stanford University and the Stanford Research Computing Center for providing computational resources and support that contributed to these research results. KL is supported by a Melvin and Joan Lane Stanford Graduate Fellowship and a Stanford Physics Department fellowship. AG acknowledges the U.S. Department of Energy, Office of Science, Office of Basic Energy Sciences, Chemical Sciences, Geosciences, and Biosciences Division, Catalysis Science Program to the SUNCAT Center for Interface Science and Catalysis.

REFERENCES

[1]U. Bergmann, C. Horne, T. Collins, J. Workman, and S. Cramer, "Chemical dependence of interatomic X-ray transition energies and intensities - a study of Mn Kβ and Kβ2, 5 spectra," Chemical Physics Letters **302**, 119–124 (1999).

[2]P. Glatzel and U. Bergmann, "High resolution 1s core hole X-ray spectroscopy in 3d transition metal complexes - Electronic and structural information," Coordination Chemistry Reviews **249**, 65–95 (2005).

[3]N. Lee, T. Petrenko, U. Bergmann, F. Neese, and S. DeBeer, "Probing valence orbital composition with iron K-beta x-ray emission spectroscopy," Journal of the American Chemical Society **132**, 9715–9727 (2010).

[4]C. J. Pollock and S. DeBeer, "Valence-to-core X-ray emission spectroscopy: A sensitive probe of the nature of a bound ligand," Journal of the American Chemical Society **133**, 5594–5601 (2011).

[5]P. Chandrasekaran, K. P. Chiang, D. Nordlund, U. Bergmann, P. L. Holland, and S. DeBeer, "Sensitivity of X-ray core spectroscopy to changes in metal ligation: A systematic study of low-coordinate, high-spin ferrous complexes," Inorganic Chemistry **52**, 6286–6298 (2013).

[6]M. U. Delgado-Jaime, S. Debeer, and M. Bauer, "Valence-to-core X-ray emission spectroscopy of iron-carbonyl complexes: Implications for the examination of catalytic intermediates," Chemistry - A European Journal **19**, 15888–15897 (2013).

[7]E. Gallo and P. Glatzel, "Valence to core X-ray emission spectroscopy," Advanced Materials **26**, 7730–7746 (2014).

[8]C. J. Pollock and S. DeBeer, "Insights into the Geometric and Electronic Structure of Transition Metal Centers from Valence-to-Core X-ray Emission Spectroscopy," Accounts of Chemical Research **48**, 2967–2975 (2015).

[9]W. Zhang, R. Alonso-Mori, U. Bergmann, C. Bressler, M. Chollet, A. Galler, W. Gawelda, R. G. Hadt, R. W. Hartsock, T. Kroll, K. S. Kjær, K. Kubiček, H. T. Lemke, H. W. Liang, D. a. Meyer, M. M. Nielsen, C. Purser, J. S. Robinson, E. I. Solomon, Z. Sun, D. Sokaras, T. B. van Driel, G. Vankó, T.-C. Weng, D. Zhu, and K. J. Gaffney, "Tracking excited-state charge and spin dynamics in iron coordination complexes." Nature **509**, 345–8 (2014).

[10]J. Kern, R. Tran, J. Hattne, R. J. Gildea, N. Echols, B. Lassalle-Kaiser, A. Lampe, G. Han, S. Gul, R. W. Grosse-Kunstleve, P. H. Zwart, P. D. Adams, N. K. Sauter, V. K. Yachandra, J. Yano, R. Alonso-Mori, D. Milathianaki, A. R. Fry, A. Miahnahri, D. W. Schafer, M. Messerschmidt, M. M. Seibert, J. E. Koglin, W. E. White, M. J. Bogan, G. J. Williams, S. Boutet, U. Bergmann, C. Glockner, J. Hellmich, D. DiFiore, A. Zouni, H. Laksmono, R. G. Sierra, S. Koroidov, J. Messinger, D. Sokaras, T.-C. Weng, J. Sellberg, M. J. La-

timer, and P. Glatzel, "Simultaneous femtosecond x-ray spectroscopy and diffraction of photosystem II at room temperature," Science **340**, 491–495 (2013).

[11]K. S. Kjær, K. Kunnus, T. C. B. Harlang, T. B. Van Driel, K. Ledbetter, R. W. Hartsock, M. E. Reinhard, S. Koroidov, L. Li, M. G. Laursen, E. Biasin, F. B. Hansen, P. Vester, M. Christensen, K. Haldrup, M. M. Nielsen, P. Chabera, Y. Liu, H. Tatsuno, C. Timm, J. Uhlig, V. Sundstöm, Z. Németh, D. S. Szemes, É. Bajnóczi, G. Vankó, R. Alonso-Mori, J. M. Glownia, S. Nelson, M. Sikorski, D. Sokaras, H. T. Lemke, S. E. Canton, K. Wärnmark, P. Persson, A. A. Cordones, and K. J. Gaffney, "Solvent control of charge transfer excited state relaxation pathways in [Fe(2,2-bipyridine)(CN) 4] 2," Physical Chemistry Chemical Physics **20**, 4238 (2018).

[12]W. Zhang, K. S. Kjær, R. Alonso-Mori, U. Bergmann, M. Chollet, L. A. Fredin, R. G. Hadt, R. W. Hartsock, T. Harlang, T. Kroll, K. Kubiček, H. T. Lemke, H. W. Liang, Y. Liu, M. M. Nielsen, P. Persson, J. S. Robinson, E. I. Solomon, Z. Sun, D. Sokaras, T. B. van Driel, T.-C. Weng, D. Zhu, K. Wärnmark, V. Sundström, and K. J. Gaffney, "Manipulating charge transfer excited state relaxation and spin crossover in iron coordination complexes with ligand substitution," Chemical Science **8**, 515–523 (2017).

[13]S. E. Canton, K. S. Kjær, G. Vankó, T. B. van Driel, S.-i. Adachi, A. Bordage, C. Bressler, P. Chabera, M. Christensen, A. O. Dohn, A. Galler, W. Gawelda, D. Gosztola, K. Haldrup, T. Harlang, Y. Liu, K. B. Møller, Z. Németh, S. Nozawa, M. Pápai, T. Sato, T. Sato, K. Suarez-Alcantara, T. Togashi, K. Tono, J. Uhlig, D. A. Vithanage, K. Wärnmark, M. Yabashi, J. Zhang, V. Sundström, and M. M. Nielsen, "Visualizing the non-equilibrium dynamics of photoinduced intramolecular electron transfer with femtosecond X-ray pulses," Nature Communications **6**, 6359 (2015).

[14]M. W. Mara, R. G. Hadt, M. E. Reinhard, T. Kroll, H. Lim, R. W. Hartsock, R. Alonsomori, M. Chollet, J. M. Glownia, S. Nelson, D. Sokaras, K. Kunnus, K. O. Hodgson, B. Hedman, U. Bergmann, K. J. Gaffney, and E. I. Solomon, "Metalloprotein entatic control of ligand-metal bonds quantified by ultrafast x-ray spectroscopy," Science **1280**, 1276–1280 (2017).

[15]R. Alonso-mori, J. Kern, D. Sokaras, T.-c. Weng, D. Nordlund, R. Tran, P. Montanez, J. Delor, and V. K. Yachandra, "A multi-crystal wavelength dispersive x-ray spectrometer," Review of Scientific Instruments **83**, 073114 (2012).

[16]A. M. March, T. A. Assefa, C. Bressler, G. Doumy, A. Galler, W. Gawelda, E. P. Kanter, Z. Németh, M. Pápai, S. H. Southworth, L. Young, and G. Vankó, "Feasibility of Valence-to-Core X-ray Emission Spectroscopy for Tracking Transient Species," Journal of Physical Chemistry C **119**, 14571–14578 (2015).

[17]A. M. March, T. A. Assefa, C. Boemer, C. Bressler, A. Britz, M. Diez, G. Doumy, A. Galler, M. Harder, D. Khakhulin, Z. Németh, M. Pápai, S. Schulz, S. H. Southworth, H. Yava, L. Young, W. Gawelda, and G. Vankó, "Probing Transient Valence Orbital Changes with Picosecond Valence-to-Core X-ray Emission Spectroscopy," Journal of Physical Chemistry C **121**, 2620–2626 (2017).

[18]M.-f. Tu, G. Doumy, A. A. Haddad, A. M. March, L. Assoufid, Y. Kumagai, D. Walko, Z. Liu, B. Shi, L. Young, and C. Bostedt, "Micro-Focused MHz Pink Beam for Time-Resolved X-ray Emission Spectroscopy," Journal of Synchrotron Radiation **26** (2019), 10.1107/S1600577519012268.

[19]A. M. March, A. Stickrath, G. Doumy, E. P. Kanter, B. Krässig, S. H. Southworth, K. Attenkofer, C. A. Kurtz, L. X. Chen, and L. Young, "Development of high-repetition-rate laser pump/x-ray probe methodologies for synchrotron facilities," Review of Scientific Instruments **82** (2011), 10.1063/1.3615245.

[20]A. M. March, G. Doumy, A. Andersen, A. Al Haddad, Y. Kumagai, M. F. Tu, J. Bang, C. Bostedt, J. Uhlig, D. R. Nascimento, T. A. Assefa, Z. Németh, G. Vankó, W. Gawelda, N. Govind, and L. Young, "Elucidation of the photoaquation reaction mechanism in ferrous hexacyanide using synchrotron x-rays with sub-pulse-duration sensitivity," Journal of Chemical Physics **151** (2019), 10.1063/1.5117318.

[21]R. Alonso-Mori, C. Caronna, M. Chollet, R. Curtis, D. S. Damiani, J. Defever, Y. Feng, D. L. Flath, J. M. Glownia, S. Lee, H. T. Lemke, S. Nelson, E. Bong, M. Sikorski, S. Song, V. Srinivasan, D. Stefanescu, D. Zhu, and A. Robert, "The X-ray Correlation Spectroscopy instrument at the Linac Coherent Light Source," Journal of Synchrotron Radiation **22**, 508–513 (2015).

[22]M. P. Minitti, J. S. Robinson, R. N. Coffee, S. Edstrom, S. Gilevich, J. M. Glownia, E. Granados, P. Hering, M. C. Hoffmann, A. Miahnahri, D. Milathianaki, W. Polzin, D. Ratner, F. Tavella, S. Vetter, M. Welch, W. E. White, and A. R. Fry, "Optical laser systems at the Linac Coherent Light Source," Journal of Synchrotron Radiation **22**, 526–531 (2015).

[23]G. Blaj, P. Caragiulo, G. Carini, S. Carron, A. Dragone, D. Freytag, G. Haller, P. Hart, J. Hasi, R. Herbst, S. Herrmann, C. Kenney, B. Markovic, K. Nishimura, S. Osier, J. Pines, B. Reese, J. Segal, A. Tomada, and M. Weaver, "X-ray detectors at the Linac Coherent Light Source," Journal of Synchrotron Radiation **22**, 577–583 (2015).

[24]J. M. Glownia, K. Gumerlock, H. T. Lemke, T. Sato, D. Zhu, and M. Chollet, "Pumpprobe experimental methodology at the linac coherent light source," Journal of Synchrotron Radiation **26**, 685–691 (2019).

[25]M. Harmand, R. Coffee, M. Bionta, M. Chollet, D. French, D. Zhu, D. M. Fritz, H. Lemke, N. Medvedev, B. Ziaja, S. Toleikis, and M. Cammarata, "Achieving few-femtosecond time-sorting at hard X-ray free-electron lasers," Nature Photonics **7**, 215–218 (2013).

[26]F. Neese, "Software update: the ORCA program system, version 4.0," Wiley Interdisciplinary Reviews: Computational Molecular Science **8** (2018), 10.1002/wcms.1327.

[27]F. Weigend and R. Ahlrichs, "Balanced basis sets of split valence, triple zeta valence and quadruple zeta valence quality for H to Rn: Design and assessment of accuracy," Physical Chemistry Chemical Physics **7**, 3297–3305 (2005).

[28]S. Grimme, J. Antony, S. Ehrlich, and H. Krieg, "A consistent and accurate ab initio parametrization of density functional dispersion correction (DFT-D) for the 94 elements H-Pu," Journal of Chemical Physics **132** (2010), 10.1063/1.3382344.

[29]S. Grimme, S. Ehrlich, and L. Goergik, "Effect of the Damping Function in Dispersion Corrected Density Functional Theory," Journal of Computational Chemistry (2011).

[30]D. N. Bowman and E. Jakubikova, "Low-spin versus high-spin ground state in pseudo-octahedral iron complexes," Inorganic Chemistry **51**, 6011–6019 (2012).

[31]V. Barone and M. Cossi, "Quantum calculation of molecular energies and energy gradients in solution by a conductor solvent model," Journal of Physical Chemistry A **102** (1998), 10.1021/jp9716997.

[32]C. van Wüllen, "Molecular density functional calculations in the regular relativistic approximation: Method, application to coinage metal diatomics, hydrides, fluorides and chlorides, and comparison with first-order relativistic calculations," Journal of Chemical Physics **109**, 392–399 (1998).

[33]E. V. Lenthe, P. E. S. Wormer, and A. V. D. Avoird, "Density functional calculations of molecular hyperfine interactions in the zero order regular approximation for relativistic effects," Journal of Chemical Physics **108**, 4783–4796 (1998).

[34]M. Shirom and G. Stein, "Excited State Chemistry of the Ferrocyanide Ion in Aqueous Solution. I. Formation of the Hydrated Electron," The Journal of Chemical Physics **55**, 3372–3378 (1971).

[35]M. Shirom and G. Stein, "Excited State Chemistry of the Ferrocyanide Ion in Aqueous Solution. II. Photoaquation," The Journal of Chemical Physics **55**, 3379–3382 (1971).

[36]M. Reinhard, G. Aubo, N. A. Besley, I. P. Clark, G. M. Greetham, M. W. D. Hanson-heine, R. Horvath, T. S. Murphy, T. J. Penfold, M. Towrie, M. W. George, and M. Chergui, "Photoaquation Mechanism of Hexacyanoferrate(II) Ions: Ultrafast 2D UV and Transient Visible and IR Spectroscopies," Journal of the American Chemical Society **139**, 73357347 (2017).

[37]S. Pommeret, R. Naskrecki, P. Van Der Meulen, M. Ménard, G. Vigneron, and T. Gustavsson, "Ultrafast events in the electron photodetachment from the hexacyanoferrate(II) complex in solution," Chemical Physics Letters **288**, 833–840 (1998).

[38]M. Ross, A. Andersen, Z. W. Fox, Y. Zhang, K. Hong, J. H. Lee, A. Cordones, A. M. March, G. Doumy, S. H. Southworth, M. A. Marcus, R. W. Schoenlein, S. Mukamel, N. Govind, and M. Khalil, "Comprehensive Experimental and Computational Spectroscopic Study of Hexacyanoferrate Complexes in Water: From Infrared to X-ray Wavelengths," Journal of Physical Chemistry B **122**, 5075–5086 (2018).

[39]K. S. Kjær, W. Zhang, R. Alonso-mori, U. Bergmann, M. Chollet, R. G. Hadt, W. Hartsock, T. Harlang, T. Kroll, K. Kubiček, H. T. Lemke, H. W. Liang, Y. Liu, M. M. Nielsen, J. S. Robinson, E. I. Solomon, D. Sokaras, T. B. V. Driel, D. Zhu, P. Persson, K. Wärnmark, V. Sundström, and K. J. Gaffney, "Ligand manipulation of charge transfer excited state relaxation and spin crossover in [Fe (2 , 2 0 -bipyridine) 2 (CN) 2]," Structural Dynamics **2** (2017), 10.1063/1.4985017.

Supplementary Material

Excited State Charge Distribution and Bond Expansion of Ferrous Complexes Observed with Femtosecond Valence-to-Core X-ray Emission Spectroscopy

Kathryn Ledbetter, Marco E. Reinhard, Kristjan Kunnus, Alessandro Gallo, Alexander Britz, Elisa Biasin, James M. Glownia, Silke Nelson, Tim B. Van Driel, Clemens Weninger, Diana B. Zederkof, Kristoffer Haldrup, Amy A. Cordones, Kelly J. Gaffney, Dimosthenis Sokaras, and Roberto Alonso-Mori

I. ORCA INPUT

The following input heading was used for ORCA calculations of XES spectra.

```
! UKS B3LYP def2-TZVP(-f) def2/J TightSCF SlowConv CPCM(water) grid4
nofinalgrid Normalprint ZORA

# specifying the CP(PPP) basis set for Fe
%basis  newgto Fe "CP(PPP)" end
end

# increasing the grid accuracy on the Fe centre (Z = 26)
%method SpecialGridAtoms 26
       SpecialGridIntAcc 7
end

%xes
CoreOrb 0,0
OrbOp 0,1
end
```

II. ENERGY SHIFT OF CALCULATED SPECTRA

The one-electron approach of Lee et al. results in a functional-dependent energy shift between calculation and experiment.[3] The reported magnitude of this shift varies (e.g. 150 eV,[16] 182 eV[3,5]) depending on the details of the calculation, including functional and treatment of relativistic effects.

Here, a single shift of 23 eV was applied to all calculated spectra. To avoid reliance on the position of the K$\beta_{1,3}$ peak, which is not well-modeled by this calculational method, the VtC position was matched directly. The shift was obtained by matching the center-of-mass position of the VtC peak (7095-7115 eV) of the ground-state calculated spectrum to the background-subtracted experimental data (a single pseudo-Voigt lineshape fit to the K$\beta_{1,3}$ main line was subtracted; see Figure S2-S3). This comparison was applied to the ground state of all three complexes, and the following shifts were obtained: $[Fe(CN)_6]^{4-}$, 22.6 eV; $[Fe(CN)_4(bpy)]^{2-}$, 23.2 eV; $[Fe(CN)_2(bpy)_2]$, 23.2 eV. The average of these, 23 eV, was used as a constant shift throughout the analysis. The relatively small value of this shift compared to other studies is largely due to the use of the zero-order regular approximation (ZORA) in calculations, which decreased the magnitude of the shift from 150 to 23 eV.

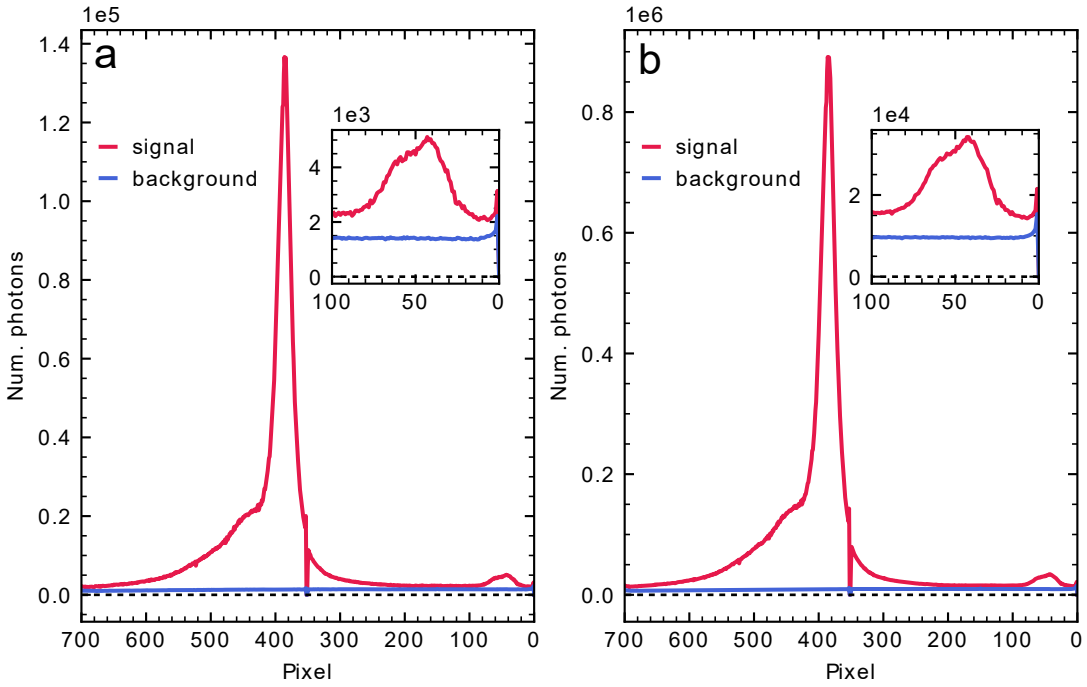

FIG. S1. Raw data from dataset shown in Figure 1**b**, with detector units scaled to x-ray photon counts. Signal (red) is averaged over the region of the area detector where the spectrum appears. Background (blue) is averaged over regions on either side of the spectrum. The discontinuity at 350 pixels is due to the seam between detector panels. Insets show the VtC region. **a**: Laser-off spectrum. **b**: Average of all laser-on shots.

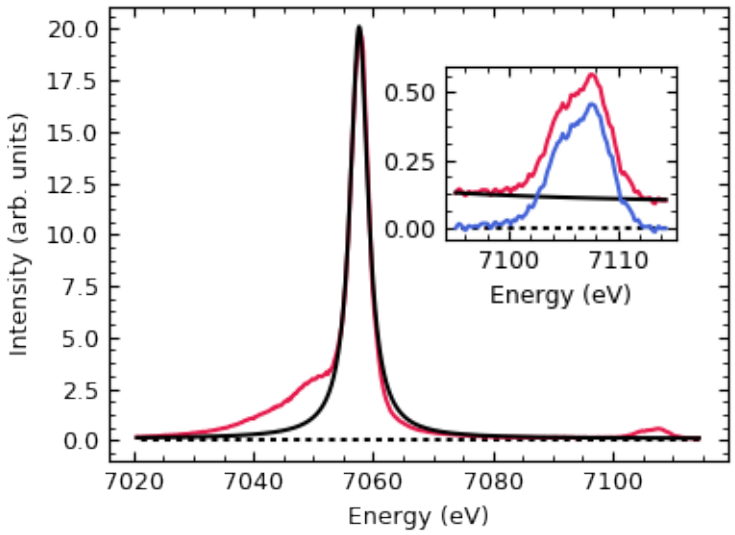

FIG. S2. Full laser-off XES spectrum of $[Fe(CN)_4(bpy)]^{2-}$ (red) in the dataset used for the area analysis shown in Table I, with single pseudo-Voigt function (variable-weighted sum of Gaussian and Lorentzian functions, plus a constant offset) fit to the main line and high-energy tail, 7050-7099 eV (black). Inset shows the VtC region and the background-subtracted spectrum (blue).

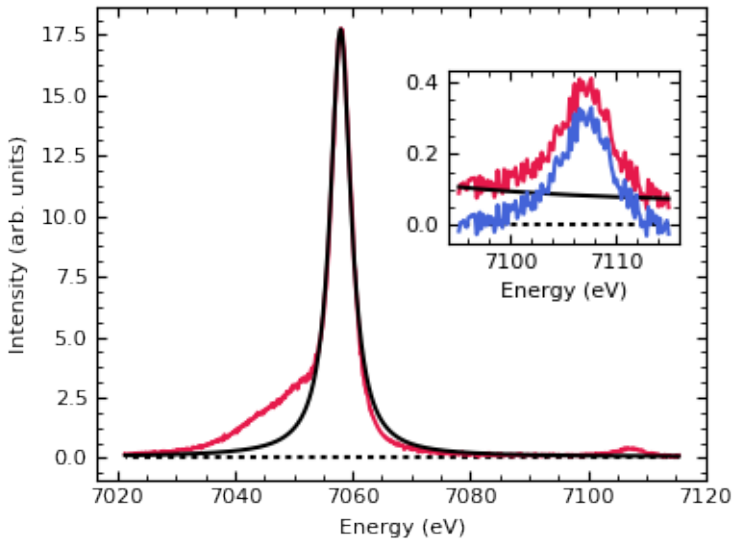

FIG. S3. Full laser-off XES spectrum of $[Fe(CN)_2(bpy)_2]$ (red) in the dataset used for the area analysis shown in Table I, with single pseudo-Voigt function (variable-weighted sum of Gaussian and Lorentzian functions, plus a constant offset) fit to the main line and high-energy tail, 7050-7099 eV (black). Inset shows the VtC region and the background-subtracted spectrum (blue).

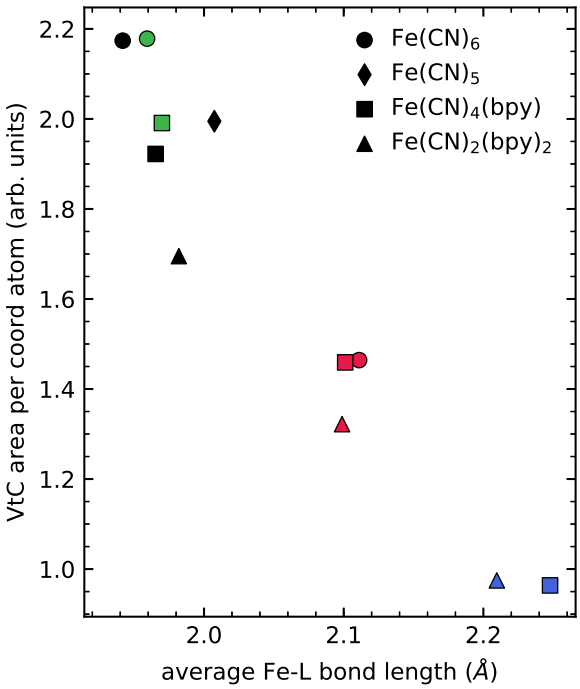

FIG. S4. Area under VtC spectrum from 7095-7115 eV as a function of Fe-ligand bond lengths for all calculated spectra shown in Figure 1, as well as $^3[Fe(CN)_6]^{4-}$, divided by the number of coordinating atoms. The penta-coordinated species aligns with the observed trend when the number of coordinating atoms is taken into account.

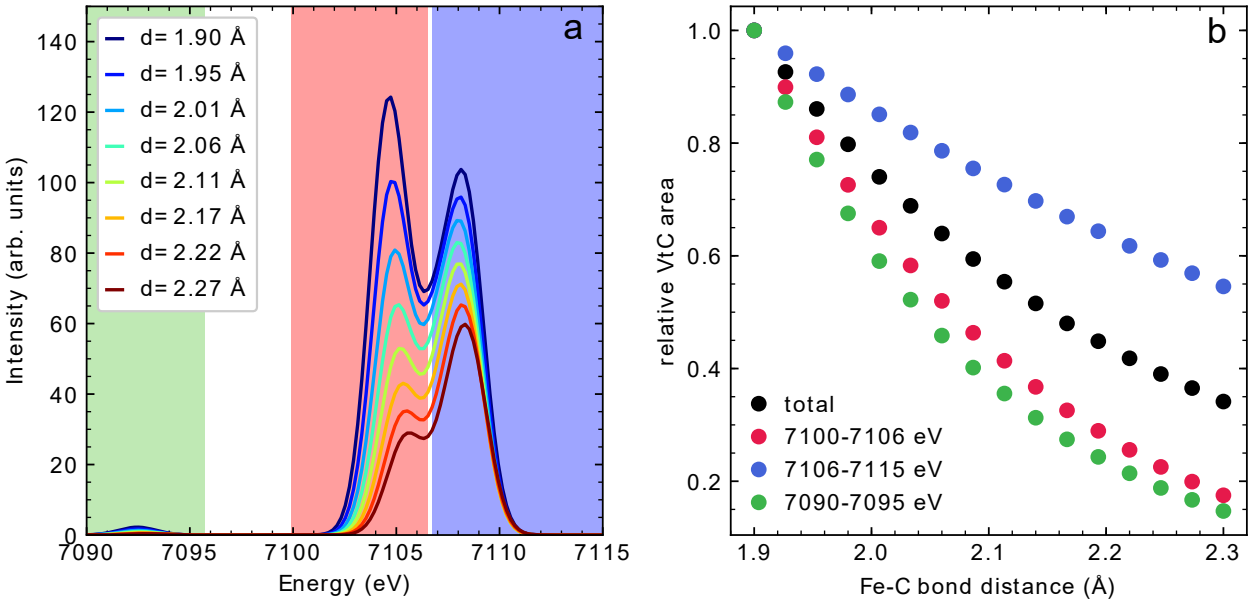

FIG. S5. **a**: Calculated spectra resulting from artificially placing six CN^- ligands in octahedral geometry at a given distance from the Fe(II) center. **b**: Areas in three regions of the spectrum, scaled by the area at shortest bond length to show relative changes. The area of the Kβ'' region has a steeper exponential relationship to bond length than the higher-energy areas of the K$\beta_{2,5}$ region.

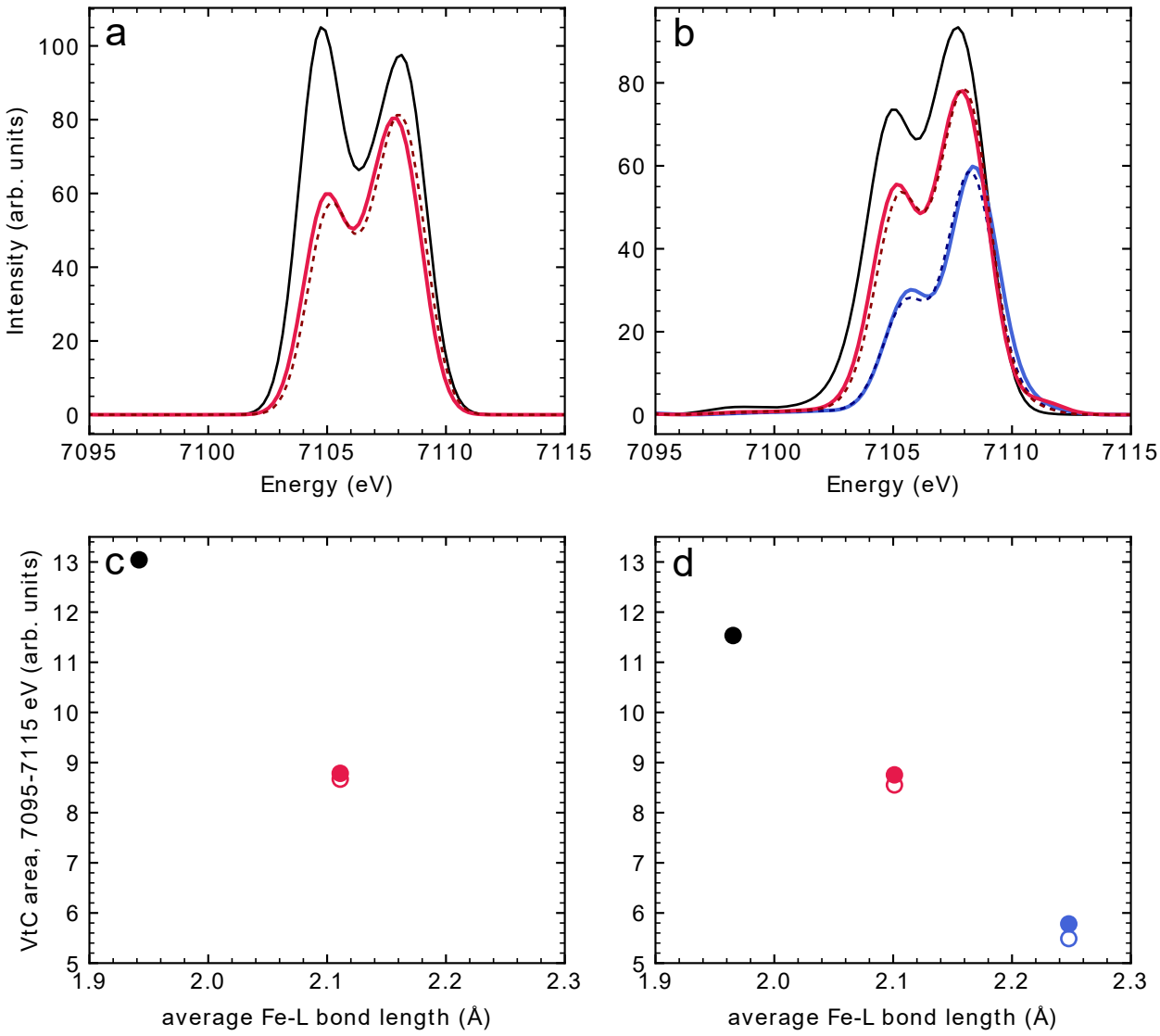

FIG. S6. **a-b**: Calculated VtC spectra of **a**: $[Fe(CN)_6]^{4-}$ and **b**: $[Fe(CN)_4(bpy)]^{2-}$, with ground state (black), triplet (red), and quintet (blue) geometries calculated in native (solid) and singlet (dashed) electronic configuration. In panel **b**, the small shoulder due to a transition at 7111.2 eV in the triplet state (red, solid), resulting from population of an orbital of primarily Fe d character, does not appear in the spectrum of the triplet geometry with singlet spin (red, dashed). **c-d**: Integrated area under the curves in **a-b** as a function of average Fe-ligand bond length, with native (solid) and singlet (open) electronic configurations.

Appendix C

Paper III

Observing the structural evolution in the photodissociation of diiodomethane with femtosecond solution X-ray scattering

Matthijs R. Panman,[1] Elisa Biasin,[2] Oskar Berntsson,[1] Markus Hermann,[3] Stephan Niebling,[1] Ashley J. Hughes,[1] Joachim Kübel,[1] Kalina Atkovska,[3] Emil Gustavsson,[1] Amke Nimmrich,[1] Asmus O. Dohn,[2] Mads Laursen,[2] Diana B. Zederkof,[2] Alireza Honarfar,[4] Kensuke Tono,[5] Tetsuo Katayama,[5] Shigeki Owada,[6] Tim B. van Driel,[7] Kasper Kjaer,[7] Martin M. Nielsen,[2] Jan Davidsson,[8] Jens Uhlig,[4] Kristoffer Haldrup,[2] Jochen S. Hub,[3] and Sebastian Westenhoff[1,*]

[1]*Department of Chemistry and Molecular Biology, University of Gothenburg, Box 462, 40530 Gothenburg, Sweden*

[2]*Centre for Molecular Movies, Department of Physics, Technical University of Denmark, DK-2800 Lyngby, Denmark*[†]

[3]*Georg-August-Universität Göttingen, Institute for Microbiology and Genetics, Justus-von-Liebig-Weg 11, 37077 Göttingen, Germany*

[4]*Department of Chemical Physics, Lund University, Box 124, S-2210, Lund, Sweden*

[5]*Japan Synchrotron Radiation Research Institute, 1-1-1 Kouto, Sayo-cho, Sayo-gun, Hyogo 679-5198, Japan*

[6]*RIKEN SPring-8 Center, 1-1-1 Kouto, Sayo-cho, Sayo-gun, Hyogo 679-5148, Japan*

[7]*LCLS, SLAC National Laboratory, Menlo Park, California 94025, USA*

[8]*Department of Chemistry, Ångström Laboratory, Uppsala University, Box 523, SE75120 Uppsala, Sweden*

(Dated: October 15, 2020)

Abstract

Resolving the structural dynamics of the initial steps of chemical reactions is challenging. We report the femtosecond time-resolved wide-angle X-ray scattering of the photodissociation of diiodomethane in cyclohexane. The data reveal with structural detail how the molecule dissociates into radicals, how the radicals collide with the solvent, and how they form the photoisomer. We extract how translational and rotational kinetic energy is dispersed into the solvent. We also find that 85% of the primary radical pairs are confined to their original solvent cage and discuss how this influences the downstream recombination reactions.

Understanding chemical reactivity requires resolving the reaction mechanism. Fundamental reaction events, such as the breaking, rearrangement, and formation of bonds as well as the interaction with solvent molecules occur on femtosecond time scales. Femtosecond time-resolved spectroscopy has yielded a wealth of information about these steps. However, most femtosecond spectroscopic methods probe electronic states or vibrational modes, reporting only indirectly on molecular structure [1, 2]. In particular, ubiquitous species in solution-state chemistry without covalent or ionic bonds, such as molecular encounter complexes, supramolecular assemblies, or solute-solvent complexes, are difficult to study [3]. Time-resolved techniques, that are sensitive to atomic position, are therefore essential to further the understanding of chemical reactivity [4–13].

The photodissociation of diiodomethane (CH_2I_2) is an ideal model reaction to study elementary chemical events. In apolar solvents, absorption of light at a wavelength of 266 nm results in impulsive C–I bond scission, yielding ($CH_2I_2 \longrightarrow CH_2I^\bullet + I^\bullet$) [14]. Within picoseconds, the fragments recombine to form a photoisomer ($CH_2I^\bullet + I^\bullet \longrightarrow CH_2I\text{–}I$) [15–17]. On nano- and microsecond time scales, the isomer and radical pair fragments undergo further bi-molecular reactions to reform the parent molecule and I_2 [15]. The photoisomer is the methylene transfer agent in the cyclopropanation of olefins with diiodomethane [15, 18].

Femtosecond optical spectra have shown that dissociation occurs impulsively within 200 fs [19, 20]. However, the translational and rotational trajectories of the fragments cannot be retrieved from the optical spectra. The structure, solvent arrangement, and separation of the formed radical pairs remains unknown. Disagreement persists on whether the isomer is formed with a lifetime of 100 fs [19], 1 ps [20], or biphasically with 1 ps to 5 ps [15]. This is probably because the spectral signatures of the photoisomer and the vibrational relaxation of $CH_2I^\bullet$ overlap. Nevertheless, the quantum yield of photoisomer formation has been determined to be between $\sim$70 % to 95 % for a variety of solvents at 100 ps [15]. The remaining portion of the initial fragments are thought to be separated by solvent molecules so that they cannot recombine into the isomer. Solvent cage escape is a common explanation of incomplete reactions on fast time scales [20–23]. Even though this is a reasonable assumption, it is untested, as the structure of the radical pair cannot be probed with spectroscopic methods.

Femtosecond time-resolved WAXS. To resolve the structural evolution of the fragments on femto- and picoseconds after photodissociation of CH_2I_2, we used time-resolved Wide-Angle X-ray Scattering (TRWAXS) at an X-ray Free Electron Laser (XFEL). We recorded the data at the Linear Coherent Light Source (LCLS) and Spring-8 Angstrom Compact free electron LAser

(SACLA). CH_2I_2 in cyclohexane (50 mmol L^{-1}) was supplied to the experiment in a liquid jet (see Supplemental Material and Fig. S1 for details of the sample preparation and delivery). The reaction was triggered with femtosecond optical laser pulses (266 nm, <60 fs FWHM duration), which overlapped with the X-ray pulses (9.5 keV photon energy, <50 fs FWHM duration) in the sample jet. The optical excitation density was 32 mJ cm^{-2}, comparable to the 20 mJ cm^{-2} used in past ultrafast optical studies [15] and in the linear excitation regime of the sample (see Supplemental Material Fig. S2). The X-ray scattering was recorded at defined delay times relative to the laser pulse with an effective time resolution of 90 fs using the timing diagnostic at the beam line [24]. The signal processing of the diffuse 2D scattering images is described in the Supplemental Material. The TRWAXS signal due to solvent heating was subtracted from the difference data prior to fitting the difference scattering (see Supplemental Material and Fig. S5-S7). In the following we present the data recorded at the LCLS, but the data obtained at SACLA confirms the conclusions drawn (see Supplemental Material Fig. S13, S14, and S16).

Direct visualization of a dissociating molecule. The azimuthally integrated difference scattering curves (Fig 1(c)) arise predominantly from the evolution of the distance of the two electron-rich I atoms. The observed momentum transfers (q) range from 0.4 $Å^{-1}$ to 4.8 $Å^{-1}$, which is sufficient for a high-quality structural determination [25, 26]. Fig 1(d) show the data in real-space, which allows inspection of the evolution of the inter-atomic distances in a model-free fashion [27]. The $r^2\Delta S(r,t)$ signal shows a negative feature with a time-dependent minimum between 3 and 4 Å, which is due to the depletion of the I$\cdots$I distance of the CH_2I_2 ground state. The position of this negative peak ought to be time-independent and the observed shift is due to the overlapping positive signals. A positive difference-scattering feature appears at 100 fs and shifts to large distances within a few hundred of femtoseconds (orange band), which we assign to the impulsive (ballistic) separation of the I atom from the parent molecule. Impulsive separation is expected from optical spectra and the time scale is reasonable for the expected time of flight for an atom to hit the neighbouring molecule [15, 20]. A pronounced positive shoulder arises after $\sim$1 ps (green band) in between 5 Å and 6 Å. Both positive peaks correspond to photo-induced structures within the first solvent shell, which has a diameter of approximately 7 Å, as estimated from our Molecular Dynamics (MD) simulations (see Supplemental Material for details). We assign the two distances to $I^\bullet$ positioned at the I- and CH_2-hemisphere of the $CH_2I^\bullet$ fragment due to the rotation of the $CH_2I^\bullet$ fragment. A third positive feature is visible at shorter I$\cdots$I distances compared to the ground state bleach (magenta band). The signal overlaps with the ground state bleach and is first

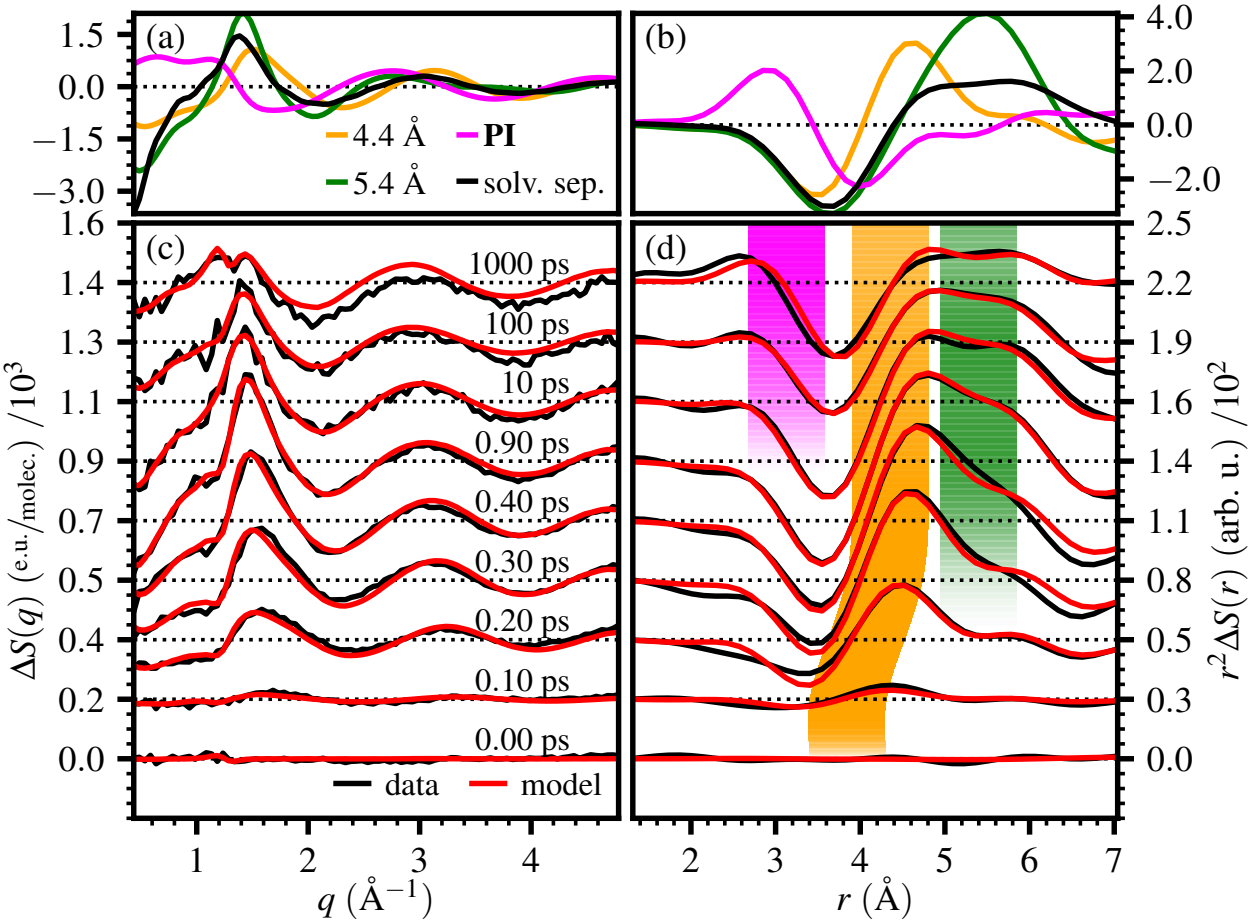

FIG. 1. (a), (b) The difference scattering profiles of refined I···I distances in reciprocal (q) and real-space (r). (c), (d) The difference scattering ($\Delta S(q)$, black) and difference scattering obtained from the structural refinement (red) are shown for selected time delays in reciprocal and real-space. The conversion between reciprocal and real space was achieved by sine-Fourier transformation. The colored bands follow the refined I···I distances and are explained in the text.

visible as an positive indent of the negative band from around ∼400 fs and more pronounced at later times. This marks the formation of the photoisomer (**PI**) [16, 28, 29]. Features associated with the rearrangement of the solvent are found at $r \geq 6.5$ Å.

Structural refinement. We continued our analysis by refining iodine distances (I···I) and their time-dependent concentrations ($A(t)$) against the difference scattering in reciprocal space. The fits were obtained by selection from a model library of 124 theoretical scattering curves for two iodine atoms constrained at distances spanning 0 Å to 15 Å (see Supplemental Material Fig. S17). The theoretical scattering was computed as $\Delta S = \sum_i A(t)_i \cdot [S_i(\mathrm{I}\cdots\mathrm{I}) - S_{gs}(\mathrm{I}\cdots\mathrm{I})]$, where three contributions are considered for the calculation of $S(\mathrm{I}\cdots\mathrm{I})$: the solute; solvent-solute; and solvent scattering terms. The solute term was computed using the Debye equation for two iodine atoms.

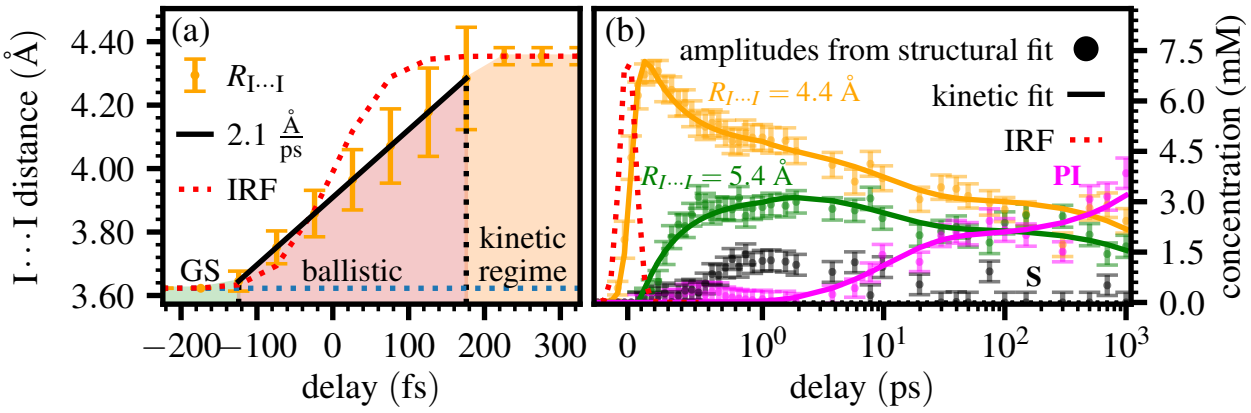

FIG. 2. (a) the I···I separation of the geminate pair species as a function of time t. The colored areas separated by dashed lines denote different dynamic regimes. The solid black line is a guide to the eye. The red-dotted line represents the instrument response function (see Supplemental Material Fig. S9) [8]. (b) time-dependence of the amplitudes obtained by the structural refinement (Fig. 1, dots) and the least-squares fit of the kinetic model (lines).

Following a common approach [16, 30], the solvent-solute term was extracted from molecular dynamics trajectories of iodine atoms in cyclohexane. The solvent-solvent term was also extracted from the same molecular dynamics trajectories (see Supplemental Material Eq. S6 Eq. S7, and Eq. S10). The scattering of ground state was assumed to be independent of time.

Following our qualitative assignments, we included four I···I distances, corresponding to three photo-induced species in the structural refinement. One distance represented the photoisomer and another one a radical pair, which was separated by solvent molecules. We fixed the latter distance to 100 Å since the difference scattering in our detected range is invariant for I···I separation $\gtrapprox$15 Å. The remaining two I···I distances represent the geminate radical pair within the same solvent shell. The $I^\bullet$ is most likely distributed continuously around the $CH_2I^\bullet$, but using the two dominating distances, which describe the $I^\bullet$ fragment on either side of the $CH_2I^\bullet$ hemisphere, is a practical approximation. We obtained optimal fits for I···I distances of the geminate pair at 4.35 ± 0.03 Å and 5.40 ± 0.02 Å, of the ground state at 3.62 ± 0.01 Å, and for the isomer at 3.13 ± 0.04 Å (red curves in Fig. 1(c) and (d), see Fig. 1(a) and (b) and Supplemental Material Fig. S10 for the individual scattering contributions of each species). The isomer and ground state distances agree with previous synchrotron studies in methanol [16, 29] and cyclohexane [28]. There are no significant discrepancies between the fit and data, indicating that the minimal model is sufficient to reproduce the experiment.

Kinetic analysis at $t < 1ps$. In order to describe the initial dissociation of the molecule, the short I···I distance of the geminate pair was allowed to increase linearly for $t < 500$ fs. Fig. 2(a)

shows that the fragments separate by 0.7 ± 0.1 Å over a period of 300 fs before stopping at the static I$\cdots$I separation of 4.35 ± 0.03 Å. The instrument response function (IRF) as extracted from the anisotropic scattering (see Supplemental Material for details) was shorter than the observed flight of the fragments (Fig. 2(b)). Thus, the observation reflects how the I$\cdots$I bond in CH_2I_2 breaks; how the fragments continue their flight; and how they finally collide with the solvent shell. The fragments travel with a relative velocity of 2.1 ± 0.4 Å ps^{-1} corresponding to 210 ± 40 m s^{-1}.

Next, we inspect the time-dependent concentrations obtained by the structural refinement (Fig. 2b). We observe that the short I$\cdots$I distance of the geminate pair rises limited by the instrument response function (yellow markers). The concentration of the longer distance of the geminate pair rises concomitantly with the a decay of the short distance (green markers). This supports our interpretation that the longer distance of the geminate pair is produced by rotation of the $CH_2I^\bullet$ fragment. The rotation of this fragment increases the distance between the two iodine atoms because the CH_2 moiety of the $CH_2I^\bullet$ takes up space between them. A high-level QM calculation shows that the distances are reasonable (see Supplemental Material Fig. S11(a) and **b**). Fig. 2b also reveals a delayed rise of the distance corresponding to the solvent-separated radical pair (black), which reflects the fragments having to travel a longer distance to escape the solvent cage. The relative amplitude of this species is a minor component of the total product species, indicating that the majority of the radical pairs stop at the first solvent shell. The distance corresponding to the photoisomer does not appear within the first picosecond (magenta; see below).

We cast these observations into a comprehensive kinetic model (Eq. S1-S30, and see Supplemental Material Fig. S15 for a visual representation) and performed a least-squares fit to the time-dependent amplitudes (solid lines, Fig. 2b). We found that the rotational transition from the short to the long distance in the geminate pair occurs with a lifetime of $\tau_r = 0.77 \pm 0.07$ ps. This τ_r corresponds to a rotational lifetime of 0.25 ± 0.02 ps rad^{-1} and an angular velocity of 4.1 ps^{-1}, which is many times faster than the predicted rotational-correlation lifetime of the steady-state $CH_2I^\bullet$ fragment as estimated from the Stokes-Einstein-Debye equation (16 ps rad^{-1}, see Supplemental Material Eq. S31–S34). The rotational motion is therefore photo-induced and not caused by the equilibrium motion of the radicals. Interestingly, τ_r is longer than the collision time with the solvent (0.34 ± 0.07 ps), which implies that the rotational energy is not fully dissipated during the initial collision with the solvent shell. This illustrates that the geometry of the solute-solvent interaction is important for determining the dissipation of energy into the solvent.

The partitioning of excess energy. Photoexcitation of a molecule transfers it into a high-lying electronic state, where the excess energy is partitioned into translational, rotational and vibrational degrees of freedom, before energy dissipates to the solvent. The separation velocity ($2.1 \pm 0.4\,\mathrm{ps\,\AA^{-1}}$) gives a translational kinetic energy of 0.02 eV (see Supplemental Material Eq. S35–S36). This represents $\sim$0.5 % of the 4.66 eV excitation photon energy or $\sim$7 % of the 0.28 eV kinetic energy found in the gas-phase dissociation reaction [31]. The rotational kinetic energy of the $CH_2I^{\bullet}$ fragment was computed from the angular velocity ($4.1\,\mathrm{ps^{-1}}$) and is 0.55 eV, representing $\sim$12 % of the 4.66 eV excitation photon energy (see Supplemental Material Eq. S37–S39). Thus, the translational energy partition is smaller than the rotational by a factor of 24. In part, this may be due to the choice of photoexcitation energy. It may also be that our measurement rather underestimates the separation velocity, because it is close to the time resolution of the experiment. However, it is consistent with that we find a low amount of solvent separated species as the initial translational energy of the fragments is insufficient to break through the solvent barrier. These considerations also show that the notable portion of the excess excitation energy is held as vibrational energy.

Kinetic analysis at $t > 1$ ps. Now inspecting the kinetics at ($t > 1$ ps), we observe that the two I$\cdots$I distances of the geminate pair decay biphasically and concurrently (Fig. 2b). The characteristic I$\cdots$I distance of the photoisomer is formed concomitantly with the biphasic decay of the geminate pair ($\tau_1 = 8 \pm 1$ ps and $\tau_2 = 2.8 \pm 0.5$ ns). This is slower that than what was concluded from optical spectroscopy [15, 19, 20]. We note that optical spectroscopic studies have never reached agreement on the time scale of isomer formation. We consider the results obtained from the TRWAXS experiment to be reliable given that the peaks of the photoisomer are well separated from other peaks in the TRWAXS data (Fig. 2b). The kinetics of heat generation in the sample also corroborates the biphasic formation of the photoisomer (see Supplemental Material and Fig. S8).

Observation of a long-lived, but chemically inactive geminate radical pair. Surprisingly, we observe that the geminate-pair is present for hundreds of picoseconds (Fig 2b and 1(b)). The concentration of the solvent-separated pair never exceeds 15 % of the total product species. We also observe a decrease of the solvent-separated species after $t > 10$ ps, but this might be due to the decrease in data statistics after this time point [32]. We tested the robustness of the fits by selectively removing species from the model for delays $t > 50$ ps. We found that, when removing each of the geminate pair distances, the goodness of the fit (χ^2) was notably reduced, but when the solvent separated species was excluded only a very minor reduction in the goodness was observed

(see Supplemental Material Fig. S18).

Strong dispersion forces confine the radical pairs within the same solvent shell. The existence of geminate pairs for hundreds of picoseconds indicate that an attractive force holds the radicals together. We investigated this interaction between $CH_2I^\bullet$ and $I^\bullet$ fragments with quantum chemical calculations at the CASSCF-MRCI level of theory (def2-SVP basis set [33]) in a three-dimensional search space (see the Supplemental Material for details). The calculated potential energy surface (see Supplemental Material Fig. S11(a)–(c)) show a Pauli repulsion at <4 Å and an attractive interaction of -0.1 eV at longer distances. The strong interaction ($\sim 4k_\mathrm{B}T$) is caused by dispersion forces of the large iodine atoms. We found that the fragment contact lifetime increased from 34 ps to 204 ps when using the force field parameterized against the results of our CASSCF-MRCI calculations compared to the standard GAFF force field (Supplemental Material Fig. S12). We conclude that the dispersion force is sufficient to hold the radical pair in a mutual solvent pocket for a few hundreds of picoseconds. This is much longer than what was previously assumed in investigations using spectroscopy and X-ray scattering. [15, 16, 21, 23, 30, 34, 35]

The long contact lifetime means that the incomplete formation of the photoisomer cannot be explained by solvent escape [15, 20–23]. Instead, a chemically inactive form of the geminate pair must exist. Although our data do not conclusively reveal the reason for this, we consider two possible explanations. Firstly, photoisomer formation may be promoted by vibrational excitation of the $CH_2I\cdot$ fragment. When the vibrational excitation is dissipated, the photo-isomerization reaction proceeds at a much slower rate (τ_2) [36]. Alternatively, a competing reaction pathway, e.g. the formation of a solvent-solute complex ($I^\bullet\cdots C_6H_{12}$ [37–39]), hydrogen atom abstraction from the solvent, or loss of spin correlation, could generate a distribution of active and chemically inactive geminate pairs. The "active" species would form the photoisomer within the first phase (τ_1) and the "inhibited" species would form the photoisomer with the second phase (τ_2). We consider the formation of triplet radical pairs as plausible since the spin flip could occur in the excited state, prior to separation of the fragments.

Conclusion. In conclusion, we have visualized the dissociation reaction of CH_2I_2 in solution using femtosecond time-resolved Wide Angle X-ray Scattering. The analysis yields a comprehensive movie for the first nanosecond of the reaction (Fig. 3). The iodine-carbon bond is broken directly after photoexcitation (I in Fig. 3), the $I\cdot$ and $CH_2I\cdot$ fragments flies apart until they collide with a solvent molecule, and the $CH_2I\cdot$ radical rotates (II). The translational motion of the fragments is stopped by the solvent collision, but the rotational motion is not fully inhibited. As a

result, the majority of radical pairs stay within the solvent shell (III). We find that the radical pairs within the solvent cage are surprisingly stable, due to previously unrecognized dispersion forces between the heavy iodine atoms, but that a notable fraction of them is unreactive (IV). Accordingly, the photoisomer production proceeds biphasically on pico- and nanosecond time scales. The sensitivity of time-resolved Wide Angle X-ray Scattering towards relative atomic positions, without the requirement of a covalent bond, was essential in uncovering this comprehensive, microscopic reaction mechanism in solution.

Use of the Linac Coherent Light Source (LCLS), SLAC National Accelerator Laboratory, is supported by the U.S. Department of Energy, Office of Science, Office of Basic Energy Sciences under Contract No. DE-AC02-76SF00515. The experiments at SACLA were performed at BL3 with the approval of the Japan Synchrotron Radiation Research Institute (JASRI) (Proposal No. 2016A8037). S.W. acknowledges the European Research Council for support (grant number: 6581802 and 279944). The DTU-affiliated authors gratefully acknowledge DANSCATT for support of the beamtime activities. E.B. and S.W. further acknowledge support from Interreg. M.H., K.A., and J.S.H. were supported by the Deutsche Forschungsgemeinschaft (grant numbers HU 1971-1/1, HU 1971-3/1, HU 1971-4/1).

* westenho@chem.gu.se

† Current affiliation: PULSE Institute, SLAC National Laboratory, Menlo Park, California 94305, USA

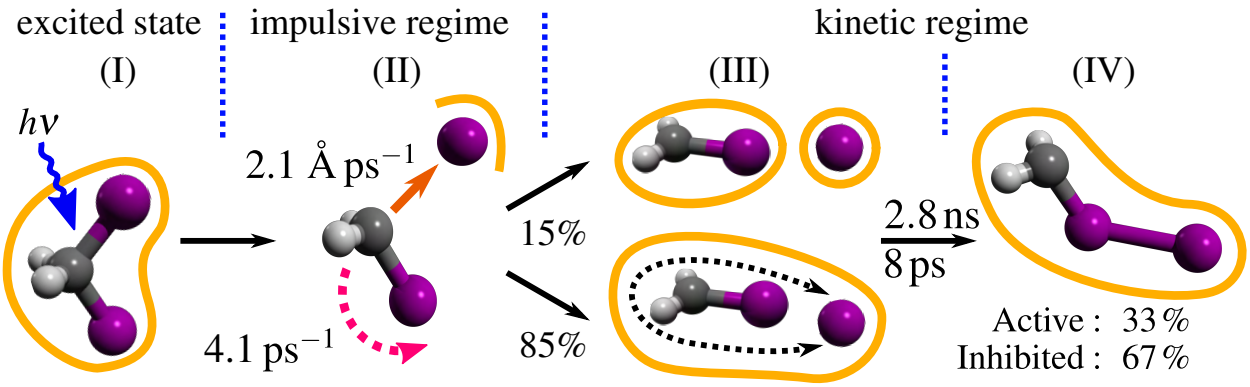

FIG. 3. Schematic representation of the revised mechanism of the photoisomer formation within 1 ns. In the impulsive regime (II), the rotational and translational speed of the fragments are given, the time constants in the kinetic regime are lifetimes. The delineating orange lines represent the solvation shells of the structures. The black dotted line indicates the positional distribution of the I atom within the solvent shell.

[1] J. Zheng, K. Kwak, J. Asbury, X. Chen, I. R. Piletic, and M. D. Fayer, Science **309**, 1338 (2005).

[2] P. Hamm and M. T. Zanni, *Concepts and Methods of 2D Infrared Spectroscopy* (Cambridge University Press, 2011).

[3] N. F. A. van der Vegt, K. Haldrup, S. Roke, J. Zheng, M. Lund, and H. J. Bakker, Chem. Rev. **116**, 7626 (2016).

[4] M. P. Minitti, J. S. Robinson, R. N. Coffee, S. Edstrom, S. Gilevich, J. M. Glownia, E. Granados, P. Hering, M. C. Hoffmann, A. Miahnahri, D. Milathianaki, W. Polzin, D. Ratner, F. Tavella, S. Vetter, M. Welch, W. E. White, and A. R. Fry, J. Synchrotron Radiat. **22**, 526 (2015).

[5] T. Ishikawa, S. A. Hayes, S. Keskin, G. Corthey, M. Hada, K. Pichugin, A. Marx, J. Hirscht, K. Shionuma, K. Onda, Y. Okimoto, S. Y. Koshihara, T. Yamamoto, H. Cui, M. Nomura, Y. Oshima, M. Abdel-Jawad, R. Kato, and R. J. Dwayne Miller, Science **350**, 1501 (2015).

[6] S. E. Canton, K. S. Kjær, G. Vanko, T. B. van Driel, S.-i. Adachi, A. Bordage, C. Bressler, P. Chabera, M. Christensen, A. O. Dohn, A. Galler, W. Gawelda, D. Gosztola, K. Haldrup, T. Harlang, Y. Liu, K. B. Moller, Z. Nemeth, S. Nozawa, M. Papai, T. Sato, T. Sato, K. Suarez-Alcantara, T. Togashi, K. Tono, J. Uhlig, D. A. Vithanage, K. Warnmark, M. Yabashi, J. Zhang, V. Sundstrom, and M. M. Nielsen, Nat. Commun. **6** (2015).

[7] K. H. Kim, J. G. Kim, S. Nozawa, T. Sato, K. Y. Oang, T. W. Kim, H. Ki, J. Jo, S. Park, C. Song, T. Sato, K. Ogawa, T. Togashi, K. Tono, M. Yabashi, T. Ishikawa, J. Kim, R. Ryoo, J. Kim, H. Ihee, and S.-i. Adachi, Nature **518**, 385 (2015).

[8] E. Biasin, T. B. van Driel, K. S. Kjær, A. O. Dohn, M. Christensen, T. Harlang, P. Chabera, Y. Liu, J. Uhlig, M. Pápai, Z. Németh, R. Hartsock, W. Liang, J. Zhang, R. Alonso-Mori, M. Chollet, J. M. Glownia, S. Nelson, D. Sokaras, T. A. Assefa, A. Britz, A. Galler, W. Gawelda, C. Bressler, K. J. Gaffney, H. T. Lemke, K. B. Møller, M. M. Nielsen, V. Sundström, G. Vankó, K. Wärnmark, S. E. Canton, and K. Haldrup, Phys. Rev. Lett. **117**, 013002 (2016).

[9] B. Wolter, M. G. Pullen, A. T. Le, M. Baudisch, K. Doblhoff-Dier, A. Senftleben, M. Hemmer, C. D. Schröter, J. Ullrich, T. Pfeifer, R. Moshammer, S. Gräfe, O. Vendrell, C. D. Lin, and J. Biegert, Science **354**, 308 (2016).

[10] A. R. Attar, A. Bhattacherjee, C. D. Pemmaraju, K. Schnorr, K. D. Closser, D. Prendergast, and S. R. Leone, Science **356**, 54 (2017).

[11] Y. Liu, S. L. Horton, J. Yang, J. P. F. Nunes, X. Shen, T. J. A. Wolf, R. Forbes, C. Cheng, B. Moore, M. Centurion, K. Hegazy, R. Li, M.-F. Lin, A. Stolow, P. Hockett, T. Rozgonyi, P. Marquetand,

X. Wang, and T. Weinacht, Phys. Rev. X **10**, 021016 (2020).

[12] N. Li, T. P. Keane, S. S. Veroneau, R. G. Hadt, D. Hayes, L. X. Chen, and D. G. Nocera, Proc. Natl. Acad. Sci. USA **117**, 16187 (2020).

[13] D. Kinschel, C. Bacellar, O. Cannelli, B. Sorokin, T. Katayama, G. F. Mancini, J. R. Rouxel, Y. Obara, J. Nishitani, H. Ito, T. Ito, N. Kurahashi, C. Higashimura, S. Kudo, T. Keane, F. A. Lima, W. Gawelda, P. Zalden, S. Schulz, J. M. Budarz, D. Khakhulin, A. Galler, C. Bressler, C. J. Milne, T. Penfold, M. Yabashi, T. Suzuki, K. Misawa, and M. Chergui, Nat. Commun. **11**, 4145 (2020).

[14] P. M. Kroger, P. C. Demou, and S. J. Riley, J. Chem. Phys. **65**, 1823 (1976).

[15] A. N. Tarnovsky, V. Sundström, E. Åkesson, and T. Pascher, J. Phys. Chem. A **108**, 237 (2004).

[16] J. Davidsson, J. Poulsen, M. Cammarata, P. Georgiou, R. Wouts, G. Katona, F. Jacobson, A. Plech, M. Wulff, G. Nyman, and R. Neutze, Phys. Rev. Lett. **94** (2005).

[17] X. Zheng and D. L. Phillips, J. Phys. Chem. A **104**, 6880 (2000).

[18] D. Phillips, W. Fang, and X. Zheng, J. Am. Chem. Soc. **123**, 4197 (2001).

[19] V. A. Borin, S. M. Matveev, D. S. Budkina, P. Z. El-Khoury, and A. N. Tarnovsky, Phys. Chem. Chem. Phys. **18**, 28883 (2016).

[20] B. J. Schwartz, J. C. King, J. Z. Zhang, and C. B. Harris, Chem. Phys. Lett. **203**, 503 (1993).

[21] J. Franck and E. Rabinowitsch, Trans. Faraday Soc. **30**, 120 (1934).

[22] T. Kühne and P. Vöhringer, J. Chem. Phys. **105**, 10788 (1996).

[23] U. Banin and S. Ruhman, J. Chem. Phys. **98**, 4391 (1993).

[24] M. Harmand, R. Coffee, M. Bionta, M. Chollet, D. French, D. Zhu, D. Fritz, H. Lemke, N. Medvedev, B. Ziaja, S. Toleikis, and M. Cammarata, Nat. Photon. **7**, 215 (2013).

[25] E. Biasin, T. B. van Driel, G. Levi, M. G. Laursen, A. O. Dohn, A. Moltke, P. Vester, F. B. K. Hansen, K. S. Kjaer, T. Harlang, R. Hartsock, M. Christensen, K. J. Gaffney, N. E. Henriksen, K. B. Møller, K. Haldrup, and M. M. Nielsen, J. Synchrotron Radiat. **25**, 306 (2018).

[26] J. G. Kim, S. Nozawa, H. Kim, E. H. Choi, T. Sato, T. W. Kim, K. H. Kim, H. Ki, J. Kim, M. Choi, Y. Lee, J. Heo, K. Y. Oang, K. Ichiyanagi, R. Fukaya, J. H. Lee, J. Park, I. Eom, S. H. Chun, S. Kim, M. Kim, T. Katayama, T. Togashi, S. Owada, M. Yabashi, S. J. Lee, S. Lee, C. W. Ahn, D.-S. Ahn, J. Moon, S. Choi, J. Kim, T. Joo, J. Kim, S.-i. Adachi, and H. Ihee, Nature **582**, 520 (2020).

[27] A. Plech, M. Wulff, S. Bratos, F. Mirloup, R. Vuilleumier, F. Schotte, and P. A. Anfinrud, Phys. Rev. Lett. **92** (2004).

[28] J. Vincent, M. Andersson, M. Eklund, A. B. Wöhri, M. Odelius, E. Malmerberg, Q. Kong, M. Wulff,

R. Neutze, and J. Davidsson, J. Chem. Phys. **130**, 154502 (2009).

[29] S. Park, J. Choi, H. Ki, K. H. Kim, K. Y. Oang, H. Roh, J. Kim, S. Nozawa, T. Sato, S.-i. Adachi, J. Kim, and H. Ihee, J. Chem. Phys. **150**, 224201 (2019).

[30] H. Ihee, M. Lorenc, T. K. Kim, Q. Y. Kong, M. Cammarata, J. H. Lee, S. Bratos, and M. Wulff, Science **309**, 1223 (2005).

[31] K.-W. Jung, T. Ahmadi, and M. El-Sayed, B. Kor. Chem. Soc. **18**, 1274 (1997).

[32] Due to technical implementation at the XFEL, the TRWAXS data was recorded in two time-ranges. Less repeats were recorded for the time range containing the time points $t \geq 10$ ps.

[33] F. Weigend and R. Ahlrichs, Phys. Chem. Chem. Phys. **7**, 3297 (2005).

[34] Q. Liu, J. K. Wang, and A. H. Zewail, Nature **364**, 427 (1993).

[35] H. Ihee, Acc. Chem. Res. **42**, 356 (2009).

[36] S. Schott, L. Ress, J. Hrušák, P. Nuernberger, and T. Brixner, Phys. Chem. Chem. Phys. **18**, 33287 (2016).

[37] S. R. Logan, R. Bonneau, J. Joussot-Dubien, and P. F. de Violet, J. Chem. Soc., Faraday Trans. 1 **71**, 2148 (1975).

[38] A. L. Harris, M. Berg, and C. B. Harris, J. Chem. Phys. **84**, 788 (1986).

[39] C. P. Anderson, K. G. Spears, K. R. Wilson, and R. J. Sension, J. Chem. Phys. **139**, 194307 (2013).

[40] K. S. Kjaer, T. B. van Driel, J. Kehres, K. Haldrup, D. Khakhulin, K. Bechgaard, M. Cammarata, M. Wulff, T. J. Sorensen, and M. M. Nielsen, Introducing a standard method for experimental determination of the solvent response in laser pump, X-ray probe time-resolved wide-angle X-ray scattering experiments on systems in solution, Phys. Chem. Chem. Phys. **15**, 15003 (2013).

[41] M. Chollet, R. Alonso-Mori, M. Cammarata, D. Damiani, J. Defever, J. T. Delor, Y. Feng, J. M. Glownia, J. B. Langton, S. Nelson, K. Ramsey, A. Robert, M. Sikorski, S. Song, D. Stefanescu, V. Srinivasan, D. Zhu, H. T. Lemke, and D. M. Fritz, The X-ray Pump–Probe instrument at the Linac Coherent Light Source, J. Synchrotron Radiat. **22**, 503 (2015).

[42] K. Tono, Y. Inubushi, T. Sato, T. Togashi, H. Ohashi, H. Kimura, S. Takahashi, K. Takeshita, H. Tomizawa, S. Goto, and M. Yabashi, Beamline for X-ray free electron laser of SACLA, J. Phys. Conf. Ser. **425**, 072006 (2013).

[43] K. Tono, T. Togashi, Y. Inubushi, T. Sato, T. Katayama, K. Ogawa, H. Ohashi, H. Kimura, S. Takahashi, K. Takeshita, H. Tomizawa, S. Goto, T. Ishikawa, and M. Yabashi, Beamline, experimental stations and photon beam diagnostics for the hard X-ray free electron laser of SACLA, New J. Phys.

15, 083035 (2013).

[44] T. Sato, T. Togashi, K. Ogawa, T. Katayama, Y. Inubushi, K. Tono, and M. Yabashi, Highly efficient arrival timing diagnostics for femtosecond X-ray and optical laser pulses, Appl. Phys. Express **8**, 012702 (2015).

[45] T. Katayama, S. Owada, T. Togashi, K. Ogawa, P. Karvinen, I. Vartiainen, A. Eronen, C. David, T. Sato, K. Nakajima, Y. Joti, H. Yumoto, H. Ohashi, and M. Yabashi, A beam branching method for timing and spectral characterization of hard X-ray free-electron lasers, Struct. Dyn. **3**, 034301 (2016).

[46] T. Sato, T. Togashi, K. Tono, Y. Inubushi, H. Tomizawa, Y. Tanaka, S. Adachi, K. Nakamura, R. Kodama, and M. Yabashi, Development of ultrafast pump and probe experimental system at SACLA, J. Phys. Conf. Ser. **425**, 092009 (2013).

[47] K.-I. Saitow, Y. Naitoh, K. Tominaga, and K. Yoshihara, Photo-induced reactions of CH_2I_2 in solution studied by the ultrafast transient absorption spectroscopy, Chem. Phys. Lett. **262**, 621 (1996).

[48] Y.-L. Li, D. Wang, and D. L. Phillips, Time-resolved resonance Raman spectroscopy and density functional theory investigation of the CH_2I-I isomer and $CH_2I_2\cdots$I molecular complex products produced from ultraviolet photolysis of CH_2I_2 in the solution phase: Comparison of the structure and chemical reactivity of polyhalomethane isomers and polyhalomethane–halogen atom molecular complexes, J. Chem. Phys. **117**, 79317941 (2002).

[49] A. N. Tarnovsky, M. Wall, M. Gustafsson, N. Lascoux, V. Sundstr¨ om, and E. Å kesson, Ultrafast study of the photodissociation of bromoiodomethane in acetonitrile upon 266 nm excitation, J. Phys. Chem. A **106**, 5999 (2002).

[50] E. Jones, T. Oliphant, P. Peterson, *et al.*, SciPy: Open source scientific tools for Python (2001–), [Online; accessed October 15, 2020].

[51] M. Newville, T. Stensitzki, D. B. Allen, and A. Ingargiola, Lmfit: Non-linear least-square minimization and curve-fitting for python, (2014).

[52] K. Haldrup, M. Christensen, and M. Meedom Nielsen, Analysis of time-resolved X-ray scattering data from solution-state systems, Acta Crystallogr. A **66**, 261 (2010).

[53] T. B. van Driel, K. S. Kjaer, E. Biasin, K. Haldrup, H. T. Lemke, and M. M. Nielsen, Disentangling detector data in xfel studies of temporally resolved solution state chemistry, Faraday Discuss. **177**, 443 (2015).

[54] T. K. Kim, J. H. Lee, M. Wulff, Q. Kong, and H. Ihee, Spatiotemporal kinetics in solution studied by time-resolved X-ray liquidography (solution scattering), ChemPhysChem **10**, 1958 (2009).

[55] A. O. Dohn, E. Biasin, K. Haldrup, M. M. Nielsen, N. E. Henriksen, and K. B. M. ller, On the calculation of X-ray scattering signals from pairwise radial distribution functions, J. Phys. B-At. Mol. Opt. **48**, 244010 (2015).

[56] R. D. B. Fraser, T. P. MacRae, E. Suzuki, and IUCr, An improved method for calculating the contribution of solvent to the X-ray diffraction pattern of biological molecules, J. Appl. Crystallogr. **11**, 693 (1978).

[57] J. Wang, R. M. Wolf, J. W. Caldwell, P. A. Kollman, and D. A. Case, Development and testing of a general amber force field., J. Comput. Chem. **25**, 1157 (2004).

[58] D. van der Spoel, P. J. van Maaren, and C. Caleman, GROMACS molecule & liquid database, Bioinformatics **28**, 752 (2012).

[59] S. Pronk, S. Páll, R. Schulz, P. Larsson, P. Bjelkmar, R. Apostolov, M. R. Shirts, J. C. Smith, P. M. Kasson, D. van der Spoel, B. Hess, and E. Lindahl, GROMACS 4.5: a high-throughput and highly parallel open source molecular simulation toolkit, Bioinformatics **29**, 845 (2013).

[60] W. F. van Gunsteren and H. J. C. Berendsen, A leap-frog algorithm for stochastic dynamics, Mol. Sim. **1**, 173 (1988).

[61] H. J. C. Berendsen, J. P. M. Postma, A. DiNola, and J. R. Haak, Molecular dynamics with coupling to an external bath, J. Chem. Phys. **81**, 3684 (1984).

[62] B. Hess, P-LINCS: A parallel linear constraint solver for molecular simulation, J. Chem. Theory Comput. **4**, 116 (2008).

[63] F. Neese, The orca program system, Wiley Interdisciplinary Reviews: Computational Molecular Science **2**, 73 (2012).

[64] F. Neese, Software update: the orca program system, version 4.0, Wiley Interdisciplinary Reviews: Computational Molecular Science , e1327 (2017).

[65] K. A. Peterson, D. Figgen, M. Dolg, and H. Stoll, Energy-consistent relativistic pseudopotentials and correlation consistent basis sets for the 4d elements ypd, J. Chem. Phys. **126**, 124101 (2007), https://doi.org/10.1063/1.2647019.

[66] M. J. Abraham, T. Murtola, R. Schulz, S. Páll, J. C. Smith, B. Hess, and E. Lindahl, GROMACS: High performance molecular simulations through multi-level parallelism from laptops to supercomputers, SoftwareX **1**, 19 (2015).

[67] H. J. C. Berendsen, J. P. M. Postma, W. F. van Gunsteren, A. DiNola, and J. R. Haak, Molecular-dynamics with coupling to an external bath, J. Chem. Phys. **81**, 3684 (1984).

[68] D. Lavalette, C. Tétreau, M. Tourbez, and Y. Blouquit, Microscopic viscosity and rotational diffusion of proteins in a macromolecular environment, Biophys. J. **76**, 2744 (1999).

[69] M. Horng, J. Gardecki, and M. Maroncelli, Rotational dynamics of coumarin 153: time-dependent friction, dielectric friction, and other nonhydrodynamic effects, J. Phys. Chem. A **101**, 1030 (1997).

[70] T. Gomti Devi and K. Kumar, Raman bandshape analysis of o-chlorobenzaldehyde: Microviscosity-dependent study, Journal of Raman Spectroscopy **35**, 835 (2004).

[71] A. Gierer and K. Wirtz, Molekulare theorie der mikroreibung, Z. Naturforsch., A: Phys. Sci. **8**, 532 (1953).

[72] N. Michaud-Agrawal, E. J. Denning, T. B. Woolf, and O. Beckstein, Mdanalysis: A toolkit for the analysis of molecular dynamics simulations, Journal of Computational Chemistry **32**, 2319 (2011).

[73] Richard J. Gowers, Max Linke, Jonathan Barnoud, Tyler J. E. Reddy, Manuel N. Melo, Sean L. Seyler, Jan Domański, David L. Dotson, Sébastien Buchoux, Ian M. Kenney, and Oliver Beckstein, MDAnalysis: A Python Package for the Rapid Analysis of Molecular Dynamics Simulations, in *Proceedings of the 15th Python in Science Conference*, edited by Sebastian Benthall and Scott Rostrup (2016) pp. 98 – 105.

[74] M. D. Hanwell, D. E. Curtis, D. C. Lonie, T. Vandermeersch, E. Zurek, and G. R. Hutchison, Avogadro: an advanced semantic chemical editor, visualization, and analysis platform, J. Cheminformatics **4**, 10.1186/1758-2946-4-17 (2012).

Bibliography

[1] C. Förster and K. Heinze, "Photophysics and photochemistry with Earth-abundant metals-fundamentals and concepts," *Chem. Soc. Rev.*, vol. 49, no. 4, pp. 1057–1070, 2020.

[2] J. K. McCusker, "Electronic structure in the transition metal block and its implications for light harvesting," *Science (80-.).*, vol. 363, no. 6426, pp. 484–488, 2019.

[3] A. H. Zewail, "Femtochemistry: Atomic-Scale Dynamics of the Chemical Bond Using Ultrafast Lasers (Nobel Lecture)," *Angew. Chemie Int. Ed.*, vol. 39, pp. 2586–2631, aug 2000.

[4] T. S. Rose, M. J. Rosker, and A. H. Zewail, "Femtosecond real-time observation of wave packet oscillations (resonance) in dissociation reactions," *J. Chem. Phys.*, vol. 88, pp. 6672–6673, may 1988.

[5] N. F. Scherer, J. L. Knee, D. D. Smith, and A. H. Zewail, "Femtosecond photofragment spectroscopy: The reaction ICN → CN + I," *J. Phys. Chem.*, vol. 89, no. 24, pp. 5141–5143, 1985.

[6] M. Dantus, M. J. Rosker, and A. H. Zewail, "Real-time femtosecond probing of "transition states" in chemical reactions [3]," *J. Chem. Phys.*, vol. 87, pp. 2395–2397, aug 1987.

[7] F. Jensen, *Introduction to Computational Chemistry*. John Wiley & Sons, 3. ed., 2017.

[8] M. Chergui and E. Collet, "Photoinduced Structural Dynamics of Molecular Systems Mapped by Time-Resolved X-ray Methods," *Chem. Rev.*, vol. 117, pp. 11025–11065, aug 2017.

[9] M. Chollet, R. Alonso-Mori, M. Cammarata, D. Damiani, J. Defever, J. T. Delor, Y. Feng, J. M. Glownia, J. B. Langton, S. Nelson, K. Ramsey, A. Robert, M. Sikorski, S. Song, D. Stefanescu, V. Srinivasan, D. Zhu, H. T. Lemke, and D. M. Fritz, "The X-ray Pump-Probe instrument at the Linac Coherent Light Source," *J. Synchrotron Radiat.*, vol. 22, pp. 503–507, may 2015.

[10] C. Bostedt, S. Boutet, D. M. Fritz, Z. Huang, H. J. Lee, H. T. Lemke, A. Robert, W. F. Schlotter, J. J. Turner, and G. J. Williams, "Linac Coherent Light Source: The first five years," *Rev. Mod. Phys.*, vol. 88, no. 1, p. 015007, 2016.

[11] D. Pile, "X-rays: First light from SACLA," *Nat. Photonics*, vol. 5, pp. 456–457, aug 2011.

[12] P. Emma, R. Akre, J. Arthur, R. Bionta, C. Bostedt, J. Bozek, A. Brachmann, P. Bucksbaum, R. Coffee, F. J. Decker, Y. Ding, D. Dowell, S. Edstrom, A. Fisher, J. Frisch, S. Gilevich, J. Hastings, G. Hays, P. Hering, Z. Huang, R. Iverson, H. Loos, M. Messerschmidt, A. Miahnahri, S. Moeller, H. D. Nuhn, G. Pile, D. Ratner, J. Rzepiela, D. Schultz, T. Smith, P. Stefan, H. Tompkins, J. Turner, J. Welch, W. White, J. Wu, G. Yocky, and J. Galayda, "First lasing and operation of an ångstrom-wavelength free-electron laser," *Nat. Photonics*, vol. 4, pp. 641–647, sep 2010.

[13] A. D. McNaught; and A. Wilkinson, *IUPAC. Compendium of Chemical Terminology.* Oxford: Blackwell Scientific Publications, 2nd ed., 1997.

[14] S. J. Chalk, "IUPAC Gold Book." https://doi.org/10.1351/goldbook, 2019.

[15] P. Atkins, T. Overton, J. Rouke, M. Weller, and F. Armstrong, *Shriver & Atkin's Inorganic Chemistry*. Oxford: Oxford University Press, 5th ed., 2010.

[16] V. Balzani, G. Bergamini, S. Campagna, and F. Puntoriero, "Photochemistry and photophysics of coordination compounds: Overview and general concepts," in *Photochem. Photophysics Coord. Compd. I.*

Top. Curr. Chem., vol. 280, pp. 1–36, Berlin, Heidelberg: Springer, Berlin, Heidelberg, may 2007.

[17] L. Lindh, P. Chábera, N. W. Rosemann, J. Uhlig, K. Wärnmark, A. Yartsev, V. Sundström, and P. Persson, "Photophysics and photochemistry of iron carbene complexes for solar energy conversion and photocatalysis," *Catalysts*, vol. 10, no. 3, 2020.

[18] M. Grätzel, "Photoelectrochemical cells," *Nature*, vol. 414, pp. 338–344, nov 2001.

[19] A. S. Polo, M. K. Itokazu, and N. Y. Murakami Iha, "Metal complex sensitizers in dye-sensitized solar cells," *Coord. Chem. Rev.*, vol. 248, no. 13-14, pp. 1343–1361, 2004.

[20] B. Bozic-Weber, E. C. Constable, and C. E. Housecroft, "Light harvesting with Earth abundant d-block metals: Development of sensitizers in dye-sensitized solar cells (DSCs)," *Coord. Chem. Rev.*, vol. 257, pp. 3089–3106, nov 2013.

[21] G. C. Vougioukalakis, A. I. Philippopoulos, T. Stergiopoulos, and P. Falaras, "Contributions to the development of ruthenium-based sensitizers for dye-sensitized solar cells," *Coord. Chem. Rev.*, vol. 255, pp. 2602–2621, nov 2011.

[22] S. Fantacci and F. De Angelis, "A computational approach to the electronic and optical properties of Ru(II) and Ir(III) polypyridyl complexes: Applications to DSC, OLED and NLO," *Coord. Chem. Rev.*, vol. 255, no. 21-22, pp. 2704–2726, 2011.

[23] D. Gust, T. A. Moore, and A. L. Moore, "Solar fuels via artificial photosynthesis," *Acc. Chem. Res.*, vol. 42, no. 12, pp. 1890–1898, 2009.

[24] T. S. Teets and D. G. Nocera, "Photocatalytic hydrogen production," *Chem. Commun.*, vol. 47, no. 33, pp. 9268–9274, 2011.

[25] H. Hennig, "Transition Metals in Photocatalysis," in *Transit. Met. Org. Synth.* (M. Beller; and B. C., eds.), vol. 2, ch. 3.5, pp. 573–581, 2004.

[26] F. Glaser and O. S. Wenger, "Recent progress in the development of transition-metal based photoredox catalysts," *Coord. Chem. Rev.*, vol. 405, p. 213129, feb 2020.

[27] J. Twilton, C. C. Le, P. Zhang, M. H. Shaw, R. W. Evans, and D. W. C. MacMillan, "The merger of transition metal and photocatalysis," *Nat. Rev. Chem.*, vol. 1, no. 7, p. 52, 2017.

[28] N. J. Farrer, L. Salassa, and P. J. Sadler, "Photoactivated chemotherapy (PACT): The potential of excited-state d-block metals in medicine," *Dalt. Trans.*, vol. 44, no. 48, pp. 10690–10701, 2009.

[29] D. E. Dolmans, D. Fukumura, and R. K. Jain, "Photodynamic therapy for cancer," *Nat. Rev.*, vol. 3, no. 5, pp. 380–387, 2003.

[30] A. Ruggi, F. W. van Leeuwen, and A. H. Velders, "Interaction of dioxygen with the electronic excited state of Ir(III) and Ru(II) complexes: Principles and biomedical applications," *Coord. Chem. Rev.*, vol. 255, no. 21-22, pp. 2542–2554, 2011.

[31] W. C. Choy, W. K. Chan, and Y. Yuan, "Recent advances in transition metal complexes and light-management engineering in organic optoelectronic devices," *Adv. Mater.*, vol. 26, no. 31, pp. 5368–5399, 2014.

[32] H. Yersin, A. F. Rausch, R. Czerwieniec, T. Hofbeck, and T. Fischer, "The triplet state of organo-transition metal compounds. Triplet harvesting and singlet harvesting for efficient OLEDs," *Coord. Chem. Rev.*, vol. 255, no. 21-22, pp. 2622–2652, 2011.

[33] B. J. Powell, "Theories of phosphorescence in organo-transition metal complexes - From relativistic effects to simple models and design principles for organic light-emitting diodes," *Coord. Chem. Rev.*, vol. 295, pp. 46–79, 2015.

[34] V. Fernández-Moreira, F. L. Thorp-Greenwood, and M. P. Coogan, "Application of d6 transition metal complexes in fluorescence cell imaging," *Chem. Commun.*, vol. 46, no. 2, pp. 186–202, 2010.

[35] V. Sathish, A. Ramdass, M. Velayudham, K. L. Lu, P. Thanasekaran, and S. Rajagopal, "Development of luminescent sensors based on

transition metal complexes for the detection of nitroexplosives," *Dalt. Trans.*, vol. 46, pp. 16738–16769, 2017.

[36] P. Chábera, L. A. Fredin, K. S. Kjær, N. W. Rosemann, L. Lindh, O. Prakash, Y. Liu, K. Wärnmark, J. Uhlig, V. Sundström, A. Yartsev, and P. Persson, "Band-selective dynamics in charge-transfer excited iron carbene complexes," *Faraday Discuss.*, vol. 216, pp. 191–210, 2019.

[37] J. E. Monat and J. K. McCusker, "Femtosecond excited-state dynamics of an iron(II) polypyridyl solar cell sensitizer model," *J. Am. Chem. Soc.*, vol. 122, pp. 4092–4097, may 2000.

[38] W. Gawelda, A. Cannizzo, V. T. Pham, F. Van Mourik, C. Bressler, and M. Chergui, "Ultrafast nonadiabatic dynamics of [FeII(bpy)3] 2+ in solution," *J. Am. Chem. Soc.*, vol. 129, no. 26, pp. 8199–8206, 2007.

[39] G. Auböck and M. Chergui, "Sub-50-fs photoinduced spin crossover in [Fe(bpy)3]2+," *Nat. Chem.*, vol. 7, no. 8, pp. 629–633, 2015.

[40] W. Zhang, R. Alonso-Mori, U. Bergmann, C. Bressler, M. Chollet, A. Galler, W. Gawelda, R. G. Hadt, R. W. Hartsock, T. Kroll, K. S. Kjær, K. Kubiek, H. T. Lemke, H. W. Liang, D. A. Meyer, M. M. Nielsen, C. Purser, J. S. Robinson, E. I. Solomon, Z. Sun, D. Sokaras, T. B. Van Driel, G. Vankó, T. C. Weng, D. Zhu, and K. J. Gaffney, "Tracking excited-state charge and spin dynamics in iron coordination complexes," *Nature*, vol. 509, no. 7500, pp. 345–348, 2014.

[41] K. S. Kjær, T. B. Van Driel, T. C. Harlang, K. Kunnus, E. Biasin, K. Ledbetter, R. W. Hartsock, M. E. Reinhard, S. Koroidov, L. Li, M. G. Laursen, F. B. Hansen, P. Vester, M. Christensen, K. Haldrup, M. M. Nielsen, A. O. Dohn, M. I. Pápai, K. B. Møller, P. Chabera, Y. Liu, H. Tatsuno, C. Timm, M. Jarenmark, J. Uhlig, V. Sundstöm, K. Wärnmark, P. Persson, Z. Németh, D. S. Szemes, É. Bajnóczi, G. Vankó, R. Alonso-Mori, J. M. Glownia, S. Nelson, M. Sikorski, D. Sokaras, S. E. Canton, H. T. Lemke, and K. J. Gaffney, "Finding intersections between electronic excited state potential energy surfaces with simultaneous ultrafast X-ray scattering and spectroscopy," *Chem. Sci.*, vol. 10, no. 22, pp. 5749–5760, 2019.

[42] Y. Jiang, L. C. Liu, A. Sarracini, K. M. Krawczyk, J. S. Wentzell, C. Lu, R. L. Field, S. F. Matar, W. Gawelda, H. M. Müller-werkmeister, and R. J. D. Miller, "Direct observation of nuclear reorganization driven by ultrafast spin transitions," *Nat. Commun.*, vol. 11, no. 1530, 2020.

[43] L. M. Lawson Daku and A. Hauser, "Ab Initio Molecular Dynamics Study of an Aqueous Solution of [Fe(bpy) 3](Cl) 2 in the Low-Spin and in the High-Spin States," *J. Phys. Chem. Lett.*, vol. 1, no. 12, pp. 1830–1835, 2010.

[44] L. M. Lawson Daku, "Spin-state dependence of the structural and vibrational properties of solvated iron(II) polypyridyl complexes from AIMD simulations: Aqueous [Fe(bpy)3]Cl2, a case study," *Phys. Chem. Chem. Phys.*, vol. 20, no. 9, pp. 6236–6253, 2018.

[45] D. Khakhulin, L. M. Lawson Daku, D. Leshchev, G. E. Newby, M. Jarenmark, C. Bressler, M. Wulff, and S. E. Canton, "Visualizing the coordination-spheres of photoexcited transition metal complexes with ultrafast hard X-rays," *Phys. Chem. Chem. Phys.*, vol. 21, no. 18, pp. 9277–9284, 2019.

[46] O. S. Wenger, "Is Iron the New Ruthenium?," *Chem. - A Eur. J.*, vol. 25, no. 24, pp. 6043–6052, 2019.

[47] Y. Liu, P. Persson, V. Sundström, and K. Wärnmark, "Fe N-Heterocyclic Carbene Complexes as Promising Photosensitizers," *Acc. Chem. Res.*, vol. 49, no. 8, pp. 1477–1485, 2016.

[48] J.-H. Shon and T. S. Teets, "Molecular Photosensitizers in Energy Research and Catalysis: Design Principles and Recent Developments," *ACS Energy Lett.*, vol. 4, pp. 558–566, feb 2019.

[49] H. E. Toma and M. S. Takasugi, "Spectroscopic studies of preferential and asymmetric solvation in substituted cyanoiron(II) complexes," *J. Solution Chem.*, vol. 12, no. 8, pp. 547–561, 1983.

[50] W. Zhang, K. S. Kjær, R. Alonso-Mori, U. Bergmann, M. Chollet, L. A. Fredin, R. G. Hadt, R. W. Hartsock, T. Harlang, T. Kroll, K. Kubiček, H. T. Lemke, H. W. Liang, Y. Liu, M. M. Nielsen, P. Persson, J. S. Robinson, E. I. Solomon, Z. Sun, D. Sokaras, T. B. Van

Driel, T. C. Weng, D. Zhu, K. Wärnmark, V. Sundström, and K. J. Gaffney, "Manipulating charge transfer excited state relaxation and spin crossover in iron coordination complexes with ligand substitution," *Chem. Sci.*, vol. 8, no. 1, pp. 515–523, 2016.

[51] K. S. Kjær, K. Kunnus, T. C. Harlang, T. B. Van Driel, K. Ledbetter, R. W. Hartsock, M. E. Reinhard, S. Koroidov, L. Li, M. G. Laursen, E. Biasin, F. B. Hansen, P. Vester, M. Christensen, K. Haldrup, M. M. Nielsen, P. Chabera, Y. Liu, H. Tatsuno, C. Timm, J. Uhlig, V. Sundström, Z. Németh, D. S. Szemes, É. Bajnóczi, G. Vankó, R. Alonso-Mori, J. M. Glownia, S. Nelson, M. Sikorski, D. Sokaras, H. T. Lemke, S. E. Canton, K. Wärnmark, P. Persson, A. A. Cordones, and K. J. Gaffney, "Solvent control of charge transfer excited state relaxation pathways in [Fe(2,2-bipyridine)(CN)4]2-," *Phys. Chem. Chem. Phys.*, vol. 20, no. 6, pp. 4238–4249, 2018.

[52] H. Ihee, M. Wulff, and J. Kim, "Ultrafast X-ray scattering : structural dynamics from diatomic to protein molecules," *Int. Rev. Phys. Chem.*, vol. 29, no. 3, pp. 453–520, 2010.

[53] J. Als-Nielsen and D. McMorrow, "Chapter 4 - Kinematical scattering I: non-crystalline materials," in *Elem. Mod. X-ray Phys.*, ch. 4, pp. 113–146, 2011.

[54] P. Willmott, "5: Scattering Techniques," in *An Introd. to Synchrotron Radiat. Tech. Appl.*, pp. 133–221, 2011.

[55] P. Debye, "Zerstreuung von Röntgenstrahlen," *Ann. Phys.*, vol. 351, pp. 809–823, jan 1915.

[56] P. Coppens, "Electron Density from X-Ray Diffraction," *Annu. Rev. Phys. Chem.*, vol. 43, no. 1, pp. 663–692, 1992.

[57] T. B. Van Driel, K. S. Kjær, E. Biasin, K. Haldrup, H. T. Lemke, and M. M. Nielsen, "Disentangling detector data in XFEL studies of temporally resolved solution state chemistry," *Faraday Discuss.*, vol. 177, pp. 443–465, 2015.

[58] K. Kunnus, M. Vacher, T. C. Harlang, K. S. Kjær, K. Haldrup, E. Biasin, T. B. van Driel, M. Pápai, P. Chabera, Y. Liu, H. Tatsuno,

C. Timm, E. Källman, M. Delcey, R. W. Hartsock, M. E. Reinhard, S. Koroidov, M. G. Laursen, F. B. Hansen, P. Vester, M. Christensen, L. Sandberg, Z. Németh, D. S. Szemes, É. Bajnóczi, R. Alonso-Mori, J. M. Glownia, S. Nelson, M. Sikorski, D. Sokaras, H. T. Lemke, S. E. Canton, K. B. Møller, M. M. Nielsen, G. Vankó, K. Wärnmark, V. Sundström, P. Persson, M. Lundberg, J. Uhlig, and K. J. Gaffney, "Vibrational wavepacket dynamics in Fe carbene photosensitizer determined with femtosecond X-ray emission and scattering," *Nat. Commun.*, vol. 11, pp. 1–11, dec 2020.

[59] M. P. Minitti, J. S. Robinson, R. N. Coffee, S. Edstrom, S. Gilevich, J. M. Glownia, E. Granados, P. Hering, M. C. Hoffmann, A. Miahnahri, D. Milathianaki, W. Polzin, D. Ratner, F. Tavella, S. Vetter, M. Welch, W. E. White, and A. R. Fry, "Optical laser systems at the Linac Coherent Light Source," *J. Synchrotron Radiat.*, vol. 22, no. 3, pp. 526–531, 2015.

[60] T. B. van Driel, *Time Resolved X-Ray Scattering of molecules in Solution: Approaching the Molecular Movie*. PhD thesis, Technical University of Denmark, Kongens Lyngby, 2014.

[61] E. Biasin, *Structural dynamics of solvated metal complexes with anisotropy-enhanced X-ray scattering*. PhD thesis, Technical University of Denmark, Kongens Lyngby, 2016.

[62] Mads Laursen, *X-ray Tracking of Electronic and Structural Dynamics During Chemical Reactions Using Free Electron Lasers*. PhD thesis, Technical University of Denmark, Kongens Lyngby, 2018.

[63] T. B. Van Driel, K. S. Kjær, R. W. Hartsock, A. O. Dohn, T. Harlang, M. Chollet, M. Christensen, W. Gawelda, N. E. Henriksen, J. G. Kim, K. Haldrup, K. H. Kim, H. Ihee, J. Kim, H. Lemke, Z. Sun, V. Sundström, W. Zhang, D. Zhu, K. B. Møller, M. M. Nielsen, and K. J. Gaffney, "Atomistic characterization of the active-site solvation dynamics of a model photocatalyst," *Nat. Commun.*, vol. 7, 2016.

[64] E. Biasin, T. B. van Driel, G. Levi, M. G. Laursen, A. O. Dohn, A. Moltke, P. Vester, F. B. K. Hansen, K. S. Kjaer, T. Harlang, R. Hartsock, M. Christensen, K. J. Gaffney, N. E. Henriksen, K. B. Møller,

K. Haldrup, and M. M. Nielsen, "Anisotropy enhanced X-ray scattering from solvated transition metal complexes," *J. Synchrotron Rad.*, vol. 25, pp. 306–315, 2018.

[65] P. Hart, S. Boutet, G. Carini, M. Dubrovin, B. Duda, D. Fritz, G. Haller, R. Herbst, S. Herrmann, C. Kenney, N. Kurita, H. Lemke, M. Messerschmidt, M. Nordby, J. Pines, D. Schafer, M. Swift, M. Weaver, G. Williams, D. Zhu, N. Van Bakel, and J. Morse, "The CSPAD megapixel x-ray camera at LCLS," *Proc. SPIE*, vol. 8504, pp. 85040C–85040C–11, 2012.

[66] G. Blaj, P. Caragiulo, G. Carini, S. Carron, A. Dragone, D. Freytag, G. Haller, P. Hart, J. Hasi, R. Herbst, S. Herrmann, C. Kenney, B. Markovic, K. Nishimura, S. Osier, J. Pines, B. Reese, J. Segal, A. Tomada, and M. Weaver, "X-ray detectors at the Linac Coherent Light Source," *J. Synchrotron Radiat.*, vol. 22, no. 3, pp. 577–583, 2015.

[67] R. Alonso-mori, D. Sokaras, D. Zhu, T. Kroll, M. Chollet, Y. Feng, J. M. Glownia, J. Kern, H. T. Lemke, D. Nordlund, A. Robert, M. Sikorski, S. Song, T.-c. Weng, and U. Bergmann, "Photon-in photon-out hard X-ray spectroscopy at the Linac Coherent Light Source," *J. Synchrotron Radiat.*, vol. 22, pp. 612–620, 2015.

[68] R. W. Hendler and R. I. Shrager, "Deconvolutions based on singular value decomposition and the pseudoinverse: a guide for beginners," *J. Biochem. Biophys. Methods*, vol. 28, no. 1, pp. 1–33, 1994.

[69] T. B. Van Driel, S. Herrmann, G. Carini, M. M. Nielsen, and H. T. Lemke, "Correction of complex nonlinear signal response from a pixel array detector," *J. Synchrotron Radiat.*, vol. 22, pp. 584–591, 2015.

[70] K. Haldrup, M. Christensen, and M. Meedom Nielsen, "Analysis of time-resolved X-ray scattering data from solution-state systems," *Acta Crystallogr. Sect. A Found. Crystallogr.*, vol. 66, no. 2, pp. 261–269, 2010.

[71] M. Harmand, R. Coffee, M. R. Bionta, M. Chollet, D. French, D. Zhu, D. M. Fritz, H. T. Lemke, N. Medvedev, B. Ziaja, S. Toleikis, and

M. Cammarata, "Achieving few-femtosecond time-sorting at hard X-ray free-electron lasers," *Nat. Photonics*, vol. 7, pp. 215–218, feb 2013.

[72] U. Lorenz, K. B. Møller, and N. E. Henriksen, "On the interpretation of time-resolved anisotropic diffraction patterns," *New J. Phys.*, vol. 12, no. 113022, pp. 1–19, 2010.

[73] J. S. Baskin and A. H. Zewail, "Ultrafast Electron Diffraction : Oriented Molecular Structures in Space and Time," *ChemPhysChem*, vol. 6, pp. 2261–2276, 2005.

[74] J. S. Baskin and A. H. Zewail, "Oriented Ensembles in Ultrafast Electron Diffraction," *ChemPhysChem*, vol. 7, pp. 1562–1574, 2006.

[75] K. Haldrup and M. M. Nielsen, "Chapter 7: Measuring and Understanding Ultrafast Pnenomena Using X-rays," in *Futur. Dyn. Struct. Sci.*, pp. 91–113, Springer, 2014.

[76] L. Gallmann, C. Cirelli, and U. Keller, "Attosecond Science: Recent Highlights and Future Trends," *Annu. Rev. Phys. Chem.*, vol. 63, pp. 447–469, may 2012.

[77] A. L. Cavalieri, N. Müller, T. Uphues, V. S. Yakovlev, A. Baltuška, B. Horvath, B. Schmidt, L. Blümel, R. Holzwarth, S. Hendel, M. Drescher, U. Kleineberg, P. M. Echenique, R. Kienberger, F. Krausz, and U. Heinzmann, "Attosecond spectroscopy in condensed matter," *Nature*, vol. 449, pp. 1029–1032, oct 2007.

[78] J. R. Lakowicz, *Principles of Fluorescence Spectroscopy*. Baltimore, Maryland, USA: Springer, 3rd ed., 2006.

[79] E. Biasin, T. B. V. Driel, K. S. Kjær, A. O. Dohn, T. Harlang, P. Chabera, Y. Liu, J. Uhlig, R. Hartsock, W. Liang, R. Alonsomori, M. Chollet, J. M. Glownia, S. Nelson, D. Sokaras, A. Tadesse, A. Britz, A. Galler, W. Gawelda, C. Bressler, J. Gaffney, H. T. Lemke, K. B. Møller, M. M. Nielsen, and V. Sundstr, "Femtosecond X-ray scattering study of ultrafast photoinduced structural dynamics in solvated [Co(terpy)2]2+," *J. Phys. Rev. Lett.*, vol. 117, no. 1, p. 013002, 2016.

[80] K. Haldrup, G. Levi, E. Biasin, P. Vester, M. G. Laursen, F. Beyer, K. S. Kjær, T. Brandt Van Driel, T. Harlang, A. O. Dohn, R. J. Hartsock, S. Nelson, J. M. Glownia, H. T. Lemke, M. Christensen, K. J. Gaffney, N. E. Henriksen, K. B. Møller, and M. M. Nielsen, "Ultrafast X-Ray Scattering Measurements of Coherent Structural Dynamics on the Ground-State Potential Energy Surface of a Diplatinum Molecule," *Phys. Rev. Lett.*, vol. 122, p. 063001, feb 2019.

[81] D. Khakhulin, L. M. Lawson Daku, D. Leshchev, G. E. Newby, M. Jarenmark, C. Bressler, M. Wulff, and S. E. Canton, "Visualizing the coordination-spheres of photoexcited transition metal complexes with ultrafast hard X-rays," *Phys. Chem. Chem. Phys.*, vol. 21, no. 18, pp. 9277–9284, 2019.

[82] M. Maroncelli, "Computer simulations of solvation dynamics in acetonitrile," *J. Chem. Phys.*, vol. 94, no. 3, pp. 2084–2103, 1991.

[83] M. Maroncelli, "The dynamics of solvation in polar liquids," *J. Mol. Liq.*, vol. 57, no. C, pp. 1–37, 1993.

[84] R. M. Stratt and M. Maroncelli, "Nonreactive dynamics in solution: The emerging molecular view of solvation dynamics and vibrational relaxation," *J. Phys. Chem.*, vol. 100, no. 31, pp. 12981–12996, 1996.

[85] A. Rosspeintner, B. Lang, and E. Vauthey, "Ultrafast Photochemistry in Liquids," *Annu. Rev. Phys. Chem.*, vol. 64, no. 1, pp. 247–271, 2013.

[86] M. Cammarata, M. Lorenc, T. K. Kim, J. H. Lee, Q. Y. Kong, E. Pontecorvo, M. Lo Russo, G. Schiró, A. Cupane, M. Wulff, and H. Ihee, "Impulsive solvent heating probed by picosecond x-ray diffraction," *J. Chem. Phys.*, vol. 124, no. 12, 2006.

[87] K. S. Kjær, T. B. van Driel, J. Kehres, K. Haldrup, D. Khakhulin, K. Bechgaard, M. Cammarata, M. Wulff, T. J. Sørensen, and M. M. Nielsen, "Introducing a standard method for experimental determination of the solvent response in laser pump, X-ray probe time-resolved wide-angle X-ray scattering experiments on systems in solution.," *Phys. Chem. Chem. Phys.*, vol. 15, no. i, pp. 15003–16, 2013.

[88] A. O. Dohn, E. Biasin, K. Haldrup, M. M. Nielsen, N. E. Henriksen, and K. B. Møller, "On the calculation of x-ray scattering signals from pairwise radial distribution functions," *J. Phys. B At. Mol. Opt. Phys.*, vol. 48, p. 244010, dec 2015.

[89] D. Dhabal, K. T. Wikfeldt, L. B. Skinner, C. Chakravarty, and H. K. Kashyap, "Probing the triplet correlation function in liquid water by experiments and molecular simulations," *Phys. Chem. Chem. Phys.*, vol. 19, no. 4, pp. 3265–3278, 2017.

[90] J. Waser and V. Schomaker, "The fourier inversion of diffraction data," *Rev. Mod. Phys.*, vol. 25, no. 3, pp. 671–690, 1953.

[91] K. T. Wikfeldt, C. Huang, A. Nilsson, and L. G. Pettersson, "Enhanced small-angle scattering connected to the Widom line in simulations of supercooled water," *J. Chem. Phys.*, vol. 134, pp. 214506–1 – 214506–16, 2011.

[92] E. Schrödinger, "An Undulatory Theory of the Mechanics of Atoms and Molecules," *Phys. Rev.*, vol. 28, pp. 1049–1070, dec 1926.

[93] E. Schrödinger, "Quantisierung als Eigenwertproblem," *Ann. Phys.*, vol. 386, pp. 109–139, jan 1926.

[94] M. Born, "Zur Quantenmechanik der Stossvorgänge," *Zeitschrift für Phys.*, vol. 37, pp. 863–867, dec 1926.

[95] D. Tanner, *Introduction to Quantum Mechanics: A Time-Dependent Perspective*. University Science Books, 1 ed., 2006.

[96] A. Szabo and Neil S. Ostlund, *Modern Quantum Chemistry: Introduction to Advanced Electronic Structure Theory*. Mineola, New York: Dover Publications, 1996.

[97] L. Piela, *Ideas of Quantum Chemistry*. Amsterdam: Elsevier B.V., first ed., 2007.

[98] M. Born and R. Oppenheimer, "Zur Quantentheorie der Molekeln," *Ann. Phys.*, vol. 389, pp. 457–484, jan 1927.

[99] F. Jensen, *Introduction to Computational Chemistry*, vol. 1. John Wiley & Sons Ltd., second ed., 2007.

[100] E. Gross, J. Dobson, and M. Petersilka, "Density functional theory of time-dependent phenomena," in *Density Funct. Theory* (R. Nalewajski, ed.), vol. 181, p. 81, Springer-Verlag Berlin Heidelberg, 1996.

[101] W. Koch and M. C. Holthausen, *A Chemist's Guide to Density Functional Theory*, vol. 3. Wiley-VCH Verlag, 2. ed., 2001.

[102] P. Hohenberg and W. Kohn, "Inhomogeneous electron gas," *Phys. Rev.*, vol. 136, no. 3B, 1964.

[103] W. Kohn and L. J. Sham, "Self-Consistent Equations Including Exchange and Correlation Effects," *Phys. Rev.*, vol. 140, pp. A1133–A1138, nov 1965.

[104] A. R. Miguel A. L. Marques, Neepa T. Maitra, Fernando M.S. Nogueira, Eberhard K.U. Gross, *Fundamentals of Time-Dependent Density Functional Theory*. Springer-Verlag Berlin Heidelberg, 1 ed., 2012.

[105] E. Runge and E. K. Gross, "Density-functional theory for time-dependent systems," *Phys. Rev. Lett.*, vol. 52, no. 12, pp. 997–1000, 1984.

[106] M. E. Casida, "Chapter 5 : Time-Dependent Density Functional Response Theory for Molecules," in *Recent Adv. density Funct. methods, part I* (D. P. Chong, ed.), ch. 5, pp. 155–192, World Scientific, 1995.

[107] M. E. Casida, "Time-dependent density-functional theory for molecules and molecular solids," *J. Mol. Struct. THEOCHEM*, vol. 914, no. 1-3, pp. 3–18, 2009.

[108] M. E. Casida and M. Huix-Rotllant, "Progress in Time-Dependent Density-Functional Theory," *Annu. Rev. Phys. Chem.*, vol. 63, pp. 287–323, 2012.

[109] G. Groenhof, "Introduction to QM/MM Simulations," in *Biomol. Simulations Methods Protoc.* (L. Monticelli and E. Salonen, eds.), ch. 3, pp. 43–66, New York: Springer - Huamana Press, 2013.

[110] J. H. Jensen, *Molecular Modeling Basics*. CRC Press, Taylor & Francis, 1. edition ed., 2010.

[111] S. A. Adcock and J. A. McCammon, "Molecular dynamics: Survey of methods for simulating the activity of proteins," *Chem. Rev.*, vol. 106, no. 5, pp. 1589–1615, 2006.

[112] A. O. Dohn, "Transient Changes in Molecular Geometries and How to Model Them," in *Springer Theses*, Springer International Publishing, 1 ed., 2015.

[113] Y. Wu, H. L. Tepper, and G. A. Voth, "Flexible simple point-charge water model with improved liquid-state properties," *J. Chem. Phys.*, vol. 124, pp. 024503–1–024503–12, 2006.

[114] H. J. Berendsen, J. R. Grigera, and T. P. Straatsma, "The missing term in effective pair potentials," *J. Phys. Chem.*, vol. 91, no. 24, pp. 6269–6271, 1987.

[115] A. Warshel and M. Levitt, "Theoretical studies of enzymic reactions: Dielectric, electrostatic and steric stabilization of the carbonium ion in the reaction of lysozyme," *J. Mol. Biol.*, vol. 103, pp. 227–249, may 1976.

[116] H. Lin and D. G. Truhlar, "QM/MM: What have we learned, where are we, and where do we go from here?," in *Theor. Chem. Acc.*, vol. 117, pp. 185–199, feb 2007.

[117] M. J. Field, P. A. Bash, and M. Karplus, "A combined quantum mechanical and molecular mechanical potential for molecular dynamics simulations," *J. Comput. Chem.*, vol. 11, no. 6, pp. 700–733, 1990.

[118] G. Lamoureux and B. Roux, "Modeling induced polarization with classical Drude oscillators: Theory and molecular dynamics simulation algorithm," *J. Chem. Phys.*, vol. 119, pp. 3025–3039, aug 2003.

[119] A. Warshel, P. K. Sharma, M. Kato, Y. Xiang, H. Liu, and M. H. M. Olsson, "Electrostatic basis for enzyme catalysis.," *Chem. Rev.*, vol. 106, pp. 3210–35, aug 2006.

[120] A. K. Rappe and W. A. Goddard, "Charge equilibration for molecular dynamics simulations," *J. Phys. Chem.*, vol. 95, pp. 3358–3363, apr 1991.

[121] H.-d. Meyer and F. Gatti, *Multidimensional Quantum Dynamics: MCTDH Theory and Applications*. WILEY-VCH Verlag GmbH & Co. KGaA, 2009.

[122] L. Verlet, "Computer "Experiments" on Classical Fluids. I. Thermodynamical Properties of Lennard-Jones Molecules," *Phys. Rev.*, vol. 159, no. 1, pp. 98–103, 1967.

[123] J. C. Tully, "Mixed quantum-classical dynamics," *Faraday Discuss*, vol. 110, pp. 407–419, 1998.

[124] M. Richter, P. Marquetand, J. González-Vázquez, I. Sola, and L. González, "SHARC: Ab initio molecular dynamics with surface hopping in the adiabatic representation including arbitrary couplings," *J. Chem. Theory Comput.*, vol. 7, pp. 1253–1258, 2011.

[125] M. Barbatti, "Nonadiabatic dynamics with trajectory surface hopping method," *Wiley Interdiscip. Rev. Comput. Mol. Sci.*, vol. 1, pp. 620–633, 2011.

[126] S. Mai, P. Marquetand, and L. González, "A general method to describe intersystem crossing dynamics in trajectory surface hopping," *Int. J. Quantum Chem.*, vol. 115, pp. 1215–1231, 2015.

[127] S. Mai, P. Marquetand, and L. González, "Nonadiabatic dynamics: The SHARC approach," *Wiley Interdiscip. Rev. Comput. Mol. Sci.*, vol. e1370, pp. 1–23, 2018.

[128] L. Wang, A. Akimov, and O. V. Prezhdo, "Recent Progress in Surface Hopping: 2011-2015," *J. Phys. Chem. Lett.*, vol. 7, pp. 2100–2112, jun 2016.

[129] J. C. Tully, "Molecular dynamics with electronic transitions," *J. Chem. Phys.*, vol. 93, no. 2, pp. 1061–1071, 1990.

[130] M. Persico and G. Granucci, "An overview of nonadiabatic dynamics simulations methods, with focus on the direct approach versus the fitting of potential energy surfaces," *Theor. Chem. Acc.*, vol. 133, no. 9, pp. 1–28, 2014.

[131] G. Granucci, M. Persico, and G. Spighi, "Surface hopping trajectory simulations with spin-orbit and dynamical couplings," *J. Chem. Phys.*, vol. 137, p. 22A501, dec 2012.

[132] F. Plasser and H. Lischka, "Analysis of Excitonic and Charge Transfer Interactions from Quantum Chemical Calculations," *J. Chem. Theory Comput.*, vol. 8, pp. 2777–2789, aug 2012.

[133] F. Plasser, M. Wormit, and A. Dreuw, "New tools for the systematic analysis and visualization of electronic excitations. I. Formalism," *J. Chem. Phys.*, vol. 141, p. 024106, jul 2014.

[134] S. Mai, F. Plasser, J. Dorn, M. Fumanal, C. Daniel, and L. González, "Quantitative wave function analysis for excited states of transition metal complexes," *Coord. Chem. Rev.*, vol. 361, pp. 74–97, 2018.

[135] K. Kalyanasundaram, "Photophysics, photochemistry and solar energy conversion with tris(bipyridyl)ruthenium(II) and its analogues," *Coord. Chem. Rev.*, vol. 46, pp. 159–244, oct 1982.

[136] A. Juris, V. Balzani, F. Barigelletti, S. Campagna, P. Belser, and A. von Zelewsky, "Ru(II) polypyridine complexes: photophysics, photochemistry, eletrochemistry, and chemiluminescence," *Coord. Chem. Rev.*, vol. 84, pp. 85–277, mar 1988.

[137] D. M. Roundhill and D. M. Roundhill, "Photochemistry, Photophysics, and Photoredox Reactions of Ru(bpy)3ˆ2+ and Related Complexes," in *Photochem. Photophysics Met. Complexes*, ch. 5, pp. 165–215, Springer Science + Business Media, 1994.

[138] K. Rangan, S. M. Arachchige, J. R. Brown, and K. J. Brewer, "Solar energy conversion using photochemical molecular devices: Photocatalytic hydrogen production from water using mixed-metal supramolecular complexes," *Energy Environ. Sci.*, vol. 2, pp. 410–419, mar 2009.

[139] D. P. Rillema, D. S. Jones, and H. A. Levy, "Structure of tris(2,2-bipyridyl)ruthenium(II) hexafluorophosphate, [Ru(bipy)3][PF6]2; X-ray crystallographic determination," *J. Chem. Soc. Chem. Commun.*, pp. 849–851, jan 1979.

[140] D. P. Rillema, D. S. Jones, C. Woods, and H. A. Levy, "Comparison of the Crystal Structures of Tris Heterocyclic Ligand Complexes of Ruthenium(ii)," *Inorg. Chem.*, vol. 31, no. 13, pp. 2935–2938, 1992.

[141] M.-E. Moret, I. Tavernelli, and U. Rothlisberger, "Combined QM/MM and Classical Molecular Dynamics Study of [Ru(bpy)_3]ˆ2+ in Water," *J. Phys. Chem B*, vol. 113, no. 22, pp. 7737–7744, 2009.

[142] P. Diamantis, J. F. Gonthier, I. Tavernelli, and U. Rothlisberger, "Study of the redox properties of singlet and triplet tris(2,2- bipyridine)ruthenium(II) ([Ru(bpy)3]ˆ2+) in aqueous solution by full quantum and mixed quantum/classical molecular dynamics simulations," *J. Phys. Chem. B*, vol. 118, pp. 3950–3959, apr 2014.

[143] F. Alary, J. Heully, L. Bijeire, P. Vicendo, P. Sabatier, and R. De, "Is the 3MLCT the Only Photoreactive State of Polypyridyl Complexes?," *Inorg. Chem.*, vol. 46, no. 8, pp. 1507–1517, 2007.

[144] K. D. Demadis, C. M. Hartshorn, and T. J. Meyer, "The Localized-to-Delocalized Transition in Mixed-Valence Chemistry," *Chem. Rev.*, vol. 101, no. 9, pp. 2655–2685, 2001.

[145] S. Wallin, J. Davidsson, J. Modin, and L. Hammarstro, "Femtosecond Transient Absorption Anisotropy Study on [Ru(bpy)3]ˆ2+ and [Ru(bpy)(py)4]ˆ2+. Ultrafast Interligand Randomization of the MLCT State," *J. Phys. Chem. A*, vol. 109, pp. 4697–4704, 2005.

[146] C. W. Stark, W. J. Schreier, J. Lucon, E. Edwards, T. Douglas, and B. Kohler, "Interligand Electron Transfer in Heteroleptic Ruthenium(II) Complexes Occurs on Multiple Time Scales," *J. Phys. Chem. A*, no. Ii, p. 150511123542002, 2015.

[147] N. H. Damrauer, G. Cerullo, A. Yeh, T. R. Boussie, C. V. Shank, and J. McCuscker, "Femtosecond Dynamics of Excited-State Evolution in [Ru(bpy)3]ˆ2+," *Science (80-.).*, vol. 275, pp. 54–57, jan 1997.

[148] A. T. Yeh, C. Shank, and J. K. McCusker, "Ultrafast Electron Localization Dynamics Following Photo-Induced Charge Transfer," *Science (80-.).*, vol. 289, pp. 935–938, aug 2000.

[149] M. E. Moret, I. Tavernelli, M. Chergui, and U. Rothlisberger, "Electron localization dynamics in the triplet excited state of [Ru(bpy)3]2+ in aqueous solution," *Chem. - A Eur. J.*, vol. 16, no. 20, pp. 5889–5894, 2010.

[150] P. A. Sánchez-Murcia, J. J. Nogueira, F. Plasser, and L. González, "Orbital-free photophysical descriptors to predict directional excitations in metal-based photosensitizers," *Chem. Sci.*, vol. 11, pp. 7685–7693, jul 2020.

[151] S. E. Canton, K. S. Kjær, G. Vankó, T. B. van Driel, S.-i. Adachi, A. Bordage, C. Bressler, P. Chabera, M. Christensen, A. O. Dohn, A. Galler, W. Gawelda, D. Gosztola, K. Haldrup, T. Harlang, Y. Liu, K. B. Møller, Z. Németh, S. Nozawa, M. Pápai, T. Sato, T. Sato, K. Suarez-Alcantara, T. Togashi, K. Tono, J. Uhlig, D. a. Vithanage, K. Wärnmark, M. Yabashi, J. Zhang, V. Sundström, and M. M. Nielsen, "Visualizing the non-equilibrium dynamics of photoinduced intramolecular electron transfer with femtosecond X-ray pulses.," *Nat. Commun.*, vol. 6, p. 6359, 2015.

[152] A. C. Bhasikuttan, M. Suzuki, S. Nakashima, and T. Okada, "Ultrafast fluorescence detection in tris(2,2-bipyridine)ruthenium(II) complex in solution: Relaxation dynamics involving higher excited states," *J. Am. Chem. Soc.*, vol. 124, pp. 8398–8405, jul 2002.

[153] A. Cannizzo, F. Van Mourik, W. Gawelda, G. Zgrablic, C. Bressler, and M. Chergui, "Broadband femtosecond fluorescence spectroscopy of [Ru(bpy)3]ˆ2+," *Angew. Chemie - Int. Ed.*, vol. 45, pp. 3174–3176, may 2006.

[154] A. J. Atkins and L. González, "Trajectory Surface-Hopping Dynamics Including Intersystem Crossing in [Ru(bpy)3]2+," *J. Phys. Chem. Lett.*, vol. 8, no. 16, pp. 3840–3845, 2017.

[155] M. Kasha, "Characterization of electronic transitions in complex molecules," *Discuss. Faraday Soc.*, vol. 9, pp. 14–19, jan 1950.

[156] W. R. Browne, C. G. Coates, C. Brady, P. Matousek, M. Towrie, S. W. Botchway, A. W. Parker, J. G. Vos, and J. J. McGarvey, "Isotope effects

on the picosecond time-resolved emission spectroscopy of tris(2,2-bipyridine)ruthenium (II)," *J. Am. Chem. Soc.*, vol. 125, pp. 1706–1707, feb 2003.

[157] W. Henry, C. G. Coates, C. Brady, K. L. Ronayne, P. Matousek, M. Towrie, S. W. Botchway, A. W. Parker, J. G. Vos, W. R. Browne, and J. J. McGarvey, "The early picosecond photophysics of ru(II) polypyridyl complexes: A tale of two timescales," *J. Phys. Chem. A*, vol. 112, pp. 4537–4544, may 2008.

[158] S. A. McFarland, F. S. Lee, K. A. Cheng, F. L. Cozens, and N. P. Schepp, "Picosecond dynamics of nonthermalized excited states in tris(2,2-bipyridine)ruthenium(II) derivatives elucidated by high energy excitation," *J. Am. Chem. Soc.*, vol. 127, pp. 7065–7070, may 2005.

[159] B. Durham, J. V. Caspar, J. K. Nagle, and T. J. Meyer, "Photochemistry of tris(2,2'-bipyridine)ruthenium(2+) ion," *J. Am. Chem. Soc.*, vol. 104, no. 18, pp. 4803–4810, 1982.

[160] K. Haldrup, "Singular value decomposition as a tool for background corrections in time-resolved XFEL scattering data," *Philos. Trans. R. Soc. Lond. B. Biol. Sci.*, vol. 369, no. 1647, p. 20130336, 2014.

[161] K. H. Kim, A. Späh, H. Pathak, C. Yang, S. Bonetti, K. Amann-Winkel, D. Mariedahl, D. Schlesinger, J. A. Sellberg, D. Mendez, G. van der Schot, H. Y. Hwang, J. Clark, O. Shigeki, T. Tadashi, Y. Harada, H. Ogasawara, T. Katayama, A. Nilsson, and F. Perakis, "Anisotropic X-Ray Scattering of Transiently Oriented Water," *Phys. Rev. Lett.*, vol. 125, p. 076002, aug 2020.

[162] R. Jimenez, G. R. Fleming, P. V. Kumar, and M. Maroncelli, "Femtosecond solvation dynamics of water," *Nature*, vol. 369, pp. 471–473, 1994.

[163] M. Maroncelli, P. V. Kumar, A. Papazyan, M. L. Horng, S. J. Rosenthal, and G. R. Fleming, "Studies of the inertial component of polar solvation dynamics," in *AIP Conf. Proc.*, vol. 298, pp. 310–333, AIP Publishing, jun 1994.

[164] S. Palese, L. Schilling, R. J. Dwayne Miller, P. Randall Staver, and W. T. Lotshaw, "Femtosecond optical Kerr effect studies of water," *J. Phys. Chem.*, vol. 98, no. 25, pp. 6308–6316, 1994.

[165] E. W. Castner, Y. J. Chang, Y. C. Chu, and G. E. Walrafen, "The intermolecular dynamics of liquid water," *J. Chem. Phys.*, vol. 102, pp. 653–659, jan 1995.

[166] D. Leshchev, T. C. Harlang, L. A. Fredin, D. Khakhulin, Y. Liu, E. Biasin, M. G. Laursen, G. E. Newby, K. Haldrup, M. M. Nielsen, K. Wärnmark, V. Sundström, P. Persson, K. S. Kjær, and M. Wulff, "Tracking the picosecond deactivation dynamics of a photoexcited iron carbene complex by time-resolved X-ray scattering," *Chem. Sci.*, vol. 9, pp. 405–414, jan 2018.

[167] D. A. Hoff, R. Silva, and L. G. Rego, "Subpicosecond dynamics of metal-to-ligand charge-transfer excited states in solvated [Ru(bpy)3]ˆ2+ complexes," *J. Phys. Chem. C*, vol. 115, pp. 15617–15626, aug 2011.

[168] J. J. Szymczak, F. D. Hofmann, and M. Meuwly, "Structure and dynamics of solvent shells around photoexcited metal complexes.," *Phys. Chem. Chem. Phys.*, vol. 15, pp. 6268–77, may 2013.

[169] I. Josefsson, S. K. Eriksson, H. Rensmo, and M. Odelius, "Solvation structure around ruthenium(II) tris(bipyridine) in lithium halide solutions," *Struct. Dyn.*, vol. 3, no. 2, 2016.

[170] A. K. Das, R. V. Solomon, F. Hofmann, and M. Meuwly, "Inner-Shell Water Rearrangement Following Photoexcitation of Tris(2,2-bipyridine)iron(II)," *J. Phys. Chem. B*, vol. 120, pp. 206–216, jan 2016.

[171] C. M. Breneman and K. B. Wiberg, "Determining atom-centered monopoles from molecular electrostatic potentials. The need for high sampling density in formamide conformational analysis," *J. Comput. Chem.*, vol. 11, pp. 361–373, apr 1990.

[172] C. I. Bayly, P. Cieplak, W. D. Cornell, and P. A. Kollman, "A well-behaved electrostatic potential based method using charge re-

straints for deriving atomic charges: The RESP model," *J. Phys. Chem.*, vol. 97, no. 40, pp. 10269–10280, 1993.

[173] A. V. Marenich, S. V. Jerome, C. J. Cramer, and D. G. Truhlar, "Charge model 5: An extension of hirshfeld population analysis for the accurate description of molecular interactions in gaseous and condensed phases," *J. Chem. Theory Comput.*, vol. 8, pp. 527–541, feb 2012.

[174] A. D. Becke, "Density-functional exchange-energy approximation with correct asymptotic behavior," *Phys. Rev. a (General Physics)*, vol. 38, no. 6, pp. 3098 – 3100, 1988.

[175] J. P. Perdew, "Density-functional approximation for the correlation energy of the inhomogeneous electron gas," *Phys. Rev. B*, vol. 33, pp. 8822–8824, jun 1986.

[176] F. Weigend and R. Ahlrichs, "Balanced basis sets of split valence, triple zeta valence and quadruple zeta valence quality for H to Rn: Design and assessment of accuracy.," *Phys. Chem. Chem. Phys.*, vol. 7, pp. 3297–305, sep 2005.

[177] H. W. Horn, W. C. Swope, J. W. Pitera, J. D. Madura, T. J. Dick, G. L. Hura, and T. Head-Gordon, "Development of an improved four-site water model for biomolecular simulations: TIP4P-Ew.," *J. Chem. Phys.*, vol. 120, pp. 9665–78, may 2004.

[178] K. J. Bowers, E. Chow, H. Xu, R. O. Dror, M. P. Eastwood, B. A. Gregersen, J. L. Klepeis, I. Kolossvary, M. A. Moraes, F. D. Sacerdoti, J. K. Salmon, and D. E. S. Yibing Shan, "Proceedings of the ACM/IEEE Conference on Supercomputing, (SC06):," in *Scalable Algorithms Mol. Dyn. Simulations Commod. Clust.*, (Tampa, Florida), IEEE, 2006.

[179] W. Humphrey, A. Dalke, and K. Schulten, "VMD: Visual molecular dynamics," *J. Mol. Graph.*, vol. 14, pp. 33–38, feb 1996.

[180] M. Reiher, O. Salomon, D. Sellmann, and B. A. Hess, "Dinuclear Diazene Iron and Ruthenium Complexes as Models for Studying Nitrogenase Activity," *Chem. - A Eur. J.*, vol. 7, pp. 5195–5202, dec 2001.

[181] O. Salomon, M. Reiher, and B. A. Hess, "Assertion and validation of the performance of the B3LYP* functional for the first transition metal row and the G2 test set," *J. Chem. Phys.*, vol. 117, no. 10, pp. 4729–4737, 2002.

[182] M. Ceriotti, W. Fang, P. G. Kusalik, R. H. McKenzie, A. Michaelides, M. A. Morales, and T. E. Markland, "Nuclear Quantum Effects in Water and Aqueous Systems: Experiment, Theory, and Current Challenges," *Chem. Rev.*, vol. 116, pp. 7529–7550, 2016.

[183] J. Enkovaara, C. Rostgaard, J. J. Mortensen, J. Chen, M. Dułak, L. Ferrighi, J. Gavnholt, C. Glinsvad, V. Haikola, H. A. Hansen, H. H. Kristoffersen, M. Kuisma, A. H. Larsen, L. Lehtovaara, M. Ljungberg, O. Lopez-Acevedo, P. G. Moses, J. Ojanen, T. Olsen, V. Petzold, N. A. Romero, J. Stausholm-Møller, M. Strange, G. A. Tritsaris, M. Vanin, M. Walter, B. Hammer, H. Häkkinen, G. K. H. Madsen, R. M. Nieminen, J. K. Nørskov, M. Puska, T. T. Rantala, J. Schiøtz, K. S. Thygesen, and K. W. Jacobsen, "Electronic structure calculations with GPAW: a real-space implementation of the projector augmented-wave method.," *J. Phys. Condens. Matter*, vol. 22, p. 253202, jun 2010.

[184] J. J. Mortensen, L. B. Hansen, and K. W. Jacobsen, "Real-space grid implementation of the projector augmented wave method," *Phys. Rev. B - Condens. Matter Mater. Phys.*, vol. 71, p. 035109, jan 2005.

[185] A. O. Dohn, E. O. Jónsson, G. Levi, J. J. Mortensen, O. Lopez-Acevedo, K. S. Thygesen, K. W. Jacobsen, J. Ulstrup, N. E. Henriksen, K. B. Møller, and H. Jónsson, "Grid-Based Projector Augmented Wave (GPAW) Implementation of Quantum Mechanics/Molecular Mechanics (QM/MM) Electrostatic Embedding and Application to a Solvated Diplatinum Complex," *J. Chem. Theory Comput.*, vol. 13, no. 12, pp. 6010–6022, 2017.

[186] A. D. Becke, "Density-functional exchange-energy approximation with correct asymptotic behavior," *Phys. Rev. A*, vol. 38, pp. 3098–3100, sep 1988.

[187] A. H. Larsen, M. Vanin, J. J. Mortensen, K. S. Thygesen, and K. W. Jacobsen, "Localized atomic basis set in the projector augmented

wave method," *Phys. Rev. B - Condens. Matter Mater. Phys.*, vol. 80, p. 195112, nov 2009.

[188] G. Levi, M. Pápai, N. E. Henriksen, A. O. Dohn, and K. B. Møller, "Solution Structure and Ultrafast Vibrational Relaxation of the Pt-POP Complex Revealed by ΔSCF-QM/MM Direct Dynamics Simulations," *J. Phys. Chem. C*, vol. 122, pp. 7100–7119, apr 2018.

[189] W. Gawelda, M. Johnson, F. M. F. de Groot, R. Abela, C. Bressler, and M. Chergui, "Electronic and molecular structure of photoexcited [Ru(II)(bpy)3]2+ probed by picosecond X-ray absorption spectroscopy.," *J. Am. Chem. Soc.*, vol. 128, no. 15, pp. 5001–5009, 2006.

[190] T. Sato, S. Nozawa, A. Tomita, M. Hoshino, S.-y. Koshihara, H. Fujii, and S.-i. Adachi, "Coordination and Electronic Structure of Ruthenium(II)- tris -2,2'-bipyridine in the Triplet Metal-to-Ligand Charge-Transfer Excited State Observed by Picosecond Time-Resolved Ru K -Edge XAFS," *J. Phys. Chem. C*, vol. 116, pp. 14232–14236, jul 2012.

[191] A. K. Soper, "Joint structure refinement of x-ray and neutron diffraction data on disordered materials: Application to liquid water," *J. Phys. Condens. Matter*, vol. 19, no. 33, 2007.

[192] K. Haldrup, G. Vankó, W. Gawelda, A. Galler, G. Doumy, A. M. March, E. P. Kanter, A. Bordage, A. Dohn, T. B. van Driel, H. T. Lemke, S. E. Canton, J. Uhlig, V. Sundström, L. Young, S. H. Southworth, M. M. Nielsen, and C. Bressler, "Guest - Host Interactions Investigated by Time-Resolved X-ray Spectroscopies and Scattering at MHz Rates: Solvation Dynamics and Photoinduced Spin Transition in Aqueous Fe(bipy)3^2+," *J. Phys. Chem. A*, vol. 116, pp. 9878–9887, 2012.

[193] A. Thompson, D. Vaughan, J. Kirz, D. Attwood, and E. Gullikson, *X-RAY DATA BOOKLET*. Lawrence Berkeley National Laboratory, second ed., 2001.

[194] H. Weise and W. Decking, "Commissioning and first lasing of the European XFEL," *Proc. 38th Int. Free. Laser Conf. FEL 2017*, pp. 9–13, 2017.

[195] W. Decking, S. Abeghyan, P. Abramian, A. Abramsky, A. Aguirre, C. Albrecht, P. Alou, M. Altarelli, P. Altmann, K. Amyan, V. Anashin, E. Apostolov, K. Appel, D. Auguste, V. Ayvazyan, S. Baark, F. Babies, N. Baboi, P. Bak, V. Balandin, R. Baldinger, B. Baranasic, S. Barbanotti, O. Belikov, V. Belokurov, L. Belova, V. Belyakov, S. Berry, M. Bertucci, B. Beutner, A. Block, M. Blöcher, T. Böckmann, C. Bohm, M. Böhnert, V. Bondar, E. Bondarchuk, M. Bonezzi, P. Borowiec, C. Bösch, U. Bösenberg, A. Bosotti, R. Böspflug, M. Bousonville, E. Boyd, Y. Bozhko, A. Brand, J. Branlard, S. Briechle, F. Brinker, S. Brinker, R. Brinkmann, S. Brockhauser, O. Brovko, H. Brück, A. Brüdgam, L. Butkowski, T. Büttner, J. Calero, E. Castro-Carballo, G. Cattalanotto, J. Charrier, J. Chen, A. Cherepenko, V. Cheskidov, M. Chiodini, A. Chong, S. Choroba, M. Chorowski, D. Churanov, W. Cichalewski, M. Clausen, W. Clement, C. Cloué, J. A. Cobos, N. Coppola, S. Cunis, K. Czuba, M. Czwalinna, B. D'Almagne, J. Dammann, H. Danared, A. d. Z. Wagner, A. Delfs, T. Delfs, F. Dietrich, T. Dietrich, M. Dohlus, M. Dommach, A. Donat, X. Dong, N. Doynikov, M. Dressel, M. Duda, P. Duda, H. Eckoldt, W. Ehsan, J. Eidam, F. Eints, C. Engling, U. Englisch, A. Ermakov, K. Escherich, J. Eschke, E. Saldin, M. Faesing, A. Fallou, M. Felber, M. Fenner, B. Fernandes, J. M. Fernández, S. Feuker, K. Filippakopoulos, K. Floettmann, V. Fogel, M. Fontaine, A. Francés, I. F. Martin, W. Freund, T. Freyermuth, M. Friedland, L. Fröhlich, M. Fusetti, J. Fydrych, A. Gallas, O. García, L. Garcia-Tabares, G. Geloni, N. Gerasimova, C. Gerth, P. Geßler, V. Gharibyan, M. Gloor, J. Głowinkowski, A. Goessel, Z. Gołębiewski, N. Golubeva, W. Grabowski, W. Graeff, A. Grebentsov, M. Grecki, T. Grevsmuehl, M. Gross, U. Grosse-Wortmann, J. Grünert, S. Grunewald, P. Grzegory, G. Feng, H. Guler, G. Gusev, J. L. Gutierrez, L. Hagge, M. Hamberg, R. Hanneken, E. Harms, I. Hartl, A. Hauberg, S. Hauf, J. Hauschildt, J. Hauser, J. Havlicek, A. Hedqvist, N. Heidbrook, F. Hellberg, D. Henning, O. Hensler, T. Hermann, A. Hidvégi, M. Hierholzer, H. Hintz, F. Hoffmann, M. Hoffmann, M. Hoffmann, Y. Holler, M. Hüning, A. Ignatenko, M. Ilchen, A. Iluk, J. Iversen, J. Iversen, M. Izquierdo, L. Jachmann, N. Jardon, U. Jastrow, K. Jensch, J. Jensen, M. Jeżabek, M. Jidda, H. Jin, N. Johansson, R. Jonas, W. Kaabi, D. Kaefer, R. Kammering, H. Kapitza, S. Karabekyan, S. Karstensen,

K. Kasprzak, V. Katalev, D. Keese, B. Keil, M. Kholopov, M. Killenberger, B. Kitaev, Y. Klimchenko, R. Klos, L. Knebel, A. Koch, M. Koepke, S. Köhler, W. Köhler, N. Kohlstrunk, Z. Konopkova, A. Konstantinov, W. Kook, W. Koprek, M. Körfer, O. Korth, A. Kosarev, K. Kosiński, D. Kostin, Y. Kot, A. Kotarba, T. Kozak, V. Kozak, R. Kramert, M. Krasilnikov, A. Krasnov, B. Krause, L. Kravchuk, O. Krebs, R. Kretschmer, J. Kreutzkamp, O. Kröplin, K. Krzysik, G. Kube, H. Kuehn, N. Kujala, V. Kulikov, V. Kuzminych, D. L. Civita, M. Lacroix, T. Lamb, A. Lancetov, M. Larsson, D. L. Pinvidic, S. Lederer, T. Lensch, D. Lenz, A. Leuschner, F. Levenhagen, Y. Li, J. Liebing, L. Lilje, T. Limberg, D. Lipka, B. List, J. Liu, S. Liu, B. Lorbeer, J. Lorkiewicz, H. H. Lu, F. Ludwig, K. Machau, W. Maciocha, C. Madec, C. Magueur, C. Maiano, I. Maksimova, K. Malcher, T. Maltezopoulos, E. Mamoshkina, B. Manschwetus, F. Marcellini, G. Marinkovic, T. Martinez, H. Martirosyan, W. Maschmann, M. Maslov, A. Matheisen, U. Mavric, J. Meißner, K. Meissner, M. Messerschmidt, N. Meyners, G. Michalski, P. Michelato, N. Mildner, M. Moe, F. Moglia, C. Mohr, S. Mohr, W. Möller, M. Mommerz, L. Monaco, C. Montiel, M. Moretti, I. Morozov, P. Morozov, D. Mross, J. Mueller, C. Müller, J. Müller, K. Müller, J. Munilla, A. Münnich, V. Muratov, O. Napoly, B. Näser, N. Nefedov, R. Neumann, R. Neumann, N. Ngada, D. Noelle, F. Obier, I. Okunev, J. A. Oliver, M. Omet, A. Oppelt, A. Ottmar, M. Oublaid, C. Pagani, R. Paparella, V. Paramonov, C. Peitzmann, J. Penning, A. Perus, F. Peters, B. Petersen, A. Petrov, I. Petrov, S. Pfeiffer, J. Pflüger, S. Philipp, Y. Pienaud, P. Pierini, S. Pivovarov, M. Planas, E. Pławski, M. Pohl, J. Polinski, V. Popov, S. Prat, J. Prenting, G. Priebe, H. Pryschelski, K. Przygoda, E. Pyata, B. Racky, A. Rathjen, W. Ratuschni, S. Regnaud-Campderros, K. Rehlich, D. Reschke, C. Robson, J. Roever, M. Roggli, J. Rothenburg, E. Rusiński, R. Rybaniec, H. Sahling, M. Salmani, L. Samoylova, D. Sanzone, F. Saretzki, O. Sawlanski, J. Schaffran, H. Schlarb, M. Schlösser, V. Schlott, C. Schmidt, F. Schmidt-Foehre, M. Schmitz, M. Schmökel, T. Schnautz, E. Schneidmiller, M. Scholz, B. Schönebürg, J. Schultze, C. Schulz, A. Schwarz, J. Sekutowicz, D. Sellmann, E. Semenov, S. Serkez, D. Sertore, N. Shehzad, P. Shemarykin, L. Shi, M. Sienkiewicz, D. Sikora, M. Sikorski, A. Silenzi, C. Simon, W. Singer, X. Singer, H. Sinn, K. Sinram, N. Skvorod-

nev, P. Smirnow, T. Sommer, A. Sorokin, M. Stadler, M. Steckel, B. Steffen, N. Steinhau-Kühl, F. Stephan, M. Stodulski, M. Stolper, A. Sulimov, R. Susen, J. Świerblewski, C. Sydlo, E. Syresin, V. Sytchev, J. Szuba, N. Tesch, J. Thie, A. Thiebault, K. Tiedtke, D. Tischhauser, J. Tolkiehn, S. Tomin, F. Tonisch, F. Toral, I. Torbin, A. Trapp, D. Treyer, G. Trowitzsch, T. Trublet, T. Tschentscher, F. Ullrich, M. Vannoni, P. Varela, G. Varghese, G. Vashchenko, M. Vasic, C. Vazquez-Velez, A. Verguet, S. Vilcins-Czvitkovits, R. Villanueva, B. Visentin, M. Viti, E. Vogel, E. Volobuev, R. Wagner, N. Walker, T. Wamsat, H. Weddig, G. Weichert, H. Weise, R. Wenndorf, M. Werner, R. Wichmann, C. Wiebers, M. Wiencek, T. Wilksen, I. Will, L. Winkelmann, M. Winkowski, K. Wittenburg, A. Witzig, P. Wlk, T. Wohlenberg, M. Wojciechowski, F. Wolff-Fabris, G. Wrochna, K. Wrona, M. Yakopov, B. Yang, F. Yang, M. Yurkov, I. Zagorodnov, P. Zalden, A. Zavadtsev, D. Zavadtsev, A. Zhirnov, A. Zhukov, V. Ziemann, A. Zolotov, N. Zolotukhina, F. Zummack, and D. Zybin, "A MHz-repetition-rate hard X-ray free-electron laser driven by a superconducting linear accelerator," *Nat. Photonics 2020 146*, vol. 14, pp. 391–397, may 2020.

[196] T. O. Raubenheimer, "The LCLS-II-HE, a high energy upgrade of the LCLS-II," in *FLS 2018 - Proc. 60th ICFA Adv. Beam Dyn. Work. Futur. Light Sources*, pp. 6–11, Joint Accelerator Conferences Website (JACoW), jun 2018.

[197] J. Stohr, "Linac Coherent Light Source II (LCLS-II) Conceptual Design Report," tech. rep., SLAC National Accelerator Laboratory (SLAC), Menlo Park, CA (United States), nov 2011.

[198] J. R. Winkler, C. Creutz, and N. Sutin, "Solvent Tuning of the Excited-State Properties of (2,2-Bipyridine)tetracyanoferrate(II): Direct Observation of a Metal-to-Ligand Charge-Transfer Excited State of Iron(II)," *J. Am. Chem. Soc.*, vol. 109, no. 11, pp. 3470–3471, 1987.

[199] R. W. Taft, N. J. Pienta, M. J. Hamlet, and E. M. Arnett, "Linear Solvation Energy Relationships. 7. Correlations between the Solvent-Donicity and Acceptor-Number Scales and the Solvatochromic Pa-

rameters π, α, and β," *J. Org. Chem.*, vol. 46, no. 4, pp. 661–667, 1981.

[200] G. N. Lewis, *Valence and the Structure of Atoms and Molecules*. New York: The Chemical Catalog Company, Inc., 1923.

[201] U. Mayer, "A semiempirical model for the description of solvent effects on chemical reactions," *Pure Appl. Chem.*, vol. 51, no. 8, pp. 1697–1712, 1979.

[202] C. J. Timpson, C. A. Bignozzi, B. Patrick Sullivan, E. M. Kober, and T. J. Meyer, "Influence of solvent on the spectroscopic properties of cyano complexes of ruthenium(II)," *J. Phys. Chem.*, vol. 100, pp. 2915–2925, feb 1996.

[203] R. M. Jay, V. Vaz Da Cruz, S. Eckert, M. Fondell, R. Mitzner, and A. Föhlisch, "Probing Solute-Solvent Interactions of Transition Metal Complexes Using L-Edge Absorption Spectroscopy," *J. Phys. Chem. B*, vol. 124, pp. 5636–5645, jul 2020.

[204] T. J. Penfold, M. Reinhard, M. H. Rittmann-Frank, I. Tavernelli, U. Rothlisberger, C. J. Milne, P. Glatzel, and M. Chergui, "X-ray spectroscopic study of solvent effects on the ferrous and ferric hexacyanide anions," *J. Phys. Chem. A*, vol. 118, pp. 9411–9418, oct 2014.

[205] K. Kunnus, L. Li, C. J. Titus, S. J. Lee, M. E. Reinhard, S. Koroidov, K. S. Kjær, K. Hong, K. Ledbetter, W. B. Doriese, G. C. O'Neil, D. S. Swetz, J. N. Ullom, D. Li, K. Irwin, D. Nordlund, A. A. Cordones, and K. J. Gaffney, "Chemical control of competing electron transfer pathways in iron tetracyano-polypyridyl photosensitizers," *Chem. Sci.*, vol. 11, no. 17, pp. 4360–4373, 2020.

[206] J. Kondrup, *Quantum Chemistry on Functional Transition-metal Complexes*. Bachelor thesis, Technical University of Denmark, 2019.

[207] S. Mai, H. Gattuso, A. Monari, and L. González, "Novel Molecular-Dynamics-Based Protocols for Phase Space Sampling in Complex Systems," *Front. Chem.*, vol. 6, no. 495, pp. 1–14, 2018.

[208] D. Case, D. Cerutti, T. Cheatham, III, T. Darden, R. Duke, T. Giese, H. Gohlke, A. Goetz, D. Greene, N. Homeyer, S. Izadi, A. Kovalenko, T. Lee, S. LeGrand, P. Li, C. Lin, J. Liu, T. Luchko, R. Luo, D. Mermelstein, K. Merz, G. Monard, H. Nguyen, I. Omelyan, A. Onufriev, F. Pan, R. Qi, D. Roe, A. Roitberg, C. Sagui, C. Simmerling, W. Botello-Smith, J. Swails, R. Walker, J. Wang, R. Wolf, X. Wu, L. Xiao, D. York, and P. Kollman, "AMBER 2017," 2017.

[209] P. Li and K. M. Merz, "MCPB.py: A Python Based Metal Center Parameter Builder," *J. Chem. Inf. Model.*, vol. 56, pp. 599–604, 2016.

[210] S. Grimme, J. Antony, S. Ehrlich, and H. Krieg, "A consistent and accurate ab initio parametrization of density functional dispersion correction (DFT-D) for the 94 elements H-Pu," *J. Chem. Phys.*, vol. 132, p. 154104, apr 2010.

[211] A. D. Becke, "A new mixing of Hartree-Fock and local density-functional theories," *J. Chem. Phys.*, vol. 98, no. 2, pp. 1372–1377, 1993.

[212] P. J. Hay and W. R. Wedt, "Ab initio effective core potentials for molecular calculations. Potentials of K to Au including the outermost core orbitals," *J. Chem. Phys*, vol. 82, no. 1, pp. 299–310, 1985.

[213] S. Mai and L. González, "Unconventional two-step spin relaxation dynamics of [Re(CO)3(im)(phen)]+ in aqueous solution," *Chem. Sci.*, vol. 10, no. 44, pp. 10405–10411, 2019.

[214] M. Barbatti and K. Sen, "Effects of different initial condition samplings on photodynamics and spectrum of pyrrole," *Int. J. Quantum Chem.*, vol. 116, pp. 762–771, may 2016.

[215] N. Klaffki, O. Weingart, M. Garavelli, and E. Spohr, "Sampling excited state dynamics: Influence of HOOP mode excitations in a retinal model," *Phys. Chem. Chem. Phys.*, vol. 14, pp. 14299–14305, nov 2012.

[216] J. P. Zobel, M. Heindl, J. J. Nogueira, and L. González, "Vibrational Sampling and Solvent Effects on the Electronic Structure of the Absorption Spectrum of 2-Nitronaphthalene," *J. Chem. Theory Comput.*, vol. 14, pp. 3205–3217, jun 2018.

[217] G. Granucci, M. Persico, and A. Toniolo, "Direct semiclassical simulation of photochemical processes with semiempirical wave functions," *J. Chem. Phys.*, vol. 114, pp. 10608–10615, jun 2001.

[218] F. Plasser, M. Ruckenbauer, S. Mai, M. Oppel, P. Marquetand, and L. González, "Efficient and Flexible Computation of Many-Electron Wave Function Overlaps," *J. Chem. Theory Comput.*, vol. 12, pp. 1207–1219, mar 2016.

[219] G. Granucci and M. Persico, "Critical appraisal of the fewest switches algorithm for surface hopping," *J. Chem. Phys.*, vol. 126, p. 134114, apr 2007.

[220] F. Neese, "The ORCA program system," *Wiley Interdiscip. Rev. Comput. Mol. Sci.*, vol. 2, pp. 73–78, jan 2012.

[221] S. Saureu and C. D. Graaf, "TD-DFT study of the light-induced spin crossover," *Phys. Chem. Chem. Phys.*, vol. 18, pp. 1233–1244, 2016.

[222] M. Pápai, G. Vankó, C. D. Graaf, and T. Rozgonyi, "Theoretical Investigation of the Electronic Structure of Fe (II) Complexes at Spin-State Transitions," *J. Chem. Theory Comput.*, vol. 9, pp. 509–519, 2013.

[223] R. G. Lee, Chengteh; Yang, Weitao; Parr, "Development of the Colle-Salvetti correlation energy formula into a functional of the electron density," *Phys. Rev. B.*, vol. 37, no. 2, pp. 785–789, 1988.

[224] P. J. Stephens, F. J. Devlin, C. F. Chabalowski, and M. J. Frisch, "Ab Initio calculation of vibrational absorption and circular dichroism spectra using density functional force fields," *J. Phys. Chem.*, vol. 98, no. 45, pp. 11623–11627, 1994.

[225] S. Faas, J. Snijders, J. van Lenthe, E. van Lenthe, and E. Baerends, "The ZORA formalism applied to the Dirac-Fock equation," *Chem. Phys. Lett.*, vol. 246, pp. 632–640, dec 1995.

[226] E. van Lenthe, E. J. Baerends, and J. G. Snijders, "Relativistic regular two-component Hamiltonians," *J. Chem. Phys.*, vol. 99, no. 6, p. 4597, 1993.

[227] F. Weigend and R. Ahlrichs, "Balanced basis sets of split valence, triple zeta valence and quadruple zeta valence quality for H to Rn: Design and assessment of accuracy," *Phys. Chem. Chem. Phys.*, vol. 7, pp. 3297–3305, sep 2005.

[228] J. P. Zobel, O. S. Bokareva, P. Zimmer, C. Wölper, M. Bauer, and L. González, "Intersystem Crossing and Triplet Dynamics in an Iron(II) N-Heterocyclic Carbene Photosensitizer," *Inorg. Chem.*, vol. 4, p. 35, 2020.

[229] M. Barbatti, G. Granucci, M. Persico, M. Ruckenbauer, M. Vazdar, M. Eckert-Maksić, and H. Lischka, "The on-the-fly surface-hopping program system Newton-X: Application to ab initio simulation of the nonadiabatic photodynamics of benchmark systems," *J. Photochem. Photobiol. A Chem.*, vol. 190, pp. 228–240, aug 2007.

[230] M. Barbatti, M. Ruckenbauer, F. Plasser, J. Pittner, G. Granucci, M. Persico, and H. Lischka, "Newton-X: A surface-hopping program for nonadiabatic molecular dynamics," *Wiley Interdiscip. Rev. Comput. Mol. Sci.*, vol. 4, pp. 26–33, jan 2014.

[231] J. Wu, M. Alías, and C. D. Graaf, "Controlling the Lifetime of the Triplet MLCT State in Fe (II) Polypyridyl Complexes through Ligand Modification," *Inorganics*, vol. 8, no. 16, pp. 1–17, 2020.

[232] L. Fodor, G. Lendvay, and A. Horváth, "Solvent dependence of absorption and emission spectra of Ru(bpy) 2(CN)2: Experiment and explanation based on electronic structure theory," *J. Phys. Chem. A*, vol. 111, pp. 12891–12900, dec 2007.

[233] T. Megyes, G. Schubert, M. Kovás, T. Radnai, T. Grósz, I. Bakó, I. Pápai, and A. Horváth, "Structure and properties of the [Ru(bpy)(CN)4]2- complex and its solvent environment: X-ray diffraction and density functional study," *J. Phys. Chem. A*, vol. 107, pp. 9903–9909, nov 2003.

[234] T. Österman, M. Abrahamsson, H. C. Becker, L. Hammarström, and P. Persson, "Influence of triplet state multidimensionality on excited state lifetimes of bis-tridentate Ru II complexes: A computational study," *J. Phys. Chem. A*, vol. 116, pp. 1041–1050, jan 2012.

[235] L. A. Fredin, M. Pápai, E. Rozsályi, G. Vankó, K. Wärnmark, V. Sundström, and P. Persson, "Exceptional excited-state lifetime of an iron(II)- N -heterocyclic carbene complex explained," *J. Phys. Chem. Lett.*, vol. 5, no. 12, pp. 2066–2071, 2014.

[236] C. de Graaf and C. Sousa, "Study of the Light-Induced Spin Crossover Process of the [Fe II (bpy) 3] 2+ Complex," *Chem. - A Eur. J.*, vol. 16, pp. 4550–4556, apr 2010.

[237] C. de Graff and C. Sousa, "On the Role of the Metal-to-Ligand Charge Transfer States in the Light-Induced Spin Crossover in FeII(bpy)3," *Int. J. Quantum Chem.*, vol. 111, pp. 3385–3393, 2011.

[238] S. Iuchi and N. Koga, "A model electronic Hamiltonian to describe low-lying d–d and metal-to-ligand charge-transfer excited states of [Fe(bpy)3]ˆ2+," *J. Comput. Chem.*, pp. 1–14, nov 2020.

[239] P. Yu, F. Yang, J. Zhao, and J. Wang, "Hydration dynamics of cyanoferrate anions examined by ultrafast infrared spectroscopy," *J. Phys. Chem. B*, vol. 118, pp. 3104–3114, mar 2014.

[240] W. Roseker, S. Lee, M. Walther, F. Lehmkühler, B. Hankiewicz, R. Rysov, S. O. Hruszkewycz, G. B. Stephenson, M. Sutton, P. H. Fuoss, M. Sikorski, A. Robert, S. Song, and G. Grübel, "Double-pulse speckle contrast correlations with near Fourier transform limited free-electron laser light using hard X-ray split-and-delay," *Sci. Rep.*, vol. 10, pp. 1–9, dec 2020.

[241] M. Pápai, T. Rozgonyi, T. J. Penfold, M. M. Nielsen, and K. B. Møller, "Simulation of ultrafast excited-state dynamics and elastic X-ray scattering by quantum wavepacket dynamics," *J. Chem. Phys.*, vol. 151, no. 10, 2019.

[242] W. Gawelda, V. T. Pham, R. M. Van Der Veen, D. Grolimund, R. Abela, M. Chergui, and C. Bressler, "Structural analysis of ultrafast extended x-ray absorption fine structure with subpicometer spatial resolution: Application to spin crossover complexes," *J. Chem. Phys.*, vol. 130, p. 124520, mar 2009.

[243] C. Bressler, C. Milne, V. T. Pham, A. ElNahhas, R. van der Veen, W. Gawelda, S. Johnson, P. Beaud, D. Grolimund, M. Kaiser,

C. Borca, G. Ingold, R. Abela, and M. Chergui, "Femtosecond XANES Study of the Light-Induced Spin Crossover Dynamics in an Iron(II) Complex," *Science*, vol. 323, no. January, pp. 489–492, 2009.

[244] N. Huse, T. K. Kim, L. Jamula, J. K. McCusker, F. M. De Groot, and R. W. Schoenlein, "Photo-induced spin-state conversion in solvated transition metal complexes probed via time-resolved soft X-ray spectroscopy," *J. Am. Chem. Soc.*, vol. 132, pp. 6809–6816, may 2010.

[245] S. Nozawa, T. Sato, M. Chollet, K. Ichiyanagi, A. Tomita, H. Fujii, S. I. Adachi, and S. Y. Koshihara, "Direct probing of spin state dynamics coupled with electronic and structural modifications by picosecond time-resolved XAFS," *J. Am. Chem. Soc.*, vol. 132, pp. 61–63, jan 2010.

[246] W. White, A. Robert, and M. Dunne, "The Linac Coherent Light Source," *J. Synchrotron Radiat.*, vol. 22, pp. 472–476, 2015.

[247] M. Yabashi, H. Tanaka, and T. Ishikawa, "Overview of the SACLA facility," *J. Synchrotron Radiat.*, vol. 22, no. 3, pp. 477–484, 2015.

[248] T. Schietinger, M. Pedrozzi, M. Aiba, V. Arsov, S. Bettoni, B. Beutner, M. Calvi, P. Craievich, M. Dehler, F. Frei, R. Ganter, C. P. Hauri, R. Ischebeck, Y. Ivanisenko, M. Janousch, M. Kaiser, B. Keil, F. Löhl, G. L. Orlandi, C. Ozkan Loch, P. Peier, E. Prat, J. Y. Raguin, S. Reiche, T. Schilcher, P. Wiegand, E. Zimoch, D. Anicic, D. Armstrong, M. Baldinger, R. Baldinger, A. Bertrand, K. Bitterli, M. Bopp, H. Brands, H. H. Braun, M. Brönnimann, I. Brunnenkant, P. Chevtsov, J. Chrin, A. Citterio, M. Csatari Divall, M. Dach, A. Dax, R. Ditter, E. Divall, A. Falone, H. Fitze, C. Geiselhart, M. W. Guetg, F. Hämmerli, A. Hauff, M. Heiniger, C. Higgs, W. Hugentobler, S. Hunziker, G. Janser, B. Kalantari, R. Kalt, Y. Kim, W. Koprek, T. Korhonen, R. Krempaska, M. Laznovsky, S. Lehner, F. Le Pimpec, T. Lippuner, H. Lutz, S. Mair, F. Marcellini, G. Marinkovic, R. Menzel, N. Milas, T. Pal, P. Pollet, W. Portmann, A. Rezaeizadeh, S. Ritt, M. Rohrer, M. Schär, L. Schebacher, S. Scherrer, V. Schlott, T. Schmidt, L. Schulz, B. Smit, M. Stadler, B. Steffen, L. Stingelin, W. Sturzenegger, D. M. Treyer, A. Trisorio, W. Tron, C. Vicario,

R. Zennaro, and D. Zimoch, "Commissioning experience and beam physics measurements at the SwissFEL Injector Test Facility," oct 2016.

[249] C. J. Milne, T. Schietinger, M. Aiba, A. Alarcon, J. Alex, A. Anghel, V. Arsov, C. Beard, P. Beaud, S. Bettoni, M. Bopp, H. Brands, M. Brönnimann, I. Brunnenkant, M. Calvi, A. Citterio, P. Craievich, M. C. Divall, M. Dällenbach, M. D'Amico, A. Dax, Y. Deng, A. Dietrich, R. Dinapoli, E. Divall, S. Dordevic, S. Ebner, C. Erny, H. Fitze, U. Flechsig, R. Follath, F. Frei, F. Gärtner, R. Ganter, T. Garvey, Z. Geng, I. Gorgisyan, C. Gough, A. Hauff, C. P. Hauri, N. Hiller, T. Humar, S. Hunziker, G. Ingold, R. Ischebeck, M. Janousch, P. Juranić, M. Jurcevic, M. Kaiser, B. Kalantari, R. Kalt, B. Keil, C. Kittel, G. Knopp, W. Koprek, H. T. Lemke, T. Lippuner, D. L. Sancho, F. Löhl, C. Lopez-Cuenca, F. Märki, F. Marcellini, G. Marinkovic, I. Martiel, R. Menzel, A. Mozzanica, K. Nass, G. L. Orlandi, C. O. Loch, E. Panepucci, M. Paraliev, B. Patterson, B. Pedrini, M. Pedrozzi, P. Pollet, C. Pradervand, E. Prat, P. Radi, J. Y. Raguin, S. Redford, J. Rehanek, J. Réhault, S. Reiche, M. Ringele, J. Rittmann, L. Rivkin, A. Romann, M. Ruat, C. Ruder, L. Sala, L. Schebacher, T. Schilcher, V. Schlott, T. Schmidt, B. Schmitt, X. Shi, M. Stadler, L. Stingelin, W. Sturzenegger, J. Szlachetko, D. Thattil, D. M. Treyer, A. Trisorio, W. Tron, S. Vetter, C. Vicario, D. Voulot, M. Wang, T. Zamofing, C. Zellweger, R. Zennaro, E. Zimoch, R. Abela, L. Patthey, and H. H. Braun, "SwissFEL: The Swiss X-ray Free Electron Laser," *Appl. Sci.*, vol. 7, no. 7, pp. 1–57, 2017.

[250] I. S. Ko, H. S. Kang, H. Heo, C. Kim, G. Kim, C. K. Min, H. Yang, S. Y. Baek, H. J. Choi, G. Mun, B. R. Park, Y. J. Suh, D. C. Shin, J. Hu, J. Hong, S. Jung, S. H. Kim, K. H. Kim, D. Na, S. S. Park, Y. J. Park, Y. G. Jung, S. H. Jeong, H. G. Lee, S. Lee, S. Lee, B. Oh, H. S. Suh, J. H. Han, M. H. Kim, N. S. Jung, Y. C. Kim, M. S. Lee, B. H. Lee, C. W. Sung, I. S. Mok, J. M. Yang, Y. W. Parc, W. W. Lee, C. S. Lee, H. Shin, J. H. Kim, Y. Kim, J. H. Lee, S. Y. Park, J. Kim, J. Park, I. Eom, S. Rah, S. Kim, K. H. Nam, J. Park, J. Park, S. Kim, S. Kwon, R. An, S. H. Park, K. S. Kim, H. Hyun, S. N. Kim, S. Kim, C. J. Yu, B. S. Kim, T. H. Kang, K. W. Kim, S. H. Kim, H. S. Lee, H. S. Lee, K. H. Park, T. Y.

Koo, D. E. Kim, and K. B. Lee, "Construction and commissioning of PAL-XFEL facility," *Appl. Sci.*, vol. 7, no. 5, pp. 1–11, 2017.